



**University of
Nottingham**

UK | CHINA | MALAYSIA

Primordial Gravitational Waves in the Cosmic Microwave Background

Thomas James Clarke

Student ID: 14275185

Thesis submitted to the University of Nottingham
for the degree of Doctor of Philosophy

August 2020

Acknowledgements



— Adam Neely

First and foremost I would like to thank my supervisors, Adam and Ed. Adam, you have devoted a great deal of effort and patience into the completion of this work and I have learnt so much from you. Ed, you have been an excellent guide throughout this project and I have enjoyed the mathematical rabbit holes we have been able to dive down together. I would also like to thank Tasos and Dani for all their comments on this thesis, finding time to read it all (despite current factors) and their help in improving it.

Thank you to everyone who I have been lucky enough to spend time with in the Particle Cosmology and Astronomy groups at the University of Nottingham. So many of you do so much to make it a brilliant place to spend a lot of time and also to make it an environment conducive to discussion, learning and creativity.

While in Nottingham I was lucky enough to live with two people who greatly enriched my experience. Martha, I learnt so much from you about the world and about myself. I think it was a year of great personal growth and I credit your influence almost exclusively with that. It was also great fun and I hope to continue to want to talk to you about every film I watch, even if they can't be viewed within the hallowed ground of Broadway. Finlay, my proof-reader extraordinaire (among many other achievements), I had so much fun with you and so much laughter. Thank you for persuading me to go to Wing Chun with you and thank you for repeatedly punching me in the head until I got a bit better at stopping it. I also had great fun climbing with you and seeing you doing things that shouldn't be possible. It was always nice having music round the house (or the JA), whether that was a gruff American Boss or folk music from our own hands.

Thank you to my parents who have supported me so wholeheartedly in myriad ways. Your efforts do not go unnoticed and I'm exceptionally grateful for everything you do. Without a Dr. Clarke before me I probably would not have thought this possible.

I am lucky enough to have friends willing to go far above and beyond the level of support that I would expect. Special thanks must go to Charutha, Malin, Sofía and Hannah; thank you for being my still points in a turning world. Thank you to Adrian and Fiona for your guidance.

Thank you to Elis and John for shining light in the dark, Deborah Frances-White for just enough guilt to learn and laugh, and the Good Doctors, Kermode and Mayo for some A-flight wittering.

To my partner, you have been truly extraordinary throughout my PhD and I'm so grateful for you helping me through this. I'll defer further, soppiest gratitude to a more direct mode of communication.

Declaration

No part of this thesis has previously been submitted for a degree or other qualification at this or any other university.

Chapters 3 and 4 are based on the following research:

- Thomas J. Clarke, Edmund J. Copeland and Adam Moss. Constraints on primordial gravitational waves from the Cosmic Microwave Background. Published in the Journal of Cosmology and Astroparticle Physics (JCAP), DOI:10.1088/1475-7516/2020/10/002, arXiv:2004.11396, 2020.

Chapter 5 contains work currently being prepared for publication.

Supervisors: Dr. A. J. Moss
Prof. E. J. Copeland

Examiners: Dr. Daniel G. Figueroa (Universidad de Valencia)
Dr. Anastasios Avgoustidis (University of Nottingham)

Submitted: 18th August 2020

Examined: 29th September 2020

Final Version: 12th January 2021

Abstract

The study of gravitational waves is one of the most exciting areas of modern physics. As a relatively young observational field it promises a great deal of new and important information about the Universe in which we find ourselves. This thesis investigates the behaviour of gravitational waves in cosmology. As such, it starts with details of: the standard model of cosmology, Λ CDM; relevant observational techniques; techniques for data analysis and the theoretical and observational details of cosmological gravitational waves.

The background details motivate further investigation of how best to constrain primordial gravitational waves using the cosmic microwave background. I present reproductions and improvements on two existing techniques, valid for short- and long-wavelength gravitational waves respectively, before developing an approach applicable for all wavelengths. This new approach is thoroughly explored, consistency checks are performed and a new constraint on primordial gravitational waves in a previously unconstrained frequency region is presented.

As a result of calculations of the evolution of gravitational waves in the new approach, attention then turns to the Hubble tension. I review existing attempts to alleviate the Hubble tension before focusing on and constraining the axion model which has emerged as one of the more successful models for addressing the H_0 problem. A model-independent approach is introduced that can be used to determine which modifications to the background expansion of the Universe are necessary to reduce the Hubble tension. This approach will be useful for comparison of models that aim to alleviate the Hubble tension by modifying the expansion history, such as the gravitational wave model introduced here.

Conventions

There are mathematical conventions used throughout Cosmology and an understanding of Einstein's general theory of relativity is assumed here (though foregoing this and assuming the equations derived are correct should not greatly reduce comprehension). The metric signature will be mostly positive, i.e. $(-, +, +, +)$.

Natural units are used where $\hbar, c, k_B = 1$, where \hbar is the reduced Planck constant, c is the speed of light and k_B is Boltzmann's constant, such that all quantities have dimensions of giga-electronvolts (GeV) and relevant powers. It is often convenient in cosmology to work solely in megaparsecs (Mpc) using the conversions, $1 \text{ GeV}^{-1} \rightarrow 6.58 \times 10^{-25} \text{ s}$, $1 \text{ GeV}^{-1} \rightarrow 6.38 \times 10^{-39} \text{ Mpc}$. The gravitational constant G will not be set to unity. Conversions between frequencies and wavenumbers are done using,

$$f = (1.55 \times 10^{-15} \text{ Hz Mpc}) \times k, \quad (1)$$

where the numerical factor comes from the speed of light and the definition of a parsec. Similarly,

$$H_0 = 3.3 \times 10^{-4} h \text{ Mpc}^{-1} \equiv 3.2 \times 10^{-18} h \text{ s}^{-1}. \quad (2)$$

Latin indices are used to denote spatial 3-vectors, e.g. x_i , while Greek indices e.g. x_μ , denote spacetime 4-vectors of the kind (t, \vec{x}) . Einstein summation convention will be utilised unless stated otherwise.

Conformal time is strongly favoured over cosmological time. τ and t will be used for conformal and cosmological time respectively. Dots will denote differentiation with respect to conformal time throughout.

The Universe is assumed to be flat throughout. This is well justified by *Planck* 2018 cosmic microwave background and Baryon Oscillation Spectroscopic Survey (BOSS) baryon acoustic oscillation data [1] which shows that the curvature density parameter, $\Omega_K = 0.001 \pm 0.002$.

It is common in the literature to see density parameters, Ω_i as constants that are evaluated today and as dynamical functions, e.g. $\Omega_i(a)$. In this thesis

all density parameters are evaluated at the current time.

The normalisation employed for Fourier transforms is,

$$f(\vec{x}) = \frac{V}{(2\pi)^3} \int d^3k f(\vec{k}) e^{i\vec{k}\cdot\vec{x}}, \quad (3)$$

$$f(\vec{k}) = \frac{1}{V} \int d^3x f(\vec{x}) e^{i\vec{k}\cdot\vec{x}}. \quad (4)$$

such that the dimensions are the same for a function and its Fourier transform. The volume factor, V can be thought of as being set to one for convenience. The volume factor doesn't enter into the integral definition of the Dirac delta function. When going to Fourier space,

$$f(x) \rightarrow f(k), \partial_i f(x) \rightarrow ik_i f(k), \partial_i \partial^i f(x) \rightarrow -k^2 f(k). \quad (5)$$

Abbreviations

BAO	baryon acoustic oscillations
BBN	Big Bang nucleosynthesis
CDM	cold dark matter
CMB	cosmic microwave background
FLRW	Friedmann–Lemaître–Robertson–Walker
GR	general relativity
GWs	gravitational waves
ISW	integrated Sachs-Wolfe
LIGO	Laser Interferometer Gravitational-Wave Observatory
MCMC	Markov chain Monte Carlo
MIA	model-independent approach
PCA	Principal component analysis
PGWs	primordial gravitational waves
PPF	parameterised post-Friedmann
TT	transverse-traceless
<i>WMAP</i>	Wilkinson Microwave Anisotropy Probe

Contents

Acknowledgements	ii
Declaration	iv
Abstract	v
Conventions	vi
Abbreviations	viii
1 The Standard Model of Cosmology	1
1.1 Introduction	1
1.2 Modern cosmology	3
1.2.1 Conformal time	6
1.2.2 Inflation	7
1.2.3 Λ CDM	8
1.3 Cosmological perturbation theory	12
1.3.1 Gauges	12
1.3.2 Perturbing Einstein's equations	16
1.3.3 Initial conditions	18
1.4 The cosmic microwave background	21
1.4.1 Power spectrum	22
1.4.2 The different contributions to the CMB power spectrum	26
1.4.3 Polarisation	29
1.4.4 CMB lensing	34
1.4.5 CMB parameters	37
1.4.6 The H_0 problem	45
1.5 Data and analysis	48

1.5.1	CAMB	48
1.5.2	Cosmological parameter estimation, MCMC and CosmoMC	49
1.5.3	Data	52
2	Cosmological Gravitational Waves	57
2.1	Introduction	57
2.2	Linearised gravity and beyond	57
2.2.1	Linearised gravity	58
2.2.2	Beyond flat, vacuum spacetime	60
2.3	The shortwave approximation	63
2.4	A non-shortwave approach	66
2.4.1	Fluctuations	73
2.5	Detection	73
2.5.1	CMB B -modes	74
2.5.2	CMB isotropy	75
2.5.3	Big bang nucleosynthesis	76
2.5.4	Shortwave gravitational waves in the CMB	77
2.5.5	Interferometers	82
2.5.6	Pulsar timing	85
2.6	Sources of primordial gravitational waves	87
2.6.1	Inflation	89
2.6.2	Particle production during inflation	91
2.6.3	Preheating	91
2.6.4	First-order phase transitions	92
2.6.5	Cosmic strings	94
2.6.6	Primordial black holes	95
3	Short-Wavelength Gravitational Waves	96
3.1	Initial conditions	96
3.1.1	Homogeneous mode	97

3.1.2	Isocurvature modes	100
3.2	Effects on the CMB	103
3.3	Planck 2018 constraints	105
3.3.1	Parameter dependencies	106
3.4	Summary and outlook	108
4	Low-Frequency Gravitational Waves	111
4.1	B -mode constraint	112
4.2	Intermediate, non-shortwave approach	116
4.2.1	Calculating the density and pressure	116
4.2.2	The equation of state	123
4.2.3	Code	130
4.2.4	Validity of the shortwave approximation for CMB constraints	131
4.2.5	Behaviour of density and pressure	132
4.2.6	Neutrino anisotropic stress	134
4.2.7	Gravitational wave perturbations	138
4.2.8	Observables	140
4.2.9	Parameter constraints	143
4.3	Summary and outlook	145
5	Alleviating the H_0 Problem	148
5.1	Theoretical models for the Hubble tension	148
5.2	CAMB axion model	151
5.2.1	Results	154
5.3	Model-independent approach	156
5.3.1	Results	161
5.4	Principal component analysis	164
5.4.1	Results	166
5.5	Summary and outlook	169
6	Conclusions	172

Appendix	177
Bibliography	182

List of Tables

1.1	<i>Planck</i> 2018 baseline parameters	11
1.2	Adiabatic initial conditions in synchronous and Newtonian gauge	20
2.1	Adiabatic and homogeneous gravitational wave initial conditions in synchronous gauge	79
3.1	Homogeneous gravitational wave initial conditions	99
3.2	Neutrino isocurvature initial conditions	101
3.3	Gravitational wave isocurvature initial conditions	102
4.1	Constraints on gravitational wave density for delta-function sources	145
5.1	Mean and best-fit parameter values for axion early dark energy model	155
5.2	Mean and best-fit parameter values for model-independent ap- proach	163

List of Figures

1.1	<i>Planck</i> 2018 map of CMB	22
1.2	<i>Planck</i> 2018 CMB power spectrum	23
1.3	CMB power spectrum from density and velocity perturbations .	27
1.4	The CMB polarisation power spectra	32
1.5	The contribution of lensing to the CMB temperature power spectrum	35
1.6	CMB power spectrum for increasing N_{eff}	40
1.7	Tension between measurements of H_0	47
2.1	Gravitational wave polarisation	60
2.2	Contributions to the CMB power spectrum for homogeneous gravitational waves	80
2.3	Cosmological gravitational wave constraints	82
2.4	Gravitational wave background from slow-roll inflation	90
3.1	Contributions to the CMB power spectrum for adiabatic and homogeneous gravitational waves	104
3.2	CMB constraints to the gravitational wave density using the shortwave approximation	107
3.3	Parameter contours for adiabatic shortwave constraint	108
3.4	Parameter contours for homogeneous shortwave constraint . . .	109
4.1	Gravitational wave density parameter posterior probabilities for low frequency analysis	114

4.2	Low frequency, B -mode CMB constraint to gravitational wave density	115
4.3	Gravitational wave equation of state in non-shortwave approach	126
4.4	Gravitational wave equation of state during matter to cosmological constant transition	130
4.5	Gravitational wave density as a function of k and t in non-shortwave approach	133
4.6	The integrated gravitational wave density and equation of state as a function of t for the non-shortwave approach	135
4.7	Gravitational wave amplitude when including neutrino anisotropic stress	136
4.8	Gravitational wave density and equation of state when including neutrino anisotropic stress	137
4.9	CMB power spectrum for shortwave and non-shortwave gravitational waves	141
4.10	Hubble rate and radius of the sound horizon for shortwave and non-shortwave gravitational waves	142
4.11	New constraints on the gravitational wave density parameter . .	144
5.1	Early dark energy density and CMB power spectrum for best-fit models	156
5.2	Posterior probability distributions for the Hubble constant . . .	157
5.3	Illustration of behaviour of model-independent fluid approach .	159
5.4	Reconstruction of axion early dark energy fraction using model-independent fluid approach	160
5.5	Early dark energy density and CMB power spectrum for model-independent approach matched to best-fit axion models	161
5.6	Reconstructed energy density and equation of state of model-independent approach with cosmological constant	165

5.7	Reconstructed energy density and equation of state of model-independent approach without cosmological constant	166
5.8	Fractional energy density contribution for principal components	167
5.9	Change in CMB power spectrum for principal components . . .	168

Chapter 1

The Standard Model of Cosmology

1.1 Introduction

One of the most fundamental philosophical debates emerges when we ask how humanity has come to exist. Cosmology is the scientific discipline which attempts to answer this question by looking at the evolution of the Universe in which we find ourselves. Because of the wealth of work in the field of cosmology we now have a rigorous understanding of the growth of the Universe from the Big Bang through almost 14 billion years of evolution to the present day and are able to make predictions about the future.

The cornerstones of Cosmology are Einstein's theory of gravity [2], commonly called general relativity (GR), and Hubble's observation of a proportionality between the distance and redshift of galaxies¹ [4]. This confirmed the prediction of an expanding Universe made by Lemaître [5]. Together GR and an expanding Universe imply the Big Bang model in which an initially dense Universe expands and dilutes with time.

One of the greatest confirmations of the Big Bang theory is the observation of the cosmic microwave background (CMB). This is the heavily redshifted light from the edge of the observable universe and allows us to look back at the Universe approximately 380,000 years after the Big Bang. Before this time the Universe was opaque to electromagnetic radiation and consequently the CMB

¹The observation of an average redshift of galaxies was made earlier by Slipher, see Peacock [3] and references therein.

is the electromagnetic radiation from closest to the Big Bang that it is possible to observe. The CMB is of very uniform temperature with anisotropies of order one part in 10^5 on large scales. These anisotropies contain a wide variety of interesting physics and tell us a large amount about the early universe from which the CMB was emitted and the resulting universe through which the CMB has travelled. Despite their very small amplitude, the temperature anisotropies have been measured to remarkable precision by satellite experiments, with *COBE*, *WMAP* and *Planck* offering increasingly high precision observations [6–8]. This has enabled very stringent constraints to be put on models describing the contents and history of the universe.

There has been a great deal of excitement in the scientific community following the first direct observation of gravitational waves (GWs) in 2015 [9]. This came almost a century after the theoretical prediction of GWs by Einstein. The confirmation of the existence of GWs is particularly exciting for cosmologists as the Big Bang is expected to produce primordial gravitational waves (PGWs). These PGWs are not absorbed in the early universe like electromagnetic radiation and consequently allow us to look back to a time even closer to the Big Bang.

One of the characteristic signatures of PGWs that cosmologists have investigated extensively is *B*-mode polarisation of the CMB [10–13]. This characteristic circulating polarisation, similar in appearance to *B*-fields in electromagnetism, is of particular interest because there is less contamination relative to predicted signals than in the radial pattern, known as *E*-mode polarisation, or the temperature anisotropies. The parameter most often constrained by *B*-modes is the tensor-to-scalar ratio r_{k_*} . This is the ratio of the initial amplitudes of tensor (gravitational wave) perturbations to scalar perturbations at a specific value of the wavenumber k_* . Note that the units of k_* are usually Mpc^{-1} such that $r_{0.05}$ is the tensor-to-scalar ratio when the reference scale, $k_* = 0.05 \text{ Mpc}^{-1}$. The current best CMB-only constraint comes from the BICEP2/Keck Array analysis [14] and constrain $r_{0.05} < 0.07$ at 95% confidence

level.

However, it is also possible to calculate the effects of gravitational waves on the temperature anisotropies. This is useful because the temperature anisotropies have been measured to very high precision and therefore provide a complementary probe to B -mode polarisation. There has already been work done to model the contribution of short wavelength GWs to the CMB anisotropies but long wavelength gravitational waves have also been shown to have interesting and potentially important effects that will influence the CMB and the expansion rate of the Universe. This thesis is primarily aimed at calculating cosmological effects of PGWs and using these to constrain the amount of gravitational waves that existed in the early universe.

This chapter is devoted to relevant background information on cosmology with a particular focus on perturbation theory, the CMB and existing data. Chapter 2 contains background information on cosmological gravitational waves and details of existing constraints on their density. Chapter 3 details original work constraining gravitational waves with wavelengths shorter than the horizon size at recombination using the CMB, building on existing analyses. Gravitational waves that do not satisfy the short wavelength condition are constrained using polarisation and a new CMB approach in chapter 4. The use of this new approach to reduce existing tensions in the determination of the Hubble constant, H_0 using gravitational waves is an interesting possible application of this method and as such an investigation of the Hubble tension is detailed in chapter 5. Chapter 6 contains conclusions and areas for future work.

1.2 Modern cosmology

The cosmological principle states that, on large scales, the Universe is homogeneous and isotropic [5, 15]. Here homogeneous implies that the Universe looks the same at all locations and isotropic implies that the Universe looks the same in all directions. If the Universe is isotropic about two separate points then

it is also homogeneous. More loosely the cosmological principle tells us that observations of the Universe do not depend on your location.

Clearly the cosmological principle does not apply on all scales. The small scale Universe has large density fluctuations (often called people, planets or galaxies) but on very large scales the Universe has been shown to be homogeneous and isotropic [6, 16, 17].

The metric for an expanding homogeneous and isotropic universe is given by the Friedmann–Lemaître–Robertson–Walker (FLRW) metric [5, 15, 18–21]

$$ds^2 = -dt^2 + a^2(t)d\vec{x}^2, \quad (1.1)$$

where s is the spacetime separation or proper distance, t is the cosmological time, \vec{x} is the 3-vector position and $a(t)$ is the *scale factor* which encodes the expansion of the universe. The scale factor is an increasing function for an expanding universe and consequently two objects staying the same *co-moving* distance apart Δx , will move away from each other. The scale factor is normalised such that at the present time t_0 , $a(t_0) = 1$ and at the Big Bang $a(t = 0) = 0$.

Applying the Einstein equations to this metric for an energy–momentum tensor for an isotropic fluid with density ρ and pressure p , $\text{diag}[-\rho, p, p, p]$, produces the acceleration and Friedmann equations [15],

$$\frac{1}{a} \frac{d^2 a}{dt^2} = -\frac{4\pi G}{3}(\rho + 3p), \quad (1.2)$$

$$\frac{1}{a^2} \left(\frac{da}{dt} \right)^2 = \frac{8\pi G}{3} \rho, \quad (1.3)$$

where $G = (8.20 \times 10^{-20} \text{GeV}^{-1})^2$ is the gravitational constant. If the contents of the universe are specified via $\rho(a)$, the evolution of the scale factor $a(t)$ can be found using the Friedmann equation.

The Hubble factor, H is defined to be,

$$H = \frac{1}{a} \frac{da}{dt}. \quad (1.4)$$

The late time value is the Hubble constant H_0 which is the constant of proportionality between the recession velocity and distance of galaxies in Hubble's law, $v = H_0 d$ [4].

While the acceleration and Friedmann equations completely specify the evolution of the scale factor, another equation is commonly used which is a combination of the two. Most often called the continuity equation,

$$\frac{d\rho}{dt} + 3H(\rho + p) = 0, \quad (1.5)$$

is particularly useful when considering the evolution of a single species. It can be derived independently of the acceleration and Friedmann equations using the conservation of the energy–momentum tensor, $T^{\mu\nu}_{;\mu}$ where the semicolon denotes covariant differentiation, and is sometimes called the energy conservation equation as a result.

It is often convenient to split the contents of the universe into separate species depending on their evolution with time (e.g. radiation, matter, cosmological constant). Thus we can write the density in the Friedmann equation,

$$\rho = \sum_i \rho_i, \quad (1.6)$$

where the subscript i labels the different components of the universe being considered. The same approach is taken to the pressure. An important quantity for each species is the equation of state parameter, which gives the ratio between the pressure and density,

$$w_i = \frac{p_i}{\rho_i}. \quad (1.7)$$

The density required for the universe to be flat is called the critical density,

$$\rho_{\text{crit}} = \frac{3H^2}{8\pi G}. \quad (1.8)$$

The density parameter for each species is defined to be the ratio of the density

in the species to the critical density today (i.e. at t_0),

$$\Omega_i = \frac{\rho_{i,0}}{\rho_{\text{crit},0}} = \frac{8\pi G\rho_{i,0}}{3H_0^2}. \quad (1.9)$$

The universe is assumed to be flat throughout this thesis due to strong observational evidence [1] (see page vi). If curvature is included, the right hand side of equation (1.2) has an extra term, $-k/a^2$ where the curvature constant, $k = -1, 0, 1$ for hyperbolic, flat and spherical universes respectively [22]. This term can be treated as an effective density component which decays $\propto a^{-2}$. Consequently it has an equation of state of $-1/3$.

Including the appropriate dependence on the scale factor, dictated by the equation of state for each component, the Friedmann equation becomes,

$$H^2 = H_0^2 \sum_i \frac{\Omega_i}{a^{3(1+w_i)}}. \quad (1.10)$$

This takes a satisfyingly simple form at the present time,

$$\sum_i \Omega_i = 1. \quad (1.11)$$

1.2.1 Conformal time

A very useful and important concept in cosmology is the conformal time τ . It is defined by

$$dt = a(\tau)d\tau. \quad (1.12)$$

Using conformal time the FLRW metric becomes;

$$ds^2 = a(\tau)^2(-d\tau^2 + d\vec{x}^2). \quad (1.13)$$

Setting the integration constant in equation (1.12) such that the conformal time is zero at the Big Bang, the conformal time gives the size of the particle horizon at a given epoch. Put differently, the conformal time tells us about the evolution of the past light cone.

The conformal Hubble factor is given by,

$$\mathcal{H} = \frac{\dot{a}}{a} = aH, \quad (1.14)$$

where a dot denotes a derivative with respect to conformal time. In terms of conformal time the three cosmological equations above become,

$$\frac{\ddot{a}}{a} = -\frac{4\pi G a^2}{3}(\rho + 3p), \quad (1.15)$$

$$\mathcal{H}^2 = \frac{8\pi G a^2}{3}\rho, \quad (1.16)$$

$$\dot{\rho} = -3\mathcal{H}(\rho + p). \quad (1.17)$$

1.2.2 Inflation

Inflation [23–27] is a period of accelerated expansion early in the Universe’s history. Referring to equation (1.15) (or equation (1.2)), accelerated expansion ($\ddot{a} > 0$) requires $\rho + 3p < 0$, so the Universe must have been dominated by a species that has an equation of state parameter $w < -1/3$, for inflation to occur. Inflation gained popularity as it solved two cosmological problems, the horizon problem and the flatness problem and has since gained further validation through the observations of the CMB anisotropies (see Weinberg [28], Chapter 4 or Dodelson [22] Chapter 6).

The horizon problem refers to the fact that the Universe appears more isotropic than expected when observed through the CMB. Regions of the CMB separated by more than about two degrees on the sky are not expected to have been in causal contact (and hence at approximately the same temperature) in the standard Big Bang. Inflation solves this because small areas that are in causal contact during inflation become very large and can cover the full range of the sky observed in the CMB. This solution of the horizon problem can be used to put a limit on the amount of inflation required of about 60 e-foldings².

The flatness problem refers to the fact that the observed flatness of the

²An e-folding of N refers to the scale factor increasing by a factor of e^N .

Universe³ [1], $\sum_i \Omega_i = 1$ is an unstable solution in the standard cosmology. Unless the curvature is exactly zero any small difference will be amplified greatly as the Universe expands. Hence a large degree of fine-tuning is required at early times for the Universe to be flat now. During inflation the curvature density decreases and consequently the value of the curvature parameter is forced towards zero. If inflation is exponential ($w = -1$) we require there to have been approximately as much expansion during inflation as there has been since for the flatness problem to be solved without requiring fine-tuning.

The final, and arguably most powerful evidence for inflation comes from the anisotropies observed in the CMB. The basic idea of this is that quantum fluctuations in the inflaton field sourcing inflation are imprinted on the other species and give rise to the observed anisotropies. The nearly scale invariant, adiabatic and Gaussian perturbations observed are predicted in a range of inflation models.

It is useful to note that in our historical picture of the evolution of the Universe, inflation must be succeeded by a period, commonly known as reheating, in which the inflaton decays into the constituents of the Universe that we observe today (see [29–33] for details of this interesting area of cosmology).

1.2.3 Λ CDM

The current concordance model for our observable universe is often referred to as Λ CDM and has been incredibly successful in explaining a wide range of cosmological observables. It is primarily a specification of the contents of the Universe and consequently what species make up ρ in the Friedmann equation (1.16). The name comes from the two components added to the model in addition to the species of the Standard Model of particle physics which are the cosmological constant, Λ and cold dark matter (CDM). With this the contents of the Universe in Λ CDM are;

Baryonic matter: consisting of protons, neutrons and electrons with density

³See conventions on page vi.

parameter Ω_b and an equation of state $w_b = 0$.

Cold dark matter: some as yet undetected massive particle that is very weakly interacting. The density parameter for CDM is Ω_c and the equation of state $w_c = 0$ as for baryonic matter. These are often grouped together and simply called matter; $\Omega_m = \Omega_c + \Omega_b$.

Radiation: relativistic components consisting of photons and massless neutrinos. The density parameter for radiation is Ω_r and for photons only is Ω_γ . The density of neutrinos is most commonly given in terms of the effective number of relativistic degrees of freedom, N_{eff} defined by;

$$\rho_r = \left[1 + \frac{7}{8} \left(\frac{4}{11} \right)^{4/3} N_{\text{eff}} \right] \rho_\gamma. \quad (1.18)$$

In Λ CDM, $N_{\text{eff}} = 3.046$ because of the three neutrinos in the Standard Model of particle physics with a small correction due to the physics of the decoupling of neutrinos. The density of photons is set by an observation of the temperature of the CMB⁴ via the Stefan–Boltzmann law, $\rho_\gamma = \pi^2 T^4/15$. The current temperature of the CMB is 2.72548 ± 0.00057 K [34]. The radiation components have equation of state $w_r = 1/3$.

Cosmological constant: a term with constant energy density, $\rho_\Lambda = \Omega_\Lambda$ which has an equation of state, $w_\Lambda = -1$.

Hence the Friedmann equation in Λ CDM can be written,

$$\mathcal{H}^2 = H_0^2 a^2(\tau) \left(\frac{\Omega_m}{a^3(\tau)} + \frac{\Omega_r}{a^4(\tau)} + \Omega_\Lambda \right). \quad (1.19)$$

One of the attractive features of Λ CDM is that it depends on only 6 parameters. There is some freedom in the choice of which parameters to use but the conventional set are,

$$\{\Omega_b h^2, \Omega_c h^2, \theta_{\text{MC}}, \tau, A_s, n_s\}. \quad (1.20)$$

⁴This expression for the energy density of photons is used because the majority of photons are CMB photons and consequently others can be neglected in the calculation of the energy density.

Ω_b and Ω_c are the density parameters for baryons and cold dark matter defined above. They are multiplied here by a factor of h^2 which is a dimensionless parameter originally introduced because of the uncertainty in the Hubble parameter, $H_0 = 100 h \text{ km s}^{-1} \text{ Mpc}^{-1}$.

θ_{MC} is the angular size of the sound horizon at last scattering in degrees. It tells us about the wavelength of the oscillations of the perturbations in the coupled matter–radiation fluid when the CMB was emitted.

τ is the optical depth to reionisation. When the first stars and galaxies form they emit radiation that ionises neutral hydrogen. The electrons Thomson scatter CMB photons which partially obscures the temperature anisotropies and introduces extra CMB polarisation. The value of τ tells us the percentage of CMB photons that last scattered at the reionisation redshift z_{re} , e.g. $\tau = 0.1$ implies that 10% of CMB photons last scattered at z_{re} .

The final two parameters in equation (1.20), A_s and n_s give the amplitude of the initial scalar perturbations from inflation and their wavenumber dependence via the scalar spectral index respectively. The initial conditions are usually quantified through the primordial power spectrum,

$$P_s(k) = A_s(k_*) \left(\frac{k}{k_*} \right)^{n_s - 1}, \quad (1.21)$$

where k_* is a pivot scale, usually taken to be 0.05 Mpc^{-1} . The power spectrum quantifies the distribution of the temperature anisotropies as a function of wavenumber such that a large value of the power spectrum suggests larger perturbations. Note that if the primordial power spectrum is independent of k then it is said to be *scale invariant*, corresponding to $n_s = 1$.

An illustrative set of parameters taken from *Planck* [1] is shown in table 1.1. With a value of the Hubble constant of $h \sim 0.7$ we see that the Universe is made up of roughly 5% baryonic matter, 25% dark matter and 70% dark energy. These 6 parameters tell us about the complete history of the Universe since inflation. First, for the period above redshift ~ 3600 , the expansion is dominated by radiation. This is followed by a transition into matter domination

Table 1.1: *Planck* 2018 baseline parameters from ref. [1].

Parameter	$\Omega_b h^2$	$\Omega_c h^2$	$100 \theta_{\text{MC}}$	τ	$\ln(10^{10} A_s)$	n_s
Value	0.02233	0.1198	1.04089	0.0540	3.043	0.9652
Error (\pm)	0.00015	0.0012	0.00031	0.074	0.0014	0.0042

and then finally into cosmological constant domination in which the Universe expands exponentially. The present epoch is situated in the transition between matter and cosmological constant domination as evidenced by $\Omega_\Lambda \sim 0.7$.

We also see that the initial perturbations were of very small amplitude and are nearly scale invariant. The sound horizon subtends an angle of approximately 1 degree on the sky and about 5% of CMB photons were last scattered due to reionisation.

Parameters including Ω_m , H_0 , the age of the Universe, the redshift of reionisation and the redshift at which matter and radiation have equal densities are called derived parameters as they can be calculated from those given in table 1.1. There are a few common extensions to Λ CDM such as allowing for curvature, variation in N_{eff} , k dependence of the scalar spectral index and a value of the dark energy equation of state different from -1 . These are well constrained by current observations.

It is common for the terms ‘dark energy’ and ‘cosmological constant’ to be used quite interchangeably however there is a precise distinction between them. *Dark energy* refers to any model that attempts to explain the accelerated expansion of the Universe by including an extra component in the energy–momentum tensor. The *cosmological constant* refers to a specific dark energy model that has a constant energy density throughout the cosmological history and an equation of state of -1 .

1.3 Cosmological perturbation theory

While the cosmological principle applies on very large scales and at early times, it is of great interest to cosmologists to model how the cosmological principle is broken and how structure in the Universe evolves. One of the primary tools for this is perturbation theory⁵. The basic idea of this is that small perturbations are added on top of the homogeneous and isotropic solution and their evolution is calculated [36, 37]. In general relativity this involves adding a perturbation to the metric,

$$g_{\mu\nu} = \tilde{g}_{\mu\nu} + \delta g_{\mu\nu}, \quad (1.22)$$

where $\tilde{g}_{\mu\nu}$ is the background FLRW metric, and $\delta g_{\mu\nu}$ is the perturbation metric. We then add perturbations to the energy–momentum tensor and calculate the relationship between these and the metric perturbations.

1.3.1 Gauges

There are many choices available for the perturbation metric that give the same field equations and have the same background metric. This freedom in the perturbations is related to the freedom in defining the coordinates of the spacetime. The choice of the perturbation metric is commonly called a *gauge*. The transformations between the gauges are given by small-amplitude coordinate transformations,

$$x^\mu \rightarrow \tilde{x}^\mu = x^\mu + \xi^\mu, \quad (1.23)$$

where ξ^μ is small compared to both of the two different coordinate systems, x^μ and \tilde{x}^μ . As a result of this, different choices of the coordinates will result in different perturbations. The two different sets of coordinates are thought of as two different gauges of the metric in the linear perturbation theory that have the same background metric.

⁵A range of approaches with non-perturbative validity use computational simulations (see Vogelsberger et al. [35] for a recent review). Despite the large range of interesting results available, simulations will not be covered here.

The most general perturbed metric for linear perturbations is [22, 28, 38–40],

$$\begin{aligned} ds^2 = a^2(\tau) \{ & - (1 + 2A)d\tau^2 - 2(\partial_i B + \hat{B}_i)dx^i d\tau \\ & + [(1 + 2C)\delta_{ij} + 2(\partial_i \partial_j - \frac{\delta_{ij}}{3}\nabla^2)E \\ & + 2\partial_{(i}\hat{E}_{j)} + \hat{h}_{ij}]dx^i dx^j \}. \end{aligned} \quad (1.24)$$

Here there are four scalar degrees of freedom A, B, C and E , four vector degrees of freedom, two each in \hat{B}_i, \hat{E}_i and two tensor degrees of freedom in \hat{h}_{ij} . All hatted quantities are divergenceless (sometimes called transverse), e.g. $\partial^i \hat{B}_i = 0$, and the tensor perturbation is traceless, $\hat{h}^i_i = 0$. Consequently the ten degrees of freedom of the symmetric metric tensor have been decomposed into scalar, vector and tensor components. This is advantageous because of the *decomposition theorem* which states that, in linear perturbation theory, scalar, vector and tensor perturbations evolve independently. As a result these types of perturbation can be treated separately without having to worry about tensors sourcing extra scalar perturbations, for example. Because of this the perturbation equations for scalars are given in this section and tensors are considered in the next chapter. Vector perturbations aren't produced by inflation and decay quickly due to the expansion of the Universe so will be neglected.

It is possible to construct *gauge-invariant* variables from combinations of the above variables, i.e. variables that do not change when there is a coordinate transformation that preserves the background metric (as mentioned above), called a *gauge transformation* [41]. These are commonly called Bardeen variables and are given by,

$$\Phi_A = A + \frac{\dot{a}}{a}(B - \dot{E}) + (\dot{B} - \ddot{E}), \quad (1.25a)$$

$$\Phi_H = -C - \frac{\dot{a}}{a}(B - \dot{E}) + \frac{1}{3}\nabla^2 E, \quad (1.25b)$$

$$\hat{\Psi}_i = \dot{\hat{E}}_i - \hat{B}_i, \quad (1.25c)$$

$$\hat{h}_{ij}. \quad (1.25d)$$

There are two advantages of using these; firstly, there are no non-physical results coming from modes that only exist due to the choice of coordinates (and hence the gauge) and secondly, the results are applicable inside and outside the cosmological horizon. This second point is particularly important because fixed gauges agree about sub-horizon behaviour but can disagree about the super-horizon behaviour of the perturbations. Because of this, a gauge-invariant approach is a necessity when the super-horizon behaviour is of interest. To be precise we are defining the sub-horizon and super-horizon regimes as $k\tau \gg 1$ and $k\tau \ll 1$ respectively. This allows us to refer to ‘short wavelength’ modes which have wavelengths shorter than the size of the horizon and ‘long wavelength’ modes with wavelengths larger than the horizon.

It is worth noting that the decomposition into scalars, vectors and tensors has picked out the gauge-invariant tensor part of the perturbations and consequently these are the only tensor degrees of freedom that need to be considered in a cosmological context (more details of this will be covered in the next chapter).

The alternative approach is to fix the gauge by putting conditions on the metric perturbations which eliminates the gauge freedom. The two most widely used gauges are the *synchronous gauge* and the *Newtonian gauge* [42]. The synchronous gauge is defined by,

$$ds^2 = a^2(\tau) \left\{ -d\tau^2 + [(1+h)\delta_{ij} + (\partial_i\partial_j - \frac{1}{3}\delta_{ij}\nabla^2)\delta\eta + \hat{h}_{ij}]dx^i dx^j \right\}, \quad (1.26)$$

where the two scalar degrees of freedom h and η are equivalent to C and E of equation (1.24) and the tensor component is unchanged. This gauge is specified by setting $A = B = \hat{B}_i = \hat{E}_i = 0$ but there is still gauge freedom which is usually removed via an initial condition.

The Newtonian gauge (sometimes called longitudinal gauge) is defined by,

$$ds^2 = a^2(\tau) \left\{ - (1 + 2\psi)d\tau^2 + [(1 - 2\phi)\delta_{ij} + \hat{h}_{ij}]dx^i dx^j \right\}, \quad (1.27)$$

where ψ and ϕ are equivalent to A and C of equation (1.24) and the tensor component is unchanged. This gauge is specified by setting $B = \hat{B}_i = E = \hat{E}_i = 0$. One of the advantages of the Newtonian gauge is that the potentials are directly related to the gauge-invariant Bardeen variables, $\Phi_A = \psi$, $\Phi_H = \phi$. This gauge also has a well defined Newtonian limit.

It is important to be able to transform between gauges. The relations between gauges can be found by requiring that the background metric is left unchanged by a general coordinate transformation. Defining α via⁶,

$$\alpha = \frac{1}{2k^2}(\dot{h} + 6\dot{\eta}), \quad (1.28)$$

the transformations between the metric potentials in k-space are given by,

$$\psi = \dot{\alpha} + \frac{\dot{a}}{a}\alpha, \quad (1.29a)$$

$$\phi = \eta - \frac{\dot{a}}{a}\alpha. \quad (1.29b)$$

While all gauge considerations so far have been concerned with the metric side of Einstein's equations, the energy-momentum components also depend on the choice of gauge and the gauge can be fixed in the energy-momentum side of Einstein's equations, though this is less common. The relations between the energy-momentum perturbations⁷ in the Newtonian and synchronous gauges are,

$$\delta_{(\text{syn})} = \delta_{(\text{Newt})} + 3\frac{\dot{a}}{a}(1 + w)\alpha, \quad (1.30a)$$

$$\theta_{(\text{syn})} = \theta_{(\text{Newt})} - k^2\alpha, \quad (1.30b)$$

$$\sigma_{(\text{syn})} = \sigma_{(\text{Newt})}, \quad (1.30c)$$

where subscripts label the synchronous (syn) or Newtonian (Newt) gauge.

⁶Note that quantities are now in Fourier space.

⁷see next section for definitions.

1.3.2 Perturbing Einstein's equations

The previous section detailed how to perturb the metric; these metric perturbations will result in perturbations in the Einstein tensor. Once the perturbations to the Einstein tensor are calculated we also need to introduce perturbations to the energy–momentum tensor that will be related to the metric perturbations by Einstein's equations.

For a viscous fluid species there are four perturbations,

$$T^0_0 = -\bar{\rho}(1 + \delta), \quad (1.31a)$$

$$T^0_i = \bar{\rho}(1 + w)v_i, \quad (1.31b)$$

$$T^i_j = \bar{\rho}w \left(1 + \frac{\delta p}{\bar{p}}\right) \delta^i_j + \Sigma^i_j, \quad (1.31c)$$

where $\bar{\rho}$ and \bar{p} are the background density and pressure and δ is the density contrast, v_i is the velocity perturbation, δp is the pressure perturbation and Σ^i_j is an anisotropic (i.e. $\Sigma^i_i = 0$) shear perturbation. As for the metric perturbations, these perturbations are gauge-dependent.

When in k -space it is convenient to use an alternative velocity perturbation,

$$\theta = ik^j v_j. \quad (1.32)$$

It is also common to use the adiabatic sound speed, $c_s^2 = \delta p / \delta \rho = w$, where the change in the density, $\delta \rho$ is related to the density contrast by $\delta = \delta \rho / \bar{\rho}$, to reduce the number of perturbations to three⁸. Finally a scalar shear perturbation, σ is defined via,

$$\bar{\rho}(1 + w)\sigma = - \left(\hat{k}_i \hat{k}_j - \frac{1}{3} \delta_{ij} \right) \Sigma^i_j. \quad (1.33)$$

This means the set of perturbations change as,

$$\{\delta, v_i, \delta p, \Sigma^i_j\} \rightarrow \{\delta, \theta, \sigma\}. \quad (1.34)$$

⁸The second equality for the sound speed is only true for species with constant equation of state. Luckily the standard Λ CDM components all satisfy this condition.

The perturbed Einstein equations in the synchronous gauge are;

$$k^2\eta - \frac{1}{2}\frac{\dot{a}}{a}\dot{h} = -4\pi Ga^2 \bar{\rho} \delta_{(\text{syn})}, \quad (1.35a)$$

$$k^2\dot{\eta} = 4\pi Ga^2 \bar{\rho}(1+w)\theta_{(\text{syn})}, \quad (1.35b)$$

$$\ddot{h} + 2\frac{\dot{a}}{a}\dot{h} - 2k^2\eta = -24\pi Ga^2 \bar{\rho}w \delta_{(\text{syn})}, \quad (1.35c)$$

$$2k^2\dot{\alpha} + 4k^2\frac{\dot{a}}{a}\alpha - 2k^2\eta = -24\pi Ga^2 \bar{\rho}(1+w)\sigma_{(\text{syn})}. \quad (1.35d)$$

In the Newtonian gauge the perturbed Einstein equations are,

$$k^2\phi + 3\frac{\dot{a}}{a}\left(\dot{\phi} + \frac{\dot{a}}{a}\psi\right) = -4\pi Ga^2 \bar{\rho} \delta_{(\text{Newt})}, \quad (1.36a)$$

$$k^2\left(\dot{\phi} + \frac{\dot{a}}{a}\psi\right) = 4\pi Ga^2 \bar{\rho}(1+w)\theta_{(\text{Newt})}, \quad (1.36b)$$

$$\ddot{\phi} + \frac{\dot{a}}{a}(\dot{\psi} + 2\dot{\phi}) + \left(2\frac{\ddot{a}}{a} - \frac{\dot{a}^2}{a^2}\right)\psi + \frac{k^2}{3}(\phi - \psi) = 4\pi Ga^2 \bar{\rho}w \delta_{(\text{Newt})}, \quad (1.36c)$$

$$k^2(\phi - \psi) = 12\pi Ga^2 \bar{\rho}(1+w)\sigma_{(\text{Newt})}. \quad (1.36d)$$

We also get an important set of equations for the energy–momentum perturbations using the conservation of the energy–momentum tensor. In the synchronous gauge,

$$\dot{\delta}_{(\text{syn})} = -(1+w)\left(\theta_{(\text{syn})} + \frac{\dot{h}}{2}\right) + 3\frac{\dot{a}}{a}(w - c_s^2)\delta_{(\text{syn})}, \quad (1.37a)$$

$$\dot{\theta}_{(\text{syn})} = -\frac{\dot{a}}{a}(1-3w)\theta_{(\text{syn})} + \frac{c_s^2}{1+w}k^2\delta_{(\text{syn})} - k^2\sigma_{(\text{syn})}. \quad (1.37b)$$

In the Newtonian gauge,

$$\dot{\delta}_{(\text{Newt})} = -(1+w)\left(\theta_{(\text{Newt})} - 3\dot{\phi}\right) + 3\frac{\dot{a}}{a}(w - c_s^2)\delta_{(\text{Newt})}, \quad (1.38a)$$

$$\dot{\theta}_{(\text{Newt})} = -\frac{\dot{a}}{a}(1-3w)\theta_{(\text{Newt})} + \frac{c_s^2}{1+w}k^2\delta_{(\text{Newt})} - k^2\sigma_{(\text{Newt})} + k^2\phi. \quad (1.38b)$$

In both cases a term in $\dot{\theta}$ that depends on \dot{w} has been dropped (when compared with the expressions in Ma and Bertschinger [42]) because all the scalar species considered in this thesis have a constant equation of state. A particularly attentive reader will have noticed that these equations depend on the shear perturbation σ but the evolution equation for σ is not given. This is usually

found from the Boltzmann hierarchy, see Ma and Bertschinger [42] for details. It should also be noted that the above equations can be applied for each species but assume that there is no interaction with other species. If there are interactions, the energy–momentum tensor of the individual species is no longer conserved and the Boltzmann equations again need to be used.

1.3.3 Initial conditions

We now have a set of differential equations that govern how perturbations evolve in the early universe. To solve these we need to set initial conditions on each of the perturbations.

This is done by inserting series expansions in $k\tau$ for each of the perturbation variables and matching coefficients that precede $k\tau$ terms of the same order. These then give a set of coupled equations for the expansion coefficients of all the perturbations. Solving these to a fixed order in $k\tau$ gives the initial conditions and small $k\tau$ evolution of the metric and energy-momentum perturbations. Explicitly the expansions take the form,

$$\zeta = \sum_{i=0}^{\infty} \zeta_i (k\tau)^i, \quad (1.39)$$

where ζ is a general perturbation variable. Hence, the aim is to calculate all of the ζ_i 's up to some fixed order, to give series solutions of the perturbation equations. For the expansion to be valid we require that the mode in question is well outside the horizon ($k\tau \ll 1$) such that the above series is valid to some truncated order. The universe is assumed to be in the radiation dominated phase of the expansion at this early time due to the observed density fractions today.

As mentioned earlier the evolution of perturbations outside the horizon is gauge dependent and consequently some care is necessary when considering these initial conditions. We shall see that the behaviour in the synchronous and Newtonian gauges is different.

In general there are two types of initial condition. *Adiabatic* initial condi-

tions correspond to perturbations that compress and expand volume elements adiabatically [42–44]. This results in all species having the same ratio of density perturbation to equation of state $\delta_i/(1 + w_i)$. Adiabatic initial conditions are a prediction of most inflationary models and we therefore expect (and have observed) these to make up the majority of the perturbations observed in the Universe. *Isocurvature* initial conditions correspond to perturbations to individual species and do not affect all the species equivalently [45–48]. A general perturbation can be constructed from a superposition of adiabatic and (often many more than one) isocurvature perturbations.

Looking at the series for the synchronous gauge⁹ metric perturbation η ,

$$\eta = \eta_0 + \eta_1 k\tau + \eta_2 (k\tau)^2 + \dots, \quad (1.40)$$

the adiabatic mode corresponds to a non-zero η_0 , with zeroth-order coefficients of all other perturbations set to zero. Similarly the baryon isocurvature, CDM isocurvature, neutrino density and neutrino velocity isocurvature modes correspond to zeroth-order coefficients in the respective perturbation variables only [48]. For example the neutrino density isocurvature mode has the zeroth-order coefficient for the neutrino density, $\delta_{\nu,0}$ non-zero, with all other zeroth-order coefficients zero. This is what is meant by a *mode* in the context of initial conditions for cosmological perturbations: it is the set of initial values and their low- $k\tau$ evolution, when only the corresponding zeroth-order coefficient is non-zero¹⁰. Note that, as suggested by the adiabatic mode, the distinctions between isocurvature modes are only clear in the synchronous gauge. A general set of initial conditions can be obtained from a sum of the separate modes, which is usually done through an *initial correlation matrix* of all the different modes. For example, for two modes, one with half the amplitude of the other and no interdependence between the modes, the correlation matrix would be $\propto \begin{pmatrix} 2 & 0 \\ 0 & 1 \end{pmatrix}$. In reality the correlation matrix will be larger and can contain

⁹See section 1.3.1 for the definition of η and the synchronous gauge.

¹⁰Some more explicit expressions for this are given in the appendix though full understanding will also require reading of chapter 3.

Table 1.2: Adiabatic initial conditions on perturbation quantities in synchronous and Newtonian gauge given to lowest order in $k\tau$.

	Synchronous gauge	Newtonian gauge
$\delta_\gamma, \delta_\nu$	$-\frac{1}{3}k^2\tau^2$	$-\frac{20}{15+4R_\nu}$
δ_b, δ_c	$-\frac{1}{4}k^2\tau^2$	$-\frac{15}{15+4R_\nu}$
θ_γ, θ_b	$-\frac{1}{36}k^4\tau^3$	$\frac{5}{15+4R_\nu}k^2\tau$
θ_ν	$\frac{23+4R_\nu}{15+4R_\nu}\theta_\gamma$	θ_γ
θ_c	0	θ_γ
σ_ν	$\frac{2}{3(15+4R_\nu)}k^2\tau^2$	$\frac{2}{3(15+4R_\nu)}k^2\tau^2$
h	$\frac{1}{2}k^2\tau^2$	—
η	$1 - \frac{(5+4R_\nu)}{12(15+4R_\nu)}k^2\tau^2$	—
ψ	—	$\frac{10}{15+4R_\nu}$
ϕ	—	$\frac{(5+2R_\nu)}{5} \frac{10}{(15+4R_\nu)}$

dependences between all the adiabatic and isocurvature modes.

As an example of the initial conditions, if the zeroth-order coefficient for η is set equal to one, then the resulting series expansions of the perturbations in synchronous and Newtonian gauges are given in table 1.2. Here the relativistic fraction for neutrinos or photons is given by,

$$R_i = \frac{\bar{\rho}_i}{\bar{\rho}_\gamma + \bar{\rho}_\nu}, \quad (1.41)$$

for $i = \gamma, \nu$.

Table 1.2 shows a few important features of cosmological perturbation theory. We can see that at early times the only component not acting as a perfect fluid and consequently having a shear contribution are the neutrinos. We also see that the density perturbation to the matter species is related to that for the relativistic species by a factor of $3/4$ as stated above and as to be expected from the equation of state parameters. Furthermore the density

perturbations grow in the synchronous gauge but are constant in the Newtonian gauge. This is an illustration of the fact that, outside the horizon perturbation behaviour is dependent on the choice of gauge. Since it is the Newtonian gauge which is directly related to the gauge-invariant variables, it is this gauge we should use to compare to observation. The fact that θ_c is zero in the synchronous gauge should not surprise us as this gauge is defined by attaching observers to dark matter particles and therefore these observers should not see a velocity perturbation for dark matter.

1.4 The cosmic microwave background

Analysis of the CMB temperature anisotropies is one of the most mature and fruitful areas of cosmology. It was first proposed in the 1940s that the Universe contains radiation obeying a black-body spectrum,

$$n(\omega, T) = \frac{2}{\pi} \frac{\omega^2}{\exp(\omega/T) - 1}, \quad (1.42)$$

where n is the photon number density, ω is the angular frequency and T is the temperature [49]. The first observation [50, 51] came in 1965 and measured an excess temperature of 3.5 ± 1.0 K. Since then the CMB temperature has been measured at a large range of frequencies confirming its black-body nature.

To look at the temperature anisotropies in the CMB due to the physics of the Universe this black-body spectrum is subtracted from the observed radiation,

$$\Delta T = T - T_{\text{CMB}}, \quad (1.43)$$

where $T_{\text{CMB}} = 2.72548 \pm 0.00057$ K is the average CMB temperature [34]. When this is done a dipole can be seen due to our movement relative to the CMB rest frame. Once this is subtracted we see temperature anisotropies at one part in 10^{-5} [52]. A 2D projection of these anisotropies on the sky – usually called a map – is shown in figure 1.1.

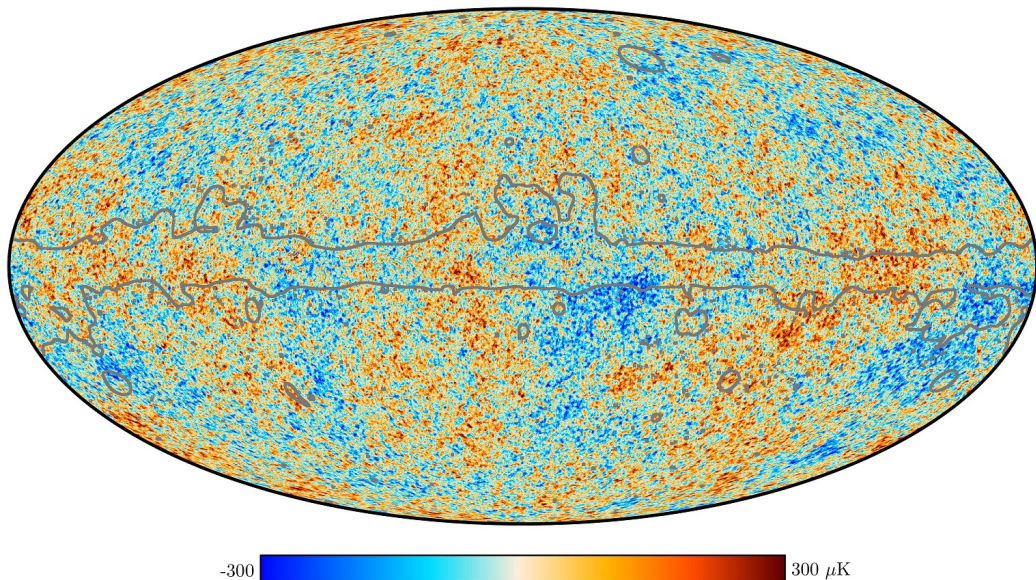


Figure 1.1: *Planck* 2018 map of the temperature anisotropies in the CMB. Areas colder than the average temperature can be seen in blue while hotter areas are yellow or red. The regions enclosed by grey lines are masked and not used in the analysis due to the large errors from galactic foregrounds.

1.4.1 Power spectrum

Because the CMB photons travel approximately the same distance to the detector from all directions the temperature anisotropies can be deconstructed in 2D spherical harmonics $Y_{\ell m}(\theta, \phi)$, where θ and ϕ are polar-coordinate angles and ℓ and m are integers, instead of a more familiar 3D Fourier series [22] (Chapter 8) [28] (Chapter 2). The spherical harmonics are functions of Legendre polynomials, $P_{\ell}(\cos \theta)$. The temperature anisotropies,

$$\Delta T(\theta, \phi) = \sum_{\ell=2}^{\infty} \sum_{m=-\ell}^{m=\ell} a_{\ell m} Y_{\ell m}(\theta, \phi), \quad (1.44)$$

where the information about the temperature anisotropies is now contained in the coefficients $a_{\ell m}$. The integer ℓ can be thought of as the 2D analogue of the wavenumber k and consequently small ℓ corresponds to large scales and large ℓ corresponds to small scales. ℓ runs from $2 \rightarrow \infty$ because the $\ell = 0$ blackbody and $\ell = 1$ dipole contributions have been subtracted¹¹. The temperature anisotropies average out over the whole sky such that $\langle \Delta T(\theta, \phi) \rangle = 0$. The

¹¹Though the relative velocity contributes primarily to $\ell = 2$ it also has a small affect on higher ℓ modes, see Weinberg [28], Chapter 2.4.

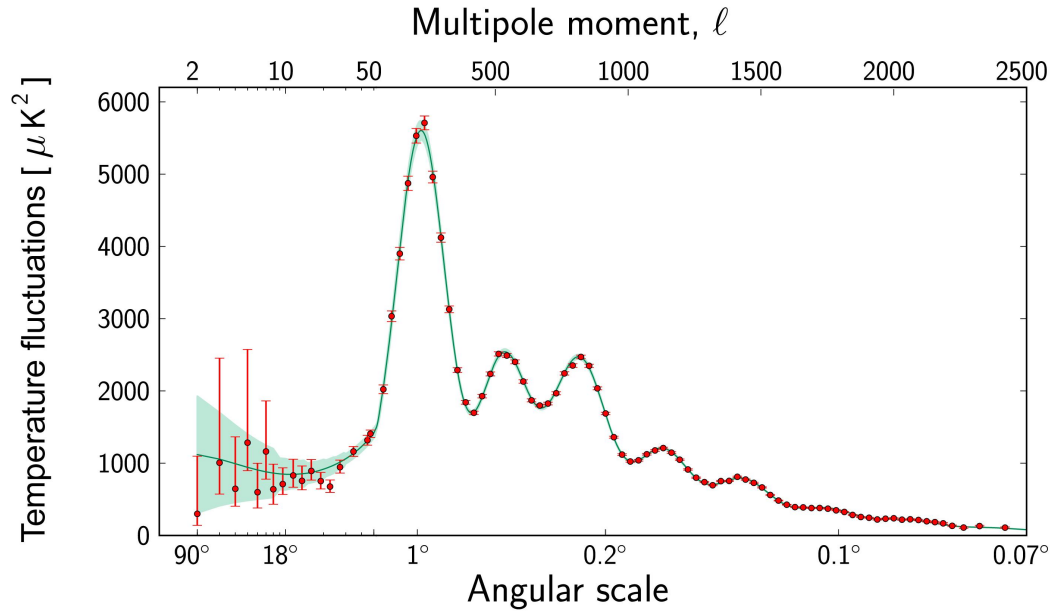


Figure 1.2: The CMB power spectrum in units of μK^2 as a function of both angular scale in degrees and multipole moment ℓ . The horizontal axis is logarithmic up to $\ell = 50$ and is then linear to show more clearly the low- ℓ behaviour. See section 1.4.2 for a discussion of the causes of the features seen here. Plot taken from [ESA](#).

isotropy of the Universe results in a power spectrum that is independent of the orientation of the function, given by m . This power spectrum is an interesting quantity containing a large amount of cosmological information. The CMB power spectrum is defined as the square of the expansion coefficients,

$$C_\ell = \frac{1}{2\ell + 1} \sum_{m=-\ell}^{m=\ell} |a_{\ell m}|^2, \quad (1.45)$$

and gives the variance of the expansion coefficients. The power spectrum C_ℓ can be computed from the observed temperature anisotropies and can be predicted from theory making it one of the key observables of CMB physics. The observed CMB power spectrum from *Planck* 2013 data [\[53\]](#) is shown in figure 1.2.

It is worth noting that there is a fundamental limit on how accurately C_ℓ can be measured due to *cosmic variance* [\[22, 28\]](#). The theoretical prediction for C_ℓ is an average of the coefficients over all the observations of the CMB from different positions in the Universe whereas the average in equation (1.45) is over the allowed values of m for each ℓ . This results in a limit on the accuracy

of the observed power spectrum,

$$\left(\frac{\delta C_\ell}{C_\ell}\right)_{\text{cosmic variance}} = \sqrt{\frac{2}{2\ell + 1}}. \quad (1.46)$$

This effect is particularly pronounced at low- ℓ and is represented by the green band in figure 1.2.

To predict the power spectrum it is helpful to expand the Fourier transform (denoted \mathcal{F}) of the temperature anisotropy,

$$\Theta(k, \theta, \phi, \tau) = \mathcal{F} \left[\frac{\Delta T}{T} \right], \quad (1.47)$$

in terms of Legendre polynomials,

$$\Theta(k, \theta, \tau) = \sum_{\ell=0}^{\infty} (2\ell + 1) (-i)^\ell \Theta_\ell(k, \tau) P_\ell(\cos \theta). \quad (1.48)$$

Θ_ℓ are called the *multipole moments* of the temperature anisotropies [22, 42, 54]. It is advantageous to separate out the evolution of the multipole moments into initial conditions, $\xi(\vec{k})$ and the CMB transfer function¹², $T_\ell(\vec{k}, \tau_0)$ such that the multipole moments are given by the Fourier space multiplication of the initial conditions and transfer function,

$$\Theta_\ell(\vec{k}, \tau_0) = \xi(\vec{k}) T_\ell(k, \tau_0), \quad (1.49)$$

where τ_0 is the conformal time today. The primordial power spectrum, $P(k)$ is the power spectrum of the initial conditions, $\xi(\vec{k})$. Consequently we can calculate the CMB power spectrum as,

$$C_\ell = (4\pi)^2 \int k^2 dk P(k) |T_\ell(k, \tau_0)|^2. \quad (1.50)$$

The problem of predicting the CMB power spectrum then becomes a case of calculating the CMB transfer function and integrating it against the primordial power spectrum which simply depends on the initial conditions from inflation.

¹²It is important to remember that this differs from the transfer function associated with the matter power spectrum.

Line of sight integral method

The CMB transfer function for relativistic species can be calculated through a hierarchy of coupled differential equations for increasing ℓ [42, 44, 55]. Practically, this can involve solving and evolving several thousand differential equations. Seljak and Zaldarriaga [56] detail an approach that requires solving considerably fewer differential equations and is therefore much faster to solve numerically. Here the evolution equation for the photon perturbation Θ is integrated along the past light cone, i.e. from $\tau = 0$ to τ_0 . This results in,

$$\Theta(k, \tau) = \int_0^{\tau_0} d\tau e^{ik\mu(\tau-\tau_0)} S(k, \tau), \quad (1.51)$$

where $\mu = \hat{k} \cdot \hat{n}$ is the angle between the observation direction and the wavevector and $S(k, \tau)$ is the *source term*. This source term is a gauge-dependent function of perturbation variables. These perturbation variables are in general the metric perturbations, matter density and velocity and moments of relativistic species up to $\ell = 4$. Hence the source term can be evaluated by solving the coupled differential equations for the perturbations.

The CMB transfer function is then simply the integral of the source function with a spherical Bessel function, j_ℓ which comes from expanding the plane wave in equation (1.51) in terms of radial and angular eigenfunctions,

$$T_\ell(k, \tau_0) = \int_0^{\tau_0} d\tau S(k, \tau) j_\ell[k(\tau_0 - \tau)]. \quad (1.52)$$

The reason that this is so computationally advantageous, on top of the fact that a much smaller hierarchy of increasing ℓ solutions is needed, is that the source term contains all the cosmological information and has no dependence on ℓ while the geometrical part coming from the Bessel function depends on ℓ but not the cosmology. As a result the Bessel functions can be calculated, stored and then re-used whenever the cosmology is being changed e.g. in cosmological parameter estimation, see section 1.5.2.

In summary, using the line of sight integral approach detailed in Seljak and

Zaldarriaga [56] the CMB power spectrum can be found by first calculating the source function from the solutions of the differential equations for low multipole perturbation variables. Then this source function is integrated with Bessel functions to get the CMB transfer function and finally the product of the transfer function and the primordial power spectrum is integrated to obtain the CMB power spectrum.

1.4.2 The different contributions to the CMB power spectrum

One of the reasons the CMB is of such interest to cosmologists is that the CMB power spectrum has a variety of different features that depend on a range of different physical effects throughout the cosmological evolution of the Universe. This subsection will detail these physical effects and the influence they have on the CMB power spectrum.

Intrinsic temperature fluctuations

The CMB photons are emitted when the opacity of the Universe drops below a critical value and photons are no longer tightly coupled. This happens when protons and electrons combine to form neutral hydrogen, a process known as *recombination*. This recombination will happen at slightly different times in different regions of space, dependent on the temperature such that the intrinsic temperature fluctuations of the plasma at last scattering are imprinted on the CMB. These give rise to a temperature anisotropy,

$$\left(\frac{\Delta T}{T}\right)_{\text{density}} = \frac{1}{4}\delta_{\gamma}. \quad (1.53)$$

This contribution is shown schematically in figure 1.3.

The Doppler effect

As well as the density perturbations at the time of last scattering there are also velocity perturbations in the plasma and these give rise to a temperature

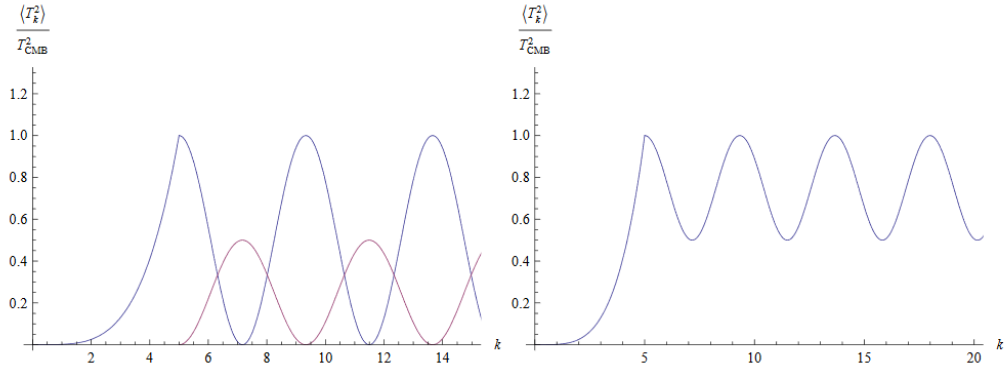


Figure 1.3: Left: a schematic plot of the effects of the intrinsic density (blue) and velocity (red) perturbations on the temperature anisotropies. Right: The combined effect of density and velocity perturbations. The negative sign in the Doppler term causes the peaks to be out of phase and as a result the combined plot does not reach $\delta T/T = 0$. Plot taken from notes by Pearson [57].

anisotropy,

$$\left(\frac{\Delta T}{T} \right)_{\text{Doppler}} = -\hat{n} \cdot \vec{v}_\gamma, \quad (1.54)$$

where \hat{n} is the unit vector along the line of sight. Simply, the perturbed radiation fluid is moving relative to the background Hubble flow which changes the temperature in different regions. This is shown in 1.3 along with the combined effect of intrinsic density and velocity perturbations. Together these account for most of the oscillatory features in the CMB power spectrum.

Gravitational redshift/the Sachs–Wolfe effect

CMB photons will also experience a gravitational redshift as they travel from the last scattering surface to us. This is commonly called the Sachs–Wolfe effect [58]. This gravitational redshift gives rise to a temperature anisotropy [28, 59],

$$\left(\frac{\Delta T}{T} \right)_{\text{SW}} = \frac{1}{3} \psi_e, \quad (1.55)$$

where the subscript e denotes that the Newtonian potential ψ is evaluated at last scattering. The anisotropy arises because the energy density, and therefore the gravitational potential, is not constant across space. This gives rise to a plateau in the CMB power spectrum at large scales.

The intrinsic temperature fluctuations and the gravitational redshift effect

are often collectively referred to as the ‘SW term’. The distinction between these two effects is gauge-dependent and consequently the distinction between gravitational redshift and temperature fluctuation is not absolute.

The integrated Sachs–Wolfe effect

As CMB photons travel through the perturbed universe they fall in and out of gravitational potentials. If these gravitational potentials are not changing with time (gravitational potentials are constant in a matter dominated background) then the photons will lose the same amount of energy as they leave the potential as they gained when they entered and will therefore have no change in observed energy. However, if the gravitational potential changes with time the photon will leave a potential with a different magnitude to the one it fell into and as a result the photon experiences a change in energy. This change in energy is the integrated Sachs-Wolfe (ISW) effect and gives rise to an anisotropy,

$$\left(\frac{\Delta T}{T}\right)_{\text{ISW}} = - \int_0^{\tau_e} (\dot{\psi} + \dot{\phi}) d\tau, \quad (1.56)$$

where τ_e is the conformal time of recombination.

Gravitational potentials change with time in both radiation and cosmological constant dominated backgrounds. Hence there are both early- and late-time ISW effects. The early-time ISW effect is due to the fact that recombination happens not long after matter–radiation equality and consequently the gravitational potential is still changing due to radiation. This primarily influences the CMB power spectrum on scales slightly larger than the first peak. The late-time ISW effect occurs because of cosmological constant domination and causes an increase in power at very large scales.

Silk/diffusion damping

Before recombination, photons can only travel a very short distance before being scattered off protons and electrons. The photons go on a random walk and diffuse from the hot regions to the colder ones, reducing the temperature

anisotropies and density perturbations on a characteristic length scale related to the photon mean free path. As recombination occurs the mean free path increases rapidly and smooths out inhomogeneities on a range of scales. This is called Silk or diffusion damping [60] and is what causes the decay in the CMB power spectrum for large- ℓ .

All of these contributions are included in the source function of Seljak and Zaldarriaga [56] (and section 1.4.1) and therefore contribute to the CMB power spectrum.

The Sunyaev–Zel’dovich effect

CMB photons are scattered as they pass through galaxy clusters by high-energy electrons [61–63]. This inverse Compton scattering increases the average energy of CMB photons. This is considered as a small-scale contaminant to the standard CMB signal but is itself an interesting observable (see Rephaeli [64], Carlstrom, Holder, and Reese [65], and Rephaeli, Sadeh, and Shimon [66] for reviews and Ade et al. [67] and Aghanim et al. [68] for *Planck* analyses).

1.4.3 Polarisation

Polarisation is a well known property of electromagnetic radiation and refers to the orientation of the wave relative to the direction of motion. The CMB is expected to be linearly polarised due to Thomson scattering of photons from electrons during recombination. Thomson scattering only polarises radiation with a quadrupole anisotropy and because photons are tightly coupled to the photon–baryon fluid before recombination very little quadrupole anisotropy is formed. Closer to recombination, as photons begin to travel further in the plasma, a quadrupole is generated and the photons Thomson scattering off the electrons that have not yet formed neutral hydrogen will become polarised [22, 28, 69, 70]. Because of these factors the polarisation anisotropies are expected to be an order of magnitude smaller than the temperature anisotropies at about 1 part in 10^6 . The CMB polarisation was first predicted by Rees [71] and first

observed using the Degree Angular Scale Interferometer [72], closely followed by the Wilkinson Microwave Anisotropy Probe (*WMAP*) [73].

The polarisation pattern can be decomposed into coordinate independent E -mode and B -mode polarisation [74, 75]. Similarly to electromagnetic fields the E -mode polarisation describes the divergence part of the polarisation while the B -mode describes the curl part. The E -mode is the part of the polarisation signal that is rotationally invariant about the direction of propagation, analogous to the rotational invariance of the electric field around a point charge. The difference between E - and B -modes can also be seen from the fact that for an E -mode polarisation pattern the orientation of the polarisation and the direction of increasing polarisation strength are either parallel or perpendicular whereas B -mode polarisation patterns have 45° between the orientation and the polarisation strength.

E - and B -modes can also be differentiated by their parity (their behaviour under an inversion of spatial coordinates). E -modes have parity $(-1)^\ell$ and B -modes have parity $(-1)^{\ell+1}$. There are six possible power spectra formed from the combination of temperature (T), E -modes and B -modes but because power spectra are expected to be invariant under spatial inversions combinations with different parity, TB and EB , have no contributions from cosmological perturbations¹³. This is equivalent to the statement that B -modes are not correlated with E -modes or temperature anisotropies. Hence we have four observables, C_ℓ^{TT} , C_ℓ^{TE} , C_ℓ^{EE} and C_ℓ^{BB} with the only cross-correlation being C_ℓ^{TE} .

The separation into E - and B -modes has important observational consequences and CMB polarisation is now an important cosmological observable. E -modes were observed first with the first significant measurement of B -mode polarisation coming from the South Pole Telescope [77].

¹³Foregrounds and contaminants may produce non-zero C_ℓ^{TB} and C_ℓ^{EB} 's and these cross-spectra can consequently be used to constrain systematics [76].

Sources of polarisation

An important advantage of the separation of the polarisation into E -modes and B -modes is that scalar perturbations only produce E -mode polarisation. The quadrupole photon perturbation only produces polarisation that is symmetric about the direction of propagation; the same rotational symmetry as the E -mode. Tensor perturbations produce E - and B -mode polarisation. Therefore (neglecting vector perturbations which decay in the early Universe), B -mode polarisation can be used to directly constrain tensor perturbations without having to disentangle the scalar perturbations. In an idealised scenario with no foregrounds or contaminants the B -mode spectrum would provide all the information about the tensor perturbations and the tensor contribution to the E -mode could be subtracted from the scalar E -mode and temperature anisotropies to tightly constrain the scalar perturbations. In reality, disentangling scalar and tensor perturbations is complex.

The separation of the tensor and scalar perturbations is also important because a background of tensor perturbations is a prediction of inflation. Hence, a detection of B -modes with the expected scale dependence would be a strong confirmation of the inflationary paradigm.

So far we have been assuming that the only sources of polarisation happen at, or before, recombination but there is an appreciable amount of polarisation produced in the late Universe due to reionisation. When UV emission from galaxies starts to reionise gas in galaxy clusters there are once again free electrons for CMB photons to Thomson scatter from. As stated previously CMB scattering from these electrons erases the temperature anisotropies at small scales but also introduces E - and B -mode polarisation on large scales (particularly $\ell \lesssim 10$). This polarisation from reionisation is at large scales because it is sourced by the CMB quadrupole ($\ell = 2$) which denotes scales close to the horizon size, which itself has grown much larger than at recombination.

The four temperature and polarisation power spectra from scalar and tensor

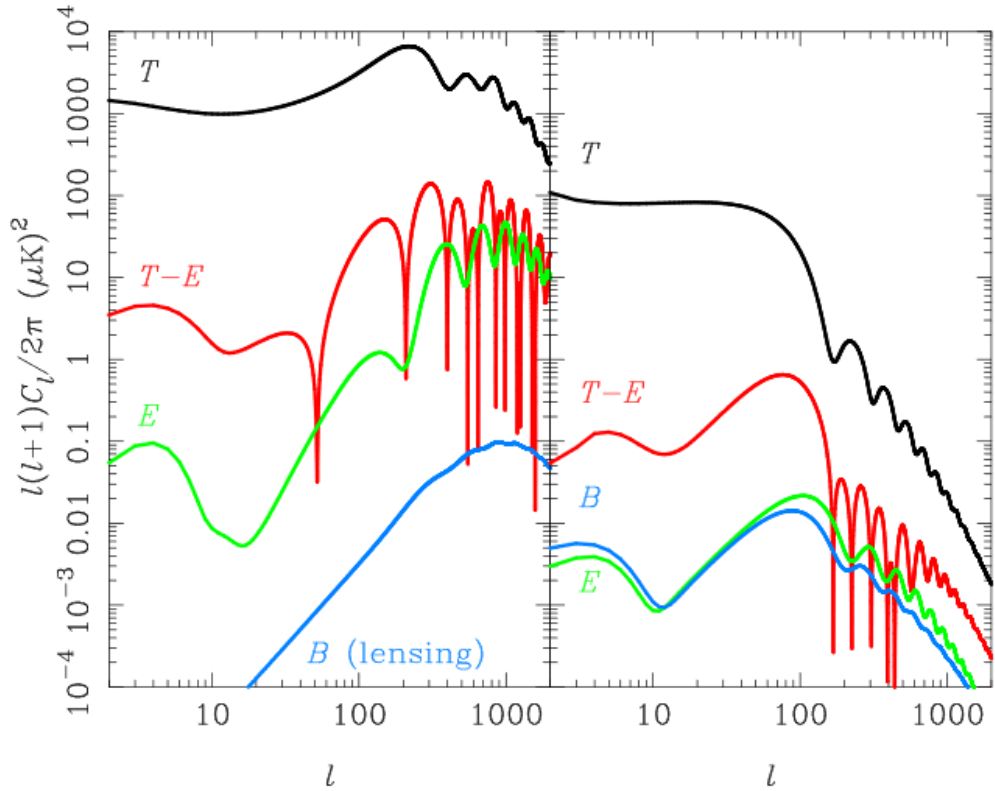


Figure 1.4: The predicted CMB temperature and polarisation power spectra for scalar perturbations (left) and tensor perturbations (right) for a value of the tensor-to-scalar ratio that was representative of constraints in 2009 [78], $r_{0.002} = 0.22$ and for the baseline Λ CDM parameters. Current best constraints on the tensor-to-scalar ratio are tighter by a factor of 2–3 (see section 1.4.5). The blue line in the left panel is purely from CMB lensing and is discussed below. Taken from Challinor and Peiris [79].

perturbations are shown in figure 1.4. The effects of reionisation are clear in the low- l behaviour of the E - and B -mode spectra for scalars and tensors. The contamination to the B -mode spectrum from lensing discussed in the next section is also shown.

Polarisation as a cosmological probe

One of the main advantages of including polarisation data in cosmological analyses is that it constrains reionisation well. Looking at temperature anisotropies alone, there is a degeneracy between the initial amplitude A_s and the optical depth to reionisation τ (see section 1.2.3 for definitions). Including E -mode polarisation breaks this degeneracy and allows for independent constraints of τ .

The large scale signature of reionisation in the EE power spectrum was first observed by *WMAP* [73]. In addition to the optical depth to reionisation, the redshift of reionisation if reionisation is assumed to happen instantaneously, z_r is also constrained by polarisation measurements. This second parameter is in general a poor approximation to the real physics of reionisation but can be thought of as an average redshift of reionisation. *WMAP* measured these parameters to be $\tau = 0.17 \pm 0.04$ and $z_r = 20_{-9}^{+10}$. This implied that almost one in five CMB photons were scattered at reionisation. This also implied a higher reionisation redshift than expected from astronomical observations.

The current state of the art constraints come from *Planck* [1]. Here the optical depth to reionisation $\tau = 0.0544_{-0.0081}^{+0.0070}$, considerably lower than the *WMAP* value. *Planck* also finds $z_r = 7.68 \pm 0.79$ as the mid-point redshift when fitting a hyperbolic tangent function to the ionisation fraction. This lower value is consistent with observations of quasars unlike the higher value from *WMAP*. Because including the EE power spectrum breaks the degeneracy of the scalar amplitude and the optical depth to reionisation, including polarisation allows for tighter constraints on the initial amplitude of scalar perturbations.

The other main use of polarisation in cosmology is in constraining primordial gravitational waves through B -mode polarisation. As mentioned previously B -mode polarisation gives a direct constraint on tensor perturbations and a background of gravitational waves is a prediction of inflation. Consequently a detection of B -mode polarisation in the CMB would be further strong evidence for inflation. Constraints are usually presented through the tensor-to-scalar ratio r_{k_*} . This is defined as the ratio of the amplitude of the initial tensor power spectrum, $A_t(k_*)$ to the amplitude of the initial scalar power spectrum, $A_s(k_*)$ (as defined in equation (1.21)) at a reference scale k_* . The tensor power spectrum is defined in equation (1.60).

In 2014 the BICEP2 experiment announced a 7.0σ detection of B -mode polarisation corresponding to $r_{0.05} = 0.20_{-0.05}^{+0.07}$ [80]. This was later reanalysed using the *Planck* measurements of the foregrounds in the region observed by

BICEP2 and the *Keck Array* which showed that the original BICEP2 signal was due to dust contamination and there was no evidence for inflationary gravitational waves [81]. Instead this analysis gives a constraint on the tensor-to-scalar ratio of $r_{0.05} < 0.12$ at 95% confidence level. This is a good example of the importance of accurately modelling foregrounds, particularly in CMB polarisation experiments.

The BICEP2/*Keck* analysis has been redone more recently and gives the tightest current constraint on the tensor-to-scalar ratio from CMB data of $r_{0.05} < 0.07$ at 95% confidence [14].

As the errors on polarisation measurements have decreased, polarisation has become more and more useful as a consistency check on other cosmological parameters. So far there are no major discrepancies between polarisation and temperature measurements and as a result these probes confirm the concordance model and together put tight constraints on Λ CDM.

1.4.4 CMB lensing

The paths of photons are bent due to the distribution of matter in the Universe. This happens in much the same way as in optics with the lens replaced by massive objects along the line of sight. This bending of light is called *gravitational lensing* and is experienced by CMB photons travelling through a universe with inhomogeneities [82, 83]. This changes the temperature and polarisation anisotropies [84] primarily at low redshifts because the Universe is least homogeneous at late times.

CMB lensing is a contaminant to the CMB temperature and polarisation anisotropies and the removal of lensing from the CMB power spectrum is a complex and well developed science. However, the CMB lensing is a tracer of the large-scale structure of the Universe and can therefore act as an independent probe of cosmological parameters [85, 86].

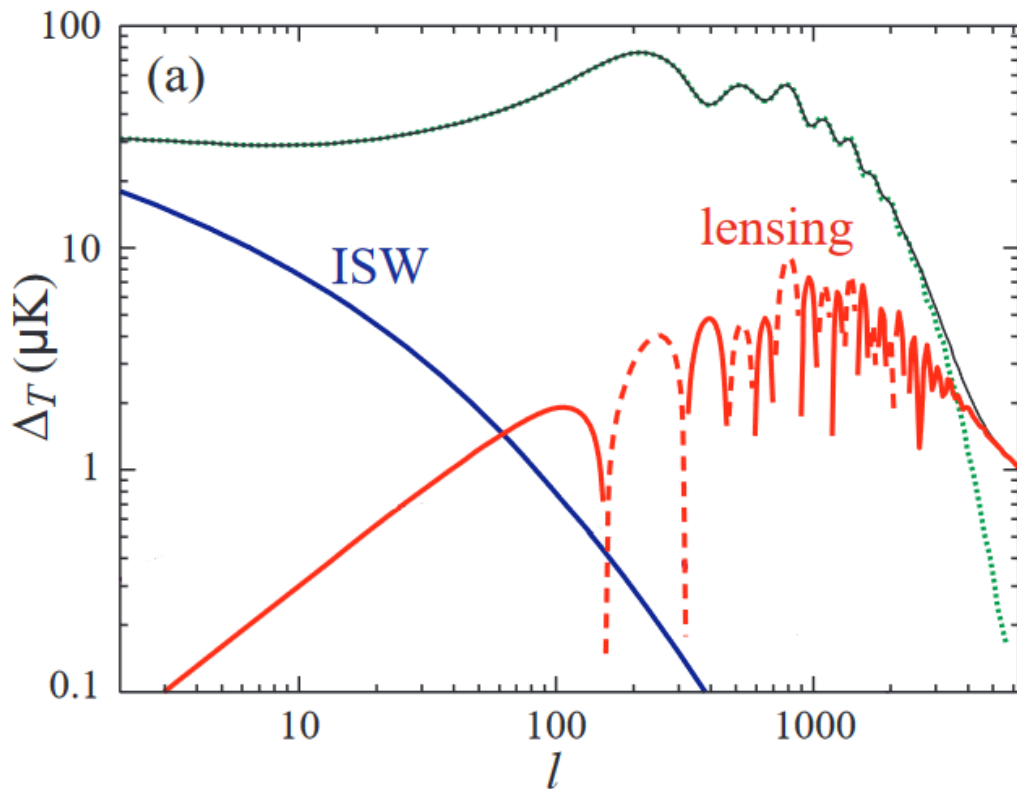


Figure 1.5: The total lensed CMB power spectrum (black) along with the contributions from the ISW effect (blue), CMB lensing alone (red) and the unlensed power spectrum (green dashed). The y-axis, $\Delta T = \sqrt{\ell(\ell+1)C_\ell}/(2\pi)$ is the square root of the conventionally plotted power spectrum. Taken from Challinor and Peiris [79].

Consequences for CMB observations

CMB lensing has three main effects on the CMB [85]. Firstly, it broadens the acoustic peaks at a level of (1-10)% for the first few peaks (or more precisely for $\ell \lesssim 2000$) before dominating the power spectrum for large ℓ . This is illustrated in figure 1.5.

A similar contribution is given to the polarisation power spectra with an important extra effect. CMB lensing converts E -mode polarisation into B -modes, which come to dominate over the predicted primordial gravitational wave signal for large ℓ . This is important because B -mode polarisation is an important observational target for observing primordial gravitational waves (as discussed above). This can be seen in figure 1.4.

Finally, CMB lensing introduces non-Gaussianity into the power spectra. The anisotropies from inflation as defined above are expected to be distributed

as a Gaussian with zero mean to high precision. The introduction of non-Gaussianity means the CMB power spectra no longer completely define the statistics of the temperature and polarisation anisotropies. There is now a non-zero *bispectrum* and *trispectrum* which are the Fourier transforms of the correlation of three and four different points on the sky respectively [87].

Lensing reconstruction and delensing

Lensing has the same frequency spectrum as the unlensed CMB unlike most other contaminants and as a result, can not be subtracted in the same way. Instead it can be done by reconstructing the lensing potential and using this to map points back to their unlensed values that tell us directly about the epoch of last scattering.

The features discussed in the previous section are important for this reconstruction of the lensing potential. Because lensing dominates the temperature spectrum for large ℓ but is negligible for small ℓ we can consider these as uncontaminated regions dominated only by lensing or the unlensed signal respectively. This is similar for *E*- and *B*-mode polarisation with the added advantage that we don't expect there to be any large scale *B*-modes due to lensing (see figure 1.4).

If the unlensed and lensing only perturbations are assumed to be perfectly Gaussian then we can also use the trispectrum to find out information about the lensing.

The above ways of gaining information about the CMB use only CMB observations to try and disentangle the lensing effect but external tracers of large-scale structure such as 21-cm hydrogen lines [88] or *Planck* cosmic infrared background observations [89] can be used to improve the removal of the lensing component.

Lensing as a cosmological probe

Lensing has now been detected to high significance in the temperature and polarisation data [89] and consequently can be used as an independent cosmological probe. Because lensing is primarily a late time effect it can give both complementary and unique information to temperature and polarisation data.

Lensing can be used to constrain Λ CDM parameters, primarily H_0 and Ω_m and also extended parameters such as the effective number of neutrino species, the sum of the neutrino masses, the dark energy equation of state, the curvature density parameter and the normalisation of the matter power spectrum σ_8 [86].

1.4.5 CMB parameters

Within the Λ CDM cosmological model there is a range of important parameters that can be derived from the conventional six base parameters and there are also parameters associated with interesting extensions to Λ CDM. Here I will detail a few of these that are relevant in the remainder of the thesis.

The Hubble constant

The Hubble constant H_0 gives the late-time rate of expansion of the Universe and is one of the most important observables in cosmology. Positive values of H_0 correspond to an average redshifting of observed sources. It is a derived parameter within Λ CDM and features in Hubble's law and the Friedmann equation (see section 1.2.3). Even in models that explain the accelerated expansion of the Universe using dynamical fields or modified gravity, the observed value of the Hubble constant is an important constraint that these models have to satisfy.

There is a large range of observational techniques that can be used to measure the Hubble constant including: the CMB, the local distance ladder (which heavily relies on type 1a supernovae), weak lensing, baryon acoustic oscillations (BAO), Big Bang nucleosynthesis (BBN) and astronomical gravitational

waves [28, 90].

The Hubble constant is difficult to measure precisely due to the large scales over which accurate distance measurements need to be made. Because of this the Hubble constant is often written as,

$$H_0 = 100 h \text{ km s}^{-1} \text{ Mpc}^{-1}, \quad (1.57)$$

where h is defined so as to contain the uncertainty in the exact value of the Hubble constant. A discussion of the current best values is given in section 1.4.6.

The inverse of the Hubble constant gives a rough estimate of the current age of the Universe of ~ 14 billion years for $h \sim 0.7$.

Number of relativistic degrees of freedom

The number of relativistic degrees of freedom N_{eff} is defined in equation (1.18)¹⁴,

$$\rho_r = \left[1 + \frac{7}{8} \left(\frac{4}{11} \right)^{4/3} N_{\text{eff}} \right] \rho_\gamma. \quad (1.18)$$

Here ρ_r is the total density of relativistic species and ρ_γ is the energy density of photons. In Λ CDM the only relativistic species are photons and neutrinos. Hence N_{eff} is sometimes referred to as the effective number of neutrino species.

The factor of $7/8$ in equation (1.18) comes from the difference in the calculation of the energy density for fermions and bosons. This calculation requires integration over the Fermi–Dirac distribution for the fermionic neutrinos and over the Bose–Einstein distribution for the bosonic photons. The distinction between these two results is a factor of $7/8$.

The factor of $(4/11)^{4/3}$ is a result of electron–positron annihilation which heats the photons but leaves the neutrinos almost unaffected. The magnitude is found by using entropy conservation during the annihilation process.

Shortly before electron–positron annihilation the neutrinos stop interacting with the radiation fluid in a process known as decoupling. If this process was

¹⁴This equation is reproduced here for ease of reading.

instantaneous such that all the entropy from electron–positron annihilation goes to the photons then $N_{\text{eff}} = 3$, corresponding to the three neutrino species of the Standard Model of particle physics. However, neutrino decoupling is not complete by the time of electron–positron annihilation and consequently some entropy, and therefore energy, is transferred to the neutrinos. Furthermore, the energy dependence of the weak interaction results in the neutrinos having a spectrum slightly distorted from the Fermi–Dirac distribution. These two effects result in the effective number of degrees of freedom having a slightly larger predicted value [91–93]: $N_{\text{eff}} = 3.046$.

The current best observations for constraining N_{eff} are the CMB and BBN (see section 1.5.3). From an analysis of Deuterium abundances combined with *Planck* 2013 CMB data $N_{\text{eff}} = 3.28 \pm 0.28$ [53, 94]. From *Planck* 2018 temperature and polarisation data $N_{\text{eff}} = 2.92^{+0.36}_{-0.37}$ [1]. Both of these are consistent with the Λ CDM prediction.

Increasing N_{eff} above the Standard Model value has distinctive effects on the CMB temperature power spectrum. Increasing the energy density of relativistic species in the early universe moves matter–radiation equality later and also alters the growth of perturbations, shifting the positions of the peaks [95]. Increasing N_{eff} also increases the amount of Silk damping. This is shown in figure 1.6.

There is a large range of possible sources of an increase in N_{eff} including; primordial gravitational waves [96], relic neutrinos [97], dynamical dark energy [98], light weakly interacting massive particles [99–101], dark radiation and its matter interactions [102] and more (see Vagnozzi [103] references 745–773 and Henrot-Versillé et al. [104] and references therein, for more examples). A significant result of $N_{\text{eff}} > 3.046$ would be evidence of extra physics in the early Universe but would not by itself determine between any of these possible sources. However, constraints on N_{eff} can be converted into constraints on these models of currently undetected physics.

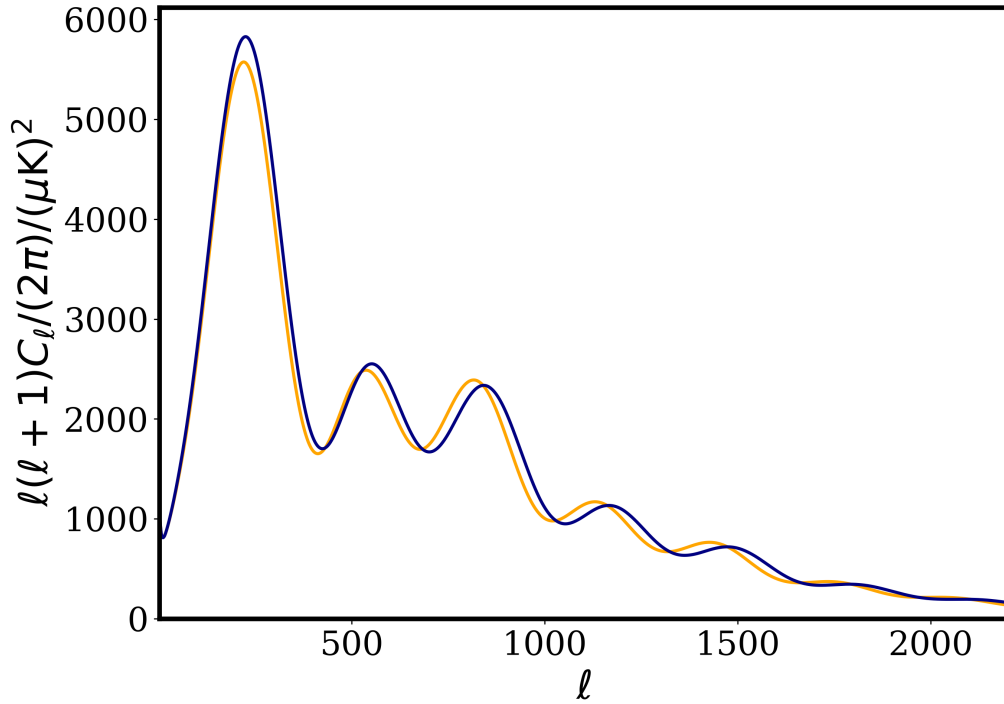


Figure 1.6: The CMB temperature power spectrum for $N_{\text{eff}} = 3.046$ (orange) as in Λ CDM and for $N_{\text{eff}} = 4.046$ (blue), i.e. with one extra neutrino. This change in N_{eff} has characteristic effects on the heights and positions of the acoustic peaks.

Sum of the neutrino masses

In standard Λ CDM neutrinos are massless (as stated in section 1.2.3). However, it has been known that neutrinos are massive since the first observation of neutrino oscillations [105]. Neutrino oscillation is the phenomenon by which neutrinos change species, e.g. electron neutrinos changing into muon neutrinos. This can only occur if at least one of the neutrinos is massive. The lepton number eigenstates¹⁵ (ν_e , ν_μ , ν_τ) are not the same as the neutrino mass eigenstates (m_1 , m_2 , m_3). This effect can be quantified by the neutrino mass splittings, $\Delta m_{ij}^2 = m_i^2 - m_j^2$ and mixing angles, θ_{ij} .

A lower limit on the sum of the neutrino masses can be obtained if the neutrino mass splittings are known. However, this depends on the *hierarchy* of the neutrino masses. It is known from solar neutrino oscillation observations¹⁶ that $m_1 < m_2$ and $\Delta m_{21}^2 \ll \Delta m_{31}^2$. Hence there are two possible orderings of

¹⁵Here we assume that there are three active neutrino species and no sterile neutrinos [106].

¹⁶If the mixing angle θ_{12} is chosen to be in the positive quadrant, see Gariazzo et al. [107].

the neutrino masses. The *normal* ordering has $m_1 < m_2 < m_3$ and the *inverted* ordering has $m_3 < m_1 < m_2$.

HyperKamiokande’s observation of neutrino oscillations constrained the sum of the neutrino masses, $\sum m_\nu > 0.02 \text{ eV}$ at 90% confidence [105]. The current best lower limits are $\sum m_\nu > 0.06 \text{ eV}$ for normal ordering and $\sum m_\nu > 0.11 \text{ eV}$ for the inverted hierarchy (both from 95% confidence intervals on Δm_{ij}^2) [108–111]. The normal ordered value is used as the baseline model for the *Planck* ΛCDM analysis instead of the assumption of zero mass used elsewhere.

Cosmology is only sensitive to the sum of the neutrino masses which is related to the energy density via [22],

$$\Omega_{\nu,\text{mass}} h^2 \approx \frac{\sum m_\nu}{94 \text{ eV}}. \quad (1.58)$$

Because massive neutrinos transition from being effectively massless when the temperature is much higher than their mass to being non-relativistic at late times they have unique effects on cosmology which allows strong upper limits to be found. The tightest upper limit¹⁷ comes from *Planck* temperature, polarisation and lensing data combined with BAO data (see section 1.5.3 for details) from the Baryon Acoustic Oscillation Survey DR12 [112], 6dF Galaxy Survey [113] and Sloan Digital Sky Survey ‘main galaxy sample’ [114],

$$\sum m_\nu < 0.12 \text{ eV}, \quad (1.59)$$

at 95% confidence level. Note that these constraints come from a single parameter extension to ΛCDM and consequently have N_{eff} fixed at 3.046.

Relativistic neutrinos affect the growth of structure due to free-streaming. This reduces inhomogeneities on small scales. However, having massive neutrinos that become non-relativistic reduces this free-streaming effect and increases the amount of structure on small scales. Therefore probes of the the large-

¹⁷The constraint tightens to 0.11 eV when including data from supernovae but these are known to have major discrepancies with *Planck* (see section 1.4.6).

scale structure, including weak lensing, 21-cm radio and galaxy surveys, offer complementary insights to the neutrino mass constraint obtained from the CMB [115].

A combination of knowledge gained from particle physics, nuclear physics and cosmology have constrained the sum of the neutrino masses to a window of less than one order of magnitude. The constraints are expected to improve significantly in the near future with new CMB, weak lensing and radio surveys coming online [109].

Tensor-to-scalar ratio

The tensor-to-scalar ratio quantifies the gravitational wave perturbations in the early universe and is zero in *Planck*'s baseline Λ CDM model [116]. Models of inflation predict primordial gravitational waves and consequently a non-zero tensor-to-scalar ratio so including this ratio in analyses is a well motivated extension to Λ CDM.

As stated in section 1.4.3 the tensor-to-scalar ratio r_{k_*} gives the ratio of the primordial tensor to scalar power spectra amplitudes at a reference wavenumber, k_* . The primordial tensor and scalar power spectra are given by power laws with the scalar spectrum being given by equation (1.21) and the tensor spectrum by,

$$P_t(k) = A_t(k_*) \left(\frac{k}{k_*} \right)^{n_t}, \quad (1.60)$$

where A_t is the tensor amplitude and n_t is the tensor tilt. Because the scalar amplitude is well determined but small ($A_s \sim 10^{-9}$) and the tensor amplitude is unknown, it is convenient and conventional to consider the tensor-to-scalar ratio,

$$r_{k_*} = \frac{A_t(k_*)}{A_s(k_*)}, \quad (1.61)$$

instead of the tensor amplitude. Hence, if the power law assumptions are correct¹⁸, there are four primordial power spectra parameters to determine,

¹⁸A common extension is to include ‘running’ of the spectral indices with k but this will not be considered here.

A_s, n_s, r_{k_*}, n_t . In models of inflation there is a *consistency relation* which relates r_{k_*} and n_t but this relation depends on the specific inflationary model. Constraints on the tensor-to-scalar ratio therefore allow discrimination between models of inflation.

Two different pivot scales are commonly used as tensor perturbations have contributions that peak in different regions for the TT and the BB power spectra (see figure 1.4). The temperature anisotropies receive the largest contribution from tensor modes for large scales ($\ell \lesssim 100$) and consequently constrain $r_{0.002}$. The predicted B -mode power spectrum peaks at $\ell \sim 100$ and as a result these constraints are usually presented in terms of $r_{0.05}$. It is easy to convert between pivot scales but care should be taken not to directly compare the constraints.

The current best constraint comes from a combination of *Planck*, BICEP2/*Keck* Array and BAO data [1, 14, 81, 112–114],

$$r_{0.002} < 0.06, \quad (1.62)$$

at 95% confidence. The constraining power from *Planck* is primarily from the TT power spectrum which combines well with the BICEP2/*Keck* B -mode spectrum as a result.

Dark energy equation of state

Λ CDM explains the late-time accelerating expansion of the Universe with the cosmological constant, a fluid component with constant energy density and therefore an equation of state of $w = -1$. A vacuum energy that would behave like a cosmological constant on large scales is predicted by quantum field theory but the value of the energy density from these predictions is too large by many orders of magnitude. This is called the cosmological constant problem [59, 117, 118]. Because of the cosmological constant problem, along with other theoretical motivations, a large range of models have been developed to explain the accelerated expansion. Models that introduce an extra component into the

energy–momentum tensor are generally called *dark energy*. Perturbation-less dark energy models can be quantified by their density, Ω_{DE} and equation of state, $w_{\text{DE}}(\tau)$. Dark energy models with equations of state < -1 are usually referred to as *phantom* dark energy and often have major theoretical problems due to quantum instabilities (see Copeland, Sami, and Tsujikawa [119] and references therein). The cosmological constant is the simplest case of a dark energy model with $\Omega_{\text{DE}} = \Omega_{\Lambda} \sim 0.7$ and $w_{\text{DE}} = -1$.

Because there is now a large range of dark energy models, [119–121] and references therein, it is beneficial to employ general parameterisations of the dark energy equation of state. In the general case of $w_{\text{DE}}(a)$ the density evolves as,

$$\rho_{\text{DE}} \propto \exp \left[3 \int_a^1 \frac{(1 + w_{\text{DE}}(a))}{a} da \right]. \quad (1.63)$$

The simplest case is a constant equation of state that is not equal to -1 for which,

$$\rho_{\text{DE}}(a) \propto a^{-3(1+w_{\text{DE}})}. \quad (1.64)$$

Going beyond this we can incorporate some time dependence by Taylor expanding about the present time which can be done in several different ways. As an example, expanding in the scale factor¹⁹,

$$w_{\text{DE}}(a) = w_0 + (1 - a)w_a, \quad (1.65)$$

where we now have a two parameter model for the dark energy equation of state using, w_0 and w_a .

A popular approach in the literature is to use the parameterised post-Friedmann (PPF) model of Fang, Hu, and Lewis [122]. This models the dark energy as a general cosmological fluid with small perturbations, due to the dark energy speed of sound being close to the speed of light, and no anisotropic stress. The main advantage of this approach is that the equation of state of the fluid can cross $w_{\text{DE}}(\tau) = -1$ while conserving energy and momentum. Hence

¹⁹If using a different expansion, such as one in the redshift, values of the constants will not be directly comparable.

it is well placed to test the observed region of parameter space either side of the phantom divide.

Current observations are consistent with a cosmological constant causing the accelerated expansion. For the constant equation of state parameterisation, *Planck* [1], in combination with BAO and supernovae, [123] finds,

$$w_{\text{DE}} = -1.028 \pm 0.031. \quad (1.66)$$

When including the Taylor expanded dependence on the scale factor from equation (1.65) the same *Planck* data set finds,

$$w_0 = -0.957 \pm 0.080 \quad , \quad w_a = -0.29^{+0.32}_{-0.26}, \quad (1.67)$$

which is also consistent with Λ CDM.

The equation of state of dark energy has degeneracies with: the matter density, Ω_{m} , the curvature parameter, Ω_K and the Hubble constant, H_0 , and consequently combinations of data that break these degeneracies are usually used in parameter constraints [124].

Dark energy models predict specific values for the parameterisation constants and can therefore be compared to data through this approach.

1.4.6 The H_0 problem

There is now a large range of observational techniques that can measure the Hubble constant, H_0 , up to $\sim 1\%$ accuracy [125]. In recent years a tension between these techniques has grown and now ranges from 3σ to 6σ ²⁰ [126–128]. The tension can be broadly separated into ‘late-’ and ‘early-’ Universe probes that disagree, with different late- and early-Universe probes being approximately consistent with each other.

Two important data sets that are in disagreement are *Planck* [1], with the

²⁰ σ estimates of the tension often come from combing errors on measurements in quadrature and can be misleading, especially when probes are not independent. Here they are only meant as an indication of the severity of the difference.

2018 temperature, polarisation and lensing data giving,

$$H_0 = (67.27 \pm 0.60) \text{ km s}^{-1} \text{ Mpc}^{-1}, \quad (1.68)$$

and the Riess et al. [129] local distance ladder observations giving,

$$H_0 = (73.48 \pm 1.66) \text{ km s}^{-1} \text{ Mpc}^{-1}. \quad (1.69)$$

The distance ladder technique relies on measuring distances in the local Universe using sources of known luminosity such as Cepheids or Type Ia supernovae. Multiple different calibrations have been used and agree with the higher value of H_0 found in Riess et al. [129], see figure 1.7. The main exception to this is the distance ladder using the tip of the red giant branch [130] which found an intermediate value, $H_0 = (69.8 \pm 1.9) \text{ km s}^{-1} \text{ Mpc}^{-1}$. However, this analysis has recently been called into question [131] and a higher value, consistent with Riess et al. [129] is suggested. The *Planck* value has support from weak lensing, BAO, BBN and independent CMB observations (from the Atacama Cosmology Telescope) [132–134].

A variety of approaches to testing whether the Hubble tension is due to systematics in either analysis have been done all failing to reconcile the data sets. This solution is increasingly unlikely as more independent approaches confirm the tension.

The H_0 tension has been seen as evidence of new physics beyond Λ CDM. Many possibilities have been put forward to explain the discrepancy including: modified gravity (see Zumalacarregui [135] and Desmond, Jain, and Sakstein [136] and references therein), non-standard interactions and early dark energy (see Knox and Millea [137] for a review). The majority of these models fail to completely resolve the tension, usually reducing it to $\sim 2\sigma$ and often do so at the expense of worsening fits to other parameters or observables. Some of the more successful theoretical approaches to alleviating the H_0 problem by modifying the cosmology will be detailed in chapter 5.

Improvements in future observations will allow for further verification of

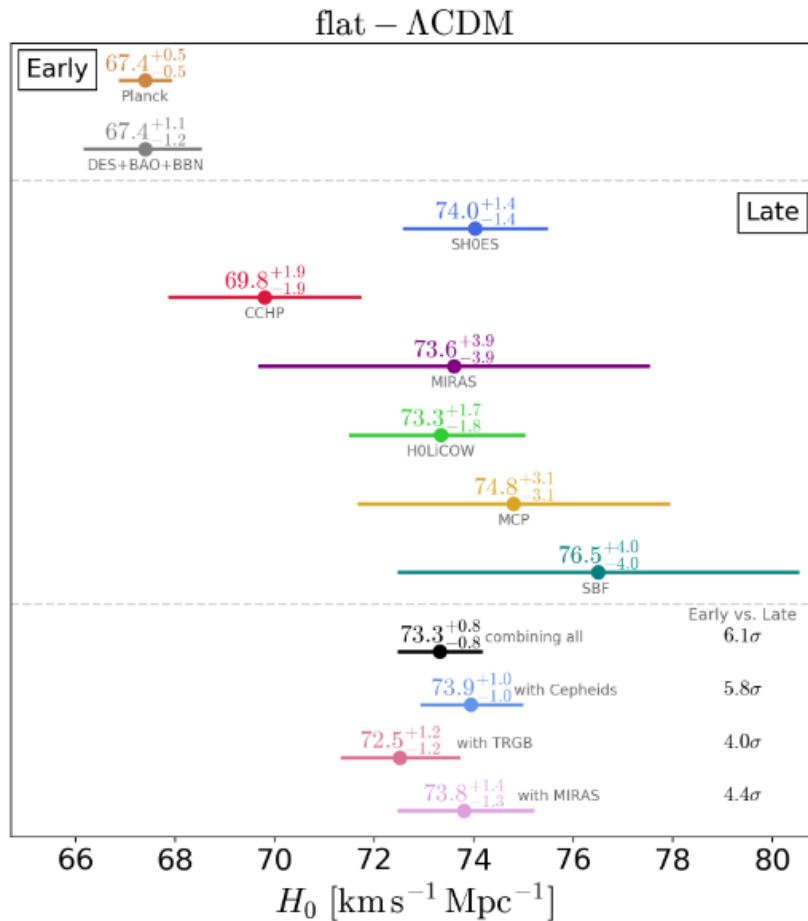


Figure 1.7: Values of the Hubble constant from a range of early and late Universe measurements including: CMB, BAO, weak lensing, BBN, local distance ladder (with different calibration methods) and strong lensing. Taken from Verde, Treu, and Riess [127].

the validity of the Hubble tension and for tests of suitable extended models that seek to explain the Hubble tension. Particularly exciting is the possibility of independent determination of the Hubble constant from astrophysical gravitational wave observations [90, 138]. Currently the error bars on gravitational wave measurements are large but these are predicted to become competitive in the next 5–10 years [139, 140].

There are some other less significant tensions in Λ CDM including disagreement between CMB and large-scale structure measurements of σ_8 , which quantifies the amplitude of fluctuations today, and Ω_m (see Bhattacharyya et al. [141] and Aghanim et al. [1] for recent discussions). There have also been discussions of internal inconsistencies in the *Planck* results between the low- ℓ

and high- ℓ data and also disagreements from consistency checks of the lensing amplitude. Aghanim et al. [1] argues that the first of these is likely to be due to statistical fluctuations but resolutions of both of these tensions, along with the Hubble tension, could reveal physics beyond Λ CDM.

1.5 Data and analysis

There are now many cosmological observations taking place that produce a very large amount of data. Processing this data and accurately comparing to theoretical predictions requires advanced numerical codes and parameter estimation techniques. This section will briefly outline the codes, techniques and observables used in later chapters.

1.5.1 CAMB

The Code for Anisotropies in the Microwave Background (CAMB) [142] is an integrated python/fortran code that calculates observables given input values of theory parameters. CAMB is based on CMBFAST [56, 143, 144] which was the first numerical code to compute the CMB power spectrum efficiently enough to be used for parameter estimation.

The main observables calculated by CAMB are the CMB temperature and polarisation power spectra, with the option to include lensing effects (see section 1.4) but CAMB can also be used to calculate the matter power spectrum (see e.g. Dodelson [22] for details), the background expansion and cosmological distance measures (among other observables).

The code solves the Friedmann equation for the background as well as the perturbation equations using conformal time and relies on the line of sight integral method detailed in section 1.4.1 to calculate the CMB power spectrum. CAMB incorporates all the CMB physics detailed in section 1.4 and has dedicated modules to include the physics of recombination (using RECFAST, which is based on Seager, Sasselov, and Scott [145]) and reionisation.

The baseline Λ CDM parameters are required as inputs with the option

of including many extended parameters. These include: isocurvature initial conditions via a correlation matrix approach (see Bucher, Moodley, and Turok [48]), the number of relativistic degrees of freedom, the sum of the neutrino masses, different parameterisations of the dark energy equation of state and the tensor-to-scalar ratio (as detailed in section 1.4.5).

A similar code, CLASS [146] is also popular amongst the cosmology community but CAMB is used throughout this work due to the ease of integration with the parameter estimation code used in *Planck* analyses, COSMOMC. CAMB's modularity makes it easy to modify and modified versions of CAMB exist for calculations incorporating modified gravity, MGCAMB [147] and ISITGR [148], and the effective field theory of cosmological acceleration, EFT-CAMB [149].

1.5.2 Cosmological parameter estimation, MCMC and CosmoMC

Once accurate predictions of observables can be made using numerical codes it is then important to be able to compare these to observations. In cosmology this is often done using Bayesian parameter estimation [150].

The quantity of interest is the probability distribution of the values of our parameters, θ given the model, M and the data d ,

$$p(M(\theta)|d) \propto p(d|M(\theta))p(M(\theta)), \quad (1.70)$$

by Bayes' theorem. $p(M(\theta)|d)$ is often called the *posterior* distribution of the parameters, $p(d|M(\theta))$ is the *likelihood* of the data given the parameters of the model and $p(M(\theta))$ is the *prior*, i.e. the existing information that is known about the model parameters. Hence Bayesian parameter estimation consists of accurately calculating the likelihood and appropriately choosing the priors. Prior choice is important and will change the calculated distributions of parameters but if the data is discriminatory enough then this change will be small [22].

For CMB analysis the data is reduced to the level of the C_ℓ 's²¹, so the more appropriate form is,

$$p(\theta|C_\ell^{\text{obs}}) \propto p(C_\ell^{\text{obs}}|\theta)p(\theta), \quad (1.71)$$

i.e. the probability distribution of our parameters, θ , given the observed C_ℓ 's [152]. Here we have assumed that the Universe is described by the Λ CDM model so we are only interested in the parameter values of that specific model but Bayesian approaches can be used to compare different models. The calculation of the likelihood is complex and requires advanced techniques (see Gerbino et al. [153] for a recent review and Aghanim et al. [151]).

Once the likelihood can be calculated accurately, a process for determining the probability distribution of the parameters is needed. The most obvious process is to take a grid of the possible values of the parameters of interest and calculate the likelihood and posterior for each value. However, the length of time needed to carry out the computation scales very poorly with the number of parameters used²² such that it quickly becomes prohibitive for cosmology. As an example it would have taken nearly four years for *WMAP* to have carried out their analysis in this way [154].

The most popular solution to this problem is to use Markov chain Monte Carlo (MCMC) [150]. A Markov chain is a stochastic process that generates a series of numbers where the step to the next number depends only on the previous one. Put another way, for a Markov process, where you jump next depends only on where you are.

The ‘Monte Carlo’ part of MCMC refers to the fact that at each point a random number is generated that decides where the next point is. For a careful choice of the algorithm used to make these jumps, the Markov chain will be a representation of the underlying probability distribution. The most common of these algorithms is the Metropolis–Hastings algorithm [150, 155].

²¹This is a very complex and in depth process, see Planck Collaboration, Ade, and others. [53] and Aghanim et al. [151]. Here we will assume that this has been done and does not introduce any significant errors.

²²It scales as M^N where N is the number of parameters and M is the number of steps used in each dimension of the parameter space.

MCMC starts off being quite inefficient if jumps are taken randomly with no knowledge of the underlying distribution. This can be improved by using the start of the Markov chains to approximate the covariance matrix which then informs the directions in which jumps are more likely to maximise the likelihood while also probing the lower likelihood regions an appropriate amount.

Metropolis–Hastings MCMC is greatly advantageous over a grid method as it scales roughly linearly with additional parameters as opposed to exponentially, making the computational cost much smaller [154, 156].

The result of MCMC is a likelihood hypersurface in the parameter space which contains information on the probability distribution of each parameter and how it depends on the other parameters. Consequently an important operation for MCMC analysis is *marginalisation*. This refers to integrating over the probability of parameters to leave lower dimensional hypersurfaces. The most common way to use this is to marginalise over all parameters except one, leaving the single probability distribution, but it is also used to generate 2D representations of the dependences between two different parameters.

One of the most widely used codes for performing parameter estimation via MCMC is `COSMOMC` [155]. `COSMOMC` is a fortran code that uses the Metropolis–Hastings algorithm to do an MCMC analysis and uses `CAMB` to calculate the theoretical power spectrum for the relevant parameters. A variety of different observational data can be used along with easy incorporation of extended parameters. Alternatives to `COSMOMC` include `MONTPYTHON` [157], which uses `CLASS` to calculate the theoretical power spectrum, `COSMOSIS` [158], which is highly modular allowing the use of code in different languages and a variety of alternative sampling methods, and `COBAYA` [159], which allows for a range of sampling methods, optimisation features and integration with different cosmological codes and likelihoods.

1.5.3 Data

A range of different data sets are used in this work and as a result a brief outline of the physics and particular methods of observation are detailed here.

The *Planck* cosmic microwave background satellite

The *Planck* satellite was launched and run by the European Space Agency and observed the full CMB sky between 2009 and 2013. It replaced *WMAP* at the cutting edge of CMB observation.

Planck observed the microwave sky in nine frequency bands between 30 and 857 GHz. The main contaminants are spinning dust [160], synchrotron radiation and free-free emission for low frequencies, and thermal dust for high frequencies [161]. The contaminants all have unique dependences on frequency which allow the subdominant CMB signal to be deduced [162, 163].

There are three main observables coming from the *Planck* data. The first is the temperature power spectrum, often denoted as TT . The second is polarisation via the E mode and temperature E mode cross-correlation power spectra, denoted EE and TE respectively (see section 1.4.3). The B mode spectra are not used because *Planck* does not measure a BB power spectrum inconsistent with zero power, due to foregrounds [151]. The third is gravitational lensing (as described in section 1.4.4). This data is publicly available²³ and is most usefully presented for parameter estimation in the *Planck* likelihood code.

The likelihoods are split into *low- ℓ* ($\ell < 30$) and *high- ℓ* ($\ell \geq 30$) with the low- ℓ likelihood being reconstructed directly and the high- ℓ likelihood being approximated by a Gaussian to decrease the numerical cost. The low- ℓ TT , TE , EE and lensing likelihoods have one nuisance parameter, the absolute calibration. The high- ℓ TT likelihood has 20 nuisance parameters that incorporate various aspects of the data reduction and calibration. The high- ℓ TE , EE likelihood has 47 nuisance parameters. The nuisance parameters

²³<https://pla.esac.esa.int>.

are marginalised over to estimate the uncertainty due to these parameters. See the [Planck likelihood wiki](#) for more information on likelihood usage.

Planck had three main data analysis releases in 2013, 2015 and 2018 with a set of verification papers released in 2011. These give the best ever determination of the parameters of Λ CDM. They show little evidence for extensions to Λ CDM with the most prominent suggestion of a problem with Λ CDM coming from the tension between *Planck* and distance ladder measurements of H_0 (see section 1.4.6).

The *Planck* temperature measurements are cosmic variance limited up to $\ell \approx 1600$ and consequently constitute the best possible determination of the temperature anisotropies down to these scales [164]. However, the polarisation and lensing measurements from *Planck* were limited by the determination and subtraction of foregrounds, so the main focus of CMB observations in the future will be on better determining the polarisation and lensing components. There is a large range of planned and current ground-based, balloon and space-based CMB observatories including; *SPTpol*, *ACTPol*, the *BICEP Array*, *POLARBEAR*, *CLASS*, *SPIDER*, the *Simons Observatory*, *CMB-S4*, *LiteBIRD*, *COrE*, *PIXIE* and *PICO* [165–178], which promise to greatly enhance our knowledge of the CMB.

Baryon acoustic oscillations

The oscillations in the baryon–photon plasma²⁴ before recombination that give rise to the peaks and troughs in the CMB power spectrum (see section 1.4.2) are also imprinted on the distribution of matter.

If we consider a single overdensity of dark matter, baryons and photons then the baryon–photon fluid will be attracted towards the centre of this overdensity. The photons provide a restoring pressure that pushes the fluid back out of the overdensity before gravitationally collapsing again. The balance between the photon pressure and the gravitational attraction give rise to acoustic oscillations

²⁴Here the cosmological convention of calling protons, neutrons and electrons ‘baryons’ is still being used.

in the plasma. The largest scale wave will be the one that is at rarefaction at recombination. Hence recombination leaves a configuration with a shell of overdense baryons around dark matter overdensities [179]. After recombination there is only gravitational attraction and the dark matter and baryons fall into each other's potential wells. The dominance of dark matter over baryons ($\Omega_c > \Omega_b$) means that more baryons fall into the dark matter well than vice versa, but the acoustic scale is nonetheless imprinted in the distribution of galaxies²⁵. When considering acoustic waves of all possible frequencies and a multitude of different sized overdensities, this effect can only be determined statistically in the galaxy correlation function or galaxy power spectrum measured by large surveys of galaxies. This was first done in 2005 by Eisenstein et al. [180] and Cole et al. [181].

The acoustic scale at recombination is easily calculated from linear physics. Therefore, how this scale changes with time probes the expansion history of the Universe. Absolute distance scales are often called *standard rulers* as they can be used to determine other distances in the Universe. Another advantage of the BAO scale is that it is large enough (~ 500 Mpc) that small-scale non-linear effects do not dominate. The validity of the linearity has been verified by perturbation theory and numerical simulations [182].

BAO are used in what is sometimes called the *inverse distance ladder* [112, 183]. The standard distance ladder uses combinations of increasingly high redshift observations to build a 'ladder' of known distances. The inverse distance ladder has the same purpose but working down from the high redshift observations of the CMB, BAO and Type Ia supernovae.

The main use of BAO in cosmology is to probe the expansion history. State-of-the-art galaxy surveys accurately measure the BAO scale and consequently the expansion rate up to a redshift of approximately 1. While the effects of curvature and dark energy are difficult to disentangle, combinations with other probes of the expansion history (e.g. the CMB) break these parameter

²⁵This is illustrated in figure 1 of Eisenstein, Seo, and White [179].

degeneracies.

The *Planck* collaboration use BAO data from multiple sources: BOSS DR12 [112]; 6dFGS [113] and SDSS-MGS [114]. These combined sources will generally be referred to as ‘BAO’ in data sets.

Big bang nucleosynthesis

Big Bang nucleosynthesis is the process by which nucleons are formed shortly after the Big Bang. Between 10 seconds and 20 minutes after the Big Bang ($z \sim 10^8$), light elements²⁶ were formed from the individual protons and neutrons by nuclear reactions. During these very early times the Universe is very smooth so light element abundances contain information about the background expansion via the densities of baryons, photons and other relativistic species. Knowledge of the species present in the early Universe and the nuclear reactions exactly determine the relative abundances of the light elements and can consequently be compared to observations [184, 185].

The light elements that are observable in the late Universe are hydrogen, deuterium, helium, helium-3 and lithium-7. Hydrogen and helium are the most prevalent, with the mass fraction of helium, $Y_p \approx 0.24$. The elements other than hydrogen and helium have mass fractions orders of magnitude smaller [186]. It is difficult to accurately determine helium fractions as helium is produced by stars. This necessitates observations of helium abundances in environments known to have little star formation. This is not the case for deuterium which is primarily produced by BBN but can have its fraction reduced by star formation. Measurements of the other light elements are possible but have much less constraining power on cosmology due to the large errors involved [1, 186].

Observations of the fractions of the light elements when combined with knowledge of the baryon–photon ratio give direct constraints on the baryon density parameter, $\Omega_b h^2$. This gave early evidence for the necessity of dark matter as $\Omega_b h^2 \sim 0.02$ measured from BBN was inconsistent with $\Omega_m \sim 0.3$

²⁶To be precise, light elements and their isotopes. I will adopt the standard approach of referring to elements and isotopes as ‘elements’.

from galaxy clusters and supernovae [28]. The light element abundances are also sensitive to the density of relativistic species during BBN and as a result, to N_{eff} .

The current best data on the helium abundance comes from Aver, Olive, and Skillman [187] and Peimbert, Peimbert, and Luridiana [188]. The best constraints on the deuterium abundance come from Cooke et al. [94] and Cooke, Pettini, and Steidel [189]. Their predictions are in good agreement with Λ CDM and other cosmological probes [1].

Chapter 2

Cosmological Gravitational Waves

2.1 Introduction

Over one hundred years after their prediction, the description of GWs is now a well developed theoretical area. However, gravitational wave astronomy is still in its infancy, only five years after the first observation of GWs (see Cervantes-Cota, Galindo-Uribarri, and Smoot [190] for a historical perspective). Nonetheless, there is now a large range of experiments aimed at constraining and testing GWs and a wide variety of possible gravitational wave sources.

This chapter will focus on cosmological GWs coming from early Universe phenomena and will not deal with GWs produced in the late Universe by astrophysical processes (see Christensen [191] for a review). It starts with relevant details of the mathematical description of gravitational waves in flat, FLRW and general curved spacetimes with a focus on the calculation of the energy–momentum carried by GWs. This is followed by a description of the main ways in which cosmological GWs are constrained experimentally before a summary of some of the most relevant early-Universe phenomena that could produce observable gravitational wave signals.

2.2 Linearised gravity and beyond

Tensor metric perturbations describe ripples in the curvature of spacetime. These perturbations obey a damped wave equation and are consequently iden-

tified as gravitational waves. They are most simply understood in linearised gravity where the background is flat and the perturbations are linear, but additional properties can be calculated by including curved backgrounds or non-linearities. This introductory section closely follows Misner, Thorne, and Wheeler [192] (Chapter 35).

2.2.1 Linearised gravity

In linearised gravity the metric is given by,

$$g_{\mu\nu} = \eta_{\mu\nu} + h_{\mu\nu}, \quad (2.1)$$

where $\eta_{\mu\nu}$ is the Minkowski metric and $h_{\mu\nu}$ is the linear perturbation metric [193]. The 0 component is time; no definition of conformal time exists for a Minkowski background. For this to be a well defined expansion we require $|h_{\mu\nu}| \ll 1$. In vacuum the perturbation satisfies the equation of motion¹,

$$h_{\mu\nu,\alpha}{}^\alpha = 0, \quad (2.2)$$

where a comma denotes partial differentiation. This permits a plane wave solution where the wavevector is null, $k_\alpha k^\alpha = 0$, so in general relativity gravitational waves travel at the speed of light. More general solutions can be built as superpositions of plane wave solutions, as in electromagnetism².

Gauge freedom is an important property when considering gravitational waves. The symmetric perturbation tensor, $h_{\mu\nu}$ has 10 degrees of freedom but only two of these are physical gravitational waves. This can be seen in general backgrounds from the scalar-vector-tensor decomposition (see below) or, in spatially-flat, vacuum spacetimes, due to the gauge freedom. Considering the second case, the most common fixed gauge for studying gravitational waves is

¹Technically I am assuming that the perturbation is traceless here. This is allowed due to the gauge freedom of general relativity and motivated by the scalar-vector-tensor decomposition detailed in section 1.3.1 (see below).

²This analogy can often be used and is helpful for those well acquainted with electromagnetism. Some care needs to be taken since the tensor nature of gravitational waves is not replicated by electromagnetic waves.

the *transverse-traceless (TT) gauge* defined by,

$$h_{\mu 0} = 0, \quad h_k^k = 0, \quad h_{ij}{}^{.j} = 0, \quad (2.3)$$

i.e. the perturbation tensor has only spatial components, vanishing trace and the components are transverse to the direction of travel of the gravitational wave.

Considering a wave travelling in the z -direction the TT conditions imply that there are only two different non-zero components of the perturbation tensor, $h_{11} = -h_{22}$ and $h_{12} = h_{21}$. Consequently the plane wave solution has only two *polarisations* and the perturbation becomes,

$$h_{\mu\nu} = \begin{pmatrix} 0 & 0 & 0 & 0 \\ 0 & h_+ & h_\times & 0 \\ 0 & h_\times & -h_+ & 0 \\ 0 & 0 & 0 & 0 \end{pmatrix} \cos[\omega(t - z)], \quad (2.4)$$

where ω is the angular frequency of the gravitational wave and the two polarisation states have been written as h_+ and h_\times . These two orthogonal polarisation states represent the two degrees of freedom of gravitational waves³.

Gravitational waves are invariant under a rotation of 180° about the direction of propagation and therefore have *helicity*, $\lambda = \pm 2$ [28]. This dictates that the two polarisations are oriented 45° apart, hence the labelling as ‘plus’, $+$ and ‘cross’, \times .

The orientation of the two polarisation states dictates the difference in behaviour when a gravitational wave passes through a region of space. The gravitational wave distorts spacetime in a characteristic pattern shown in figure 2.1. This shows the behaviour of a ring of test masses in the x - y plane when a gravitational wave travels through the ring in the z -direction with $+$ or \times polarisation.

It is often convenient to work in Fourier space. In this case the gravitational

³The two degrees of freedom could also be decomposed into left and right circular polarisation analogously to electromagnetic waves.

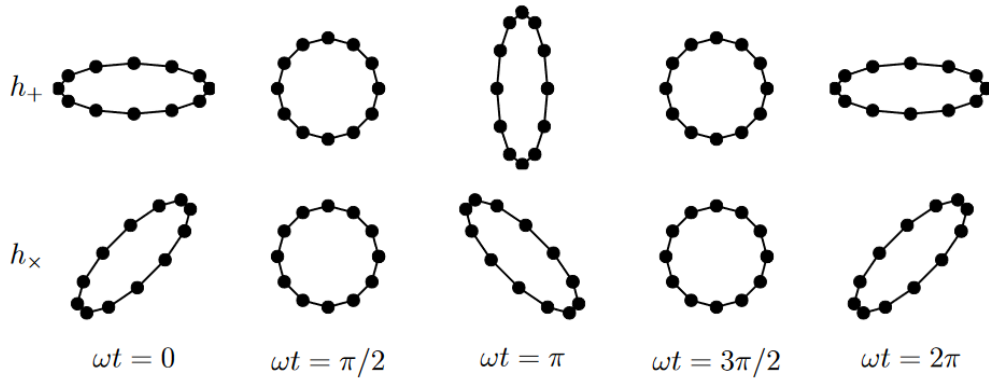


Figure 2.1: The effect of a gravitational wave passing through a ring of test masses for one full cycle for the + an \times polarisations. Taken from Li [193].

wave perturbation can be expanded as,

$$h_{ij}(\vec{x}, t) = \sum_{\lambda=\pm 2} \int \frac{d^3k}{(2\pi)^3} \epsilon_{ij}(\hat{k}, \lambda) \tilde{h}(k, \lambda, t) e^{i\vec{k}\cdot\vec{x}}, \quad (2.5)$$

where the sum is over the helicity, λ , and the polarisation tensor ϵ_{ij} represents the +, \times polarisations⁴ and depends only on the direction of propagation, \hat{k} .

2.2.2 Beyond flat, vacuum spacetime

The approach detailed so far relies on the assumption of a flat, vacuum spacetime to define the TT gauge but the cosmology in which we live has curvature and sources of perturbations. Consequently, the previous approach needs to be revised to take this into account. However the two helicities, and hence two polarisation states of gravitational waves, are an inherent feature of GR and consequently we expect the conclusion of two gravitational wave degrees of freedom to be true in general [194].

In this case the perturbed metric is decomposed into scalar, vector and tensor components as⁵,

$$\begin{aligned} ds^2 = a^2(\tau) \{ & - (1 + 2A)d\tau^2 - 2(\partial_i B + \hat{B}_i)dx^i d\tau \\ & + [(1 + 2C)\delta_{ij} + 2(\partial_i \partial_j - \frac{\delta_{ij}}{3}\nabla^2)E \\ & + 2\partial_{(i} \hat{E}_{j)} + \hat{h}_{ij}]dx^i dx^j \}, \end{aligned} \quad (1.24)$$

⁴Or right, left circular polarisations.

⁵Reproduced here for ease of reading.

as detailed in section 1.3.1. Under the conditions, $\hat{B}_{i,i} = \hat{E}_{i,i} = \hat{h}_{ij,j} = \hat{h}_{ii} = 0$ this constitutes the 10 degrees of freedom that would be expected for a symmetric 4×4 tensor.

Also as in section 1.3.1, it is helpful to consider infinitesimal coordinate transformations and then construct gauge-invariant quantities from combinations of the above perturbations, to verify if any of the existing degrees of freedom are gauge artefacts. In doing so we are left with two scalar degrees of freedom, two vector degrees of freedom and two tensor degrees of freedom, for a total of six physical degrees of freedom in the metric perturbations. The tensor, \hat{h}_{ij} is itself gauge-invariant and consequently constitutes the two tensor degrees of freedom in the perturbed metric.

Looking at the Einstein equations for these six metric degrees of freedom (see for example ref. [194]), the only two obeying a wave equation are in the tensor part, \hat{h}_{ij} . Consequently these two degrees of freedom are identified with gravitational waves as before and the TT gauge is seen to pick out the physical, gauge-invariant perturbations that are radiative. Because of this, hats will be dropped from now on and the two gravitational wave degrees of freedom will be labelled by the symmetric 3×3 tensor, h_{ij} .

While linearised gravity demonstrates many of the interesting properties of gravitational waves and is sufficient for some detection calculations, it is also missing important effects that can only be seen in the non-linear theory. Gravitational waves carry energy and consequently curve the background metric. The gravitational waves have their properties changed by the curvature of the background produced by their own energy density. Hence, a more advanced, non-linear approach is necessary to calculate the full observable consequences of gravitational waves for cosmology. Both the assumption of a flat background and the assumption of linear perturbations will be relaxed in the following discussion.

Allowing for a curved background and second order perturbations the metric

to second order is,

$$g_{\mu\nu} = \tilde{g}_{\mu\nu} + h_{\mu\nu} + j_{\mu\nu}, \quad (2.6)$$

where $\tilde{g}_{\mu\nu}$ is the background metric, $h_{\mu\nu}$ is the first order perturbation and $j_{\mu\nu}$ is the second order perturbation. However, there is now an issue in clearly separating the background and perturbations. In linearised gravity it was clear that the background was the Minkowski metric and the gravitational wave perturbation existed in this background spacetime, but in curved space it is harder to make such a distinction. The most common approach for implementing this separation is detailed in the next section, however we first give expressions for the Ricci tensor to second order under the above perturbation scheme;

$$R_{\mu\nu} = \tilde{R}(\tilde{g}_{\mu\nu}) + R_{\mu\nu}^{(1)}(h_{\mu\nu}) + R_{\mu\nu}^{(2)}(h_{\mu\nu}) + R_{\mu\nu}^{(1)}(j_{\mu\nu}), \quad (2.7)$$

where [192],

$$R_{\mu\nu}^{(1)}(h_{\mu\nu}) = \frac{1}{2}(-h_{|\mu\nu} - h_{\mu\nu|\alpha}{}^\alpha + h_{\alpha\mu|\nu}{}^\alpha + h_{\alpha\nu|\mu}{}^\alpha), \quad (2.8a)$$

$$R_{\mu\nu}^{(2)}(h_{\mu\nu}) = \frac{1}{2} \left[\frac{1}{2} h_{\alpha\beta|\mu} h^{\alpha\beta}{}_{|\nu} + h_\nu{}^{\alpha|\beta} (h_{\alpha\mu|\beta} - h_{\beta\mu|\alpha}) \right. \\ \left. + h^{\alpha\beta} (h_{\alpha\beta|\mu\nu} + h_{\mu\nu|\alpha\beta} - h_{\alpha\mu|\nu\beta} - h_{\alpha\nu|\mu\beta}) \right. \\ \left. - \left(h^{\alpha\beta}{}_{|\beta} - \frac{1}{2} h^{|\alpha} \right) (h_{\alpha\mu|\nu} + h_{\alpha\nu|\mu} - h_{\mu\nu|\alpha}) \right], \quad (2.8b)$$

with an upright line denoting a covariant derivative with respect to the *background* metric and the trace of the perturbation, $h = h^i{}_i$. $R_{\mu\nu}^{(1)}(j_{\mu\nu})$ is functionally identical to $R_{\mu\nu}^{(1)}(h_{\mu\nu})$ such that it is given by equation (2.8a) and is a second order quantity⁶. These expressions are valid in all cases where,

$$|j_{\mu\nu}| \ll |h_{\mu\nu}| \ll |\tilde{g}_{\mu\nu}| \quad (\sim 1). \quad (2.9)$$

It is worth noting the behaviour of the first order equation for a cosmological background. So far gravitational waves have only been considered in vacuum, but the equation of motion can also include a source term. In an

⁶The superscript on the Ricci tensor labels the order the function is in its argument irrespective of whether the argument is first or second order.

FLRW background, using conformal time and considering the gauge-invariant tensor perturbation, i.e. the TT part, the equation of motion coming from equation (2.8a) is,

$$\ddot{h}_{ij} + 2\mathcal{H}\dot{h}_{ij} - h_{ij,k}{}^k = 16\pi G a^2 \Pi_{ij}^{(T)}, \quad (2.10)$$

where $\Pi_{ij}^{(T)}$ is the anisotropic inertia tensor which is the transverse-traceless perturbation part of the energy–momentum tensor⁷. The tensor metric perturbation, h_{ij} contains two degrees of freedom as before and the anisotropic inertia tensor, $\Pi_{ij}^{(T)}$ encodes the two degrees of freedom of the perturbed energy–momentum tensor and hence the gravitational wave sources. The anisotropic inertia tensor can often be neglected so the equation of motion can be solved as in vacuum, though there is a correction to the gravitational wave evolution due to the anisotropic inertia from neutrinos [28, 194, 195]. The dependence on the metric in the Boltzmann equation for neutrinos results in the neutrino shear being a functional of the derivative of the gravitational wave amplitude. Consequently neutrino shear acts as an increase in the damping term for gravitational waves which can result in a $\sim 30\%$ decrease in the amplitude of the B -mode power spectrum⁸ [28, 195].

Gravitational waves can also be sourced by an anisotropic stress from a variety of processes in the early Universe, see section 2.6.

2.3 The shortwave approximation

The shortwave approximation [192, 193, 196, 197] separates the background and perturbation by requiring that the scale that the first order perturbation fluctuates on, $\lambda = \lambda/(2\pi)$ is much less than the scale that the background varies on, \mathcal{R} ;

$$\lambda \ll \mathcal{R}. \quad (2.11)$$

⁷It is the tensor part of Σ_j^i in equation (1.31c). See Weinberg [28], equation 5.1.39.

⁸The equations are usually solved numerically and are an optional extension in cosmological codes such as CAMB.

There is a clear distinction between perturbation and background when the gravitational waves have a ‘short’ wavelength compared to the background.

To proceed further, an averaging length scale l is introduced which satisfies,

$$\lambda \ll l \ll \mathcal{R}. \quad (2.12)$$

When averaging over volumes associated with l the perturbations will average to zero whereas the background will be approximately constant. The smooth part of the Ricci tensor is,

$$R_{\mu\nu}^{(\text{smooth})} = \tilde{R}_{\mu\nu} + \langle R_{\mu\nu}^{(2)}(h_{\mu\nu}) \rangle_l, \quad (2.13)$$

where $\langle \dots \rangle_l$ denotes averaging over a volume with sides of length l . Therefore the averaged second order perturbation on the Ricci tensor modifies the curvature of the background. The fluctuating part is given by,

$$R_{\mu\nu}^{(\text{fluc})} = R_{\mu\nu}^{(1)}(h_{\mu\nu} + j_{\mu\nu}) + R_{\mu\nu}^{(2)}(h_{\mu\nu}) - \langle R_{\mu\nu}^{(2)}(h_{\mu\nu}) \rangle_l. \quad (2.14)$$

In vacuum both of these expressions are required to be equal to zero. Consequently equation (2.13) gives the Einstein equation,

$$\tilde{R}_{\mu\nu} - \frac{1}{2}\tilde{g}_{\mu\nu}\tilde{R} = 8\pi GT_{\mu\nu}^{(\text{GW})}, \quad (2.15)$$

where $\tilde{R} = \tilde{R}^\mu{}_\mu$ and the gravitational wave *effective energy–momentum tensor* is given by,

$$T_{\mu\nu}^{(\text{GW})} = -\frac{1}{8\pi G} \langle R_{\mu\nu}^{(2)}(h_{\mu\nu}) - \frac{1}{2}\tilde{g}_{\mu\nu}R^{(2)}(h_{\mu\nu}) \rangle_l, \quad (2.16)$$

with the trace, $R^{(2)}(h_{\mu\nu}) = \tilde{g}^{\mu\nu}R_{\mu\nu}^{(2)}(h_{\mu\nu})$. It follows that, in the shortwave approximation, we can define the energy–momentum carried by a gravitational wave by averaging over many wavelengths. It is important to note that this equation is independent of the averaging scale, l because of the hierarchy of scales given in equation (2.12). This can be elucidated by considering the simple model of a sinusoidal solution for $h_{\mu\nu}$. In this case all the linear terms

in equation (2.8a) will vanish under averaging because they enclose equal positive and negative areas. For second order terms that depend on products of derivatives of $h_{\mu\nu}$ the situation is more complicated, as some of these terms will be in anti-phase and hence cancel out, and some will be in phase and consequently reinforce each other. The separation of scales is vital so that the average is over many wavelengths, such that the above statements are true, and also so that the averaging scale is less than the background scale, such that physical variations are not being averaged away. Consequently equation (2.16) is an expression for a gravitational wave effective energy–momentum tensor which is independent of l and which can be used in Einstein’s equations in the same way any energy–momentum tensor can.

While this expression was derived assuming gravitational wave propagation in vacuum, the gravitational waves can be treated in the same way in the presence of matter and the right-hand side of the Einstein equations will then just be a sum of the energy–momentum tensor for matter and the effective energy–momentum tensor for gravitational waves [198].

The effective energy–momentum tensor for gravitational waves can be explicitly evaluated. In the TT gauge, using cosmological time and equations (2.8),

$$T_{\mu\nu}^{(\text{GW})} = \frac{1}{32\pi G} \langle h_{\alpha\beta|\mu} h^{\alpha\beta}_{|\nu} \rangle_t. \quad (2.17)$$

This can also be derived from the Landau–Lifshitz pseudo-tensor (see Landau and Lifshitz [199] and Su and Zhang [200] for details).

In spacetimes that are close to flat, covariant derivatives can be approximated by partial derivatives and the equation of motion assuming zero anisotropic stress becomes,

$$h_{\mu\nu,\alpha}{}^\alpha = 0, \quad (2.18)$$

for a gravitational wave propagating in the z - or 3-direction. This equation of motion has solutions that depend on the retarded time, $t - z$. Consequently spatial and temporal derivatives can be interchanged and the trace of the

effective energy–momentum tensor,

$$T^{(\text{GW})} = \frac{1}{32\pi G} (\langle h_{ij,3} h^{ij,3} \rangle - \langle h_{ij,0} h^{ij,0} \rangle) = 0. \quad (2.19)$$

The full solution is a sum of plane waves of positive and negative frequencies along all three spatial directions (such that it is isotropic), but this argument applies to each of these spatial directions separately. Therefore, under the short-wave approximation, gravitational waves have an equation of state parameter, $w_{\text{GW}} = 1/3$, as for a massless radiation species.

The above argument holds in an FLRW background with the retarded time depending on $\tau - z$ instead. Therefore cosmological gravitational waves are expected to have the same background behaviour as massless neutrinos when the shortwave approximation is valid [192, 193].

2.4 A non-shortwave approach

Mukhanov, Abramo, and Brandenberger [38, 201] calculate an effective energy–momentum tensor for gravitational waves that is valid for all wavelengths. This approach still requires the condition $|h_{\mu\nu}| \ll 1$ that keeps the metric expansion well defined but relaxes the condition on the length scales associated with the curvature, allowing λ to vary on scales \mathcal{R} or larger. The approach is formulated using gauge-invariant cosmological perturbations where the background is fixed to FLRW (see section 1.3.1). The averaging over many wavelengths of the shortwave approximation is replaced with averaging over all space, defined by,

$$\langle A \rangle_x = \lim_{V \rightarrow \infty} \frac{1}{V} \int A \, dV, \quad (2.20)$$

for a general function A . Under this averaging, linear perturbations average to zero by definition, but terms quadratic in the linear perturbations do not. Note that terms depending on the second order metric perturbation $j_{\mu\nu}$ vanish under this averaging, as they do in the shortwave approximation.

Expanding the Einstein equations to second order and averaging over all

space,

$$\tilde{G}^\mu{}_\nu + \langle \delta^{(2)} G^\mu{}_\nu \rangle_x = 8\pi G \left(\tilde{T}^\mu{}_\nu + \langle \delta^{(2)} T^\mu{}_\nu \rangle_x \right), \quad (2.21)$$

where $\tilde{G}^\mu{}_\nu$ and $\tilde{T}^\mu{}_\nu$ are the background Einstein and energy–momentum tensors respectively, and $\delta^{(2)} G^\mu{}_\nu$ and $\delta^{(2)} T^\mu{}_\nu$ are the second order perturbations to the Einstein and energy–momentum tensor respectively. This allows the effective energy–momentum tensor, $T^{(\text{GW})\mu}{}_\nu$ to be defined,

$$T^{(\text{GW})\mu}{}_\nu = \frac{1}{8\pi G} \left(8\pi G \langle \delta^{(2)} T^\mu{}_\nu \rangle_x - \langle \delta^{(2)} G^\mu{}_\nu \rangle_x \right). \quad (2.22)$$

The gauge invariance is complicated for scalar perturbations but for tensor perturbations it only requires that the perturbation is in the TT gauge. In terms of cosmological time, the expanding TT metric is defined by⁹,

$$ds^2 = -dt^2 + a^2(t)(\delta_{ij} + h_{ij})dx^i dx^j, \quad (2.23)$$

where $a(t)$ is the scale factor as in the previous chapter and in comparing to the previous section the tensor perturbation has changed from $h_{ij} \rightarrow a^2 h_{ij}$. In this case the evaluation of the effective energy–momentum tensor for gravitational waves simplifies to evaluating the perturbed Einstein tensor,

$$T^{(\text{GW})\mu}{}_\nu = -\frac{1}{8\pi G} \langle \delta^{(2)} G^\mu{}_\nu \rangle_x. \quad (2.24)$$

Using equation (2.8b) and the equation of motion in vacuum for cosmological time,

$$\frac{d^2 h_{ij}}{dt^2} + 3H \frac{dh_{ij}}{dt} - \frac{1}{a^2} h_{ij,k}{}^k = 0, \quad (2.25)$$

the (00) and (ij) components of the effective energy–momentum tensor are,

$$T^{(\text{GW})0}{}_0 = \frac{1}{8\pi G} \left[H \left\langle \frac{dh_{ij}}{dt} h_{ij} \right\rangle_x + \frac{1}{8} \left(\left\langle \frac{dh_{ij}}{dt} \frac{dh_{ij}}{dt} \right\rangle_x + \frac{1}{a^2} \langle h^{ij,k} h_{ij,k} \rangle_x \right) \right], \quad (2.26a)$$

⁹Abramo, Brandenberger, and Mukhanov [38] use a mostly negative metric, I have changed this here to be consistent with other sections.

$$T^{(\text{GW})i}_j = \frac{1}{8\pi G} \left[\delta^i_j \left(\frac{3}{8} \left\langle \frac{dh^{kl}}{dt} \frac{dh_{kl}}{dt} \right\rangle_x - \frac{3}{8a^2} \langle h^{kl,m} h_{kl,m} \rangle_x \right) - \frac{a^2}{2} \left\langle \frac{dh^{ik}}{dt} \frac{dh_{kj}}{dt} \right\rangle_x - \frac{1}{4} \langle h^{kl,i} h_{kl,j} \rangle_x + \frac{1}{2} \langle h^{ik,l} h_{jk,l} \rangle_x \right]. \quad (2.26b)$$

The $(0i)$ components of the effective energy–momentum tensor are zero under the averaging of equation (2.20), assuming an isotropic source of gravitational waves.

The (00) component of the effective energy–momentum tensor can be interpreted as the effective energy density of gravitational waves, ρ_{gw} . However, $T^{(\text{GW})i}_j$ is not simply related to the pressure because the effective energy–momentum tensor defined in this way is not conserved, $T^{(\text{GW})\mu}_{\nu|\mu} \neq 0$. This is linked to the problem of distinguishing the background from the gravitational wave perturbation, or put another way due to the interactions of matter and gravitational waves [200, 202]. This interaction between gravitational waves and the background is seen in the conservation equation for the effective energy–momentum tensor. The covariant derivative, $T^{(\text{GW})\mu}_{\nu|\mu}$, results in the conservation equation,

$$\frac{d\rho_{\text{gw}}}{dt} + 3H \left(\rho_{\text{gw}} + \left[-\frac{1}{3} T^{(\text{GW})i}_i \right] \right) = \langle \Gamma^{(2)\alpha}_{\alpha 0} \rangle_x (\bar{\rho} + \bar{p}), \quad (2.27)$$

where the term on the right depends on the background and the gravitational wave amplitude. To restore the required conserved nature of the background fluid this extra term is incorporated into the pressure. When interactions between gravitational waves and matter are not considered this term vanishes.

Alternatively this can be seen by considering the fact that it is the total energy–momentum tensor that is conserved,

$$(\tilde{T}^\mu_\nu + T^{(\text{GW})\mu}_\nu)_{|\mu} = 0. \quad (2.28)$$

Expanding this to second order, averaging the resulting equation and assuming an isotropic background with no perturbations¹⁰, we see that there is an extra

¹⁰This is essentially assuming that the decomposition theorem is still valid. This is valid under averaging at second order [203].

term missing from the expression for the effective pressure, if just the effective energy–momentum tensor is used, which depends on the background density, $\bar{\rho}$, and pressure, \bar{p} via the background equation of state parameter, \bar{w} . Including this term, the gravitational wave density and pressure satisfy the continuity equation,

$$\frac{d\rho_{\text{gw}}}{dt} + 3H(\rho_{\text{gw}} + p_{\text{gw}}) = 0, \quad (2.29)$$

where they are given by,

$$\rho_{\text{gw}} = T^{(\text{GW})0}_{0}, \quad (2.30a)$$

$$p_{\text{gw}} = -\frac{1}{3}T^{(\text{GW})i}_{i} - \frac{1}{3H}\langle\Gamma^{(2)\alpha}_{\alpha 0}\rangle_x(\bar{\rho} + \bar{p}), \quad (2.30b)$$

$$= -\frac{1}{3}T^{(\text{GW})i}_{i} + \frac{1}{8\pi G 2}H(1 + \bar{w})\left\langle h^{ij}\frac{dh_{ij}}{dt}\right\rangle_x, \quad (2.30c)$$

and $2\Gamma^{(2)\alpha}_{\alpha 0} = -\langle h^{ij}(dh_{ij}/dt)\rangle_x$ is a summed component of the second-order perturbed Christoffel symbol. The gravitational wave-matter interaction term vanishes in the case that there are no matter interactions ($\bar{\rho} + \bar{p} = 0$) which confirms the statement above; in the absence of matter the effective energy-momentum tensor alone is needed. Su and Zhang [200] show that this extra term is negligible for short-wavelength gravitational waves, for all cosmological backgrounds since inflation.

It is worth noting that because of the averaging, the density and pressure are total quantities for a homogeneous and isotropic background of gravitational waves and consequently depend only on time, as one would expect for a background density and pressure.

Abramo, Brandenberger, and Mukhanov [38] use these expressions for the gravitational wave density and pressure to find the equation of state of gravitational waves in the long- and short-wavelength limits¹¹. They find the equation of state in the short-wavelength limit similarly to how it was done in the short-wave approximation in the previous section. In this regime a time average over a period $T \ll H^{-1}$ results in the terms with two time and two space deriva-

¹¹Ref. [38] also details the application of this formalism to the backreaction of scalar perturbations during inflation.

tives being the same and hence the equation of state is $1/3$, as a result of the pre-factors in equations (2.26). As this is shown without considering a specific background it is expected that short-wavelength gravitational waves behave like radiation independent of the universe that the gravitational wave perturbations are being considered in. This confirms the shortwave approximation result for the gravitational wave equation of state.

Ref. [38] then details long-wavelength expansion solutions of the equation of motion (equation (2.25)) for the gravitational wave perturbation, h_{ij} , for de Sitter (i.e. cosmological constant) and radiation backgrounds. The long-wavelength gravitational waves are defined by the condition $k \ll aH$. Putting these expansions into the expressions for the density and pressure and taking the long-wavelength limit gives an equation of state of $-1/3$ for both backgrounds. Consequently the energy density of long-wavelength gravitational waves decreases as a^{-2} .

Brandenberger and Takahashi [203] revisited this methodology more recently. They follow the above approach for calculating the gravitational wave density and pressure but instead work in conformal time¹². They extend the work of ref. [38] by also giving the relevant expressions for the gravitational wave density and pressure in Fourier space. Rewriting equation (2.5) in terms of conformal time, the gravitational wave perturbation is written as,

$$h_{ij}(\tau, \vec{x}) = \sum_{\lambda=+,\times} \int \frac{d^3k}{(2\pi)^3} \epsilon_{ij}^\lambda(\vec{k}) h^\lambda(\tau, \vec{k}) e^{i\vec{k}\cdot\vec{x}}, \quad (2.31)$$

where $\epsilon_{ij}^\lambda(\vec{k})$ is the polarisation tensor with helicity λ and $h^\lambda(\tau, \vec{k})$ is the scalar gravitational wave amplitude as before. This is advantageous as analytic solutions to the helicity-independent equation of motion for the gravitational wave amplitude (compare to the real-space, tensor equation of motion in terms of cosmological time in equation (2.25)),

$$\ddot{h}(\tau, \vec{k}) + 2\mathcal{H}\dot{h}(\tau, \vec{k}) + k^2 h(\tau, \vec{k}) = 0, \quad (2.32)$$

¹²This was also done in detail in appendix A of Giovannini [202].

can be found for one-component cosmological backgrounds. It is also useful as it allows for the standard approach of separating the initial conditions from the time and space evolution and parameterising the stochastic average of these initial conditions by the primordial power spectrum (see section 1.4.1) [28]. Therefore the gravitational wave amplitude,

$$h^\lambda(\tau, k) = A^\lambda(k)f(\tau, k) \quad (2.33)$$

where $A^\lambda(k)$ is the initial condition and $f(\tau, k)$ describes the time evolution and satisfies $f(0, k) = 1$. These quantities depend only on the magnitude k due to isotropy. The total gravitational wave density and pressure are,

$$\rho_{\text{gw}} = \frac{1}{8\pi G a^2} \int_{k_{\text{min}}}^{k_{\text{max}}} d \ln k \tilde{\rho}_{\text{gw}}(k, \tau) \mathcal{P}_t(k), \quad (2.34a)$$

$$p_{\text{gw}} = \frac{1}{8\pi G a^2} \int_{k_{\text{min}}}^{k_{\text{max}}} d \ln k \tilde{p}_{\text{gw}}(k, \tau) \mathcal{P}_t(k), \quad (2.34b)$$

where k_{min} is an infrared cutoff and k_{max} is an ultraviolet cutoff set by the Hubble radius at the end of inflation and,

$$\tilde{\rho}_{\text{gw}}(k, \tau) = \left[\frac{1}{8} \left(k^2 f^2 + \dot{f}^2 \right) + \mathcal{H} \dot{f} f \right], \quad (2.35a)$$

$$\tilde{p}_{\text{gw}}(k, \tau) = \frac{7k^2}{24} f^2 - \frac{5}{24} \dot{f}^2 + \frac{\mathcal{H}}{2} (1 + \bar{w}) \dot{f} f. \quad (2.35b)$$

These are the analogous expression to equations (2.26) and (2.30) but for conformal time and with the gravitational wave equation of motion solutions in k -space.

Brandenberger and Takahashi [203] use the same argument for the short-wavelength limit as ref. [38] – that time and space derivative terms are equivalent – to show that the equation of state for short-wavelength gravitational waves is $1/3$. This is done using the real space expressions. They go on to find the solutions of the equation of motion for de Sitter, radiation and matter backgrounds and use these to give explicit expressions¹³ for $\tilde{\rho}_{\text{gw}}(k)$ in

¹³Ref. [203] uses a different definition of $\tilde{\rho}_{\text{gw}}$ to the one here. It differs only by a constant factor of a stochastic average over the initial conditions, $\langle |A^\lambda(k)|^2 \rangle_Q$ (see section 4.2 for more details of this averaging).

the long-wavelength limit ($k\tau \ll 1$). They then state that the pressure is $\tilde{p}_{\text{gw}}(k) = -\tilde{\rho}_{\text{gw}}(k)/3$ in this limit, as in ref. [38].

The equation of state of gravitational waves that governs the time evolution is $w_{\text{gw}}(\tau) = p_{\text{gw}}(\tau)/\rho_{\text{gw}}(\tau)$. However statements are often made about the equation of state from the value of the spectral equation of state, $\tilde{w}_{\text{gw}}(k, \tau) = \tilde{p}_{\text{gw}}(k, \tau)/\tilde{\rho}_{\text{gw}}(k, \tau)$. These are equivalent if the spectral equation of state is constant. In this case the integrals in equations (2.34) become,

$$\rho_{\text{gw}} = \frac{1}{8\pi G a^2} \int_{k_{\text{min}}}^{k_{\text{max}}} d \ln k \tilde{\rho}_{\text{gw}}(k, \tau) \mathcal{P}_t(k), \quad (2.36a)$$

$$p_{\text{gw}} = \frac{1}{8\pi G a^2} \int_{k_{\text{min}}}^{k_{\text{max}}} d \ln k \tilde{w}_{\text{gw}} \tilde{\rho}_{\text{gw}}(k, \tau) \mathcal{P}_t(k). \quad (2.36b)$$

Clearly the constant \tilde{w}_{gw} can be taken out of the second integral and $w_{\text{gw}} = \tilde{w}_{\text{gw}}$. Therefore, if the spectral equation of state is shown to be constant, the ‘true’, integrated equation of state is equal to the same constant. As a result w_{gw} and \tilde{w}_{gw} will be used interchangeably in future chapters when the spectral equation of state is constant.

The gravitational wave density in the long-wavelength limit is negative in all the backgrounds considered. Because of this and the equation of state it is concluded that the backreaction of long-wavelength gravitational waves has the same effect as a change in the spatial curvature. It is important to note that this is only valid for small gravitational wave perturbations and consequently this approach shows that the *backreaction* of long-wavelength gravitational waves reduces the total density in the same way as curvature, not that these gravitational waves truly have a negative energy density.

The condition that the gravitational wave density is small,

$$\rho_{\text{gw}} \ll \rho_{\text{crit}}, \quad (2.37)$$

which is required to be valid at all times in the history of the Universe, can be used to constrain the tensor-to-scalar ratio, r_{k_*} and tensor tilt, n_t , assuming a power-law initial spectrum [203]. This condition, that gravitational waves

do not dominate the early universe, comes from the requirement that the perturbation expansion is well defined, $|h_{\mu\nu}| \ll \tilde{g}_{\mu\nu}$. Note that ρ_{crit} depends on the background; this condition is required to be true regardless of the background. The constraints found in this way are dependent on the model of inflation.

2.4.1 Fluctuations

We have so far neglected the rapidly fluctuating component of the gravitational wave perturbations as these have been shown to have no affect on the background evolution. The backreaction of this fluctuating component will change the ‘perturbations’ i.e. the first order part of the Einstein equations [203]. This was done for the backreaction of long-wavelength scalar modes in an inflationary background in ref. [204] but has not been considered for the tensor perturbation or other cosmological backgrounds.

2.5 Detection

There is a range of different observational techniques that are currently being used to constrain the density of PGWs. These are typically presented as constraints on the gravitational wave density parameter, $\Omega_{\text{gw}}h^2$. The most common observational methods are detailed in this section.

It is important to note that there are two main types of constraint, *non-integral* and *integral* constraints [194, 205–207]. Non-integral constraints, are constraints on the density as a function of frequency, f ,

$$\Omega_{\text{gw}}(f) = \frac{1}{\rho_{\text{crit}}} \frac{d\rho_{\text{gw}}}{d \log f}, \quad (2.38)$$

in a specific frequency range determined by the sensitivity of the observational probe used. Integral constraints are constraints on,

$$\Omega_{\text{gw}} = \int_{f_{\text{min}}}^{f_{\text{max}}} d(\log f) \Omega_{\text{gw}}(f), \quad (2.39)$$

and therefore need to be treated carefully when comparing to frequency-

dependent, non-integral constraints [208]. Here f_{\min} is a low-frequency limit coming from the experimental probe being used and f_{\max} is a high-frequency limit which is usually related to the energy scale at the end of inflation [209]. Because this energy scale is usually very high, and motivated by the high-frequency dependence of gravitational wave backgrounds, this upper limit is often taken to infinity, but it is important to emphasise that the lower limit does not go to zero [194]. Integrated constraints only include contributions from gravitational waves that have frequencies greater than f_{\min} . Integral constraints are often plotted as flat lines on constraint plots and are consequently assuming a power-law spectrum across their range of validity. It is possible that a very sharply peaked source of gravitational waves could violate this constraint but such a source is not expected from any currently predicted cosmological mechanism (see section 2.6). As mentioned above the integral constraints typically have limits set by specific considerations of the observational methodology.

2.5.1 CMB B -modes

The reader is referred to section 1.4.3 for details of CMB B -mode constraints to PGWs. However, it is important here to comment on the conversion between constraints on the tensor-to-scalar ratio and the gravitational wave density parameter, $\Omega_{\text{gw}}h^2$.

A constraint on the tensor-to-scalar ratio, r_{k_*} can be converted to the gravitational wave density parameter [205, 210–212]. Assuming the initial spectrum is described by a power-law, the gravitational wave density parameter as a function of wavenumber is,

$$\Omega_{\text{gw}}(k)h^2 = \frac{3}{128}\Omega_{\text{r}}h^2 r_{k_*} A_{\text{s}}(k_*) \left(\frac{k}{k_*}\right)^{n_{\text{t}}} \left[\frac{1}{2} \left(\frac{k_{\text{eq}}}{k}\right)^2 + \frac{16}{9} \right], \quad (2.40)$$

where $k_{\text{eq}} = \sqrt{2}H_0\Omega_{\text{m}}/\sqrt{\Omega_{\text{r}}}$ is the wavenumber of a mode that enters the horizon at matter–radiation equality and k_* is the pivot scale (as in section 1.4). This is derived from considerations of the *short wavelength* transfer

function of the tensor perturbations during and after slow-roll inflation and assuming a power-law initial power spectrum [194]. However, here, and in many existing applications, the short wavelength transfer function is not valid, as the gravitational waves are super-horizon (or only slightly sub-horizon) at the time of the observational probe, in this case CMB decoupling. Consequently, it should be stressed that, while this conversion is prevalent in the scientific literature, it is incorrect to use it for the B -mode constraint. Nonetheless equation (2.40) is presented here due to its widespread usage for this conversion, but should only be considered as a first approximation to the true conversion between the tensor-to-scalar ratio and the gravitational wave density parameter when the gravitational waves considered are not suitably sub-horizon.

2.5.2 CMB isotropy

One of the earliest constraints to the gravitational wave density came from *COBE* measurements of the low- ℓ multipoles [213]. A background of long-wavelength gravitational waves results in an increase in the Sachs–Wolfe effect at very large scales decreasing the isotropy of the Universe. Therefore, observations of the low- ℓ multipoles tightly constrain the gravitational wave density at low frequencies. The constraint is [206, 214],

$$\Omega_{\text{gw}}(f)h^2 < 7 \times 10^{-11} \left(\frac{H_0}{f} \right)^2, \quad (2.41)$$

for the frequency range, $3 \times 10^{-18} \text{ Hz} < f < 10^{-16} \text{ Hz}$ [207]. Written instead in terms of k this constraint is,

$$\Omega_{\text{gw}}(k)h^2 < 3 \times 10^{-9} \left(\frac{H_0}{k} \right)^2, \quad (2.42)$$

for the k range, $2 \times 10^{-3} \text{ Mpc}^{-1} < k < 0.06 \text{ Mpc}^{-1}$. This is tightest at the upper edge of its validity where the gravitational wave density parameter is constrained to $\sim 10^{-13}$. This is roughly the same frequency range probed when including B -mode polarisation, which allows for tighter constraints and consequently the CMB isotropy constraint is rarely presented anymore.

2.5.3 Big bang nucleosynthesis

As detailed in section 1.5.3, BBN is highly sensitive to the number of neutrino species. Because gravitational waves obeying the shortwave approximation have the same equation of state as massless neutrinos they are expected to have the same effect on the expansion history and therefore contribute to N_{eff} [207, 214]. Therefore, assuming N_{eff} has its standard model value, an observation of $N_{\text{eff}} > 3.046$ can be attributed to gravitational waves. Conversely when there is no excess this can instead be used to constrain the gravitational wave density¹⁴ via,

$$\begin{aligned}\Omega_{\text{gw}}h^2 &= \int_{f_{\text{min}}}^{\infty} d(\log f) h^2 \Omega_{\text{gw}}(f) \\ &\simeq 5.6 \times 10^{-6} (N_{\text{eff}} - 3.046) = 5.6 \times 10^{-6} N_{\text{gw}},\end{aligned}\quad (2.43)$$

where $N_{\text{gw}} = N_{\text{eff}} - 3.046$, is the effective number of neutrino degrees of freedom contributed by gravitational waves. The constant in the second line of equation (2.43) comes from the definition of N_{eff} (equation (1.18)). Consequently, the conversion factor between the density parameter and the number of gravitational wave degrees of freedom is

$$\frac{7}{8} \left(\frac{4}{11} \right)^{4/3} \Omega_{\gamma} h^2 = 5.605 \times 10^{-6}, \quad (2.44)$$

where the observed CMB temperature has been used to determine $\Omega_{\gamma} h^2$. Rounding this gives the commonly presented value of 5.6×10^{-6} as seen above.

This is an indirect integral constraint which is valid for all gravitational wave frequencies which obeyed the shortwave approximation during BBN. The frequency corresponding to the Hubble radius at the time of BBN is $f_{\text{BBN}} \approx 1.5 \times 10^{-12}$ Hz [194]. Consequently BBN constraints are typically assumed to apply above $f_{\text{min}} \approx 10^{-10}$ Hz to give gravitational waves enough

¹⁴Any additional relativistic particle in the early Universe will increase N_{eff} but constraints apply to all of the possible species. In some ways this is preferable. If an excess was observed there would be a huge range of possible candidates that would require other observations to discern between them. In this case a constraint can confidently be put on gravitational waves from the fact that N_{eff} is close to 3.046.

time to become oscillatory after coming inside the horizon and hence obey the shortwave approximation [96, 215].

While BBN measurements of N_{eff} were considered contentious around the turn of the 21st century due to large systematic errors, they provided the tightest constraint to gravitational waves at high frequencies even for the most conservative upper limits on N_{eff} [207, 216]. Recent BBN measurements have reached stronger consensus and constrain,

$$\Omega_{\text{gw}} h^2 < 4.8 \times 10^{-6}, \quad (2.45)$$

at 95% confidence [94, 217].

2.5.4 Shortwave gravitational waves in the CMB

Similarly to BBN, the CMB is also sensitive to the expansion history and therefore N_{eff} . Hence the CMB power spectrum can also be used to constrain the density of short-wavelength gravitational waves. However, unlike BBN, the CMB is also sensitive to the perturbations in the species present at recombination. While the shortwave approximation justifies the assumption that gravitational waves have the same background behaviour as massless neutrinos it makes no statement about the appropriate choice of gravitational wave perturbations.

Smith, Pierpaoli, and Kamionkowski [96] assume that gravitational wave perturbations obey the same fluid equations as neutrinos¹⁵,

$$\dot{\delta}_{\text{gw}} + \frac{4}{3}\theta_{\text{gw}} + \frac{2}{3}\dot{h} = 0, \quad (2.46a)$$

$$\dot{\theta}_{\text{gw}} - \frac{1}{4}k^2(\delta_{\text{gw}} - 4\sigma_{\text{gw}}) = 0, \quad (2.46b)$$

$$\dot{\sigma}_{\text{gw}} - \frac{2}{15}(2\theta_{\text{gw}} + \dot{h} + 6\dot{\eta}) = 0, \quad (2.46c)$$

and consider two choices of initial conditions for the perturbations, *adiabatic* and *homogeneous* initial conditions. Adiabatic initial conditions are the same

¹⁵The fluid equations are given in the synchronous gauge for illustrative purposes. The gravitational wave equations in any other gauge would also be identical to those for massless neutrinos.

as the initial conditions for neutrinos and in this case gravitational waves contribute to the perturbations identically to neutrinos, such that a CMB constraint on N_{eff} can be converted directly into a constraint on short-wavelength, adiabatic gravitational waves via equation (2.43). This is the appropriate choice if gravitational waves are a thermalised species produced by the decay of the inflaton. However, most known sources of a cosmological gravitational wave background, including quantum fluctuations during inflation, reheating and cosmic strings, produce an unperturbed background (see Caprini and Figueroa [194] section 4.1 or Maggiore [218] section 22.7.2). Consequently the second choice of gravitational wave initial conditions, *homogeneous* initial conditions, have no initial density perturbation (in the Newtonian gauge). In this case the gravitational wave perturbations evolve differently to the neutrino perturbations such that the degeneracy between Ω_{gw} and N_{eff} is broken. There are no physical justifications for gravitational waves having adiabatic initial conditions and they are only calculated here for comparison and as a first approximation.

A detailed calculation of the homogeneous initial conditions including translation into the synchronous gauge and into a form appropriate to input directly into CAMB (see section 1.5.1) is given in appendix B of Smith [219]. The basic idea is to solve the coupled perturbation equations (as detailed in section 1.3.3) in the Newtonian gauge while requiring that $\delta_{\text{gw}} = 0$. The homogeneous initial condition calculated here makes the assumption that the zeroth order coefficients of the photons and the neutrinos are the same, $\delta_\gamma(\tau \rightarrow 0) = \delta_\nu(\tau \rightarrow 0)$ and that $R_{\text{gw}} < R_\gamma, R_\nu$ so that the gravitational wave relativistic ratio can be defined as $R_{\text{gw}} = \rho_{\text{gw}}/(\rho_\nu + \rho_\gamma)$.

The initial conditions for adiabatic and homogeneous gravitational waves are given in the synchronous gauge in table 2.1. The adiabatic and homogeneous modes are the same in the limit $R_{\text{gw}} \rightarrow 0$ as one would expect.

Including short-wavelength gravitational waves in the CMB analysis affects the background expansion as it does for the BBN constraint [194]. The redshift of matter–radiation equality and the time of decoupling are shifted later by

Table 2.1: Adiabatic and homogeneous initial conditions for short-wavelength gravitational wave perturbations in the synchronous gauge. For the adiabatic mode, terms are given to lowest order in $k\tau$. For the homogeneous mode, terms are given to lowest order except where these terms vanish in the limit $R_{\text{gw}} \rightarrow 0$. It is clear that the homogeneous and adiabatic modes are the same in this limit.

	Adiabatic	Homogeneous
$\delta_\gamma, \delta_\nu$	$-\frac{1}{3}k^2\tau^2$	$-\frac{20R_{\text{gw}}}{15+4R_\nu} - \frac{1}{3}\left(1 - \frac{10R_{\text{gw}}}{15+4R_\nu}\right)k^2\tau^2$
δ_b	$-\frac{1}{4}k^2\tau^2$	$\frac{3}{4}\delta_\gamma$
δ_c	$-\frac{1}{4}k^2\tau^2$	$-\frac{15R_{\text{gw}}}{15+4R_\nu} - \frac{1}{4}k^2\tau^2$
θ_γ, θ_b	$-\frac{1}{36}k^4\tau^3$	$-\frac{5R_{\text{gw}}}{15+4R_\nu}k^2\tau - \frac{1}{36}\left(1 - \frac{10R_{\text{gw}}}{15+4R_\nu}\right)k^4\tau^3$
θ_ν	$\frac{23+4R_\nu}{15+4R_\nu}\theta_\gamma$	$-\frac{5R_{\text{gw}}}{15+4R_\nu}k^2\tau - \frac{1}{36}\left(\frac{23+4R_\nu}{15+4R_\nu} - \frac{18R_{\text{gw}}}{15+4R_\nu}\right)k^4\tau^3$
θ_c	0	0
σ_ν	$\frac{2}{3(15+4R_\nu)}k^2\tau^2$	$\frac{2(1-R_{\text{gw}})}{3(15+4R_\nu)}k^2\tau^2$
δ_{gw}	$-\frac{1}{3}k^2\tau^2$	$\frac{20}{15+4R_\nu}$
θ_{gw}	$\frac{23+4R_\nu}{15+4R_\nu}\theta_\gamma$	$\frac{5}{15+4R_\nu}k^2\tau$
σ_{gw}	$\frac{2}{3(15+4R_\nu)}k^2\tau^2$	$\frac{4}{3(15+4R_\nu)}k^2\tau^2$
h	$\frac{1}{2}k^2\tau^2$	$\frac{1}{2}k^2\tau^2$
η	$1 - \frac{(5+4R_\nu)}{12(15+4R_\nu)}k^2\tau^2$	$1 - \frac{(5+4R_\nu)}{12(15+4R_\nu)}k^2\tau^2$

extra relativistic species and such a shift is well constrained by the CMB power spectrum. The background change will also affect BAO observations.

The effect due to the gravitational wave perturbations is dependent on the choice of initial conditions. For adiabatic initial conditions an increase in $\Omega_{\text{gw}}h^2$ is indistinguishable from an increase in N_{eff} . The changes due to perturbations with homogeneous initial conditions are more complex. Smith [219] illustrates this by splitting up the contributions to the CMB power spectrum from the Sachs–Wolfe (SW), Integrated Sachs–Wolfe (ISW) and Doppler (DOP) terms in the line of sight integral (see section 1.4.1). This is done by separating the

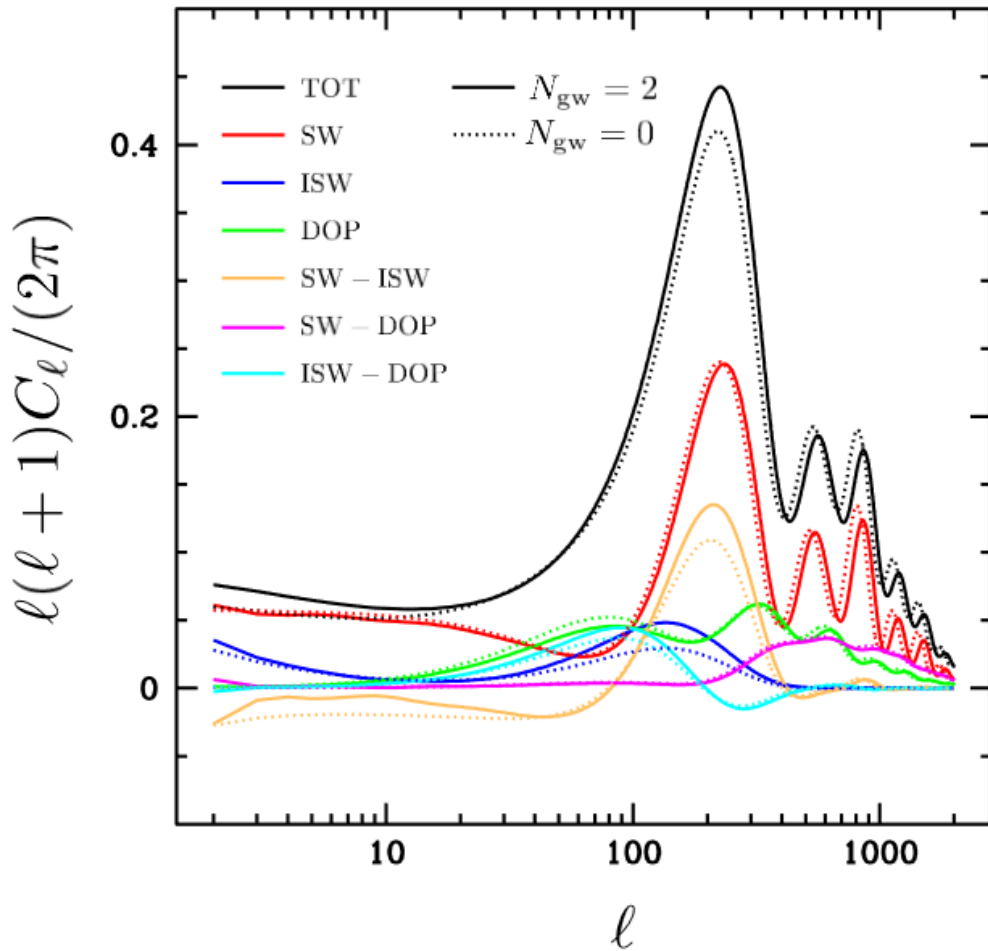


Figure 2.2: The contributions to the CMB power spectrum for homogeneous gravitational waves. The contributions are separated into Sachs–Wolfe (SW), Integrated Sachs–Wolfe (ISW) and Doppler (DOP) terms and their cross-correlations. Taken from ref. [219].

transfer functions (compare to equation (1.50)) as,

$$C_\ell^{TT} = (4\pi)^2 \int k^2 dk P(k) [T_\ell^{\text{SW}}(k) + T_\ell^{\text{ISW}}(k) + T_\ell^{\text{DOP}}(k)]^2. \quad (2.47)$$

Consequently there are 6 different terms that contribute to the power spectrum from the three effects and their cross-correlations. The change in the power spectrum from each of these terms is shown in figure 2.2 for homogeneous gravitational waves contributing an extra two neutrino degrees of freedom. This shows that there is an increase in power at large scales due to changes in the SW–ISW correlation and the ISW effect. There is also a significant increase in the height of the first peak from the same two terms. The shift in peak position for small scales is primarily due to the SW effect.

As for BBN, this is an integral constraint. It has a range of validity that also comes from consideration of when the shortwave approximation is valid. However, the horizon size at decoupling is appreciably bigger than the horizon size at the time of BBN; the frequency corresponding to the horizon size is $f_{\text{CMB}} \approx 7 \times 10^{-18}$ Hz. To allow the shortwave approximation to be valid the integrated gravitational wave constraint from the CMB is usually taken to apply for $f > f_{\text{min}} \approx 10^{-15}$ Hz.

This constraint was first presented in Smith, Pierpaoli, and Kamionkowski [96] where the gravitational wave density,

$$\begin{aligned}\Omega_{\text{gw}} h^2 &< 3.9 \times 10^{-5} \quad (\text{adiabatic}), \\ \Omega_{\text{gw}} h^2 &< 6.9 \times 10^{-6} \quad (\text{homogeneous}),\end{aligned}\tag{2.48}$$

at 95% confidence using a combination of data from *WMAP* (among other CMB data), SDSS and the Lyman- α forest [220]. This constraint is shown in figure 2.3 along with comparisons to a variety of other cosmological data sets, see ref. [96] for details. The CMB constraint is the only constraint on the gravitational wave density in the frequency range 10^{-15} Hz $< f < 10^{-9}$ Hz and is comparable in magnitude to the BBN constraint.

These constraints have been updated using *WMAP* seven-year data, finding $\Omega_{\text{gw}} h^2 < 8.7 \times 10^{-6}$ for adiabatic and $\Omega_{\text{gw}} h^2 < 1.0 \times 10^{-6}$ for homogeneous gravitational waves at 95% confidence [221]. The adiabatic result has been obtained for *Planck* 2013 data in combination with other CMB data and BOSS DR9 BAO, finding $\Omega_{\text{gw}} h^2 < 3.8 \times 10^{-6}$ at 95% confidence [222]. This was then updated using *Planck* 2015, BAO and BBN data by Pagano, Salvati, and Melchiorri [223], finding $\Omega_{\text{gw}} h^2 < 1.2 \times 10^{-6}$ at 95% confidence. Henrot-Versillé et al. [104] consider constraints on N_{eff} from a range of *Planck* 2015 likelihoods which can be converted easily to adiabatic gravitational wave constraints. The homogeneous result has not been recently updated.

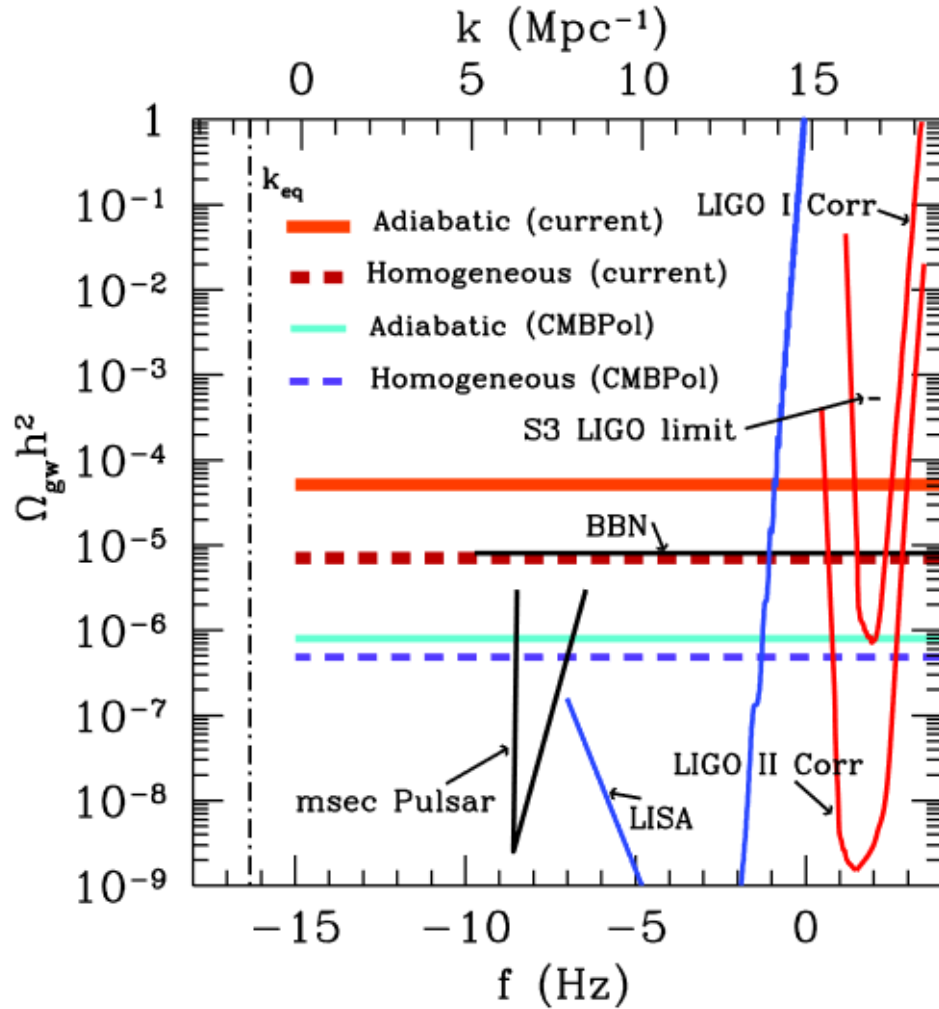


Figure 2.3: Constraints on the gravitational wave density parameter $\Omega_{\text{gw}} h^2$. Short-wave approximation integral constraints from BBN and the CMB are shown as horizontal lines along with non-integral constraints from pulsar timing and gravitational wave interferometry via LIGO. There are also projected constraints for CMBPol, upgrades to LIGO and from LISA. Taken from Smith, Pierpaoli, and Kamionkowski [96].

2.5.5 Interferometers

Gravitational waves were first detected directly in 2015 by the Laser Interferometer Gravitational-Wave Observatory (LIGO) [9]. These were astrophysical gravitational waves emitted from the merging of two black holes. The LIGO collaboration utilises two laser interferometers, in Washington and Louisiana, America, to detect tiny changes in propagation of the laser beams due to gravitational waves. They work much like a normal interferometer with two beams of light passing down long, perpendicular arms ($\sim 4\text{km}$ long) before

being combined together. The interference pattern is observed to detect any shift in the length of the two arms due to a gravitational wave passing through the detector [198, 207]. The length of the arms of the LIGO detectors set the observable frequency range of $10 \text{ Hz} \lesssim f \lesssim 10 \text{ kHz}$ with peak sensitivity around 100 Hz [224].

The Virgo detector in Italy is very similar in design to the LIGO detectors and the two groups now work together as the LIGO–Virgo collaboration [225]. A smaller detector in Germany, GEO600 also collaborates with LIGO [226]. The Kamioka Gravitational Wave Detector built underground in Japan started its first observing run in 2020 and is also used in conjunction with LIGO [227, 228]. This international network of gravitational wave detectors allows for concurrent verification of gravitational wave observations.

The main problem facing gravitational wave interferometers is discerning the gravitational wave signal from background noise. A variety of techniques have been developed to isolate and cool the mirrors and hence reduce the noise as much as possible. Ground-based detectors are limited at low frequencies ($\sim 1 \text{ Hz}$) by seismic and environmental noise, in the intermediate region by thermal effects and at $f \gtrsim 1 \text{ kHz}$ the laser shot noise dominates [194, 207, 224]. These combined considerations give the sensitivity of each detector (and therefore the shape of the LIGO projected constraint in figure 2.3).

Two detectors observing at the same time but separated by a large distance (such as LIGO’s two detectors) should have uncorrelated noise. Consequently combinations of the two data sets can be used to increase the confidence that a signal is not caused by unknown local vibrations. Using multiple detectors also has the advantage that it allows for triangulation of astrophysical sources. The difference in arrival time between the detectors gives a region in space that the gravitational wave originated from. This is what allowed for the first multi-messenger observations of a neutron star binary merger¹⁶ [229].

¹⁶This observation put a tight constraint on the speed of gravitational waves, consistent with gravitational waves travelling at the speed of light, as predicted by general relativity.

While astrophysical gravitational waves from resolvable sources are of great scientific interest, cosmological gravitational waves do not appear as point sources but as an isotropic background of gravitational waves¹⁷. The observed background will be made up of unresolved astrophysical gravitational wave sources and cosmological gravitational waves [198, 230]. Therefore observation of this gravitational wave background is an important target for gravitational wave interferometers.

For a single detector, a gravitational wave background can only be observed if it is above the level of the noise. However, observation with more than one detector gives huge advantages in signal sensitivity. As an illustration, two detectors with completely uncorrelated noise will improve their sensitivity to a gravitational wave background by about five orders of magnitude when combining together their data [194]. The signal from the gravitational wave background grows faster with observational time than the signal from the noise meaning long observations of the gravitational wave background will increase the constraining power via this method [214].

Constraints on the gravitational wave background from interferometers are often presented as integrated curves given a specific value of the tilt [194, 205, 208]. Cosmological gravitational waves are typically assumed to be independent of frequency within the band observed by ground-based interferometers. The most recent constraint comes from LIGO's second observing run [231] giving,

$$\Omega_{\text{gw}} < 6.0 \times 10^{-8}, \quad (2.49)$$

at 95% confidence, for $f = 25$ Hz. This corresponds to the tightest constraint on gravitational waves in the LIGO frequency range, stronger than the integrated constraints from BBN and the CMB.

With gravitational wave astronomy being such a young field there are a large number of plans for future observatories. The next step for ground-

¹⁷The gravitational wave background is expected to be isotropic like the CMB, but this requires experimental verification.

based observations will be the Einstein Telescope [232]. This is expected to be ~ 10 times more sensitive than existing interferometers and extend to lower frequencies. The gravitational wave background will be probed to $\Omega_{\text{gw}} \sim 10^{-12}$ by the Einstein Telescope.

Space-based detectors are able to probe to much lower frequencies due to the reduction in seismic and environmental noise and the ability to have much longer arm lengths. The first such interferometer will be the Laser Interferometer Space Antenna (LISA) [233]. This is planned to be launched in 2034. It will probe $10^{-4} \text{ Hz} \lesssim f \lesssim 0.1 \text{ Hz}$ which corresponds to gravitational waves produced around the electroweak phase transition [191]. LISA is expected to reach $\Omega_{\text{gw}} h^2 \sim 10^{-13}$ for the stochastic background. Further in the future the DECI-hertz Interferometer Gravitational Wave Observatory (DECIGO) [234] and the Big Bang Observer (BBO) [235, 236] aim to take observations even further. They both aim to probe the frequency range $0.1 - 10 \text{ Hz}$ with the goal of reaching $\Omega_{\text{gw}} \sim 10^{-17}$ [194]. To do this they aim to detect all the astrophysical foregrounds to the cosmological signal in much the same way *Planck* does for the CMB. This would revolutionise observations of astrophysical and cosmological gravitational waves.

2.5.6 Pulsar timing

Observations of neutron stars with large magnetic fields that emit beams of radiation from their magnetic poles, referred to as *pulsars*, gave the first experimental evidence for gravitational waves [237–239]. These early observations supported the existence of astrophysical gravitational waves but pulsars can also be used to detect a background of primordial gravitational waves. Because of the rotation of these neutron stars the beams of radiation give regular pulses of detectable radiation on Earth if aligned correctly [240].

Of particular use are *msec pulsars* which have rotational periods $\sim 10 \text{ ms}$. The period of these pulsars is not perfectly constant but averaging over a number of pulses gives a very consistent value which can allow pulsars to

be used as a cosmic clock. These msec pulsars can be used to constrain gravitational waves because a gravitational wave passing between the Earth and the pulsar will change the arrival time of the pulse due to the warping of spacetime [194, 206, 214]. The Earth–pulsar system acts like one arm of an interferometer. The frequency of the gravitational waves that can be constrained in this manner is linked to the observation time. Observing a pulsar for a length of time T (typically ~ 10 years) gives a bound strongest at frequency, $f \approx 1/T$. Consequently most constraints from pulsars are strongest around 10^{-9} Hz. As observation times increase the bounds get stronger and move to lower frequencies. As an example, the constraint from Thorsett and Dewey [241] is,

$$\Omega_{\text{gw}} h^2 < 1.0 \times 10^{-8}, \quad (2.50)$$

at 95% confidence for a frequency of 4.4×10^{-9} Hz. The bound roughly scales $\propto f^2$ above this frequency and gives no constraint below due to the way in which pulsar arrival times are modelled [194, 207]. This frequency dependence explains the wedge shaped msec pulsar constraint in figure 2.3 which uses the bound from¹⁸ Lommen [242] and Kaspi, Taylor, and Ryba [243].

Better sensitivity and stronger discernment of the origins of a background of gravitational waves can be obtained by combining observations of multiple msec pulsars [240, 244, 245]. When this is done for a large number ($\sim 20 - 80$ for current observations) it is referred to as a *pulsar timing array*. Similarly to correlated data from multiple gravitational wave interferometers the pulsar timing array can then look for correlated signals across a large set of pulsars and therefore determine their origin. Three such observatories are currently operational, the European Pulsar Timing Array (EPTA) [246], The Parkes Pulsar Timing Array (PPTA) [247] and the North American Nanohertz Observatory for Gravitational Waves (NANOGrav) [248]. A pulsar timing array observing across the sky allows for better subtraction of systematics than single

¹⁸The statistical analysis of [242] has been called into question, see ref. Caprini and Figueroa [194] section 4.3, for a discussion. Regardless, it has been surpassed by more recent constraints.

observations and consequently tighter constraints. The current best constraint comes from the PPTA¹⁹ [205],

$$\Omega_{\text{gw}} < 2.3 \times 10^{-10}, \quad (2.51)$$

at 95% confidence for a frequency, $f \approx 4 \times 10^{-9}$ Hz.

Observations from pulsars give a non-integral constraint that applies over a small range of frequencies. The constraint is usually dependent on the choice of the tensor tilt. Pulsars constrain all sources of gravitational waves though pulsar timing arrays are better at isolating astrophysical gravitational waves. However, there is an appreciable foreground from mergers of supermassive black holes (see [249] or [194] section 4.3), which are usually discerned from primordial gravitational waves by the frequency dependence of the gravitational wave background. However, primordial signals below the level of the signal from supermassive black holes may be unobservable [194].

Pulsar timing constraints are expected to improve in the near future when the EPTA, PPTA and NANOGrav arrays combine in the International Pulsar Timing Array [250]. Further in the future the Square Kilometre Array will improve the sensitivity to a gravitational wave background by 4–5 orders of magnitude [194, 251].

2.6 Sources of primordial gravitational waves

There is a range of Standard Model and beyond Standard Model mechanisms that can produce gravitational waves in the early Universe. Consequently, observation of a primordial gravitational wave background can open a window on physics at energies that are currently inaccessible by other means.

This section will provide a few common examples of possible mechanisms for primordial production of gravitational waves. It is not exhaustive and does not contain any alternative cosmologies (see Caprini and Figueroa [194] for

¹⁹Note that this constraint doesn't include the factor of h^2 common to others.

details of these).

A rough estimate of the characteristic frequency today, and the production time, of gravitational waves produced by causal mechanisms²⁰ can be found using entropy conservation arguments [194, 207]. Because entropy is conserved during matter and radiation domination the redshifting of gravitational waves depends only on the production temperature, T_* and the number of effective energy degrees of freedom at that time, $g(T_*)$. The effects of the particular production mechanism are incorporated through a parameter,

$$\epsilon = \lambda_* H_* , \quad (2.52)$$

where λ_* is the wavelength of the gravitational waves at production and H_* is the Hubble factor at production. ϵ is expected to be less than or equal to one from causality arguments. Consequently the frequency today of gravitational waves produced at temperature, T_* is,

$$f_0 \simeq \frac{1.65 \times 10^{-7}}{\epsilon} \left(\frac{T_*}{\text{GeV}} \right) \left(\frac{g_*}{100} \right)^{1/6} \text{ Hz} . \quad (2.53)$$

The time of production can then be found from,

$$t_* \simeq \frac{6.6 \times 10^{-21}}{\epsilon^2} \left(\frac{\text{Hz}}{f_0} \right)^2 \left(\frac{100}{g_*} \right)^{1/6} \text{ s} . \quad (2.54)$$

This illustrates an important general point. Higher frequency gravitational waves are produced at earlier times and at higher temperatures. If, assuming $\epsilon \approx 1$, you want to probe gravitational waves produced at $T_* \simeq 6 \times 10^6 \text{ GeV}$ (corresponding to lookback times of about $7 \times 10^{-21} \text{ s}$), then the signal will be strongest at a frequency of about 1 Hz [207]. While exact calculations require a great deal more complexity and more consideration of the production mechanism the above is illustrative of necessary considerations. Calculations of the specific production mechanism will also be necessary to find the behaviour of the full spectrum of gravitational waves.

²⁰All of the mechanisms considered here are causal apart from inflation.

2.6.1 Inflation

Tensor perturbations are produced by quantum mechanical fluctuations during inflation rather than by an anisotropic stress (see equation (2.10)). These are amplified by the expansion in the same way as the scalar perturbations. Consequently this is not a causal process and the arguments of the previous section about the characteristic frequencies of primordial gravitational waves do not apply for inflationary gravitational waves. The quantum mechanical perturbations have a constant amplitude after they become super-horizon. The expansion of the Universe results in the quantum perturbations becoming stochastic classical perturbations when they re-enter the horizon after inflation [252–254]. Therefore a background of these gravitational waves is a common prediction of inflationary models [194].

The spectrum of gravitational waves is usually represented by a power-law over a large range of frequencies. While this has been shown to be a good approximation for most inflation models, recent studies including a k dependence in the tilt²¹ show an error of $\simeq 39\%$ on high-frequency observations from LIGO when ignoring this running [255]. Nonetheless, a power-law with a constant spectral index is common throughout the literature.

Assuming exactly exponential inflation which transitions into a radiation dominated universe, the power-law spectrum will be scale invariant, $n_t = 0$. The relaxing of both of these assumptions is required in more realistic models. In slow-roll inflation the Hubble factor is no longer constant and the consistency relation gives,

$$n_t(k_*) = -r_{k_*}/8. \quad (2.55)$$

The tensor-to-scalar ratio is constrained to small values so the gravitational wave background is nearly scale invariant in this case. Including matter and radiation in the universe results in the spectrum turning up at large scales. This is because, after matter–radiation equality (corresponding to $f \sim 10^{-17}$ Hz)

²¹Commonly referred to as a ‘running’ of the spectral index.

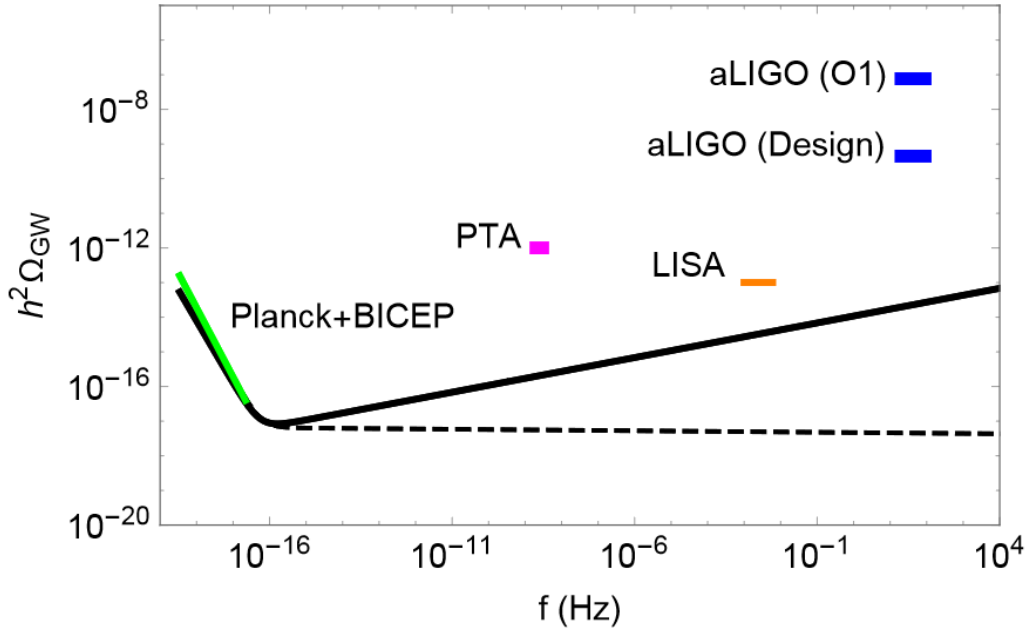


Figure 2.4: The gravitational wave background from inflation for $r_{0.05} = 0.07$, with $n_t = -r_{0.05}/8$ from the slow-roll consistency relation (black dashed) and $n_t = 0.2$ (black solid), along with observational constraints. The green constraint comes from CMB B -modes and shows that the spectrum plotted is approximately the maximum allowed by current observations [256]. Constraints from pulsar timing (PTA) and interferometers (advanced LIGO and LISA) are also shown. Taken from Caprini and Figueroa [194].

the differing dependence of the scale factor ($\propto \tau^2$ instead of τ) results in a dependence on f^{-2} in the gravitational wave density for frequencies below those associated with matter–radiation equality [207]. Consequently the predicted spectrum for slow-roll inflation has the form of the black dashed curve in figure 2.4.

As mentioned in previous sections, the current best constraint on inflationary gravitational waves comes from CMB B -mode observations from the BICEP2/*Keck* Array combined with *Planck* temperature and E -mode observations and BAO [1]. This provides the constraint,

$$r_{0.002} < 0.06, \quad (2.56)$$

at 95% confidence, which can then be converted to a gravitational wave density parameter using equation (2.40) (see section 2.5.1). The maximum allowed inflationary spectrum is at the level of $\Omega_{\text{gw}} h^2 \sim 10^{-17}$ above $f \sim 10^{-16}$ Hz and

consequently is well below the sensitivity of any other current (or near future) observations but may be detectable by DECIGO or BBO (see section 2.5.5).

2.6.2 Particle production during inflation

Gravitational waves can be produced as a result of anisotropic stress coming from the non-perturbative production of particles during inflation [257–260]. There are various models for the different types of particles that can result in anisotropic stresses (see Caprini and Figueroa [194] section 6.1 and references therein). One of the most promising mechanisms that can allow for a detectable signal is the production of a gauge field. If this gauge field is coupled to the inflaton appropriately then particles are produced continuously throughout inflation, at scales close to the horizon size, and can therefore build up an observable signal of tensor (and scalar) perturbations [261]. The appropriate interaction term is possible in a range of inflationary models.

One of the advantages of this mechanism of gravitational wave production is that it makes strong predictions for the shape of the gravitational wave spectrum with the signal potentially becoming observable in interferometers for large coupling strengths due to a (non-constant) positive tilt above the CMB frequency. It also predicts a characteristic degree of non-Gaussianity which can be used to constrain or confirm the model²² [258, 262–265]. LISA will be able to improve on existing constraints coming from CMB non-Gaussianity [266–268].

2.6.3 Preheating

At the end of inflation almost all of the energy in the Universe is stored in the inflaton field. Therefore a process is needed to convert this energy from the inflaton into the Standard Model particles (primarily photons) that are known to dominate the early Universe. If this proceeds through perturbative²³ decay of the inflaton it is referred to as ‘reheating’. If the process is non-perturbative

²²The gravitational wave background would also be chiral (see Caprini and Figueroa [194]) which is also a distinctive signature of particle production.

²³Here perturbative means that it can be treated by the first-order perturbation theory of particle physics (not cosmology), see Amin et al. [30] or Allahverdi et al. [33].

then it is referred to as ‘preheating’ [29–33, 194]. The focus here will be on preheating, as the non-perturbative nature of these mechanisms produces a background of gravitational waves.

The highly turbulent state of the Universe during preheating induces non-zero anisotropic stresses and consequently sources gravitational waves (see equation (2.10)). These gravitational waves will have a characteristic frequency, given by equation (2.53), corresponding to a time shortly after the end of inflation. Hence, gravitational waves from preheating probe the state of the very early Universe, the model and energy scale of inflation and the couplings of the particles produced by preheating.

There is a large range of different preheating mechanisms that have different signatures in the gravitational wave background (such as large anisotropies and specific frequency dependence) and the gravitational wave background will also depend on the inflationary model (see Caprini and Figueroa [194] for a review or Bassett [269] and Khlebnikov and Tkachev [270] for early examples). In general these mechanisms produce gravitational waves at high frequencies, at interferometer frequencies or above, dependent on the energy scale of inflation and do so in a relatively narrow band, when compared to other mechanisms [261]. Gravitational waves from preheating can have large density parameters ($\sim 10^{-10}$) but would be unobservable if produced at a frequency above the LIGO range, corresponding to inflation at $\gtrsim 10^{11}$ GeV [207].

2.6.4 First-order phase transitions

Cosmological phase transitions can be thought of analogously to common phase transitions such as changes of states of matter. In these, the lowest energy state of the system changes due to a change in the temperature. Analogous phase transitions are believed to have occurred in the evolution of the Universe as it cools (see ref. [271] for a review). The transition is said to be first order if there is a discontinuous change in ground state or equivalently if the entropy changes discontinuously and is second order if this happens continuously [191,

272].

During a first-order phase transition the universe finds itself in a false vacuum. Regions of space can then lower their energy by quantum tunnelling into the true vacuum. This will give rise to bubbles of true vacuum that expand very rapidly. These bubbles are typically spherical and therefore emit no gravitational waves but when they collide with each other they do emit gravitational waves in a complex process²⁴ that is highly inhomogeneous and consequently produces an anisotropic stress (see equation (2.10)) [273, 274].

The phase transition is required to be first order to produce a detectable amount of gravitational waves. The two phase transitions predicted by the Standard Model of particle physics – the QCD and electroweak phase transitions – are not expected to be first order but this can change in Standard Model extensions such as supersymmetry. The order of the electroweak phase transition is not constrained by measurements from the Large Hadron Collider. Therefore, a background of gravitational waves from a first-order phase transition would probe physics beyond the Standard Model of particle physics that is currently inaccessible [194, 207, 261].

The amplitude of the primordial gravitational wave background depends on the strength of the phase transition, and the peak frequency depends on the temperature of the phase transition, via equation (2.53). Therefore the frequency dependence will depend on the specifics of the phase transition and the particle physics motivating it. The most popular in the literature is a first-order electroweak phase transition that can produce a measurable background for interferometer experiments such as LISA [191, 261, 275, 276]. The gravitational wave density generally has a constant tilt up to a peak frequency before decreasing more slowly to high frequencies.

²⁴Which includes compression waves, turbulence and the effects of the background plasma [191, 194].

2.6.5 Cosmic strings

In some models of phase transitions *topological defects* are produced [277, 278]. Cosmic strings are one-dimensional examples of topological defects²⁵. They are predicted in the phase transitions of grand unified theories [279] and consequently are produced at earlier times than the phase transitions considered in the previous section. Cosmic strings can exist for a long time after their formation.

Cosmic strings produce gravitational waves through two processes; a continuous energy loss due to the evolution of the cosmic strings and the formation and decay of cosmic string loops [280]. These give rise to a characteristic spectrum of gravitational waves that is approximately scale invariant over a large frequency range above a critical value [194].

A network of cosmic strings is characterised by its string tension²⁶. This is a dimensionless quantity given by the product of Newton's constant and the mass per unit length, $G\mu$. Hence, constraints on the gravitational wave signal from cosmic strings can be converted into constraints on the string tension.

The most recent LIGO constraints [231] give $G\mu < 1.1 \times 10^{-6}$ for the model detailed in Blanco-Pillado, Olum, and Shlaer [281] and $G\mu < 2.1 \times 10^{-14}$ for the model detailed in Lorenz, Ringeval, and Sakellariadou [282]. This illustrates the fact that there is still a large amount of uncertainty in how best to model cosmic strings and this can result in large differences in the amplitude of the predicted gravitational wave spectrum. The disagreement from the pulsar timing constraint is smaller, with $G\mu < 1.6 \times 10^{-11}$ and $G\mu < 6.2 \times 10^{-12}$ for the same two models as the LIGO constraint [205, 231]. Consequently cosmic string constraints will improve both as the modelling improves and with future pulsar timing and interferometer observations.

²⁵Two-dimensional topological defects are called *domain walls* but are not considered here.

²⁶Assuming that the reconnection probability is one, as it is in field theories [261].

2.6.6 Primordial black holes

Primordial Black Holes (PBHs) [283–287] are hypothesised black holes produced from scalar, large-amplitude, small-scale perturbations generated by inflation and formed in the radiation-dominated era, which are a possible dark matter candidate [288, 289]. Perturbations with these properties are possible in various models of inflation including slow-roll models. To satisfy the large-scale CMB constraints on the scalar tilt, n_s but also generate large perturbations at small scales the power-law spectrum must be broken due to a running of the spectral index.

Gravitational waves are produced by; the backreaction of the large amplitude scalar perturbations sourcing tensor perturbations during inflation, the gravitational collapse that forms the PBHs in the radiation era and from the mergers of PBHs in the matter-dominated era. These can produce a detectable gravitational wave background if the curvature power spectrum of the scalar perturbations has a large broad peak [194, 290]. The spectrum can peak at a large range of frequencies depending on the average mass of primordial black holes. One of the reasons PBHs have gained interest recently is because the LIGO black hole merger observations come from black holes with intermediate masses ($\sim 30M_\odot$) which are not easily formed in simulations of stellar collapse [290, 291]. If these were primordial black holes the gravitational wave background could be detectable by LISA or future pulsar timing arrays [191, 290].

Chapter 3

Short-Wavelength Gravitational Waves

This chapter details efforts to reproduce and update the CMB gravitational wave constraint that uses the shortwave approximation (as detailed in section 2.5.4) with the most recent CMB data from *Planck* 2018. The main complication of this approach comes from finding appropriate initial conditions for the gravitational wave perturbations.

3.1 Initial conditions

The initial conditions are calculated as in Bucher, Moodley, and Turok [48] as detailed in section 1.3.3. The gravitational wave fluid equations are given by equations (2.46a) and the gravitational wave perturbations enter into the Einstein equations as for the other species (see section 1.3.2). The adiabatic initial conditions are by definition identical to the ones presented previously with the gravitational wave perturbation initial conditions being the same as those of neutrinos. Note that baryon and cold dark matter perturbations are not calculated here but can be simply calculated from those for the radiation species using the tight coupling approximation for baryons and the standard fluid and Einstein equations for dark matter [292].

3.1.1 Homogeneous mode

The homogeneous mode is more physically motivated than the adiabatic mode and consequently the use of this set of initial conditions is preferred over the adiabatic initial conditions when constraining primordial gravitational waves.

There are three main differences between the approach to calculating the homogeneous mode presented here and the approach in Smith [219]. Firstly, in [219] the homogeneous mode is defined by the gravitational wave density perturbation being zero in the Newtonian gauge at all orders considered in the expansion. Here the gravitational wave density is only assumed to be zero at lowest order so it is only the zeroth order coefficient of the gravitational wave density perturbation that is zero in the Newtonian gauge. This allows for the evolution of gravitational wave density perturbations from an initially homogeneous state.

Secondly, the initial conditions are calculated in the synchronous gauge to systematically find the possible isocurvature initial conditions¹. When doing this there is one unknown left in the system of coupled coefficients. This is fixed by transforming to the Newtonian gauge using the standard relations given in equations (1.30) [42] and enforcing the homogeneous condition described above². Consequently the isocurvature initial conditions that allow the homogeneous gravitational wave condition are found as well as the ‘adiabatic’ one and these isocurvature modes are detailed in the next section.

Finally, the gravitational wave density is not assumed to be sub-dominant to the densities of the other species. Hence these initial conditions are valid in the case that $R_{\text{gw}} \sim R_\nu, R_\gamma$. While $R_{\text{gw}} \ll R_\nu, R_\gamma$ from current constraints this should be proved self-consistently before being assumed.

The explicit calculation of the homogeneous mode is given in the appendix. The homogeneous modes found here and in ref. [219] are given in table 3.1.

¹More detail of this can be found in the appendix.

²Mathematically this condition is, $\tilde{\delta}_{\text{gw},0} = 0$, where the tilde denotes the Newtonian gauge and $\delta_{\text{gw},i}$ is the coefficient of $(k\tau)^i$ in the expansion of the perturbation.

The initial conditions are given to the lowest order that is non-vanishing in the limit $R_{\text{gw}} \rightarrow 0$. It is clear from the table of initial conditions that both homogeneous modes simplify to the adiabatic mode in the limit where there are no gravitational waves.

The main difference between the homogeneous mode calculated here and in [219] is in the initial conditions of the neutrino sector. The homogeneous mode used in the current literature is a linear sum of the homogeneous mode here and the neutrino density isocurvature mode (see below). These two modes can be combined in the initial condition correlation matrix (as detailed in ref. [48] and section 1.3.3) to get the homogeneous mode in ref. [219]. Schematically this combination of the initial conditions (ICs) will look like,

$$\text{Smith ICs} = \text{Homogeneous ICs} + A \times (\text{Neutrino density ICs}), \quad (3.1)$$

where A is a constant given by R_γ , R_ν , and R_{gw} . Looking at the neutrino density initial conditions in tables 3.1 and 3.2 it is clear that the necessary value of the factor is,

$$A = -\frac{20R_{\text{gw}}}{19 - 4R_\gamma}. \quad (3.2)$$

It is easy to show that, when the homogeneous and neutrino density isocurvature initial conditions given here are combined in this way, the homogeneous mode of ref. [219] is recovered for all of the species³. This is the factor that would be required in the correlation matrix to regain the homogeneous mode used in Smith, Pierpaoli, and Kamionkowski [96] and Smith [219]. Hence, the homogeneous mode given here that is the true independent homogeneous mode for gravitational waves. Because these modes have noticeably different initial conditions for the neutrinos different parameter constraints are expected when comparing tot ref. [96] even if the same data was used.

The two modes also differ as the one calculated here relaxes the condition, $R_{\text{gw}} \ll R_\gamma, R_\nu$. It is clear that the two modes agree in all but the neutrino

³The reader is reminded that the approach in ref. [219] assumes that gravitational waves are subdominant to the photons and neutrinos, $R_{\text{gw}} \ll R_\gamma, R_\nu$. The modes do not agree without this approximation.

	Homogeneous - Smith	Homogeneous
h	$\frac{1}{2}k^2\tau^2$	$\frac{1}{2}k^2\tau^2$
η	$1 - \frac{(9-4R_\gamma)}{12(19-4R_\gamma)}k^2\tau^2$	$1 - \frac{(9-4R_\gamma+4R_{\text{gw}})}{12(19-4R_\gamma+4R_{\text{gw}})}k^2\tau^2$
δ_γ	$-\frac{20R_{\text{gw}}}{19-4R_\gamma} - \frac{1}{3}\left(1 - \frac{10R_{\text{gw}}}{19-4R_\gamma}\right)k^2\tau^2$	$-\frac{20R_{\text{gw}}}{R_\gamma(19-4R_\gamma+4R_{\text{gw}})} - \frac{1}{3}\left(1 - \frac{10R_{\text{gw}}}{R_\gamma(19-4R_\gamma+4R_{\text{gw}})}\right)k^2\tau^2$
δ_ν	$-\frac{20R_{\text{gw}}}{19-4R_\gamma} - \frac{1}{3}\left(1 - \frac{10R_{\text{gw}}}{19-4R_\gamma}\right)k^2\tau^2$	$-\frac{1}{3}k^2\tau^2$
θ_γ	$-\frac{5R_{\text{gw}}}{19-4R_\gamma}k^2\tau - \frac{1}{36}\left(1 - \frac{10R_{\text{gw}}}{19-4R_\gamma}\right)k^4\tau^3$	$-\frac{5R_{\text{gw}}}{R_\gamma(19-4R_\gamma+4R_{\text{gw}})}k^2\tau - \frac{1}{36}\left(1 - \frac{10R_{\text{gw}}}{R_\gamma(19-4R_\gamma+4R_{\text{gw}})}\right)k^4\tau^3$
θ_ν	$-\frac{5R_{\text{gw}}}{19-4R_\gamma}k^2\tau - \frac{1}{36}\left(\frac{27-4R_\gamma}{19-4R_\gamma} - \frac{18R_{\text{gw}}}{19-4R_\gamma}\right)k^4\tau^3$	$-\frac{27-4R_\gamma+4R_{\text{gw}}}{36(19-4R_\gamma+4R_{\text{gw}})}k^4\tau^3$
σ_ν	$\frac{2(1-R_{\text{gw}})}{3(19-4R_\gamma)}k^2\tau^2$	$\frac{2}{3(19-4R_\gamma+4R_{\text{gw}})}k^2\tau^2$
δ_{gw}	$\frac{20}{19-4R_\gamma}$	$\frac{20}{19-4R_\gamma+4R_{\text{gw}}}$
θ_{gw}	$\frac{5}{19-4R_\gamma}k^2\tau$	$\frac{5}{19-4R_\gamma+4R_{\text{gw}}}k^2\tau$
σ_{gw}	$\frac{4}{3(19-4R_\gamma)}k^2\tau^2$	$\frac{4}{3(19-4R_\gamma+4R_{\text{gw}})}k^2\tau^2$
$\tilde{\delta}_\gamma$	$-\frac{20(R_{\text{gw}}+1)}{19-4R_\gamma}$	$-\frac{20(R_\gamma+R_{\text{gw}})}{R_\gamma(19-4R_\gamma+4R_{\text{gw}})}$
$\tilde{\theta}_\gamma$	$-\frac{5(R_{\text{gw}}-1)}{19-4R_\gamma}k^2\tau$	$\frac{5(R_\gamma-R_{\text{gw}})}{R_\gamma(19-4R_\gamma+4R_{\text{gw}})}k^2\tau$
$\tilde{\delta}_\nu$	$-\frac{20(R_{\text{gw}}+1)}{19-4R_\gamma}$	$-\frac{20}{19-4R_\gamma+4R_{\text{gw}}}$
$\tilde{\theta}_\nu$	$-\frac{5(R_{\text{gw}}-1)}{19-4R_\gamma}k^2\tau$	$\frac{5}{19-4R_\gamma+4R_{\text{gw}}}k^2\tau$
$\tilde{\delta}_{\text{gw}}$	$\mathcal{O}(k^3\tau^3)$	$\mathcal{O}(k\tau)$
$\tilde{\theta}_{\text{gw}}$	$\frac{10}{19-4R_\gamma}k^2\tau$	$\frac{10}{19-4R_\gamma+4R_{\text{gw}}}k^2\tau$
Φ	$\frac{14-4R_\gamma}{19-4R_\gamma}$	$\frac{14-4R_\gamma+4R_{\text{gw}}}{19-4R_\gamma+4R_{\text{gw}}}$
Ψ	$\frac{10}{19-4R_\gamma}$	$\frac{10}{19-4R_\gamma+4R_{\text{gw}}}$

Table 3.1: Initial conditions for the homogeneous mode calculated in Smith, Pierpaoli, and Kamionkowski [96] and Smith [219] (see section 2.5.4) and here. Initial conditions are given in the synchronous gauge (top) and Newtonian gauge (bottom - with tildes). Both reproduce the adiabatic mode (see table 2.1) in the limit $R_{\text{gw}} \rightarrow 0$. The main difference between the modes is that the homogeneous mode presented in [219] is a linear combination of the homogeneous mode here and the neutrino density isocurvature mode (presented in the third column of table 3.2). The shear is not given in the Newtonian gauge as it is gauge-invariant and hence unchanged.

sector if R_{gw} is dropped in the denominator of most of the terms. There is also a change of $R_{\text{gw}} \rightarrow R_{\text{gw}}/R_\gamma$ in the density and velocity of photons.

3.1.2 Isocurvature modes

As stated previously, calculating the initial conditions in the synchronous gauge and enforcing the homogeneous gravitational wave condition in the Newtonian gauge allows for the systematic calculation of isocurvature initial conditions. In the absence of gravitational waves there are two neutrino isocurvature modes corresponding to zeroth order coefficients in the density and velocity respectively [48]. These modes are modified in the presence of gravitational waves. Both sets of neutrino isocurvature modes are shown in table 3.2.

The neutrino density isocurvature mode with gravitational waves only has small differences when compared to the same mode without gravitational waves. These are primarily due to the inclusion of R_{gw} in the total radiation density. However, the neutrino velocity isocurvature mode is changed significantly by the inclusion of homogeneous gravitational waves. There are no longer any perturbations to the metric or the photons⁴.

There are new isocurvature modes when homogeneous gravitational waves are included. These are given in table 3.3 and the choice of the zeroth order conditions are stated in the appendix. The gravitational wave density isocurvature mode is a rescaled version of the neutrino density isocurvature mode and as such is not independent. However, it does make clearer the relationship between the photon, neutrino and gravitational wave initial conditions in this case. The gravitational wave velocity isocurvature mode is very similar to the neutrino velocity isocurvature mode (without gravitational waves) with the gravitational waves playing the role of the neutrinos. In the Newtonian gauge densities and potentials have terms that go as $1/(k\tau)$. This is a consequence of the Newtonian gauge being inadequate when there is a non-zero anisotropic stress and does not mean that the perturbations diverge as $k\tau \rightarrow 0$ [48].

⁴See below for a discussion of the effects of this mode on the CMB.

	Neut. Dens. IC	Neut. Vel. IC	Neut. Dens. IC w/ GWs	Neut. Vel. IC w/ GWs
h	$\mathcal{O}(k^3\tau^3)$	$\mathcal{O}(k^3\tau^3)$	$\mathcal{O}(k^3\tau^3)$	$\mathcal{O}(k^3\tau^3)$
η	$-\frac{R_\nu}{6(19-4R_\gamma)}k^2\tau^2$	$-\frac{4R_\nu}{3(9-4R_\gamma)}k\tau$	$-\frac{R_\nu}{6(19-4R_\gamma+4R_{\text{gw}})}k^2\tau^2$	$\mathcal{O}(k^3\tau^3)$
δ_γ	$-\frac{R_\nu}{R_\gamma} + \frac{R_\nu}{6R_\gamma}k^2\tau^2$	$\frac{4R_\nu}{3R_\gamma}k\tau$	$-\frac{R_\nu(19-4R_\gamma)}{R_\gamma(19-4R_\gamma+4R_{\text{gw}})}$	$\mathcal{O}(k^3\tau^3)$
θ_γ	$-\frac{R_\nu}{4R_\gamma}k^2\tau$	$-\frac{R_\nu}{R_\gamma}k$	$-\frac{R_\nu(19-4R_\gamma)}{4R_\gamma(19-4R_\gamma+4R_{\text{gw}})}k^2\tau$	$\mathcal{O}(k^4\tau^3)$
δ_ν	$1 - \frac{1}{6}k^2\tau^2$	$-\frac{4}{3}k\tau$	$1 - \frac{1}{6}k^2\tau^2$	$-\frac{4}{3}k\tau$
θ_ν	$\frac{1}{4}k^2\tau$	$k - \frac{13-4R_\gamma}{6(9-4R_\gamma)}k^3\tau^2$	$\frac{1}{4}k^2\tau$	$k - \frac{3}{10}k^3\tau^2$
σ_ν	$\frac{1}{2(19-4R_\gamma)}k^2\tau^2$	$\frac{4}{3(9-4R_\gamma)}k\tau$	$\frac{15+8R_{\text{gw}}}{30(19-4R_\gamma+4R_{\text{gw}})}k^2\tau^2$	$\frac{4}{15}k\tau$
δ_{gw}	-	-	$\frac{4R_\nu}{19-4R_\gamma+4R_{\text{gw}}}$	$\frac{4R_\nu}{3R_{\text{gw}}}k\tau$
θ_{gw}	-	-	$\frac{R_\nu}{19-4R_\gamma+4R_{\text{gw}}}k^2\tau$	$-\frac{R_{\text{gw}}}{R_\nu}k + \frac{3R_{\text{gw}}}{10R_\nu}k^3\tau^2$
σ_{gw}	-	-	$\frac{R_\nu}{15(19-4R_\gamma+R_{\text{gw}})}k^2\tau^2$	$-\frac{4R_\nu}{15R_{\text{gw}}}k\tau$
$\tilde{\delta}_\gamma$	$-\frac{R_\nu(19-8R_\gamma)}{R_\gamma(19-4R_\gamma)}$	$\frac{16R_\nu}{9-4R_\gamma} \frac{1}{k\tau}$	$-\frac{R_\nu(19-8R_\gamma)}{R_\gamma(19-4R_\gamma+4R_{\text{gw}})}$	$\mathcal{O}(k\tau)$
$\tilde{\theta}_\gamma$	$-\frac{19R_\nu}{4R_\gamma(19-4R_\gamma)}k^2\tau$	$-\frac{9R_\nu}{R_\gamma(9-4R_\gamma)}k$	$-\frac{19R_\nu}{4R_\gamma(19-4R_\gamma+4R_{\text{gw}})}k^2\tau$	$\mathcal{O}(k^3\tau^2)$
$\tilde{\delta}_\nu$	$\frac{23-8R_\gamma}{19-4R_\gamma}$	$\frac{16R_\nu}{9-4R_\gamma} \frac{1}{k\tau}$	$\frac{23-8R_\gamma}{19-4R_\gamma+4R_{\text{gw}}}$	$\mathcal{O}(k\tau)$
$\tilde{\theta}_\nu$	$\frac{15}{4(19-4R_\gamma)}k^2\tau$	$\frac{5}{9-4R_\gamma}k$	$\frac{15+8R_{\text{gw}}}{4(19-4R_\gamma+4R_{\text{gw}})}k^2\tau$	k
$\tilde{\delta}_{\text{gw}}$	-	-	$\mathcal{O}(k\tau)$	$\mathcal{O}(k\tau)$
$\tilde{\theta}_{\text{gw}}$	-	-	$-\frac{2R_\nu}{19-4R_\gamma+4R_{\text{gw}}}k^2\tau$	$-\frac{R_{\text{gw}}}{R_\nu}k$
Φ	$-\frac{2R_\nu}{19-4R_\gamma}$	$-\frac{4R_\nu}{9-4R_\gamma} \frac{1}{k\tau}$	$-\frac{2R_\nu}{19-4R_\gamma+4R_{\text{gw}}}$	$\mathcal{O}(k\tau)$
Ψ	$\frac{R_\nu}{19-4R_\gamma}$	$\frac{4R_\nu}{9-4R_\gamma} \frac{1}{k\tau}$	$\frac{R_\nu}{19-4R_\gamma+4R_{\text{gw}}}$	$\mathcal{O}(k\tau)$

Table 3.2: Initial conditions for the neutrino isocurvature (IC) modes with and without homogeneous gravitational waves to second order in $k\tau$ in the synchronous gauge (top) and Newtonian gauge (bottom - with tildes). When including homogeneous gravitational waves the density mode changes only by extra terms that are dependent on R_{gw} in the prefactors of the $k\tau$ expansion. The velocity mode does not have metric or photon perturbations when homogeneous gravitational waves are included.

	GW Dens. IC	GW Vel. IC	GW. Shear IC
h	$\mathcal{O}(k^3\tau^3)$	$\mathcal{O}(k^3\tau^3)$	$\mathcal{O}(k^3\tau^3)$
η	$-\frac{1}{24}k^2\tau^2$	$-\frac{4R_{\text{gw}}}{3(9-4R_\gamma)}k\tau$	$\mathcal{O}(k^3\tau^3)$
δ_γ	$-\frac{(19-4R_\gamma)}{4R_\gamma}$	$\frac{4R_{\text{gw}}}{3R_\gamma}k\tau$	$\mathcal{O}(k^3\tau^3)$
θ_γ	$-\frac{(19-4R_\gamma)}{16R_\gamma}k^2\tau$	$-\frac{R_{\text{gw}}}{R_\gamma}k + \frac{1}{6}\frac{R_{\text{gw}}}{R_\gamma}k^3\tau^2$	$\mathcal{O}(k^4\tau^3)$
δ_ν	$\frac{19-4R_\gamma+4R_{\text{gw}}}{4R_\nu}$	$\mathcal{O}(k^3\tau^3)$	$-\frac{2R_{\text{gw}}}{3R_\nu}k^2\tau^2$
θ_ν	$\frac{19-4R_\gamma+4R_{\text{gw}}}{16R_\nu}k^2\tau$	$\frac{8R_{\text{gw}}}{15(9-4R_\gamma)}k^3\tau^2$	$\frac{R_{\text{gw}}}{R_\nu}k^2\tau$
σ_ν	$\frac{15+8R_{\text{gw}}}{120R_\nu}k^2\tau^2$	$-\frac{16R_{\text{gw}}}{15(9-4R_\gamma)}k\tau$	$-\frac{R_{\text{gw}}}{R_\nu} + \frac{R_{\text{gw}}}{R_\nu}\frac{2}{15}k^2\tau^2$
δ_{gw}	1	$-\frac{4}{3}k\tau$	$\frac{2}{3}k^2\tau^2$
θ_{gw}	$\frac{1}{4}k^2\tau$	k	$-k^2\tau$
σ_{gw}	$\frac{1}{60}k^2\tau^2$	$\frac{4}{15}\left(1 - \frac{4R_{\text{gw}}}{9-4R_\gamma}\right)k\tau$	$1 - \frac{2}{15}k^2\tau^2$
$\tilde{\delta}_\gamma$	$-\frac{(19-8R_\gamma)}{4R_\gamma}$	$\frac{16R_{\text{gw}}}{9-4R_\gamma}\frac{1}{k\tau}$	$\mathcal{O}(k\tau)$
$\tilde{\theta}_\gamma$	$-\frac{19}{16R_\gamma}k^2\tau$	$-\frac{9R_{\text{gw}}}{R_\gamma(9-4R_\nu)}k$	$\mathcal{O}(k^3\tau^2)$
$\tilde{\delta}_\nu$	$\frac{23-8R_\gamma}{4R_\nu}$	$\frac{16R_{\text{gw}}}{9-4R_\gamma}\frac{1}{k\tau}$	$\mathcal{O}(k\tau)$
$\tilde{\theta}_\nu$	$\frac{15+8R_{\text{gw}}}{16R_\nu}k^2\tau$	$-\frac{4R_{\text{gw}}}{9-4R_\gamma}k$	$\frac{R_{\text{gw}}}{R_\nu}k^2\tau$
$\tilde{\delta}_{\text{gw}}$	$\mathcal{O}(k\tau)$	$\frac{16R_{\text{gw}}}{9-4R_\gamma}\frac{1}{k\tau}$	$\mathcal{O}(k\tau)$
$\tilde{\theta}_{\text{gw}}$	$-\frac{1}{2}k^2\tau$	$\frac{R_{\text{gw}}(9-4R_\gamma-4R_{\text{gw}})}{9-4R_\gamma}k$	$-k^2\tau$
Φ	$-\frac{1}{2}$	$\frac{4R_\gamma}{9-4R_\gamma}\frac{1}{k\tau}$	$\mathcal{O}(k\tau)$
Ψ	$\frac{1}{4}$	$-\frac{4R_\gamma}{9-4R_\gamma}\frac{1}{k\tau}$	$\mathcal{O}(k\tau)$

Table 3.3: Initial conditions for the gravitational wave (GW) isocurvature (IC) modes to lowest order in $k\tau$ in the synchronous gauge (top) and Newtonian gauge (bottom - with tildes). The GW density IC mode is a rescaling of the neutrino density IC mode. The GW velocity IC mode is analogous to the neutrino density IC mode. The GW shear IC mode is a mode with previously unseen behaviour; the GW and neutrino perturbations balance such that there is no perturbation to the photons or to the metric.

Finally, the gravitational wave shear isocurvature mode is a completely new phenomenon that is not possible without gravitational waves. Because there are now two components with shear, a new mode is possible where these shears balance each other. As for the neutrino density velocity mode (with gravitational waves) there are no perturbations to the metric or photon sectors for the gravitational wave shear mode.

3.2 Effects on the CMB

The changes in the CMB power spectrum when including adiabatic or homogeneous gravitational waves are shown in figure 3.1. The contributions from the Sachs–Wolfe effect (SW), integrated Sachs–Wolfe effect (ISW) and Doppler shift (DOP) are shown separately, along with the cross-correlations between them⁵. The homogeneous case can be compared to figure 2.2, taken from Smith [219]. The homogeneous mode calculated here has different effects to the effects presented in [219]. Most notably increasing the effective number of neutrino degrees of freedom contributed by gravitational waves, N_{gw} , the homogeneous mode here reduces the power whereas the one given in [219] increases it. This change also has qualitatively different effects for different ℓ regions.

Comparing the modes calculated here, the most noticeable difference between the adiabatic and homogeneous initial conditions is that homogeneous gravitational waves decrease the total power whereas adiabatic gravitational waves increase the total power. This is because the homogeneous gravitational wave and photon perturbations are out of phase with each other when inside the horizon due to the initial conditions having opposite signs (e.g. δ_γ and δ_{gw} in table 3.1).

Including adiabatic gravitational waves has a very small effect on the Doppler term. Most of the change in the first peak of the power spectrum is due to the SW effect and the SW-ISW cross-correlation. This is also true for the homogeneous mode with the addition of a large change in the low- ℓ

⁵As in section 2.5.4.

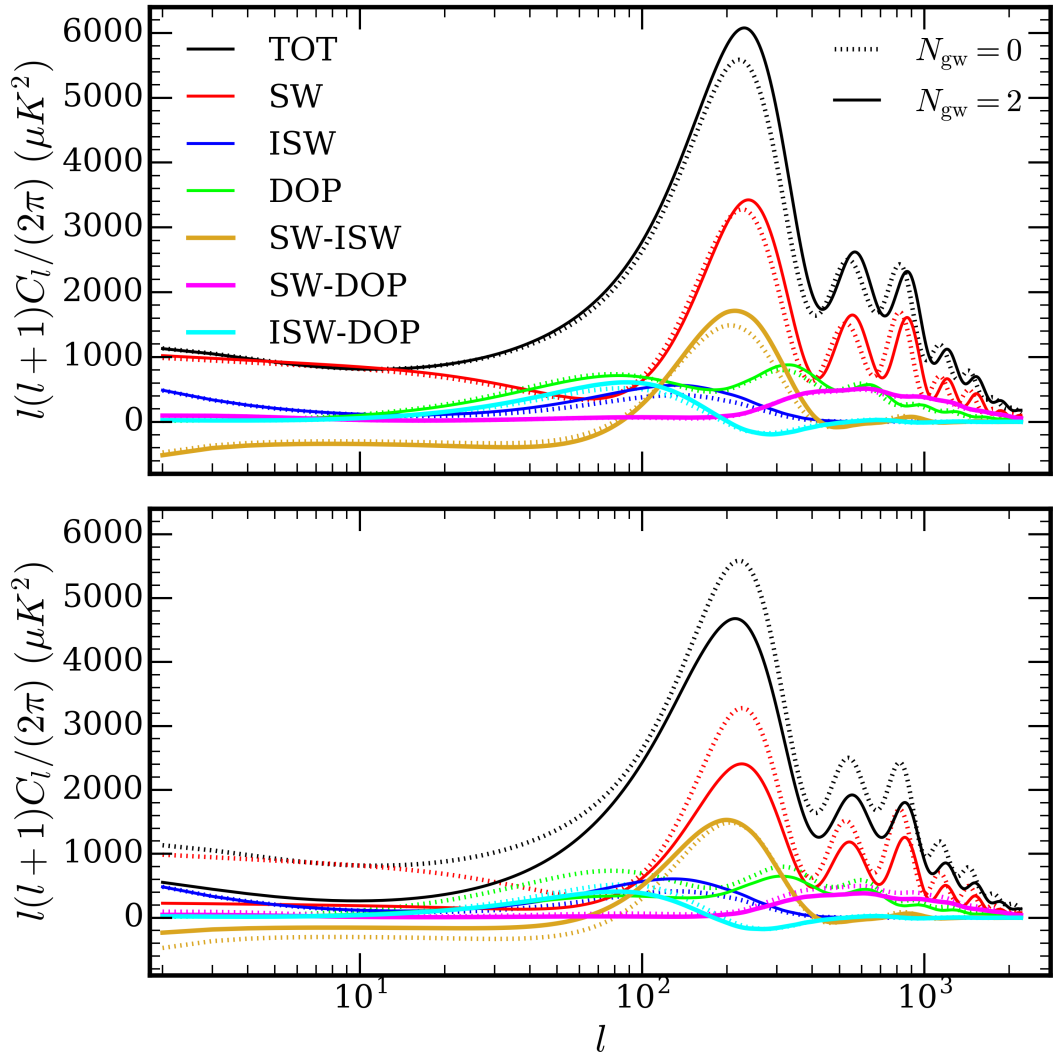


Figure 3.1: The contributions to the CMB power spectrum for gravitational waves with adiabatic (top) and homogeneous (bottom) initial conditions contributing the equivalent of 0 and 2 effective neutrino degrees of freedom. The contributions are separated into Sachs–Wolfe (SW), Integrated Sachs–Wolfe (ISW) and Doppler (DOP) terms and their cross-correlations.

part of the spectrum, driven by the SW, SW–ISW and Doppler terms. The enhancement of the first peak and the decrease at low- ℓ is a background effect (i.e. still observable when the gravitational wave perturbations are turned off).

For the neutrino velocity isocurvature mode and the gravitational wave shear isocurvature mode the initial conditions for the neutrino and gravitational wave sectors balance in such a way that the right-hand side of the relevant Einstein equations are zero, e.g. $\sum_i R_i \delta_i = 0$. Consequently no metric perturbations are generated and the photon perturbations stay zero for all times. Using the line-of-sight integral approach of Seljak and Zaldarriaga [56] (section

1.4.1), it is clear that there is no contribution to the CMB power spectrum from these two modes. As a result, both of these modes are unobservable from the CMB.

Isocurvature modes are well constrained by current CMB observations with the dark matter, neutrino density and neutrino velocity isocurvature modes all constrained to less than 2% of the temperature variance [293], such that we will only consider constraints to the adiabatic and homogeneous modes. The baryon isocurvature mode is not calculated and baryon and cold dark matter perturbations are not given here⁶.

3.3 Planck 2018 constraints

To update the CMB constraints *Planck* 2018 data [151] is used in combination with BAO data from BOSS DR12 [112], 6dFGS [113] and SDSS-MGS [114] (as detailed in section 1.5.3). The precise *Planck* likelihoods used are the TT, TE and EE spectra at $\ell \geq 30$, the low- ℓ likelihood using the `COMMANDER` component separation algorithm and the low- ℓ EE likelihood from the `SIMALL` algorithm in combination with *Planck* 2018 lensing [163]. This corresponds to the TT,TE,EE + lowE + lensing + BAO data-set used in Aghanim et al. [1].

The parameter estimation is done using modified versions of `COSMOMC` and `CAMB` (see section 1.5). The `CAMB` code modifications required duplicating the neutrino equations of motion and including the new initial conditions detailed above. The analysis constitutes a one-parameter extension to Λ CDM⁷ due to the additional requirement to constrain $\Omega_{\text{gw}}h^2$. The 95% confidence upper limits on the gravitational wave density parameter are,

$$\Omega_{\text{gw}}h^2 < 1.7 \times 10^{-6} \quad (\text{adiabatic}), \quad (3.3)$$

$$\Omega_{\text{gw}}h^2 < 2.9 \times 10^{-7} \quad (\text{homogeneous}). \quad (3.4)$$

⁶The matter perturbations are given for the adiabatic, homogeneous, neutrino density isocurvature, gravitational wave velocity isocurvature and gravitational wave shear isocurvature modes in [292].

⁷The sum of the neutrino masses is fixed to 0.06 eV as in *Planck* analyses.

These constraints are plotted in figure 3.2 along with LIGO interferometer, pulsar and BBN constraints for comparison [94, 217, 231, 241]. The adiabatic constraint is a factor ~ 2 tighter than the previous constraint using similar data⁸ from Henrot-Versillé et al. [222]. The homogeneous constraint has not been updated since before *Planck* and tightens by a factor ~ 4 compared to the constraint in Sendra and Smith [221]. The lower limit of the CMB constraint is set by the validity of the shortwave approximation at decoupling and is calculated in detail in section 4.2.4. The scale of matter–radiation equality, k_{eq} is shown for comparison. Note that the limits from BBN and the CMB are integrated constraints (as discussed in section 2.5).

3.3.1 Parameter dependencies

The parameter estimation code used to find the constraints on the gravitational wave density can also be used to investigate the interdependence of cosmological parameters. This is done for the baseline Λ CDM parameters along with the gravitational wave density parameter and the Hubble constant. The gravitational wave density is parameterised by the number of effective neutrino degrees of freedom contributed by gravitational waves,

$$N_{\text{gw}} = \frac{\Omega_{\text{gw}} h^2}{5.6 \times 10^{-6}}. \quad (3.5)$$

The dependencies for gravitational waves with adiabatic initial conditions are shown in figure 3.3. None of the parameters differ significantly from the *Planck* 2018 values [1] but a slight increase in $\Omega_c h^2$, n_s and H_0 is favoured for a non-zero gravitational wave contribution. The acoustic angular scale, θ_{MC} favours a smaller value in this case. There are increases in $\Omega_b h^2$ and the amplitude of the scalar power spectrum but these are of smaller magnitude than for the other parameters. The optical depth to reionisation, τ shows no change with increasing N_{gw} and is consequently not shown in figure 3.3.

The dependencies for gravitational waves with homogeneous initial con-

⁸It is not quite as tight as the adiabatic constraint from Pagano, Salvati, and Melchiorri [223] mentioned in section 2.5.4, but this also included BBN data.

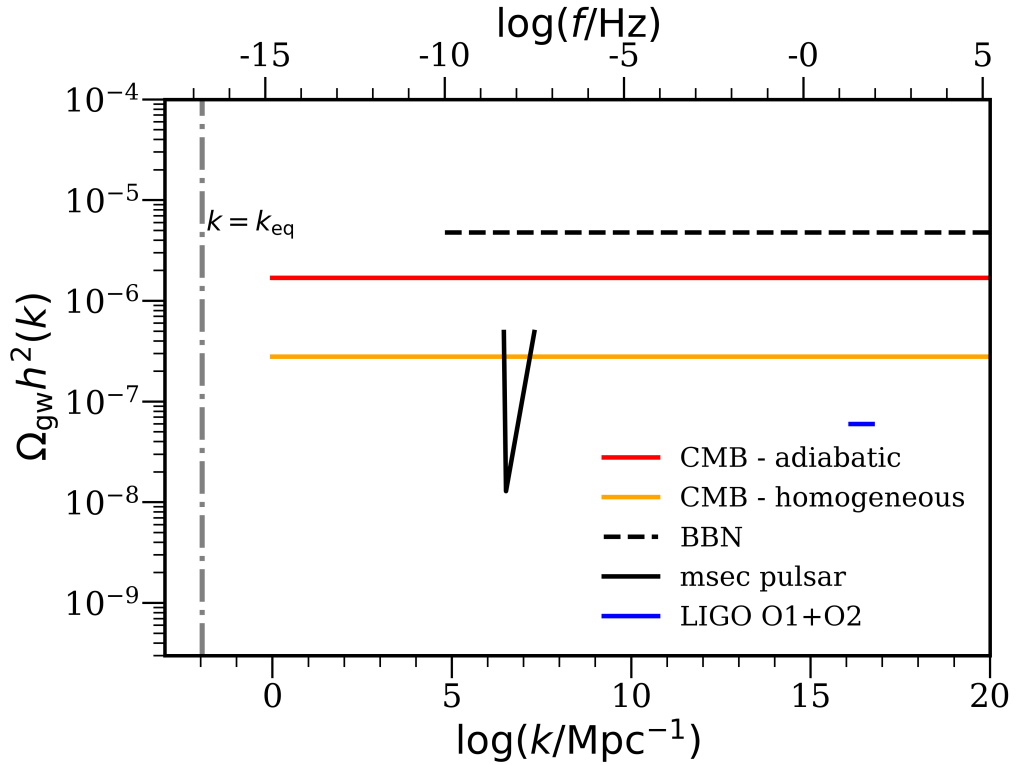


Figure 3.2: CMB constraints on the gravitational wave density parameter for adiabatic (red solid) and homogeneous (orange solid) initial conditions calculated in this work. Constraints from other observations are shown for comparison. The LIGO interferometer constraint (blue) comes from Abbott et al. [231]. The BBN constraint (black dotted) comes from Cooke et al. [94] which uses the Helium abundance data of Izotov, Stasinska, and Guseva [217]. The pulsar constraint comes from Thorsett and Dewey [241]. The vertical grey dot-dashed line denotes the scale of matter–radiation equality and is shown for comparison to the lower-limit of the CMB constraint.

ditions are shown in figure 3.4. Again parameter values are consistent with *Planck* 2018 values. The strongest dependence N_{gw} has is with the acoustic angular scale which favours a smaller value for an increased gravitational wave density similar to the adiabatic case. $\Omega_c h^2$ and the amplitude of the scalar power spectrum favour very slightly increased values for non-zero N_{gw} . For homogeneous gravitational waves $\Omega_b h^2$, n_s , H_0 and τ are all unchanged as the gravitational wave density increases.

The similarity of the decrease in the acoustic angular scale in both these cases is as expected as this is a background quantity and hence doesn't depend on the perturbations.

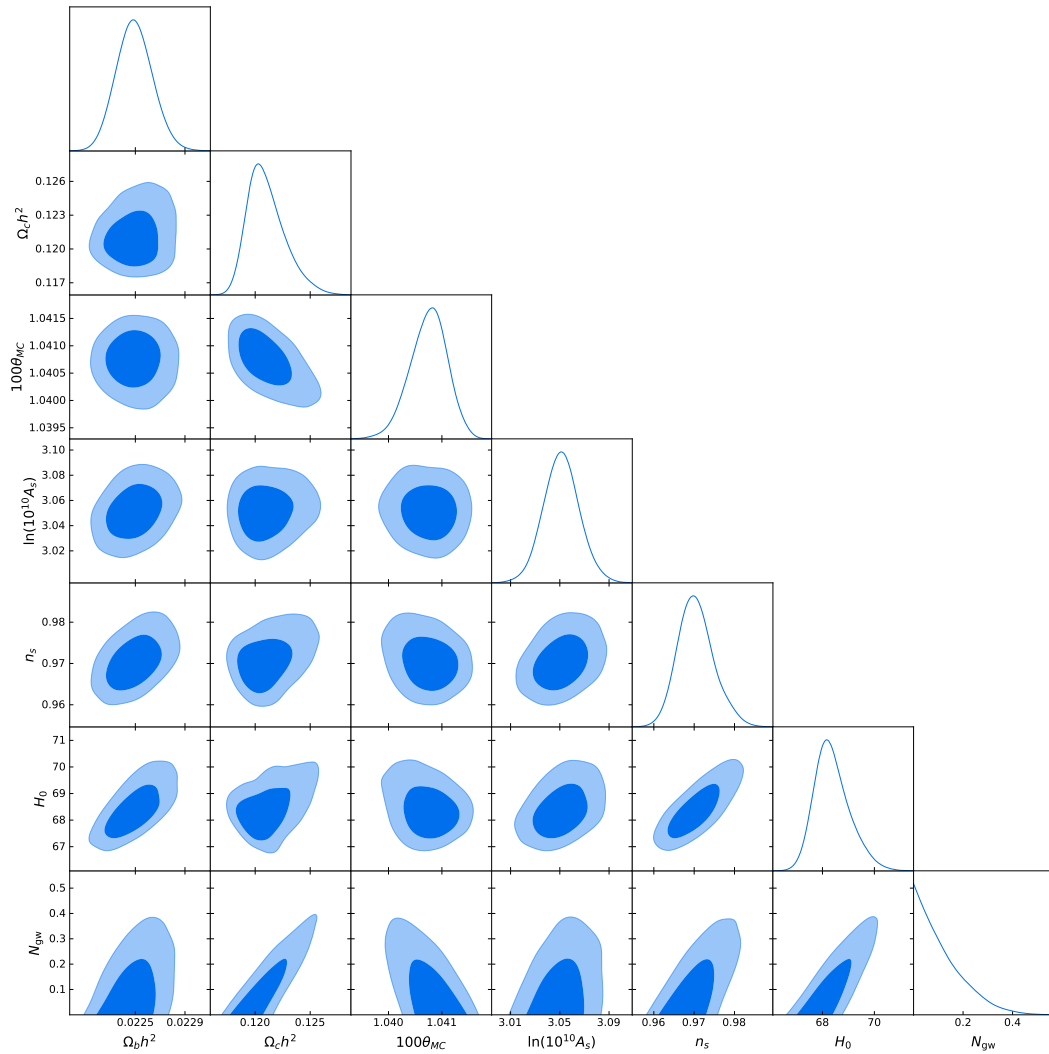


Figure 3.3: 68% and 95% confidence contours for the standard Λ CDM parameters plus N_{gw} and H_0 , for adiabatic gravitational wave initial conditions. The optical depth to reionisation, τ is not shown as it has no dependence on N_{gw} .

3.4 Summary and outlook

In this chapter the methodology used for calculating gravitational wave constraints from the CMB using the shortwave approximation was reproduced. In doing so, differences with the homogeneous mode initial conditions calculated previously were found and the importance of favouring this homogeneous mode over the adiabatic mode was stressed, due to considerations of possible gravitational wave sources. New isocurvature modes were calculated and the behaviour of these, along with the updated homogeneous mode, was investigated.

Existing constraints on gravitational waves with adiabatic and homogeneous

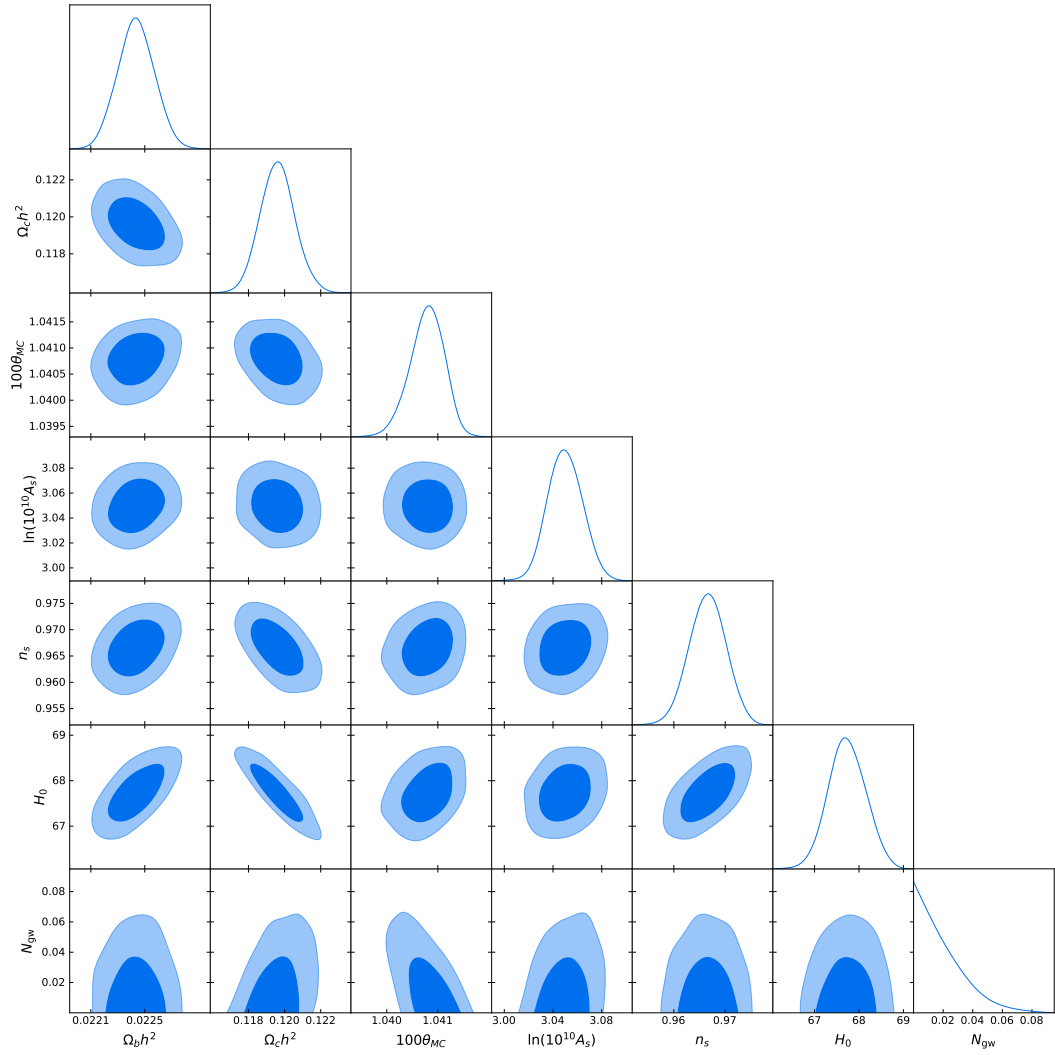


Figure 3.4: 68% and 95% confidence contours for the standard Λ CDM parameters plus N_{gw} and H_0 , for homogeneous gravitational wave initial conditions. The optical depth to reionisation, τ is not shown as it has no dependence on N_{gw} .

initial conditions were updated using *Planck* 2018 data finding the tightest current constraints from CMB+BAO data. These constraints are valid for frequencies, $f \gtrsim 10^{-15}$ Hz. For adiabatic initial conditions, $\Omega_{\text{gw}} h^2 < 1.7 \times 10^{-6}$ and for homogeneous initial conditions, $\Omega_{\text{gw}} h^2 < 2.9 \times 10^{-7}$ (both at 95% confidence). The effect of including short-wavelength gravitational waves on the Λ CDM parameters was also investigated finding significantly more parameter interdependencies for the adiabatic mode than for the homogeneous mode and that the Λ CDM best-fit values are not changed significantly by the inclusion of gravitational waves.

These constraints are unlikely to improve significantly in the future. *Planck*

2018 was the final data release and the *Planck* satellite was cosmic variance limited up to $\ell \approx 1600$. Consequently measurements of the temperature anisotropies are unlikely to improve appreciably. The observational emphasis is shifting towards measurement of CMB polarisation. Improvements in the measurement of the *E*-mode polarisation will improve the constraint slightly but the main focus is *B*-mode polarisation which will primarily constrain gravitational waves at lower frequencies than the validity of the shortwave approximation allows.

Chapter 4

Low-Frequency Gravitational Waves

This section details two CMB methodologies for constraining gravitational waves with frequencies below that allowed by the shortwave approximation. The first of these is an updated approach to the standard B -mode constraint (see sections 1.4.3 and 2.5.1) that reconstructs the tensor primordial power spectrum from the available data and hence does not rely on the power-law assumption used elsewhere.

The second utilises the gauge-invariant formalism presented by Abramo, Brandenberger, and Mukhanov [38] (see section 2.4) to define an effective energy-momentum tensor and hence find the density and pressure of the homogeneous gravitational wave fluid. This shows a range of interesting physical effects which are investigated. The validity of this approach is verified using consistency checks and the effects on the CMB are compared with those found when using the shortwave approximation (as detailed in the previous chapter). This approach has not previously been applied to the CMB and there was previously no constraint on gravitational waves in the two orders of magnitude between the constraints from B -modes and the shortwave approximation. The new constraint is presented and is competitive in magnitude to the constraint from the shortwave approximation.

Some of the code and parameter estimation in this chapter was written or performed by Dr. Adam Moss in preparation for a paper [292]. Where this is

the case it will be explicitly stated in the footnotes.

4.1 *B-mode constraint*

Existing low-frequency constraints use the temperature and polarisation of the CMB to look for the effects of gravitational waves. These are roughly called the ‘*B-mode constraint*’ here, though it is stressed that temperature and *E-mode* data is also used. The contribution of the gravitational waves is dependent on the gravitational wave density, $\Omega_{\text{gw}}(f)$ which is simply related to the tensor primordial power spectrum by equation (2.40) [205]. As discussed in section 2.5.1 this equation is incorrect when applied to super-horizon gravitational waves and hence to the *B-mode constraint*. However, due to the prevalence of equation (2.40) in the literature it will also be used here to convert from the tensor power spectrum to a gravitational wave density and is treated as a first approximation to the super-horizon behaviour. The tensor primordial power spectrum is assumed to be a power-law parameterised by the tensor-to-scalar ratio, r_{k_*} and the tensor tilt n_t , which can be related to r_{k_*} using the single field slow-roll inflation consistency relation,

$$n_t = -\frac{r_{k_*}}{8}. \quad (4.1)$$

An alternative approach is taken here, with the primordial power spectrum being reconstructed directly from the CMB data. This is done in logarithmic frequency bins across the range in which the CMB constraints are most sensitive which corresponds to $-3.5 \lesssim \log_{10}[k \text{ Mpc}] \lesssim -0.3$. The lower limit is set roughly by the size of the horizon today and the range is approximately centred on the horizon size at recombination. To accurately represent the frequency dependence of the *B-mode constraint* without drastically increasing the computational time required we use a bin size, $\Delta \log_{10}[k \text{ Mpc}] = 0.2$, such that there are 16 bins in total.

The constraint¹ is obtained using *Planck* TT,TE,EE + lowE + lensing

¹This constraint was obtained using COBAYA by Dr. Adam Moss.

+ BAO data as in chapter 3 [112–114, 151] along with *B*-mode data from BICEP2/*Keck* [14]. The *B*-mode polarisation data is valid for $20 < \ell < 330$.

A standard Λ CDM model is used for the parameter estimation where the neutrino sector is fixed to three neutrinos species, two of these massless and a single massive neutrino with mass 0.06 eV. *Planck* and BICEP2/*Keck* nuisance parameters are marginalised over and the other parameters have flat priors. Four MCMC chains are run using a Metropolis–Hastings algorithm and the chains are stopped and said to have converged when the Gelman and Rubin $R - 1$ statistic is < 0.05 .

The sampling is done on the power spectrum, $\mathcal{P}_T(k)$. $\Omega_{\text{gw}}(k)h^2$ is added as a derived parameter using equation (2.40) which results in the gravitational wave constraint including the variation of $\Omega_b h^2$ and $\Omega_c h^2$. The effect of these extra variations is small when compared to directly converting between the power spectrum and the density parameter using best-fit values of parameters in equation (2.40). As noted previously this conversion is not valid due to equation (2.40) only being valid for short wavelength gravitational waves, but the conversion is used here for consistency with existing results. It is however stressed that it is only a first approximation to the ‘true’ constraint on Ω_{gw} because of this, but the constraints on $\mathcal{P}_T(k)$ have no such problems as, until the conversion to the density parameter, the approach is independent of any short wavelength assumptions.

The posterior probabilities of the gravitational wave density parameter for each of the 16 bins are shown in figure 4.1. The 2σ upper limits for each of the 16 bins are used as the low-frequency constraint and are shown in figure 4.2. The maximal sensitivity gives $\Omega_{\text{gw}} h^2 \lesssim 4 \times 10^{-16}$ for $\log_{10}[k \text{ Mpc}] \simeq -2.0$, corresponding approximately to the horizon size at recombination. Above this the constraint weakens due to the decay of the gravitational wave amplitude once they enter the horizon, becoming weaker than the shortwave approximation constraints (though applying for lower frequencies) for $f \gtrsim 10^{-16}$ Hz. Figure 4.2 also shows the gravitational wave density parameter for a power-law primordial

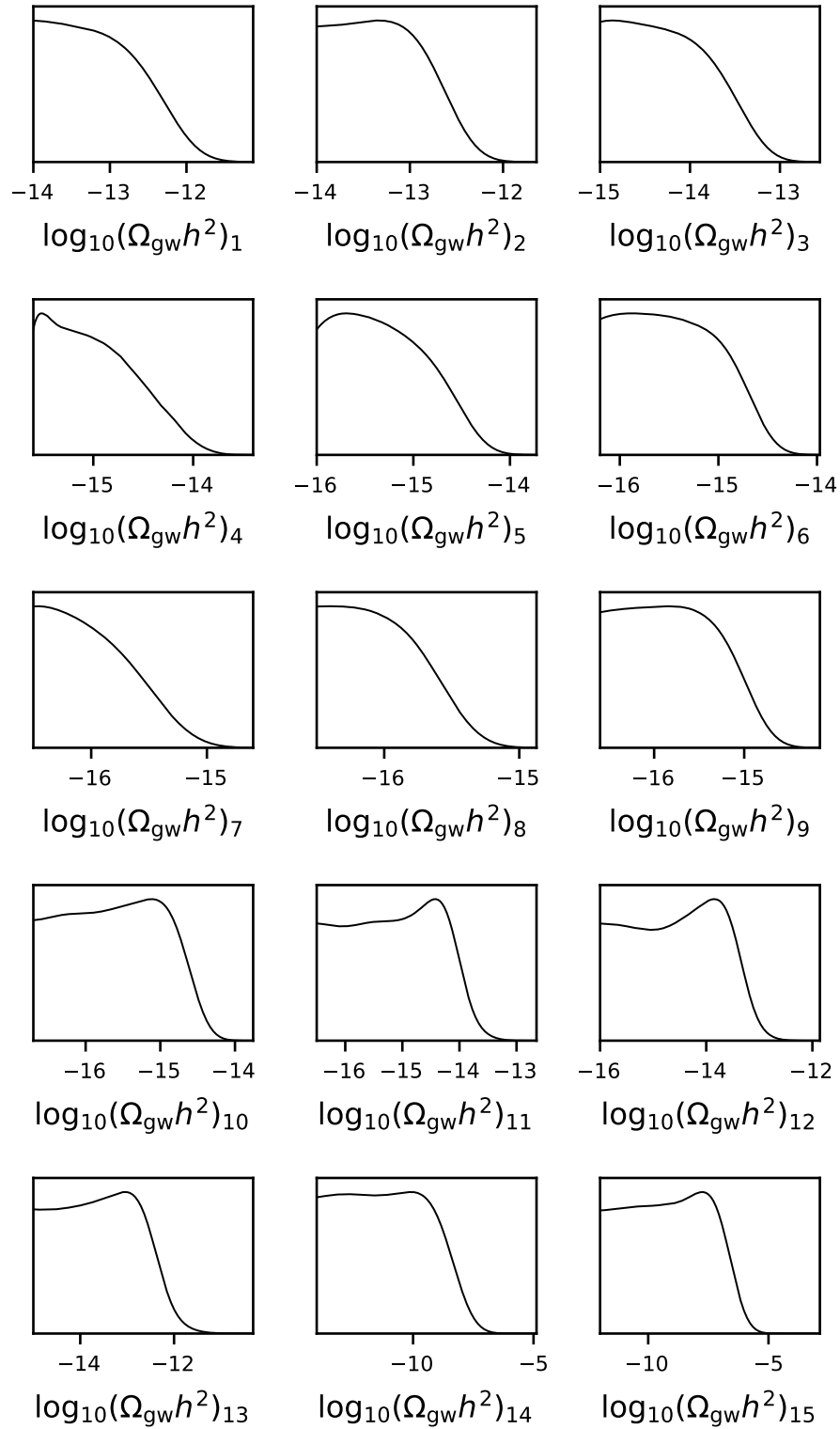


Figure 4.1: Posterior probabilities of the gravitational wave density parameter for each logarithmic k -bin used for the low-frequency polarisation constraint. This uses equation (2.40) to convert the direct constraint on the tensor power spectrum into a constraint on the gravitational wave density parameter and is consequently only a first approximation to the true super-horizon behaviour. The bins are numbered from $\log_{10}[k \text{ Mpc}] = -3.5$ and increase in steps of 0.2. The final bin, with $-0.5 \leq \log_{10}[k \text{ Mpc}] < -0.3$, is unconstrained and is not shown. The 95% confidence limits of each posterior are used for the constraint in figure 4.2.

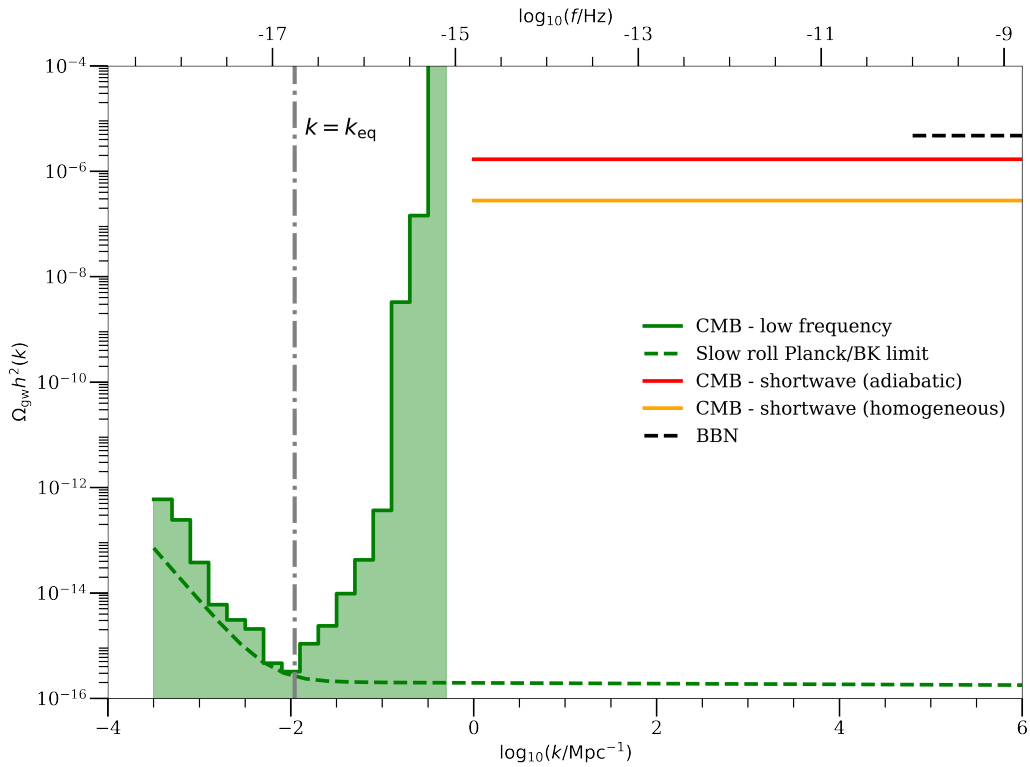


Figure 4.2: The constraint on the gravitational wave density parameter from reconstruction of the tensor power spectrum using CMB temperature and polarisation data (green). The homogeneous and adiabatic shortwave CMB results from chapter 3 are also shown for comparison along with the BBN constraint from Cooke et al. [94]. The scale of matter–radiation equality is shown as an illustration of the scale associated with the horizon at the time of CMB emission, which corresponds to the peak in sensitivity of the B -mode constraint.

power spectrum from slow-roll inflation obeying the *Planck* and *BICEP2/Keck* constraint on the tensor-to-scalar ratio, $r_{0.002} < 0.056$ [14]. The consistency relation for this value of the tensor-to-scalar ratio implies that $n_t = -0.007$. These values of the tensor-to-scalar ratio and tensor tilt, like the power spectrum for the B -mode constraint, are converted to a gravitational wave density using the short wavelength assumption of equation (2.40) and consequently the comparison curve in figure 4.2 is also a first approximation to the behaviour for super-horizon gravitational waves. A constraint was found using a similar methodology to the power spectrum reconstruction detailed here, and a similar maximal sensitivity of $\Omega_{\text{gw}} h^2 \sim 10^{-15}$ was found, in Namikawa et al. [294].

4.2 Intermediate, non-shortwave approach

The shortwave approximation has been frequently used to constrain PGWs from the CMB. However, gravitational waves that do not satisfy the shortwave condition at CMB decoupling are only constrained by B -mode polarisation. This constraint weakens significantly for $f \gtrsim 10^{-16}$ Hz, therefore an alternative CMB constraint in this region could provide a much stronger constraint. The rest of this chapter will detail the approach that was developed to address this. This has a range of interesting physical consequences and applications and as a by-product, it can also be used to test the validity of the shortwave approximation.

The core idea is to use the gauge-invariant, non-shortwave approach presented in section 2.4 [38, 201]. This allows for calculation of the density and pressure of gravitational waves of all frequencies.

4.2.1 Calculating the density and pressure

The calculation of the perturbed Einstein tensor and consequently the effective energy–momentum tensor for gravitational waves is a lengthy calculation that was fully reproduced and verified. As a result, the methodology of this calculation will be presented in detail here and some of the notation in previous papers [38, 203] will be clarified and made more explicit.

The calculation of the Einstein tensor from the metric proceeds as in standard general relativistic calculations, through the calculation of the Christoffel symbols from the metric, the calculation of the Ricci tensor and then the Einstein tensor. This is complicated in the perturbative calculation by the fact that the zeroth, first and second order components of all these quantities contribute to the proceeding quantity and hence all of these need to be calculated to find the second order components of the Einstein tensor, $G^{(2)0}_0$ [202, 203, 295, 296].

The transverse-traceless expanding gravitational wave metric is used,

$$ds^2 = -a^2(\tau)d\tau^2 + a^2(\tau)(\delta_{ij} + h_{ij})dx^i dx^j, \quad (4.2)$$

where $j_{\mu\nu}$ of equation (2.6) is implicitly neglected as it does not contribute to the Einstein tensor under averaging. The metric is written as,

$$g_{\mu\nu} = \tilde{g}_{\mu\nu} + \delta g_{\mu\nu}, \quad (4.3)$$

such that $\tilde{g}_{\mu\nu}$ is the conformal time FLRW metric. The Christoffel symbols are calculated as,

$$\Gamma^{(0)\alpha}_{\beta\gamma} = \frac{1}{2}\tilde{g}^{\alpha\rho}(\tilde{g}_{\rho\beta,\gamma} + \tilde{g}_{\rho\gamma,\beta} - \tilde{g}_{\beta\gamma,\rho}), \quad (4.4a)$$

$$\begin{aligned} \Gamma^{(1)\alpha}_{\beta\gamma} &= \frac{1}{2}\tilde{g}^{\alpha\rho}(\delta g_{\rho\beta,\gamma} + \delta g_{\rho\gamma,\beta} - \delta g_{\beta\gamma,\rho}) \\ &\quad + \frac{1}{2}\delta g^{\alpha\rho}(\tilde{g}_{\rho\beta,\gamma} + \tilde{g}_{\rho\gamma,\beta} - \tilde{g}_{\beta\gamma,\rho}), \end{aligned} \quad (4.4b)$$

$$\Gamma^{(2)\alpha}_{\beta\gamma} = \frac{1}{2}\delta g^{\alpha\rho}(\delta g_{\rho\beta,\gamma} + \delta g_{\rho\gamma,\beta} - \delta g_{\beta\gamma,\rho}). \quad (4.4c)$$

From these the Ricci tensors are,

$$R^{(0)}_{\alpha\beta} = \Gamma^{(0)\rho}_{\alpha\beta,\rho} - \Gamma^{(0)\rho}_{\rho,\beta\alpha} + \Gamma^{(0)\rho}_{\rho\lambda}\Gamma^{(0)\lambda}_{\alpha\beta} - \Gamma^{(0)\rho}_{\alpha\lambda}\Gamma^{(0)\lambda}_{\rho\beta}, \quad (4.5a)$$

$$\begin{aligned} R^{(1)}_{\alpha\beta} &= \Gamma^{(1)\rho}_{\alpha\beta,\rho} - \Gamma^{(1)\rho}_{\rho,\beta\alpha} + \Gamma^{(0)\rho}_{\rho\lambda}\Gamma^{(1)\lambda}_{\alpha\beta} + \Gamma^{(1)\rho}_{\rho\lambda}\Gamma^{(0)\lambda}_{\alpha\beta} \\ &\quad - \Gamma^{(0)\rho}_{\alpha\lambda}\Gamma^{(1)\lambda}_{\rho\beta} - \Gamma^{(1)\rho}_{\alpha\lambda}\Gamma^{(0)\lambda}_{\rho\beta}, \end{aligned} \quad (4.5b)$$

$$\begin{aligned} R^{(2)}_{\alpha\beta} &= \Gamma^{(2)\rho}_{\alpha\beta,\rho} - \Gamma^{(2)\rho}_{\rho,\beta\alpha} + \Gamma^{(0)\rho}_{\rho\lambda}\Gamma^{(2)\lambda}_{\alpha\beta} + \Gamma^{(1)\rho}_{\rho\lambda}\Gamma^{(1)\lambda}_{\alpha\beta} \\ &\quad + \Gamma^{(2)\rho}_{\rho\lambda}\Gamma^{(0)\lambda}_{\alpha\beta} - \Gamma^{(0)\rho}_{\alpha\lambda}\Gamma^{(2)\lambda}_{\rho\beta} \\ &\quad - \Gamma^{(1)\rho}_{\alpha\lambda}\Gamma^{(1)\lambda}_{\rho\beta} - \Gamma^{(2)\rho}_{\alpha\lambda}\Gamma^{(0)\lambda}_{\rho\beta}. \end{aligned} \quad (4.5c)$$

The components of the Christoffel symbols and Ricci tensors for the metric given by equation (4.2) are presented in Appendix A of Giovannini [202]².

Finally the Einstein tensor is given by [297],

$$G^{(2)}_{\mu\nu} = R^{(2)}_{\mu\nu} - \frac{1}{2}\tilde{g}_{\mu\nu}\left(\tilde{g}^{\alpha\beta}R^{(2)}_{\alpha\beta} - \delta g^{\alpha\beta}R^{(1)}_{\alpha\beta} + \delta g^\alpha_\rho\delta g^{\rho\beta}R^{(0)}_{\alpha\beta}\right)$$

²Note that these are for the opposite metric signature and the $(i0)$ components are neglected. These equations were only found by the author during the writing of this document.

$$-\frac{1}{2}\delta g_{\mu\nu}\left(\tilde{g}^{\alpha\beta}R^{(1)}_{\alpha\beta}-\delta g^{\alpha\beta}R^{(0)}_{\alpha\beta}\right). \quad (4.6)$$

Applying all this to the cosmological gravitational wave metric the second order components of the Einstein tensor are,

$$G^{(2)0}_0 = \frac{1}{4a^2}\left(\frac{1}{2}\dot{h}^{km}\dot{h}_{km} + 4\mathcal{H}h^{km}\dot{h}_{km} - 2h^{km}h_{km,f}{}^f + h^{km,j}h_{kj,m} - \frac{3}{2}h^{km,j}h_{km,j}\right), \quad (4.7a)$$

$$G^{(2)0}_i = \frac{1}{4a^2}\left(-\dot{h}^{km}h_{km,i} - 2h^{km}\dot{h}_{km,i} + 2h^{km}\dot{h}_{ik,m}\right), \quad (4.7b)$$

$$G^{(2)i}_0 = \frac{1}{4a^2}\left(\dot{h}_{km}h^{km,i} + 2h_{km}\dot{h}^{km,i} - 2h_{km}\dot{h}^{ik,m} + 4\mathcal{H}h_{km}h^{km,i} - 4\mathcal{H}h_{km}h^{ik,m}\right), \quad (4.7c)$$

$$G^{(2)i}_j = \frac{1}{4a^2}\left(-2\dot{h}^{ik}\dot{h}_{jk} - 2h^{ik}\ddot{h}_{jk} + \frac{3}{2}\delta^i_j\dot{h}^{km}\dot{h}_{km} + 2\delta^i_jh^{km}\ddot{h}_{km} - 4\mathcal{H}h^{ik}\dot{h}_{jk} + 4\mathcal{H}\delta^i_jh^{km}\dot{h}_{km} - 2h_{jm,k}h^{ik,m} + 2h_{jk,m}h^{ik,m} - 2\delta^i_jh^{km}h_{km,j}{}^j + \delta^i_jh_{kj,m}h^{km,j} - \frac{3}{2}\delta^i_jh_{km,j}h^{km,j} + h^{km,i}h_{km,j} + 2h^{km}h_{km}{}^i{}_j - 2h^{km}h_{jk}{}^i{}_m - 2h^{km}h^i{}_{k,jm} + 2h^{km}h^i{}_{j,km} + 2h^{ik}h_{jk,m}{}^m\right). \quad (4.7d)$$

These expressions agree with equations (8–11) of [203] except for the last two terms of equation (4.7c). It does however agree with equation (2.30) of [296]. This could be due to an ambiguity in the notation, to be clear, $\dot{h}^{km,i}$ means $\partial^i\partial_0h^{km}$ here. All terms that can be written as total derivatives will vanish under averaging and consequently this difference does not affect the background behaviour.

Under spatial averaging defined (as in section 2.4) by,

$$\langle A \rangle_x = \lim_{V \rightarrow \infty} \frac{1}{V} \int A dV, \quad (2.20)$$

for a general function, A , the second order Einstein tensor becomes,

$$\langle G^{(2)0}_0 \rangle_x = \frac{1}{a^2}\left(\mathcal{H}\langle h^{km}\dot{h}_{km} \rangle_x + \frac{1}{8}\langle \dot{h}^{km}\dot{h}_{km} \rangle_x + \frac{1}{8}\langle h^{km,j}h_{km,j} \rangle_x\right), \quad (4.8a)$$

$$\langle G^{(2)0}{}_i \rangle_x = \frac{1}{a^2} \left(\langle h^{mk} \dot{h}_{k[i,m]} \rangle_x - \frac{1}{4} \langle \dot{h}^{mk} h_{mk,i} \rangle_x \right), \quad (4.8b)$$

$$\langle G^{(2)i}{}_0 \rangle_x = \frac{1}{a^2} \left(\frac{1}{4} \langle \dot{h}_{mk} h^{mk,i} \rangle_x - \langle h_{mk} \dot{h}^{k[i,m]} \rangle_x \right), \quad (4.8c)$$

$$\begin{aligned} \langle G^{(2)i}{}_j \rangle_x &= \frac{3}{8a^2} \delta^i_j \left(\langle \dot{h}_{km} \dot{h}^{km} \rangle_x - \langle h^{km,n} h_{km,n} \rangle_x \right) \\ &\quad + \frac{1}{2a^2} \left(-\langle \dot{h}^{ik} \dot{h}_{kj} \rangle_x - \frac{1}{2} \langle h^{km,i} h_{km,j} \rangle_x + \langle h^{ik,m} h_{kj,m} \rangle_x \right), \end{aligned} \quad (4.8d)$$

where tensor anti-symmetrisation is denoted by $h_{k[i,m]} = (h_{ki,m} - h_{km,i})/2$. These are consistent with the equations given in [203].

As in section 2.4, the effective energy momentum tensor for gravitational waves is calculated from the Einstein tensor as³,

$$T^{(\text{GW})\mu}{}_{\nu} = -\frac{1}{8\pi G} \langle G^{(2)\mu}{}_{\nu} \rangle_x. \quad (2.24)$$

The (00) component of the effective energy momentum tensor gives the effective energy density of gravitational waves, ρ_{gw} . However, the gravitational wave pressure, p_{gw} picks up an extra term from the interaction of gravitational waves with matter which can be calculated using considerations of the conservation of the full energy–momentum tensor, see section 2.4 and refs. [38, 200, 202]. The density and pressure rely on a stochastic average over the initial conditions for the gravitational wave perturbation. This averaging is implicit in previous analyses but is not stated. For example, in equation (93) of [38] and equation (27) and (28) of [203] the angled brackets denote stochastic averaging not spatial averaging⁴. This stochastic averaging is made explicit throughout this work and is denoted by $\langle \dots \rangle_Q$. The density and pressure are written,

$$\rho_{\text{gw}} = \frac{1}{8\pi G} \langle \delta^{(2)} G^0{}_0 \rangle_{Q,x} \quad (4.9a)$$

$$p_{\text{gw}} = \frac{1}{8\pi G} \left(\frac{1}{3} \langle \delta^{(2)} G^i{}_i \rangle_{Q,x} + \frac{1}{2a^2} \mathcal{H}(1 + \tilde{w}) \langle h^{ij} \dot{h}_{ij} \rangle_{Q,x} \right), \quad (4.9b)$$

where \tilde{w} is the equation of state of the background cosmology containing the

³Reproduced here for ease of reading.

⁴The quantities in the angled brackets in these examples are independent of space such that these averages cannot be spatial. This was clarified in a correspondence from Prof. Robert Brandenberger.

gravitational wave perturbations. Writing these expressions explicitly in terms of the gravitational wave perturbation using equations (4.8),

$$\rho_{\text{gw}} = \frac{1}{8\pi G a^2} \left(\frac{1}{8} \langle (\nabla h_{ij})^2 \rangle_{Q,x} + \frac{1}{8} \langle (\dot{h}_{ij})^2 \rangle_{Q,x} + \mathcal{H} \langle h^{ij} \dot{h}_{ij} \rangle_{Q,x} \right), \quad (4.10a)$$

$$p_{\text{gw}} = \frac{1}{8\pi G a^2} \left(\frac{7}{24} \langle (\nabla h_{ij})^2 \rangle_{Q,x} - \frac{5}{24} \langle (\dot{h}_{ij})^2 \rangle_{Q,x} + \frac{\mathcal{H}}{2} (1 + \tilde{w}) \langle h^{ij} \dot{h}_{ij} \rangle_{Q,x} \right). \quad (4.10b)$$

These are the key equations of this approach. The equation of motion is obtained from the first order equation, and gives⁵,

$$\ddot{h}_{ij} + 2\mathcal{H}\dot{h}_{ij} - h_{ij,k}{}^k = 16\pi G a^2 \Pi_{ij}^{(T)}, \quad (2.10)$$

where $\Pi^{(T)}$ is the anisotropic inertia tensor. This can be solved to give $h_{ij}(\vec{x}, t)$, if the anisotropic stress is known (or assumed zero), which can then be used to calculate the density and pressure of gravitational waves using equations (4.10).

As in [203], this approach is reformulated in k -space. This results in solutions of the equation of motion being calculable numerically and, for simple backgrounds, analytically. It also means the standard approach used for separating and stochastically averaging the initial conditions can be closely mirrored.

The Fourier transform of the tensor perturbation is given by equation (2.5)⁶;

$$h_{ij}(\vec{x}, t) = \sum_{\lambda=\pm 2} \int \frac{d^3 k}{(2\pi)^3} \epsilon_{ij}(\hat{k}, \lambda) \tilde{h}(k, \lambda, t) e^{i\vec{k}\cdot\vec{x}}. \quad (2.5)$$

In Fourier space the spatial averaging of a product of two general, polarisation-dependent functions,

$$\langle f^{ij}(\vec{x}, \tau) g_{ij}(\vec{x}, \tau) \rangle_x = \int \frac{d^3 k}{(2\pi)^3} f^{ij*}(\vec{k}, \tau) g_{ij}(\vec{k}, \tau), \quad (4.11)$$

where the complex exponentials from the Fourier transforms have been rewritten as a Dirac delta function and the delta function has been used to do one of

⁵Reproduced here for ease of reading.

⁶Reproduced here for ease of reading.

the wavenumber integrals. Here $V = 1$ as it is only included in the definition of the averaging to keep track of dimensions (see conventions or [59] chapter 3). This integral can be done in spherical polar coordinates to find,

$$\langle f^{ij}(\vec{x}, \tau) g_{ij}(\vec{x}, \tau) \rangle_x = \int d \ln k \frac{k^3}{\pi^2} \tilde{f}^*(k, \tau) \tilde{g}(k, \tau), \quad (4.12)$$

where the products of the polarisation tensor have been evaluated using [28],

$$\sum_{\lambda} \epsilon_{ij}^*(\hat{q}, \lambda) \epsilon^{jk}(\hat{q}, \lambda) = 2\delta_i^k - 2\hat{q}_i \hat{q}^k. \quad (4.13)$$

Using this for the density and pressure of gravitational waves and dropping the helicity dependence, we obtain,

$$\rho_{\text{gw}}(\tau) = \frac{1}{8\pi G a^2} \int d \ln k \frac{k^3}{\pi^2} \tilde{\rho}_{\text{gw},Q}(k, \tau), \quad (4.14a)$$

$$p_{\text{gw}}(\tau) = \frac{1}{8\pi G a^2} \int d \ln k \frac{k^3}{\pi^2} \tilde{p}_{\text{gw},Q}(k, \tau), \quad (4.14b)$$

where,

$$\begin{aligned} \tilde{\rho}_{\text{gw},Q}(k, \tau) &= \frac{k^2}{8} \langle |\tilde{h}(k, \tau)|^2 \rangle_Q + \frac{1}{8} \langle |\dot{\tilde{h}}(k, \tau)|^2 \rangle_Q \\ &\quad + \mathcal{H} \langle |\tilde{h}^*(k, \tau) \dot{\tilde{h}}(k, \tau)|^2 \rangle_Q, \end{aligned} \quad (4.15a)$$

$$\begin{aligned} \tilde{p}_{\text{gw},Q}(k, \tau) &= \frac{7k^2}{24} \langle |\tilde{h}(k, \tau)|^2 \rangle_Q - \frac{5}{24} \langle |\dot{\tilde{h}}(k, \tau)|^2 \rangle_Q \\ &\quad + \frac{1}{2} \mathcal{H} (1 + w^{(0)}) \langle |\tilde{h}^*(k, \tau) \dot{\tilde{h}}(k, \tau)|^2 \rangle_Q. \end{aligned} \quad (4.15b)$$

The initial condition can be separated from the time evolution of the gravitational wave amplitude as [28],

$$\tilde{h}(k, \tau) = A_k D(k, \tau), \quad (4.16)$$

such that the primordial power spectrum,

$$\mathcal{P}_t(k) = \frac{k^3}{\pi^2} \langle |A_k|^2 \rangle_Q, \quad (4.17)$$

specifies the ensemble average of stochastic initial conditions mentioned previously.

The time evolution of the gravitational wave amplitude is now described by

the function⁷ $D(k, \tau)$ which obeys the gravitational wave equation of motion,

$$\ddot{D} + 2\mathcal{H}\dot{D} + k^2 D = 16\pi G a^2 \Pi^{(T)}, \quad (4.18)$$

where $\Pi^{(T)}$ is the Fourier transform of the anisotropic stress tensor decomposed in terms of the gravitational wave polarisation [28]. The helicity dependence of $\tilde{h}(k, \tau)$ was dropped earlier because this equation of motion is helicity independent.

The final expressions for the density and pressure are,

$$\rho_{\text{gw}}(\tau) = \frac{1}{8\pi G a^2} \int_{k_{\text{min}}}^{k_{\text{max}}} d \ln k \tilde{\rho}_{\text{gw}}(k, \tau) \mathcal{P}_t(k), \quad (4.19a)$$

$$p_{\text{gw}}(\tau) = \frac{1}{8\pi G a^2} \int_{k_{\text{min}}}^{k_{\text{max}}} d \ln k \tilde{p}_{\text{gw}}(k, \tau) \mathcal{P}_t(k), \quad (4.19b)$$

where the choice of k_{min} and k_{max} defines the range of gravitational waves considered⁸,

$$\tilde{\rho}_{\text{gw}}(k, \tau) = \left[\frac{1}{8} \left(k^2 D^2 + \dot{D}^2 \right) + \mathcal{H} \dot{D} D \right], \quad (4.20a)$$

$$\tilde{p}_{\text{gw}}(k, \tau) = \frac{7k^2}{24} D^2 - \frac{5}{24} \dot{D}^2 + \frac{\mathcal{H}}{2} (1 + \tilde{w}) \dot{D} D, \quad (4.20b)$$

and the primordial power spectrum of equation (4.17) is conventionally parameterised via equation (1.60)⁹,

$$\mathcal{P}_t(k) = A_t(k_*) \left(\frac{k}{k_*} \right)^{n_t}. \quad (1.60)$$

Consequently the methodology for calculating the density and pressure of gravitational waves is as follows. The gravitational wave equation of motion (equation (4.18)) is solved for a given background cosmology and anisotropic stress and the solution for $D(k, \tau)$ is used to evaluate the k -space density and pressure using equations (4.20). This is then integrated with the power spectrum of equation (1.60) to get the total homogeneous density and pressure

⁷This function is called $f(\tau, k)$ in [203].

⁸These are essentially an ultraviolet and infrared cutoff to the equations for gravitational waves and can be set from consideration of inflation, see [203] or by specific considerations of the cosmology.

⁹Reproduced here for ease of reading.

according to equations (4.19). As in previous cases the gravitational waves are then treated as a cosmological fluid defined at the background level by its density and pressure.

4.2.2 The equation of state

As shown previously, short-wavelength gravitational waves have an equation of state of $1/3$. Here it is verified that this is the case for single fluid backgrounds, in the absence of anisotropic stress, using the above approach. The equation of state for long-wavelength gravitational waves is also calculated from analytic expressions for the gravitational wave amplitude $D(k, \tau)$.

While it is the integrated quantities, $\rho_{\text{gw}}, p_{\text{gw}}$ that give the equation of state of gravitational waves, w_{gw} , it is clear from equations (4.19) that if $\tilde{w}_{\text{gw}} = \tilde{p}_{\text{gw}}/\tilde{\rho}_{\text{gw}}$ is a constant then w_{gw} will be equal to the same constant. The equation of state can be calculated analytically for single fluid backgrounds consisting of radiation, matter or a cosmological constant [203]¹⁰. For convenience I have defined $x = k\tau$ for this discussion of the equation of state for single fluid backgrounds and an initial condition $D(0) = B$ is used to eliminate decaying modes. B is conventionally set to 1 to calculate the gravitational wave transfer function.

Radiation:

For a radiation background, the equation of motion is,

$$\dot{D} + \frac{2}{\tau}\dot{D} + k^2 D = 0, \quad (4.21)$$

with solution, $D(x) = B \text{sinc } x$, where $\mathcal{H} = 1/\tau$ and the equation of state of the background is $1/3$. Therefore,

$$\tilde{\rho}_{\text{gw}} = \frac{B^2}{4x^2\tau^2} (-7 + 2x^2 + 7 \cos 2x + 6x \sin 2x), \quad (4.22)$$

¹⁰The solutions of the equation of motion and the verification of the equation of state for long wavelengths are presented in [203], however the explicit verification for short wavelengths or the expressions for the density and pressure have not previously been presented in the literature.

$$\tilde{p}_{\text{gw}} = \frac{B^2}{12x^2\tau^2} [3(7 - 4x^2) \cos 2x + 26x \sin 2x + 2x^2 - 21]. \quad (4.23)$$

Matter:

For a matter background, the equation of motion is,

$$\dot{D} + \frac{4}{\tau} \dot{D} + k^2 D = 0, \quad (4.24)$$

with solution, $D(x) = 3B(\text{sinc } x - \cos x)/x^2$, $\dot{a}/a = 2/\tau$ and the equation of state of the background is 0. Hence,

$$\begin{aligned} \tilde{\rho}_{\text{gw}} = \frac{9B^2}{4x^6\tau^2} [& -39 - 28x^2 + 2x^4 \\ & + (39 - 50x^2) \cos 2x + 6x(13 - 2x^2) \sin 2x], \end{aligned} \quad (4.25)$$

$$\begin{aligned} \tilde{p}_{\text{gw}} = \frac{3B^2}{4x^6\tau^2} [& -117 - 56x^2 + 2x^4 \\ & + x(234 - 68x^2) \sin 2x + (117 - 178x^2 + 12x^4) \cos 2x]. \end{aligned} \quad (4.26)$$

Cosmological Constant:

Finally, for a cosmological constant (sometimes called de Sitter) background the equation of motion is,

$$\dot{D} - \frac{2}{\tau} \dot{D} + k^2 D = 0, \quad (4.27)$$

with solution,

$$D(x) = Bx \left(\sin x + \frac{\cos x}{x} \right) + Cx(\text{sinc } x - \cos x), \quad (4.28)$$

$\dot{a}/a = -1/\tau$ and the equation of state of the background is -1 . Note that B corresponds to an even term while C represents the odd part of $D(x)$. In cases of cosmological interest $D(x=0)$ is set to 1 and consequently $C=0$. However, the conclusions below about the equation of state are true with or without the odd terms.

The density and pressure are,

$$\begin{aligned} \tilde{\rho}_{\text{gw}} = \frac{k^2}{32\pi G} \left\{ (B^2 + C^2)(-7 + 2x^2) \right. \\ \left. + (-7B^2 + 7C^2 + 12BCx) \cos 2x \right. \\ \left. - 2[7BC + 3(B - C)(B + C)x] \sin 2x \right\}, \end{aligned} \quad (4.29)$$

$$\begin{aligned} \tilde{p}_{\text{gw}} = \frac{\tau^{-2}}{96\pi G} \left\{ x^2(B^2 + C^2)(7 + 2x^2) \right. \\ \left. - x^2[(7 - 12x^2)(B^2 - C^2) - 28BCx] \cos 2x \right. \\ \left. - 2x^2[(7 - 12x^2)BC + 7x(B^2 - C^2)] \sin 2x \right\}. \end{aligned} \quad (4.30)$$

Corresponding Equations of State:

For the above backgrounds the equation of state parameter $\tilde{w}_{\text{gw}}(x)$ is calculated in the super-Hubble, long-wavelength, regime ($x \ll 1$) by expanding in x and evaluating the lowest order terms and in the sub-Hubble, short-wavelength regime ($x \gg 1$) by averaging over many wavelengths, equivalent to averaging trigonometric functions, e.g., $\langle \sin 2x \rangle_x = \langle \cos 2x \rangle_x = 0$. Doing this,

$$\tilde{w}_{\text{gw}} = \begin{cases} -\frac{1}{3}, & \text{if } k\tau \ll 1, \\ +\frac{1}{3}, & \text{if } k\tau \gg 1, \end{cases} \quad (4.31)$$

for radiation, matter and de Sitter backgrounds. Therefore, the energy density of long-wavelength gravitational waves decays as $1/a^2$, like curvature, and short-wavelength gravitational waves behave like massless neutrinos, as concluded in the shortwave approximation.

The equation of state for a general Λ CDM background can be solved numerically, and is shown in figure 4.3 for *Planck* 2018 parameter values and $k = 0.05 \text{ Mpc}^{-1}$. It starts at $-1/3$ when the mode is outside the horizon, then goes through a transition period where it goes through large negative and positive values before exhibiting stable oscillations about an average value of $w_{\text{gw}} = 1/3$.

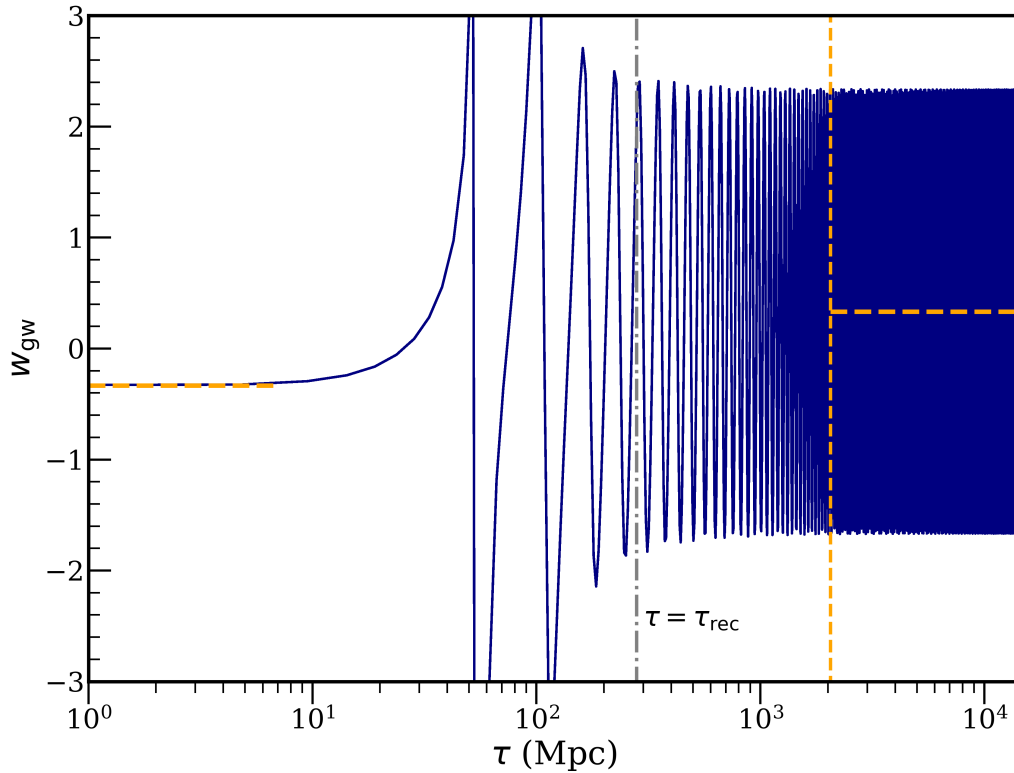


Figure 4.3: The equation of state of gravitational waves, w_{gw} , as a function of conformal time for a representative mode with $k = 0.05 \text{ Mpc}^{-1}$. It is $-1/3$ when the mode is outside the horizon, goes through a transition region and then oscillates about $1/3$ when well inside the horizon. The conformal time at recombination (grey dot-dash) is shown for reference. The small and large scale values of $-1/3$ and $1/3$ are shown in orange (dashed) and the vertical orange (dashed) line shows where the shortwave approximation becomes valid (see section 4.2.4).

Matter-Cosmological Constant Transition

We observed through numerical calculations that the equation of state of super-horizon gravitational waves decreases during the matter-cosmological constant transition in the late Universe. This phenomenon has not been mentioned previously and is an interesting departure from the behaviour shown above for single fluid backgrounds. This behaviour can be verified analytically using solutions for early, intermediate and late times that are matched together at the appropriate times. The details of these solutions are presented below.

In a matter and cosmological constant background the scale factor,

$$a(t) = \left(\frac{\Omega_m}{\Omega_\Lambda} \right)^{1/3} \left[\sinh \left(\frac{3}{2} H_0 \sqrt{\Omega_\Lambda} t \right) \right]^{2/3}. \quad (4.32)$$

So the gravitational wave equation of motion in terms of cosmological time (compare to equation (4.18)),

$$\frac{d^2 D}{dt^2}(k, t) + 3H(t) \frac{dD}{dt}(k, t) + \frac{k^2}{a^2(t)} D(k, t) = 0, \quad (4.33)$$

becomes,

$$D''(\kappa, x) + 2 \coth x D'(\kappa, x) + \kappa^2 (\sinh x)^{-4/3} D(\kappa, x) = 0, \quad (4.34)$$

where,

$$x = \frac{3}{2} H_0 \sqrt{\Omega_\Lambda} t, \quad \kappa = \left(\frac{\Omega_\Lambda}{\Omega_m} \right)^{1/3} \frac{2k}{3H_0 \sqrt{\Omega_\Lambda}}, \quad (4.35)$$

and primes denote differentiation with respect to x . κ and x are reduced wavenumber and time variables respectively and x is not equivalent to the definition in the previous section.

The equation of motion is solved in a power series for κ^2 ;

$$D(\kappa, x) = D_0(x) + \kappa^2 D_1(x), \quad (4.36)$$

because the modes of importance are super-horizon at current (and near future) times such that $\kappa \ll 1$.

Background solution:

D_0 is the solution of the simpler, zeroth order equation in the κ^2 expansion,

$$D_0''(x) + 2 \coth x D_0'(x) = 0. \quad (4.37)$$

The general solution is $D_0(x) = \bar{D}_0 - \alpha \coth x$. Imposing that the gravitational wave amplitude is finite as $x \rightarrow 0$,

$$D_0(x) = \bar{D}_0. \quad (4.38)$$

This constant would be set to 1 for most physical applications.

Perturbed solutions:

The equation of motion to order κ^2 is,

$$D_1''(x) + 2 \coth x D_1'(x) + (\sinh x)^{-4/3} \bar{D}_0 = 0. \quad (4.39)$$

This can be solved in three separate regimes, low- x , intermediate- x and high- x and these solutions and their first derivatives can be matched together at x_a and x_b .

For small- x the equation of motion is,

$$D_1''(x) + \frac{2}{x} D_1'(x) + \frac{\bar{D}_0}{x^{4/3}} = 0, \quad (4.40)$$

with solution,

$$D_1(x) = -\frac{9}{10} \bar{D}_0 x^{2/3}, \quad (4.41)$$

where the initial condition is $D_1(0) = 0$.

The intermediate solution is the most complicated and consequently new variables are defined to simplify the solution. Expanding about the midpoint of the intermediate region,

$$\lambda = \frac{x_a + x_b}{2}, \quad (4.42)$$

the intermediate solution is valid for more of the intermediate region than if either x_a or x_b was used. This results in the equation of motion becoming,

$$D_1''(x) + 2(\alpha + \beta x) D_1'(x) + \bar{D}_0(\gamma + \eta x) = 0, \quad (4.43)$$

where,

$$\begin{aligned} \alpha &= \coth \lambda - \lambda \beta, & \beta &= 1 - \coth^2 \lambda, \\ \gamma &= \frac{3 \sinh \lambda + 4 \lambda \cosh \lambda}{3(\sinh \lambda)^{7/3}}, & \eta &= -\frac{4 \cosh \lambda}{3(\sinh \lambda)^{7/3}}. \end{aligned} \quad (4.44)$$

Making the further definition,

$$\bar{x} = \frac{\alpha + \beta x}{\sqrt{\beta}}, \quad (4.45)$$

to simplify the solution, the intermediate solution for $D_1(x)$ is,

$$D_1(x) = \bar{D}_0 \left\{ C_1 + \frac{C_2 \sqrt{\pi} e^{\alpha^2/\beta} \operatorname{erf} \bar{x} - \sqrt{\beta} \eta x}{2\beta^{3/2}} \right. \\ \left. + \frac{(\beta\gamma - \alpha\eta)}{4\beta^3} \left[2\beta \bar{x}^2 {}_1F_2(\{1, 1\}; \{3/2, 2\}; \bar{x}^2) - \pi\beta \operatorname{erf} \bar{x} \operatorname{erfi} \bar{x} \right] \right\} \quad (4.46)$$

where $\operatorname{erf} x$ is the error function, $\operatorname{erfi} x$ is the imaginary error function, ${}_pF_q$ is the generalised hypergeometric function and the matching onto the low- x solution at x_a determines the coefficients C_1 and C_2 .

For large x the equation of motion becomes,

$$D_1''(x) + 2D_1'(x) + 2^{4/3} \bar{D}_0 e^{-4x/3} = 0. \quad (4.47)$$

The high- x solution is,

$$D_1(x) = C_3 - \frac{C_4}{2} e^{-2x} + \frac{9\bar{D}_0}{2^{5/3}} e^{-4x/3}. \quad (4.48)$$

C_3 and C_4 are determined by matching onto the intermediate solution at x_b .

GW equation of state parameter:

The gravitational wave equation of state parameter for a matter + cosmological constant background from the above analytics and from a numerical computation can be seen in figure 4.4. The analytic solutions were matched at $x_a = 0.35$ and $x_b = 1.15$ to get the best agreement with the numerics. They confirm the fact that the equation of state departs from $-1/3$ for super-horizon GWs during the matter-cosmological constant transition but returns back to $-1/3$ when the cosmological constant comes to dominate. There are discontinuities due to imperfect matching of the solutions. Effectively the solutions are not of high enough order to fully encompass the behaviour in their specific regimes. This could be improved by using the intermediate solution twice and having four separate matched regimes but the analysis given here is sufficient to verify the numerical behaviour.

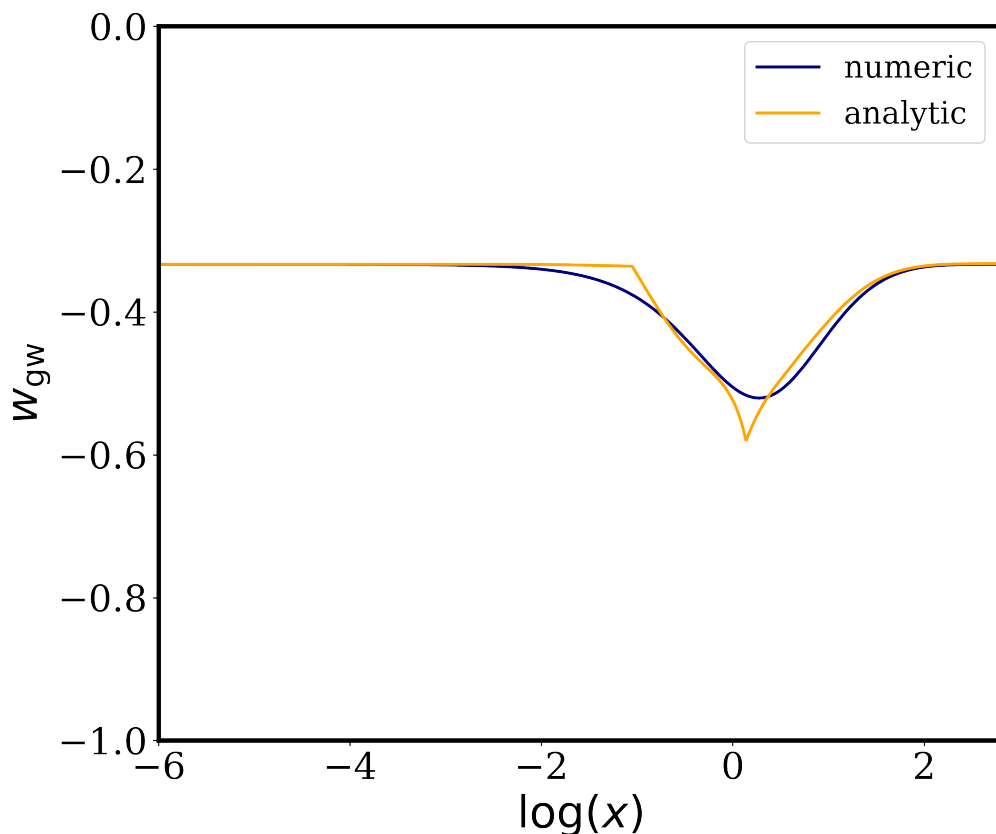


Figure 4.4: The equation of state for gravitational waves as a function of x for $\kappa = 0.045$ (corresponding to $k = 10^{-5} \text{Mpc}^{-1}$) from a numerical solution of the gravitational wave equation of motion (blue) and from an analytic solution found by matching solutions for small, intermediate and large x (orange). The analytic solutions are matched together at $x_a = 0.35$ and $x_b = 1.15$ and verify the behaviour observed in the numerical solution.

4.2.3 Code

For realistic backgrounds the gravitational wave equation of motion can only be solved numerically. New code was written to do this and then calculate the gravitational wave density, pressure and equation of state. This was integrated into CAMB¹¹ to allow for calculation of cosmological observables, primarily the CMB power spectrum, in the presence of gravitational waves. To do this the gravitational waves were incorporated into an effective dark energy fluid that also included the cosmological constant. This dark energy fluid has an equation of state corresponding to that of gravitational waves for most of the cosmological history until cosmological constant domination occurs at late time

¹¹see section 1.5.1.

and the effective dark energy equation of state approaches -1 . The density is negative at early times when dominated by super-horizon gravitational waves (as detailed in section 2.4 here and section 4 of ref. [203]) before transitioning to an epoch dominated by sub-horizon gravitational waves and then by the cosmological constant (dependent on the choice of k_{\min} and k_{\max}).

This modified version of CAMB can be used to test a range of physical properties of the model. It can also be integrated into a parameter estimation code to obtain constraints on the gravitational wave parameters. Here COBAYA is used¹².

4.2.4 Validity of the shortwave approximation for CMB constraints

As this approach allows observables to be calculated when gravitational waves of super-horizon scales are included it can be used to calculate where the shortwave approximation becomes valid. It is usually stated that the shortwave approximation is valid if the gravitational wave can be averaged over a “sufficient number of wavelengths” or in the language of section 2.3, if $\lambda \ll l \ll \mathcal{R}$ where l is the averaging length scale. This has resulted in the lower limit for the CMB shortwave constraint being imprecisely defined.

Using the approach developed in the previous sections the region for which fixing a constant equation of state, $w_{\text{gw}} = 1/3$ introduces small enough errors into cosmological observables can be found. A cosmic variance limited CMB experiment like *Planck*, measuring the CMB power spectrum up to a given ℓ requires a precision of approximately [298],

$$\frac{\delta C_\ell}{C_\ell} = \frac{3}{\ell}, \quad (4.49)$$

which corresponds to 0.1–0.2% for $\ell = 2000$.

The error in the CMB power spectrum was found when the gravitational wave equation of state was fixed to $1/3$ after different numbers of oscillations

¹²see section 1.5.2.

to find the number of oscillations required to achieve the necessary precision. This was done for different numbers of oscillations between 5 and 100 and then compared to the case with 100 oscillations¹³. The gravitational wave source is assumed to be delta-function-like for a given frequency. Note that the effect of the shortwave assumption decreases for smaller values of $\Omega_{\text{gw}}h^2$. For this test the density is fixed to the equivalent of one neutrino degree of freedom in the shortwave approximation and hence $\Omega_{\text{gw}}h^2 = 5.6 \times 10^{-6}$. Hence the gravitational wave source has approximately the largest allowed effect on the background evolution at matter–radiation equality.

To satisfy $\delta C_\ell/C_\ell < 0.2\%$ for all ℓ , approximately 50 oscillations are required by the epoch of equality. This corresponds to a lower limit of $k \simeq 1 \text{ Mpc}^{-1}$ for the shortwave constraint as shown in figures 3.2 and 4.2. Note that, from figure 2 of Smith, Pierpaoli, and Kamionkowski [96], previous constraints use a factor of ~ 20 wavelengths. This analysis suggests that a slightly more conservative limit is required.

Figure 4.3 shows the oscillatory behaviour and also denotes the point at which this k -mode ($k = 0.05 \text{ Mpc}^{-1}$) satisfies the shortwave approximation as defined above. This is shown as a vertical, dashed, orange line. The conformal time of recombination is also represented with a grey vertical line and this shows that this k -mode does not have a sufficiently short wavelength to contribute to the constraint despite the fact that it comes inside the horizon before recombination. This is as one would expect as this k -value is less than the 1 Mpc^{-1} shortwave limit.

4.2.5 Behaviour of density and pressure

The gravitational wave density and equation of state exhibit a range of interesting physical behaviours. Figure 4.5 shows these for standard Λ CDM parameter values as a function of k and t in the absence of neutrino anisotropic stress. A smoothing has been applied to w_{gw} to more clearly show the behaviour

¹³My integration code was modified by Dr. Adam Moss to do this analysis.

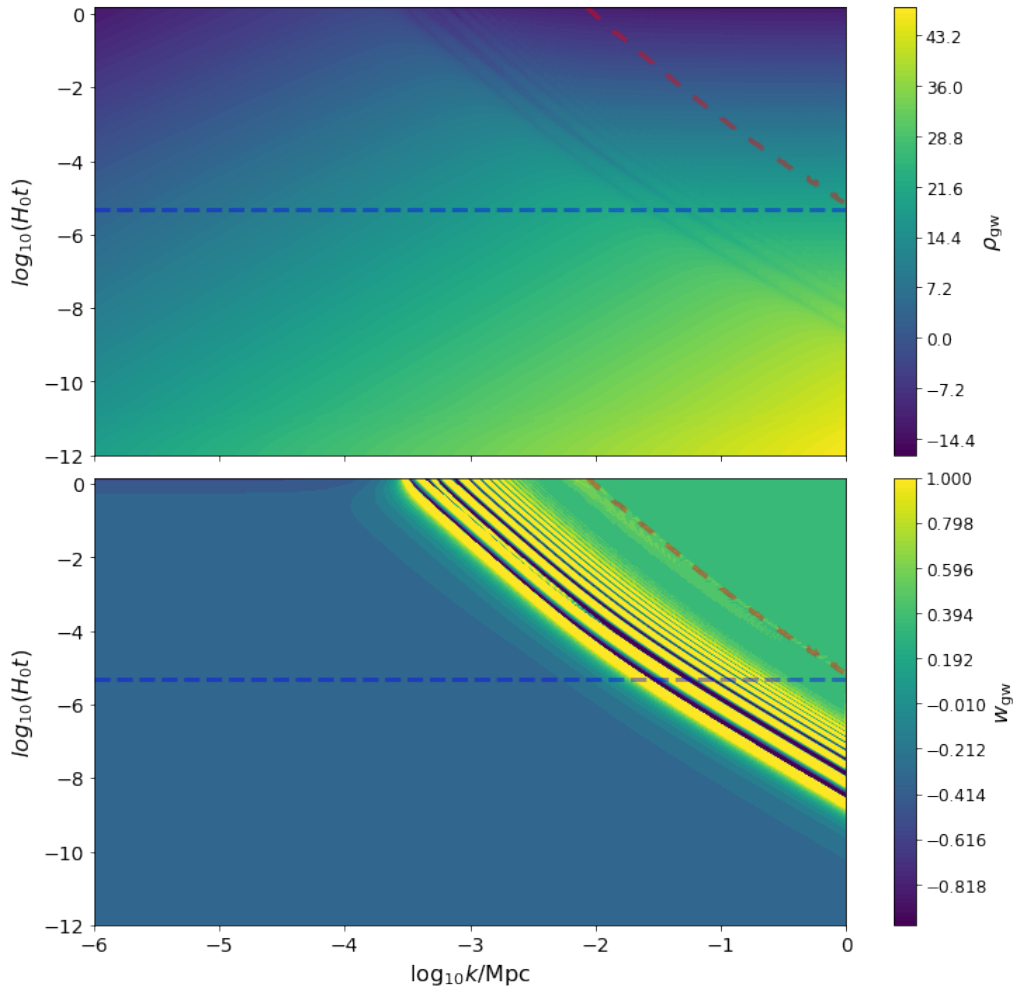


Figure 4.5: Contour plots of the gravitational wave density, ρ_{gw} and equation of state, w_{gw} as functions of wavenumber and cosmological time for standard Λ CDM parameter values without neutrino anisotropic stress. The transition between $w_{\text{gw}} = -1/3$ and $w_{\text{gw}} = 1/3$ can be seen clearly. The plot of the equation of state also shows an interesting feature in which super-horizon gravitational waves have an equation of state which goes below $-1/3$ during the matter to cosmological constant transition. The (red) long-dashed contour shows when each mode has undergone 50 oscillations, and the (blue) short-dashed contour the epoch of matter–radiation equality.

when the gravitational wave amplitude is highly oscillatory. The super-horizon and sub-horizon regimes can be seen clearly, along with the transition region between the two. The epoch of matter–radiation equality is shown as a blue dashed line. The shortwave approximation is valid for the region above the red, long-dashed line. The pressure is not shown as it is simply related to the density and equation of state.

When super-horizon the gravitational wave equation of state is $-1/3$ as verified above, apart from at late times, during the matter to cosmological

constant transition, when it goes below $-1/3$ as discussed in section 4.2.2. This is just starting to happen to super-Horizon modes in our Universe, which can be seen by closely inspecting the top-left of the lower panel of figure 4.5.

The integrated density of equation (4.19) and the subsequent equation of state are shown in figure 4.6, for a representative primordial gravitational wave source with $n_t = 3$, $k_{\min} = 0.1 \text{ Mpc}^{-1}$ and $k_{\max} = 1 \text{ Mpc}^{-1}$. The lower cutoff is chosen to be compatible with the low-frequency constraint, and the spectral index must be relatively steep, $n_t \gtrsim 3$, to also satisfy this constraint. The high-frequency cutoff is chosen as the shortwave approximation can be used for frequencies above this. The sub- and super- Hubble regimes are clear in both cases and the transition region between the two can also be seen. The equation of state changes from $-1/3$ to $1/3$ as shown for the un-integrated density and pressure. Note that the integration over k acts to smooth the oscillations in the equation of state to $1/3$ when sub-horizon.

The energy density is *negative* for super-Hubble modes (denoted by a dashed line in the top panel of figure 4.6), as stated in section 4 of [203] and section 2.4 here. Reiterating, since $w_{\text{gw}} = -1/3$ the negative density can be interpreted as additional positive curvature. This contribution can lead to a reduction in the expansion rate, depending on the integration limits and primordial spectrum in equation (4.19).

4.2.6 Neutrino anisotropic stress

So far anisotropic stress has been neglected in the equation of motion for gravitational waves given in equation (2.10). Weinberg [195] showed that anisotropic stress from free-streaming neutrinos has a non-negligible affect on the gravitational wave evolution¹⁴. The neutrino anisotropic stress, $\Pi_{\nu}^{(T)}$ is a functional of the time derivative of the gravitational wave amplitude so the gravitational wave equation of motion becomes an integro-differential equation for the gravitational wave amplitude (see [28] for details). The effect of this

¹⁴Damping of GWs by photons has been shown to be small but can in principle be detectable via CMB spectral distortions [299].

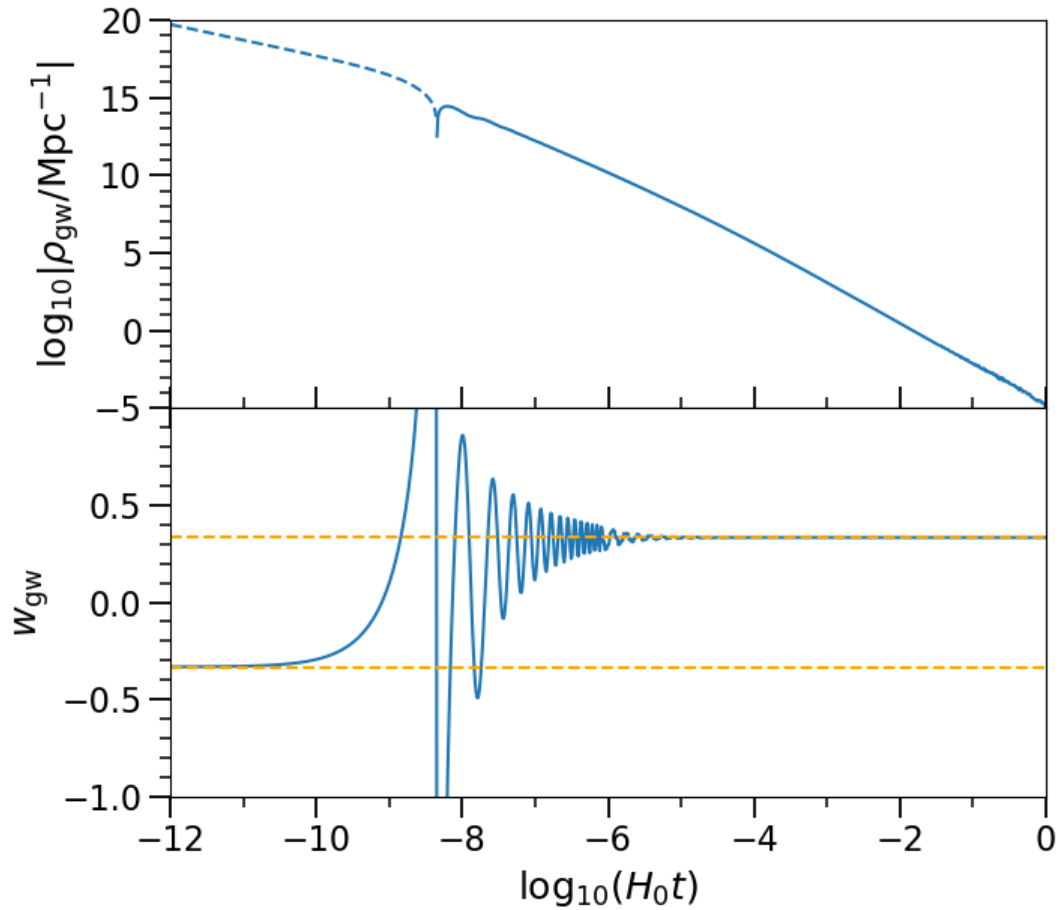


Figure 4.6: The gravitational wave density and equation of state as a function of cosmological time after k -integration for a representative primordial gravitational wave source with $n_t = 3$, $k_{\min} = 0.1 \text{ Mpc}^{-1}$ and $k_{\max} = 1 \text{ Mpc}^{-1}$. The density has two regimes, one where it goes as a^{-2} with a negative density (dashed) and one where it goes as a^{-4} with a positive density (solid), with a transition in between. The transition region has a positive density and consequently is also shown as a solid line but the scale factor dependence is more complicated than $\propto a^{-4}$ here. These regimes can be seen more clearly in the equation of state. There is some numerical noise as the equation of state approaches $1/3$ but this has no observable consequences.

is to increase the damping term in the equation of motion and reduce the gravitational wave amplitude. This will change the analysis detailed above as, for example, the gravitational wave density and pressure are quadratic in the gravitational wave amplitude or its time derivative.

The numerical solutions for the gravitational wave amplitude and its conformal time derivative are shown in figure 4.7 for a Λ CDM background. The oscillations in the amplitude are in phase which shows that the wavelength evolution of gravitational waves is unaffected by anisotropic stress. The change in the amplitude confirms the statement above that including neutrino anisotropic

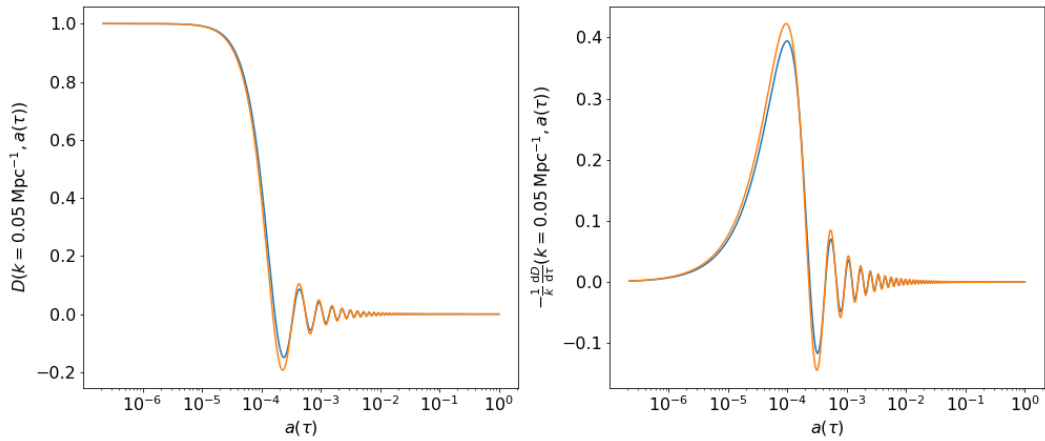


Figure 4.7: The gravitational wave amplitude and its conformal time derivative as a function of the scale factor when there is no anisotropic stress (orange) and when neutrino anisotropic stress is included (blue) for $k = 0.05 \text{ Mpc}^{-1}$ (as in figure 4.3). Including neutrino anisotropic stress acts as a damping to the gravitational wave amplitude and its time derivative when the gravitational wave comes inside the horizon.

stress acts as an increased damping. This effect is most prominent just after each k -mode comes inside the horizon. Consequently, this is expected to alter the behaviour of the gravitational wave density and pressure for the intermediate constraint but result in the shortwave approximation constraints still being valid¹⁵. This is expected from the analysis of [195], where the sub-horizon amplitude is multiplied by a constant factor when including neutrino anisotropic stress and is confirmed in figure 4.8, where the equation of state in the shortwave regime is still $1/3$ as the density and pressure both decrease by the same factor.

The contour plots of the gravitational wave density and equation of state in figure 4.8 gives the ratios of these quantities in the presence and absence of anisotropic stress and shows other interesting effects. It is helpful to consider figure 4.5 when comparing the absolute values of these quantities instead of their ratios. The equation of state of super-horizon gravitational waves before matter–radiation equality is ≈ -0.52 and therefore considerably more negative than its value of $-1/3$ without anisotropic stress. This is due to the change in

¹⁵This is neglecting the changes in the degrees of freedom in the early Universe which change the behaviour of the neutrino sector, see [212] for details of this which are valid in the shortwave approximation.

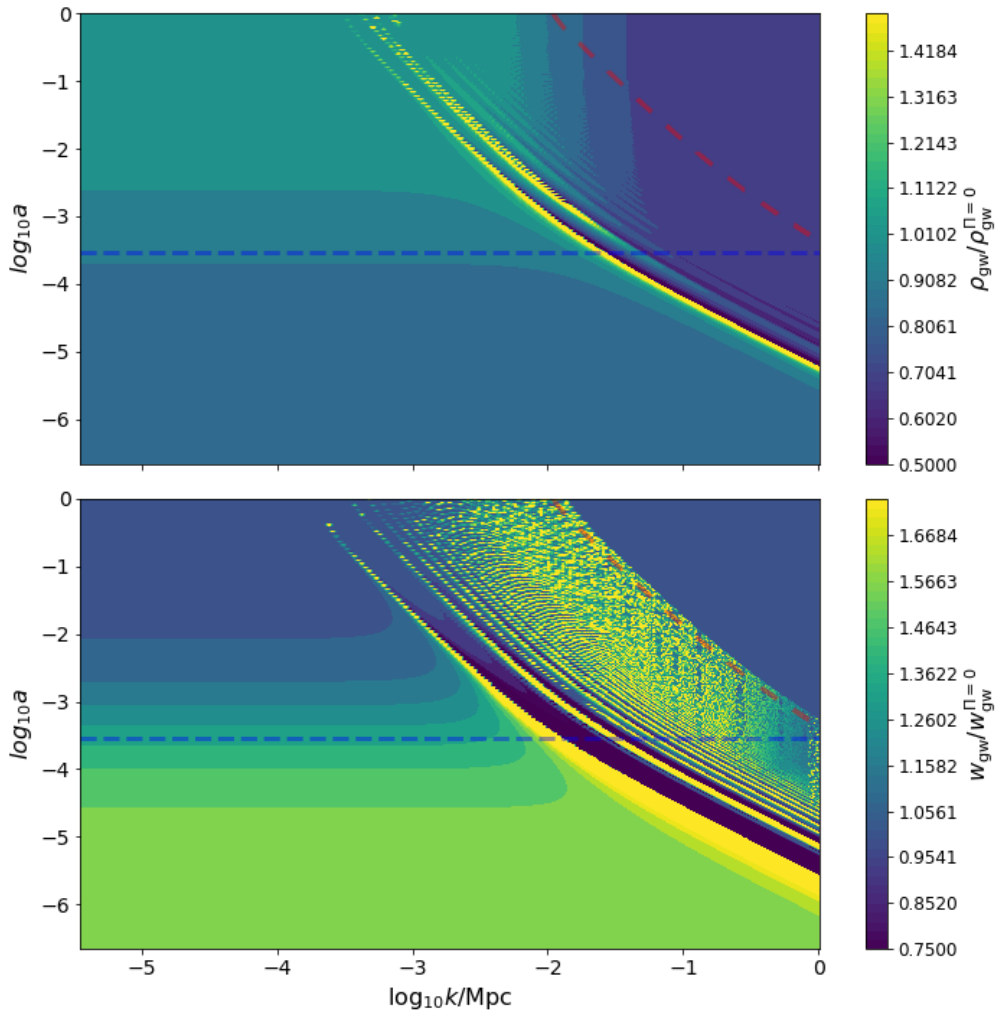


Figure 4.8: Top panel: The ratio of the gravitational wave densities with and without neutrino anisotropic stress. Bottom panel: The ratio of the gravitational wave equation of state with and without neutrino anisotropic stress. The density roughly halves in the shortwave region but this is compensated by an equivalent reduction in the pressure such that the equation of state is still $1/3$. The equation of state becomes more negative for super-horizon scales before neutrino free-streaming. The absolute values in the absence of anisotropic stress are shown in figure 4.5.

the initial condition for the time derivative of the gravitational wave amplitude when shear is included, which increases in magnitude by a factor of ≈ 1.1 . This change in \dot{D} changes the density and pressure via the third terms¹⁶ (which depend on $\dot{D}D$) in equations (4.20). The tensor initial conditions when including anisotropic stress are calculated in [300] and show,

$$\dot{D} = -\frac{5}{15 + 4R_\nu} k^2 \tau + \mathcal{O}(k^3 \tau^2), \quad (4.50)$$

¹⁶The first terms (dependent on $k^2 D^2$) are unchanged and the second terms (dependent on \dot{D}^2) do not contribute for super-horizon modes at early times.

$$\Pi_\nu^{(\text{T})} = \frac{4}{15 + 4R_\nu} k^2 \tau^2 + \mathcal{O}(k^3 \tau^3). \quad (4.51)$$

So the initial equation of state for super-horizon gravitational waves is,

$$w_{\text{gw,init}} = -\frac{1}{3} \left(\frac{25 + 28R_\nu}{25 - 4R_\nu} \right). \quad (4.52)$$

This gives $w_{\text{gw,init}} \approx -0.52$ for Λ CDM parameter values as seen in the numerical calculation. The equation of state increases around matter–radiation equality until the super-horizon gravitational waves have an equation of state of $\approx -1/3$ after redshift ~ 100 . The change in the equation of state for super-horizon modes during the matter–cosmological constant transition (see section 4.2.2) is unaffected by neutrino anisotropic stress.

The neutrino anisotropic stress $\rightarrow 0$ in the matter-dominated era which results in the density of k -modes being nearly unchanged by the inclusion of neutrino anisotropic stress. This can be seen above the blue-dashed line in the top panel of figure 4.8 and was noted in [212].

4.2.7 Gravitational wave perturbations

The components of a general energy–momentum tensor at linear order, T^μ_ν are given by equations¹⁷ 1.31 (see section 1.3.2),

$$T^0_0 = -\bar{\rho}(1 + \delta), \quad (1.31a)$$

$$T^0_i = \bar{\rho}(1 + w)v_i, \quad (1.31b)$$

$$T^i_j = \bar{\rho}w \left(1 + \frac{\delta P}{\bar{P}} \right) \delta^i_j + \Sigma^i_j. \quad (1.31c)$$

Previously the density and pressure of gravitational waves have been calculated via the backreaction of the perturbations at second order. The second order fluctuating part (see section 2.3 and specifically equation (2.14)) of the gravitational wave effective energy momentum tensor can be calculated by subtracting the spatial average and assuming the second order perturbation $j_{\mu\nu}$ does not

¹⁷Reproduced here for ease of reading.

contribute;

$$\Delta^\mu{}_\nu = T^{(\text{GW})\mu}{}_\nu - \langle T^{(\text{GW})\mu}{}_\nu \rangle_x. \quad (4.54)$$

Theoretically the gravitational wave perturbations can then be calculated using the perturbed Einstein tensor in equations (4.7) and using the fluctuating part of the effective energy momentum tensor, $\Delta^\mu{}_\nu$ as an effective first-order perturbation energy–momentum tensor. However, the numerical prescription required is more complicated than the background case as the components of the effective perturbation energy–momentum tensor cannot easily be written in terms of the initial spectrum of fluctuations. The development of a treatment of the gravitational wave perturbations using the effective energy–momentum tensor is a possible area of future research. Note that the difference in the perturbed Einstein tensor found here when compared to [203] (where perturbations are not considered) will result in a very different expression for the velocity perturbation.

To proceed, a phenomenological approach to the gravitational wave perturbations is adopted where gravitational waves are treated as an effective PPF fluid¹⁸ through the model developed in Fang, Hu, and Lewis [122]. The PPF framework is usually used in ‘smooth’ dark energy models, but has several properties useful to model gravitational wave perturbations. Firstly, it is able to cross the $w = -1$ divide, which occurs for gravitational wave oscillations after entering the horizon. Secondly, it is designed to conserve energy and momentum on large scales, where PGWs behave like positive curvature with $w_{\text{gw}} = -1/3$ in the absence of anisotropic stress. The gravitational wave density and pressure are constructed explicitly to conserve energy and momentum. Finally, on small scales the PPF fluid is designed to be smooth compared to cold dark matter, which one would expect for PGWs due to the pressure support with $w_{\text{gw}} = 1/3$. In the approach used here the default PPF parameters in CAMB are used.

¹⁸This model was introduced in section 1.4.5 when discussing the dark energy equation of state.

It is worth mentioning that in the shortwave approximation, PGWs are modelled as an effective neutrino species, with a hierarchy of moments describing the perturbations. In the second-order method no such hierarchy exists, and the fluid is described by its effective energy–momentum tensor. There is no theoretical reason to expect a hierarchy of moments. There are therefore two main observable differences expected for the treatment detailed here, when compared to the shortwave treatment, due to the background evolution and the treatment of perturbations. These are detailed in the next section.

4.2.8 Observables

The effects of short-wavelength gravitational waves on cosmological observables (see chapter 3) can be compared to the intermediate gravitational wave analysis of this section. Figure 4.9 shows the CMB power spectrum for $\Omega_{\text{gw}}h^2 = 5.6 \times 10^{-6}$, for gravitational waves obeying the shortwave approximation with adiabatic and homogeneous initial conditions. The intermediate gravitational waves are shown for the same density with representative parameters of $n_t = 3$ and $k_{\text{min}}, k_{\text{max}} = (0.1, 1) \text{ Mpc}^{-1}$ without neutrino anisotropic stress. The intermediate analysis changes the temperature anisotropies in similar ways to the adiabatic shortwave gravitational waves with a slightly smaller magnitude. The homogeneous shortwave gravitational waves have markedly different behaviour for low- ℓ .

The fractional changes in the Hubble rate, $H(z)$, and the scale of the sound horizon, r_s , are shown in figure 4.10. As expected, due to these quantities only depending on the background and not the perturbations, the adiabatic and homogeneous high-frequency gravitational waves have identical affects on these parameters. The intermediate gravitational waves increase the Hubble rate similarly to the SWA result when dominated by high-frequency, $w_{\text{gw}} = 1/3$ modes but decreases the Hubble rate at high redshift when dominated by $w_{\text{gw}} = -1/3$ modes. The same effect is seen in the scale of the sound horizon but with opposite sign and a small move to lower redshift.

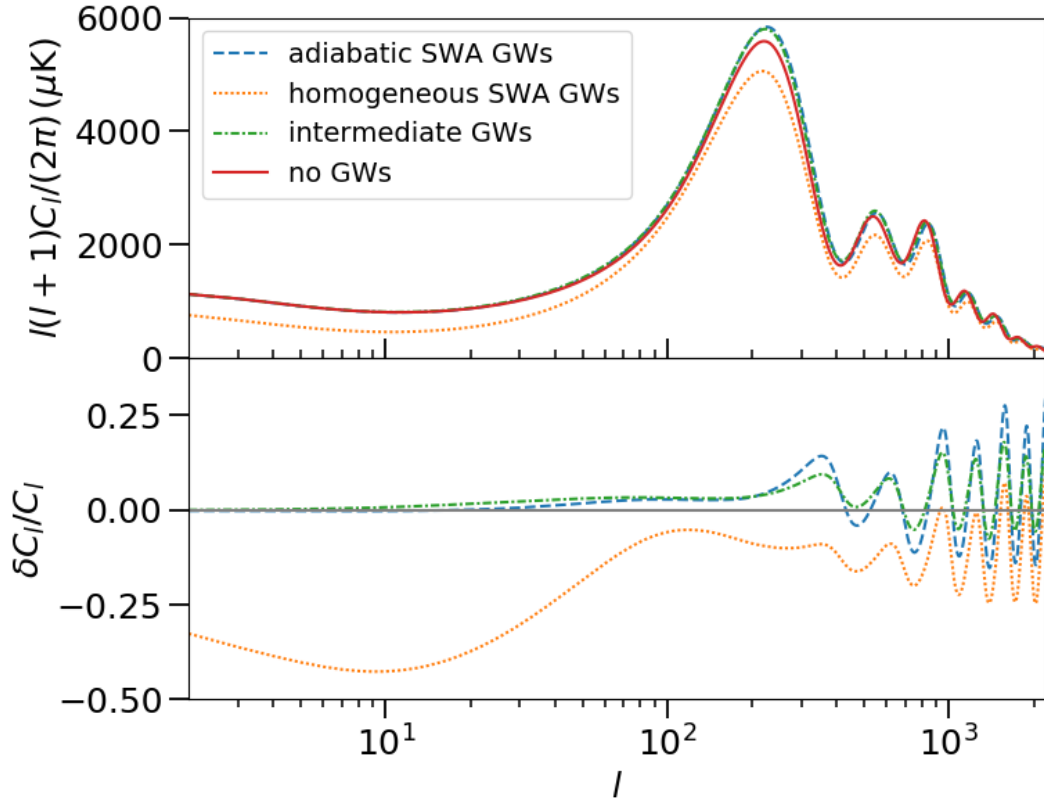


Figure 4.9: Top panel: The CMB temperature power spectrum for $\Omega_{\text{gw}}h^2 = 5.6 \times 10^{-6}$ with adiabatic shortwave approximation (SWA) initial conditions (blue dashed), homogeneous SWA initial conditions (orange dotted) (as detailed in chapter 3) and using the intermediate frequency method of this section (green dot-dash). Bottom panel: the fractional difference in the CMB power spectrum due to gravitational waves as described above when compared to the case where there are no PGWs.

The intermediate model shares some similarities with the axion model that can potentially alleviate the Hubble tension (see chapter 5) [301]. In particular, there is an early dark energy phase with $w_{\text{gw}} = -1/3$ before a radiation phase with $w_{\text{gw}} = 1/3$ and a density that only contributes a small fraction of the total density. Even though the energy density is negative when $w_{\text{gw}} = -1/3$, the sound horizon can still be reduced at the time of recombination. This motivated the work of chapter 5 which details a model-independent approach to alleviating the Hubble tension, which could be used in the future to compare the effectiveness of models such as the gravitational wave model presented here in reducing the Hubble tension.

This analysis assumes that the gravitational wave density is small enough that it can be calculated as a perturbation on a Λ CDM background. As a

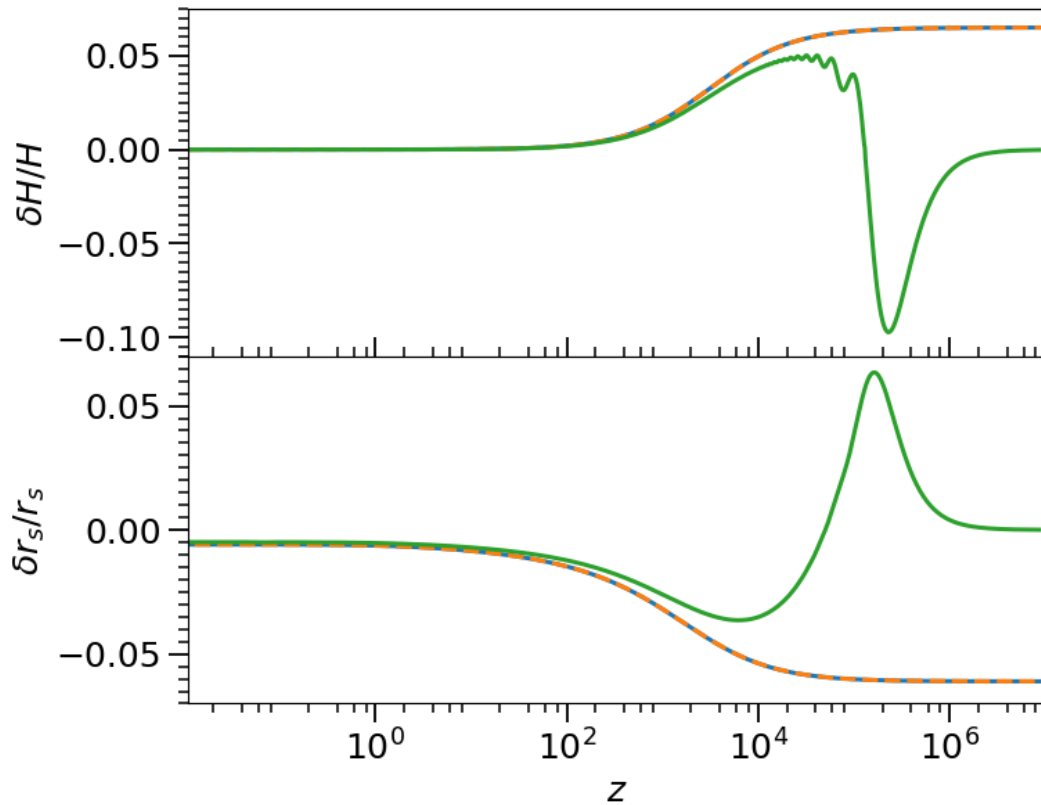


Figure 4.10: Top panel: The fractional change in the Hubble rate as a function of redshift. The shortwave approximation analysis of chapter 3 is used with adiabatic (blue) and homogeneous (orange dashed) initial conditions. The effects due to the intermediate frequency analysis of this section are shown in green. When the equation of state of the intermediate frequency analysis goes negative a reduction in the Hubble rate occurs in contrast to the increase at early times seen for the shortwave analysis. Bottom panel: The fractional change in the size of the comoving sound horizon with line styles as above.

consistency check, this was tested by iteratively recalculating the background including gravitational waves. Repeating this procedure until convergence shows an error of less than 0.01% in $H(z)$ over all z , for the maximum value of $\Omega_{\text{gw}} h^2$ allowed by data. It was concluded that this is a small enough error to use the approximation that gravitational wave backreaction can be calculated on a standard Λ CDM background.

Sources

The observable consequences of primordial gravitational waves depends on the source function considered. Two source functions are considered here. So far a steep primordial power spectrum with tilt, $n_t \geq 3$ has been used. This

is motivated by the existing constraints and is used for frequencies between $\sim 10^{-16}$ Hz and $\sim 10^{-15}$ Hz. The second sources that will be considered are delta-function sources for specific frequencies. These give constraints that are independent of any assumptions about the spectrum of gravitational waves. These sources therefore give the upper-limit dependent only on the data and can be used as a consistency check on the steep sources as well as functioning as an independent constraint.

4.2.9 Parameter constraints

To obtain limits on $\Omega_{\text{gw}}h^2$, the modified version of CAMB was integrated into COBAYA to perform an MCMC analysis. The *Planck* 2018 TT,TE,EE + lowE + lensing + BAO data set is used, as in chapter 3, with an otherwise standard Λ CDM model. For the parameters of the PGWs, $k_{\text{min}} = 0.1 \text{ Mpc}^{-1}$ is chosen as below this the low-frequency constraint dominates, and $k_{\text{max}} = 1 \text{ Mpc}^{-1}$ is chosen as above this the shortwave approximation can be used. The tensor spectral index, n_t is marginalised over in the prior range 3 to 5, where the lower limit is chosen to be compatible with the low-frequency constraint. The upper limit is chosen to allow for non-negligible variation in the tilt. It is important to note that no known sources of gravitational waves could give rise to such a steep index in this frequency range and consequently this is a toy model constraint representative of possible constraints allowed by this methodology, not a constraint on known models (see section 2.6 and ref. [194] for details of gravitational wave sources).

The 95% upper limit on the gravitational wave density parameter in the absence of neutrino anisotropic stress is,

$$\Omega_{\text{gw}}h^2 < 8.4 \times 10^{-7}. \quad (4.55)$$

When including neutrino anisotropic stress the constraint has almost the same magnitude,

$$\Omega_{\text{gw}}h^2 < 8.6 \times 10^{-7}. \quad (4.56)$$

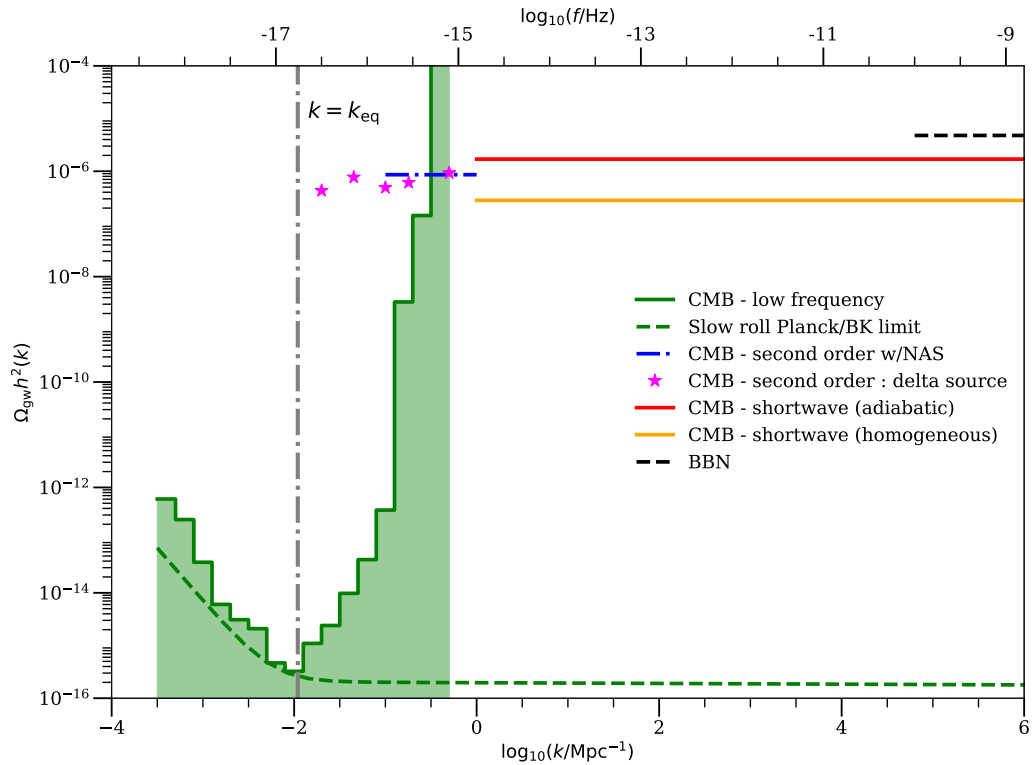


Figure 4.11: Constraints on the gravitational wave density parameter from the CMB along with the constraint from BBN (black dashed) for comparison [94]. The B -mode constraint from section 4.1 is shown in green along with the constraint from *Planck* and *BICEP2/Keck* on the tensor-to-scalar ratio (green dashed) [14]. The constraint using the intermediate approach of this section are shown for a steep source with neutrino anisotropic stress (NAS) and for delta-function sources, also with NAS (magenta stars). The steep source constraint is valid between $k = 0.1 \text{ Mpc}^{-1}$ and $k = 1 \text{ Mpc}^{-1}$. The shortwave approximation integrated constraints of chapter 3 are shown for adiabatic (red) and homogeneous (orange) initial conditions.

These are similar in magnitude to the shortwave adiabatic result and are tighter than the B -mode constraint for most of the region where the constraints overlap. These are integrated constraints and the constraint with neutrino anisotropic stress is shown as a horizontal line in figure 4.11 for the frequency range considered.

There are no strong interdependencies between the Λ CDM parameters and the gravitational wave density parameter with or without neutrino anisotropic stress. There is however a small preference for larger values of the CDM density and the Hubble constant when the gravitational wave density is non-zero.

Table 4.1: Constraints on the gravitational wave density for delta-function sources with wavenumber, k . The corresponding value of the frequency, f is also shown. The constraint weakens slightly for lower frequencies but is of a similar magnitude to the adiabatic shortwave constraint for all k considered.

$k / (\text{Mpc}^{-1})$	0.02	0.045	0.1	0.18	0.5
$10^{17} \times f / \text{Hz}$	3.1	7.0	16	28	78
$10^7 \times \Omega_{\text{gw}} h^2$ (95% upper limit)	4.3	7.7	4.9	6.1	9.3

Delta-function sources

The values of the constraint on the gravitational wave density parameter for different wavenumbers in the range $(0.02 - 0.5) \text{ Mpc}^{-1}$ (or in terms of frequency, $\sim (3 - 80) \times 10^{-17} \text{ Hz}$), when using delta-function sources and including anisotropic stress, are shown in table 4.1. They are also plotted in figure 4.11 as stars. The constraint is extended to lower frequencies than the constraint for a steep source and tightens slightly as the frequency decreases but is of nearly the same magnitude for the region of overlap.

As for the steep source, there are minimal interdependencies of the ΛCDM parameters with the gravitational wave density parameter when considering delta-function sources. For the larger k -values ($k = 0.18 \text{ Mpc}^{-1}$ and $k = 0.5 \text{ Mpc}^{-1}$) there is a small favouring of an increase in $\Omega_c h^2$ for non-zero $\Omega_{\text{gw}} h^2$. For the smallest k considered, $k = 0.02 \text{ Mpc}^{-1}$, there is a small preference for lower values of $\Omega_b h^2$ and H_0 as the gravitational wave density is increased.

4.3 Summary and outlook

In this chapter constraints on low-frequency PGWs from the CMB have been presented. This includes updated constraints from B -mode polarisation at the lowest frequencies and a new intermediate constraint that bridges the region of applicability of the two. These constraints are compatible with each other as well as with the result using the shortwave approximation (see chapter 3) and provide the tightest current constraints in their particular frequency ranges.

Existing B -mode analyses use a short wavelength approximation to convert constraints on the tensor-to-scalar ratio to constraints on the gravitational wave density parameter despite this depending on super-horizon gravitational waves. This was discussed and it was emphasised that using this conversion is only a first approximation to the gravitational wave density. This conversion is used as a first approximation and also for consistency with existing constraints and in this case the direct constraint on the tensor power spectrum becomes a constraint on the gravitational wave density. The constraint from low- ℓ polarisation shows that peak sensitivity occurs for scales close to the horizon size at recombination, corresponding to $f \sim 10^{-17}$ Hz, with a gravitational wave density $\Omega_{\text{gw}}h^2 \sim 10^{-16}$. These limits become much weaker for $f \gtrsim 10^{-16}$ Hz, and at $f \sim 3 \times 10^{-16}$ Hz a stronger result comes from the second-order backreaction of gravitational waves. This approach allows a limit of $\Omega_{\text{gw}}h^2 < 8.4 \times 10^{-7}$ (at 95% confidence) to be placed for a steep source and also allows limits to be obtained for delta-function sources, in a previously unconstrained frequency region of 10^{-15} Hz $\gtrsim f \gtrsim 3 \times 10^{-16}$ Hz. The effects of including neutrino anisotropic stress can be investigated and the constraint is shown to be almost unchanged. This approach can also be used to find the region of validity of the shortwave approximation used for higher frequency gravitational waves.

These constraints will be tightened by future ground and space based CMB observations from CMB-S4 and from polarisation via LiteBIRD, CORE and PIXIE among others (see section 1.5.3) [175–178]. These will result in an order of magnitude improvement in the measurement of extra relativistic degrees of freedom and an even greater improvement in the tensor-to-scalar ratio. Combining these with other cosmological observables promises to further illuminate the early Universe.

There are several possibilities for future work. Due to the numerical challenges of calculating the fluctuations due to the second-order backreaction, in this analysis we have treated them as an effective PPF fluid. In future work

this could be done via an effective perturbation energy–momentum tensor and the line-of-sight CMB formalism. It is worth noting though that, even in the shortwave limit, differences are expected compared to modelling gravitational waves as an effective neutrino species with a hierarchy of moments.

Chapter 5

Alleviating the H_0 Problem

As seen in the previous chapter, gravitational waves change the background expansion in a similar way to existing *early dark energy* (EDE) models that aim to alleviate the H_0 problem and as a result we investigate what properties of EDE are required to reduce the Hubble tension. The observational details of the H_0 problem were presented in section 1.4.6. The reader is referred there for details. This section will contain details of some of the theoretical models aiming to reduce the Hubble tension and will also present work done to develop a model-independent approach (MIA) that shows what kind of modifications to the background evolution provide the best fit to observations.

5.1 Theoretical models for the Hubble tension

There are two basic approaches to explaining the Hubble tension. Either there are systematic errors in the observations which bias the measurement of H_0 , or new physics, not included in Λ CDM, is changing the value of H_0 measured using different observational probes. The focus here is on the latter of these explanations but it is still possible that systematics are the cause and the Hubble tension will go away with future observations [126, 302, 303].

One of the most popular models that reduces the Hubble tension involves the addition of an oscillating scalar field (called the *axion model* here¹), which is presented in Poulin et al. [301, 304, 305]. Aghanim et al. [1] claim that the

¹This model is more general than the axion model often considered as a dark matter candidate.

Hubble tension cannot be resolved by modifying dark energy in the late Universe but models of EDE that change the expansion at or before recombination have the possibility of changing the scale of the sound horizon, and consequently the CMB determination of H_0 , without negatively impacting the fit to other parameters or observables (such as BAO). In the axion model the early dark energy component acts as a cosmological constant, but with negligible contribution to the overall energy density of the universe at early times, before reaching a critical era around matter–radiation equality, when it becomes of order 10% of the background density. After this the EDE component quickly drops away with an equation of state which, around this time, transforms from -1 to a positive value large enough that it decays faster than the dominant background fluid. It is commonly assumed to decay at least as quickly as radiation and hence have an equation of state $\geq 1/3$. The parameters of the model can be picked so that this happens before recombination, the effects only occur for a small range of redshifts and so that the new field never dominates the total energy density.

One of the key properties of this model is the choice of scalar field potential,

$$V(\phi) \propto \left(1 - \cos \frac{\phi}{f}\right)^n, \quad (5.1)$$

where ϕ is the field value, f is the decay constant and n is a (not-necessarily integer) constant. The choice, $n = 1$ corresponds to the standard axion potential whilst other choices of n constitute a generalisation of this [305]. As stated above, the equation of state is -1 before the critical redshift and after oscillates about an average value such that it behaves like a fluid with an equation of state,

$$w_n = \frac{n - 1}{n + 1}. \quad (5.2)$$

For $n = 2$ the fluid evolves with the same time dependence as massless neutrinos or radiation. The cosmological effects were originally calculated using the above fluid approximation when the Hubble parameter fell below a critical value,

chosen to be close to the value during the transition regime [301]. More recently a method solving the axion equation of motion throughout the evolution was developed² [305].

The axion model is implemented in `CAMB` (see section 1.5.1) using the fluid approximation throughout the evolution. This is explained explicitly in section 5.2.

The highest value of the Hubble constant obtained for the axion model is³, $H_0 = 71.45_{-1.4}^{+1.1} \text{ km s}^{-1} \text{ Mpc}^{-1}$ [305] when solving the equation of motion of the scalar field in full (instead of using a fluid approximation), marginalising over the parameter controlling the potential, n and using *Planck* 2015 temperature and polarisation, SHOES distance ladder, BAO, and Pantheon supernova data (see ref. [305] for details). It is also shown that compared to ΛCDM , the fit to CMB data is improved by the axion model with the above value of H_0 .

In ref. [305] it is suggested that the fit to the density fluctuation amplitude parameter, σ_8 , is worsened by the axion model. Consequently an independent group [306] have analysed the effects of this model on large-scale structure (LSS) data. While the authors of ref. [306] reproduce the CMB only analysis⁴ the addition of LSS data weakens the detection of an EDE component to below 2σ and increases other tensions. Hence, they conclude that the axion model is no better than ΛCDM and suggest that it will not solve the H_0 problem.

Another approach to addressing the H_0 tension is to suggest that dark energy could cross into having a phantom equation of state ($w < -1$) at late times [307]. This is modelled through an expansion of the energy density of the dark energy component in terms of the scale factor, up to third order. Using CMB and BAO data, the early-Universe value of the Hubble constant found in this model is $H_0 = 71.0_{-3.8}^{+2.9} \text{ km s}^{-1} \text{ Mpc}^{-1}$, which is consistent with the local measurements, primarily due to the increased errors. When including

²Both of these codes are publicly available. [Using the fluid approximation and solving the equation of motion.](#)

³This and all future error bars in this chapter are at 68% confidence unless stated otherwise.

⁴The code used is available at github.com/mwt5345/class_edc.

data from local measurements and supernovae, the Hubble constant is $H_0 = 70.25 \pm 0.78 \text{ km s}^{-1} \text{ Mpc}^{-1}$ with the phantom crossing happening at a scale factor of $0.851_{-0.031}^{+0.048}$. This leaves a 2.3σ tension with Riess et al. [308] which, coupled with the fact there are serious theoretical issues with having phantom fields such as the nature of vacuum instabilities, leave this model somewhat disfavoured.

Another attempt to solve the Hubble tension by changing the late-Universe physics and hence the local determination of H_0 was presented in Benevento, Hu, and Raveri [309]. They argued that a change in the dark energy behaviour at $z \ll 0.1$ when compared to Λ CDM can provide equally as good a fit while resulting in values of H_0 that agree with [308]. However, supernovae data goes to redshifts well above the required transition redshift and these strongly constrain the possible increase in the Hubble parameter from this model. The value found when considering CMB, BAO, distance ladder and supernovae is $H_0 = 69.17 \pm 1.09 \text{ km s}^{-1} \text{ Mpc}^{-1}$ which only slightly reduces the tension.

The theoretical model which, to date, allows for the highest value of the Hubble parameter is New Early Dark Energy (NEDE) [310, 311]. A dark sector phase transition before recombination is suggested as a method for changing the expansion before the CMB was emitted. This acts similarly to the axion model as the phase transition results in a change in the value of the cosmological constant which is analogous to a period where dark energy affects the expansion at early times, before redshifting away faster than the background. Using data from the CMB, BAO and supernovae, $H_0 = 71.4 \pm 1.0 \text{ km s}^{-1} \text{ Mpc}^{-1}$. This reduces the Hubble tension to 1.5σ using distance-ladder observations from ref. [308].

5.2 CAMB axion model

The axion dark energy model first presented in ref. [304] (and introduced above) is implemented in the default version of the code CAMB. As this is used for the subsequent analysis some more detail of the exact implementation is given.

For the axion model there are 4 theory parameters $(n, \Theta_i, \mu, \alpha)$ that control the behaviour. Θ_i is the initial field value, n is the index of the potential (see equation (5.1)), μ is the parameter controlling the mass of the axion and α is the coupling parameter. The axion implementation in CAMB uses the fluid approximation throughout. This fluid approximation is also governed by 4 parameters, $(a_c, \Omega_{a,0}, w_n, \bar{\omega}_0)$. The first, a_c is the critical value of the scale factor at which the fluid transitions away from evolving as a cosmological constant. $\Omega_{a,0}$ is the fractional density of the axion fluid at the present time. It is more common in the literature to use $\Omega_a(a_c)$ to quantify the density but the current value is more easily implemented into solving the background evolution and is hence used in CAMB. The equation of state of the axion fluid after the transition is given by w_n and is related to n by equation (5.2). Finally, $\bar{\omega}_0$ governs the scale dependence of the effective sound-speed and is consequently the parameter governing the perturbations [304]. The theory and fluid parameters can be related under certain approximations and hence allow the behaviour of the axion model to be solved under these conditions. This is also important to be able to numerically calculate the evolution of the axion model if the four fluid parameters are specified.

Given the initial value of the axion density the evolution is given by⁵,

$$\Omega_a(a) = \frac{\Omega_{a,0} \left(a_c^{-3(1+w_n)} + 1 \right)}{(a/a_c)^{3(1+w_n)} + 1}. \quad (5.3)$$

A critical time, x_c is defined such that the field value at this time is given by, $\Theta(x_c) = \mathcal{F}\Theta_i$, where \mathcal{F} is an arbitrarily defined number that specifies the fractional change in the field value. Numerical evolution suggests that $\mathcal{F} = 7/8$ works best in calculations of a_c [304]. The mass parameter, μ is given by [304],

$$\mu = \frac{1}{x_c} (1 - \cos \Theta_i)^{-(n-1)/2} \sqrt{\frac{(1 - \mathcal{F})(6p + 2)\Theta_i}{n \sin \Theta_i}}, \quad (5.4)$$

where p is a constant that is equal to $1/2$ during radiation domination and $2/3$

⁵This is equivalent to the expression in terms of $\Omega_a(a_c)$ given in ref. [304]. The conversion is done by evaluating equation (15) of ref. [304] at the current value of the scale factor, a_0 .

during matter domination. The constant, p is usually set to $1/2$ as the initial field value is set during the radiation epoch. In CAMB this is calculated via,

$$x_c = \frac{a_c^2}{2} \sqrt{\frac{8\pi G a^2 \rho_r}{3}}, \quad (5.5)$$

where ρ_r includes photons and neutrinos. Consequently the theory parameter, μ can be calculated from Θ_i and n for a given background cosmology. Note that the expression for μ is only valid for $\Theta_i \lesssim \pi - 0.1$ as the expansion used for the potential breaks down above this limit [304].

Assuming that the fraction of the total density for the field at the critical scale factor, $f_a(a_c) \ll 1$ the parameter controlling the perturbations, $\bar{\omega}_0$ is given by [304],

$$\begin{aligned} \bar{\omega}_0 = & \mu (1 - \cos \Theta_i)^{(n-1)/2} \frac{\sqrt{\pi} \Gamma[\frac{n+1}{2n}]}{\Gamma[1 + \frac{1}{2n}]} 2^{-(n^2+1)/2n} 3^{(\frac{1}{n}-1)/2} \\ & a_c^{-\frac{6}{n+1}+3} (a_c^{6n/(n+1)+1})^{(\frac{1}{n}-1)/2}, \end{aligned} \quad (5.6)$$

where $\Gamma(x)$ is the standard gamma function.

Once the perturbation evolution equations are specified, the full evolution of the axion fluid can be calculated. In the synchronous gauge (with potentials h and η as defined in section 1.3.1) the equations for the density contrast, δ_a and heat-flux u_a , for the mode k , are of the form [312],

$$\begin{aligned} \dot{\delta}_a = & - \left[k u_a + (1 + w_a) \frac{\dot{h}}{2} \right] - 3\mathcal{H} (c_{s,\text{axion}}^2 - w_a) \left(\delta_a + 3\mathcal{H} \frac{u_a}{k} \right) \\ & - 3\mathcal{H} \frac{\dot{w}_a}{(1 + w_a)} \frac{u_a}{k}, \end{aligned} \quad (5.7)$$

$$\dot{u}_a = -(1 - 3c_{s,\text{axion}}^2) \mathcal{H} u_a + \frac{\dot{w}_a}{(1 + w_a)} u_a + k c_{s,\text{axion}}^2 \delta_a, \quad (5.8)$$

where the heat-flux, $u_a \equiv (1 + w_a)v_a$ is favoured over the velocity, v_a for numerical stability when $w_a \approx -1$. The axion sound speed,

$$c_{s,\text{axion}}^2 = \frac{2a^{(2-6w_a)} \bar{\omega}_0 (n-1)^2 + k^2}{2a^{(2-6w_a)} \bar{\omega}_0 (n+1)^2 + k^2}. \quad (5.9)$$

Note that, for $n \rightarrow \infty$, $w_a \rightarrow 1$ and $c_{s,\text{axion}}^2 \rightarrow 1$.

These equations together are all that is required to calculate the evolution

of the axion model given the 4 model parameters, $(a_c, \Omega_{a,0}, w_n, \bar{\omega}_0)$. To reiterate the equations are valid for $\Theta_i \lesssim \pi - 0.1$ and $f_a(a_c) \ll 1$.

5.2.1 Results

We use *Planck* 2018 data [1] in combination with baryon-acoustic oscillation (BAO) data from BOSS DR12 [112], 6dFGS [113] and SDSS-MGS [114]. The *Planck* likelihoods used are the TT, TE and EE spectra at $\ell \geq 30$, the low- ℓ likelihood using the COMMANDER component separation algorithm [163], the low- ℓ EE likelihood from the SIMALL algorithm, and lensing [89]. We refer to this TT,TE,EE + lowE + lensing + BAO combination as our base data set. The local H_0 measurement is included using data from [308]. We refer to this as our base + H_0 data set.

We do an MCMC analysis, using COBAYA and the two data combinations above, over the 6 Λ CDM baseline parameters, with $N_{\text{eff}} = 3.046$ and the sum of the neutrino masses fixed to 0.06 eV as before. The CAMB axion fluid is constrained in two forms. One where the equation of state after the transition, w_n is free to vary and one where it is forced to be close to 1. In the second case the sound speed, $c_{s,\text{axion}}^2$ is also close to 1 and the fluid approximation is expected to describe this case more accurately. In both of these $\Theta_i = \pi/2$ with $(w_n, a_c, f_a(a_c))$ as the extra parameters quantifying the axion models. We assume flat priors on the Λ CDM parameters, and the log of the fractional energy density of the axion models at the transition scale.

The mean and best-fit values of the Λ CDM and axion parameters, along with the χ^2 , for the base + H_0 data set are shown in table 5.1. The best-fit value of the Hubble constant is increased for the axion models which confirms previous conclusions that it can be used to reduce the Hubble tension [301, 304, 305]. The best-fit χ^2 is decreased in the axion model, with $\delta\chi^2 = -11.6$, which also supports previous analyses which showed that the axion model fits the data better than Λ CDM. The same data (Planck 2018 and ref. [308] distance ladder), fluid approximation and model parameters as the axion model

Parameter	Λ CDM	Axion	Axion (high w_n)
$\log(10^{10} A_s)$	$3.051 (3.053) \pm 0.012$	$3.063 (3.065) \pm 0.015$	$3.063 (3.073) \pm 0.015$
n_s	$0.9696 (0.9695) \pm 0.0029$	$0.9826 (0.989) \pm 0.0075$	$0.9808 (0.983) \pm 0.0063$
H_0	$68.23 (68.32) \pm 0.32$	$70.4 (70.9) \pm 1.0$	$70.22 (70.3) \pm 0.92$
$\Omega_b h^2$	$0.02253 (0.02255) \pm 0.00011$	$0.02284 (0.02290) \pm 0.00023$	$0.02287 (0.02291) \pm 0.00023$
$\Omega_c h^2$	$0.11814 (0.11799) \pm 0.00070$	$0.1270 (0.1275) \pm 0.0038$	$0.1263 (0.1259) \pm 0.0033$
τ_{reio}	$0.0594 (0.0607) \pm 0.0060$	$0.0580 (0.0598) \pm 0.0074$	$0.0569 (0.0603) \pm 0.0074$
w_n	-	$> 0.549 (0.536)$	$> 0.915 (0.983)$
$\log_{10}(a_c)$	-	$-3.65 (-3.74)_{-0.097}^{+0.16}$	$-3.552 (-3.520)_{-0.050}^{+0.071}$
$f_a(a_c)$	-	$0.057 (0.055)_{-0.020}^{+0.022}$	$0.063 (0.064)_{-0.022}^{+0.025}$
χ^2	(2074.49)	(2062.9)	(2065.3)

Table 5.1: Mean (best-fit) values of the axion model parameters and the baseline Λ CDM parameters for the axion model with 1σ errors. The axion fluid model is considered along with an axion model in which the late-time equation of state is constrained to be close to 1. The values in a Λ CDM run are shown for comparison along with the χ^2 for the full base + H_0 data set which suggest that the axion models fit the data slightly better than Λ CDM. The increased values of H_0 support the conclusion that the axion model reduces the Hubble tension.

considered here, have not been considered together in previous work, but the decrease in χ^2 appears to be smaller here than in ref. [305] where $\delta\chi^2 = -20.33$ and n is similarly free to vary. The change in χ^2 for the high w_n axion model of -9.6 is similar to that quoted in ref. [301].

The density fraction and change in the CMB power spectrum for the two best-fit axion models are shown in figure 5.1. The axion model when $w_n \approx 1$ has a narrower, taller peak in the energy fraction and peaks slightly later than the normal axion model. The maximum values are both less than 1% and hence the assumption that $f_a(a_c) \ll 1$ is satisfied. The changes in the CMB power spectrum when compared to the best-fit Λ CDM model are $\mathcal{O}(1\%)$.

The posterior probability for the Hubble constant for the Λ CDM model with base and base + H_0 data, along with the axion model for base + H_0 data are shown in figure 5.2. It confirms the fact that the axion model alleviates the Hubble tension through a combination of increasing the best-fit value of

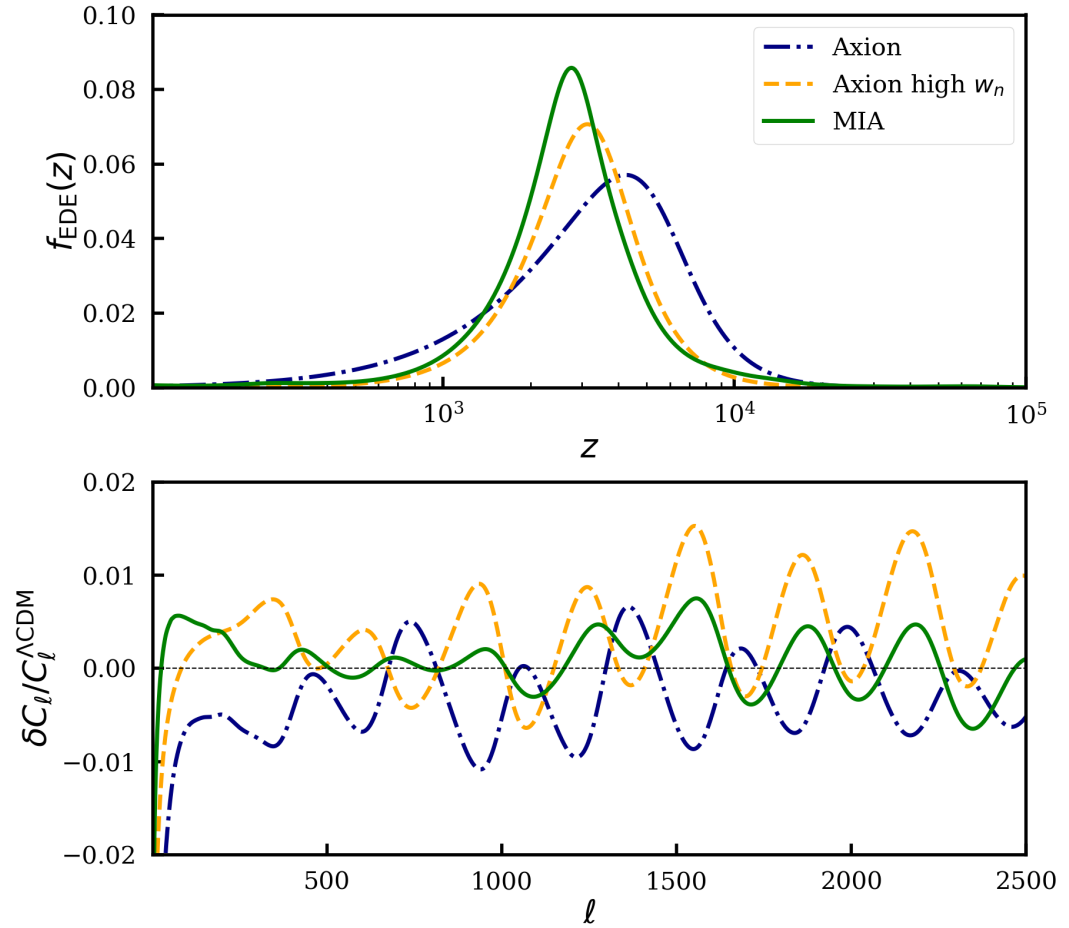


Figure 5.1: Comparisons of the early dark energy fraction, $f_{\text{EDE}}(z)$ and the change in the CMB power spectrum for the best-fit models from MCMC of the base + H_0 data set for the axion fluid (blue dot-dash), axion fluid with $w_n \approx 1$ (orange dash) and model-independent approach (MIA) (green solid).

H_0 and increasing the width of the posterior, i.e. increasing the error bar.

5.3 Model-independent approach

As there are increasingly many theoretical models (for recent examples see refs. [313–323]) seeking to reduce the Hubble tension through modifications of the expansion history, it is important to understand what generic features of these models are contributing to better fitting the observations.

With that goal in mind our idea is to use a set of basis functions that categorise modifications to the cosmological background for different redshifts, constrain the equation of state and energy density of the new dark energy component in each redshift bin and then calculate which redshift regions are

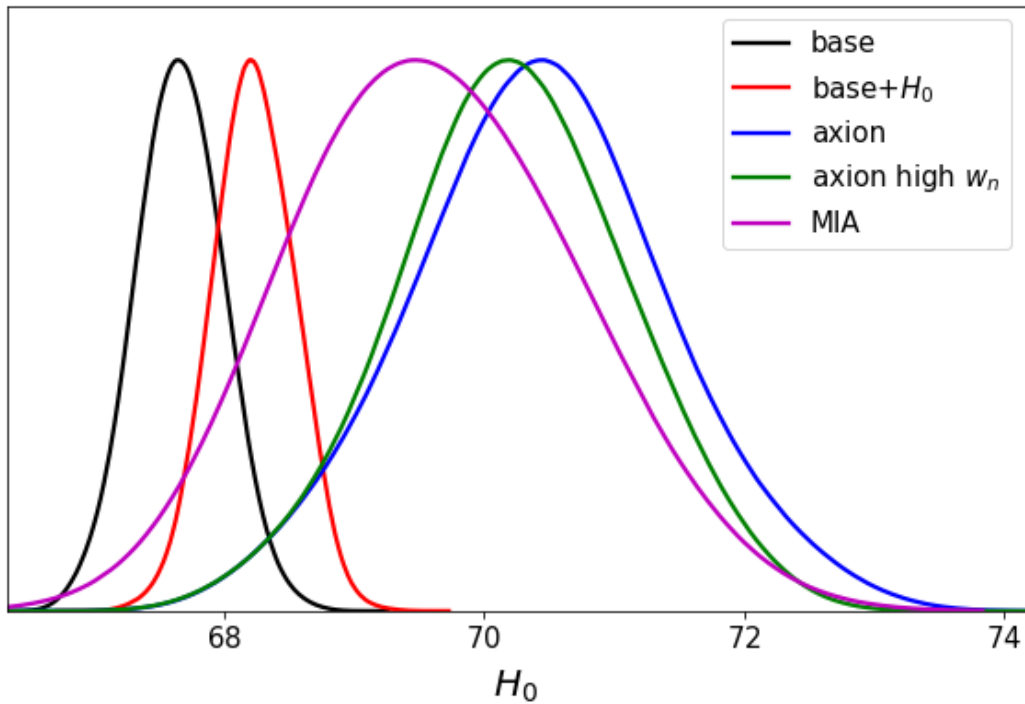


Figure 5.2: The posterior probability distribution for H_0 for a variety of data and models. The lowest value is for the base data set (black) with the second lowest for base + H_0 (red). The other three curves are all for base + H_0 data for extensions to Λ CDM aimed at alleviating the Hubble tension. In order of increasing mean H_0 these are: the model-independent approach (MIA) (magenta); axion fluid with $w_n \approx 1$ (green) and the axion fluid with no constraint on w_n (blue).

most important for alleviating the H_0 tension.

We do this by including a set of N fluids with energy density, Ω_i that are relevant for different redshift regions. This could also be interpreted as a single fluid with an effective equation of state that includes contributions from all of the redshift regions (see equation (5.15) below). The set of fluids modify the Friedmann equation as,

$$H^2(a) = H_0^2 \left[\Omega(a) + \sum_{i=1}^N \Omega_i(a) \right], \quad (5.10)$$

where $\Omega(a)$ is the total density in Λ CDM. We choose a functional form for the equation of state of each fluid such that it scales like a cosmological constant before a transition scale, a_i and as a stiff fluid ($w = 1$) after, via,

$$w_i(a) = \frac{2}{1 + (a_i/a)^\beta} - 1, \quad (5.11)$$

where β is a parameter that sets the speed of the transition between the two regimes. The reason we choose a stiff fluid is that it provides the most rapid decay of its energy density that is consistent with having a perfect fluid equation of state. The equation of state implies that the energy density of the fluid has the form,

$$\Omega_i(a) = \Omega_i(a_i) \left(\frac{2a_i^\beta}{a^\beta + a_i^\beta} \right)^{6/\beta}, \quad (5.12)$$

where $\Omega_i(a_i)$ is the density at the transition scale. We parameterise this in terms of the fractional density compared to a reference Λ CDM value at the transition scale, i.e. $f_i = \Omega_i(a_i)/\Omega_i^{\text{ref}}(a_i)$, where the reference model is chosen to be the *Planck* best-fit. Note that if $\beta = 6$, this is the same scaling of density and equation of state as in the fluid approximation to the axion model [304]. Consequently the model for each of the fluids is similar to the axion model but allows for faster transitions between the two limits of the equation of state.

Perturbations are included via effective values for the total fluid found by summing the contributions of the N separate fluids. Similarly to the axion fluid model, the synchronous gauge equations for the density contrast, δ and heat-flux u , for the mode k , are of the form [312],

$$\begin{aligned} \dot{\delta} = & - \left[ku + (1 + w_{\text{eff}}) \frac{\dot{h}}{2} \right] - 3\mathcal{H}(\hat{c}_s^2 - w_{\text{eff}}) \left(\delta + 3\mathcal{H} \frac{u}{k} \right) \\ & - 3\mathcal{H} \frac{\dot{w}_{\text{eff}}}{(1 + w_{\text{eff}})} \frac{u}{k}, \end{aligned} \quad (5.13)$$

$$\dot{u} = -(1 - 3\hat{c}_s^2)\mathcal{H}u + \frac{\dot{w}_{\text{eff}}}{(1 + w_{\text{eff}})}u + k\hat{c}_s^2\delta. \quad (5.14)$$

where $\mathcal{H} = aH$, \hat{c}_s^2 is the sound speed in the frame co-moving with the fluid, and w_{eff} is the effective equation of state, given by

$$w_{\text{eff}} = \frac{\sum_i \Omega_i w_i}{\sum_i \Omega_i}. \quad (5.15)$$

The heat-flux, u , is again favoured over v for numerical stability. The adiabatic sound speed is

$$c_a^2 \equiv \frac{\dot{P}_a}{\dot{\rho}_a} = w_{\text{eff}} - \frac{\dot{w}_{\text{eff}}}{3(1 + w_{\text{eff}})\mathcal{H}}, \quad (5.16)$$

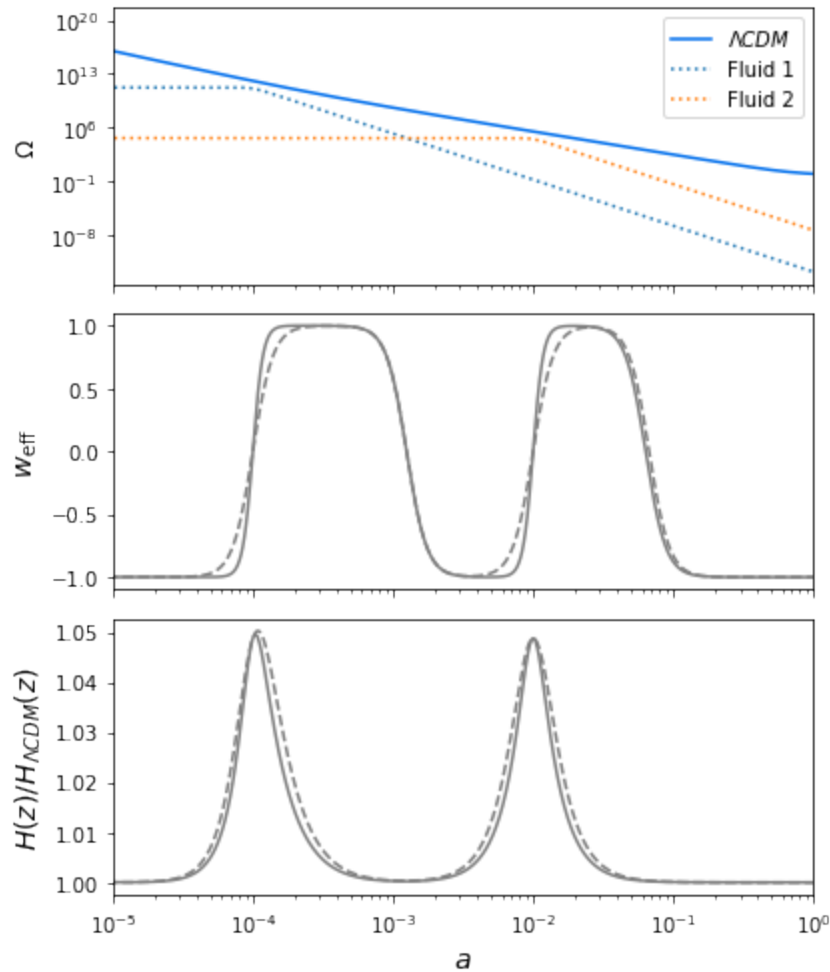


Figure 5.3: (Top) Density, $\Omega(a)$, for a 2-component model with transition scales $a_i = 10^{-4}, 10^{-2}$, each with an energy density of $f_i = 0.1$ of the background at the transition scale. The solid blue line is the total Λ CDM density (called $\Omega(a)$ in equation (5.10)). (Middle) Effective equation of state of the 2-component fluid. (Bottom) Relative change in the Hubble rate compared to Λ CDM with 2-components. The case with $\beta = 6$ is given by the dashed line in the bottom two panels and $\beta = 12$ is the solid line.

and is bounded by $-(1 + \beta/3) < c_a^2 < 1$. For simplicity \hat{c}_s^2 will be set to 1 for all applications considered here.

The set of fluids defined above can be thought of as a set of well-defined basis expansions for $\delta(H^2)$ as they obey $-1 \leq w_{\text{eff}} \leq 1$ by construction. The basis expansion is capable of reconstructing any modification to $\delta(H^2)$ that satisfies $-1 \leq w_{\text{eff}} \leq 1$, for a sufficiently large number of components. We choose β to be large enough such that the basis has a high temporal resolution but remains numerically stable. 2-component models with $\beta = 6$ and $\beta = 12$ are illustrated in figure 5.3 showing the behaviour of the density of the fluids,

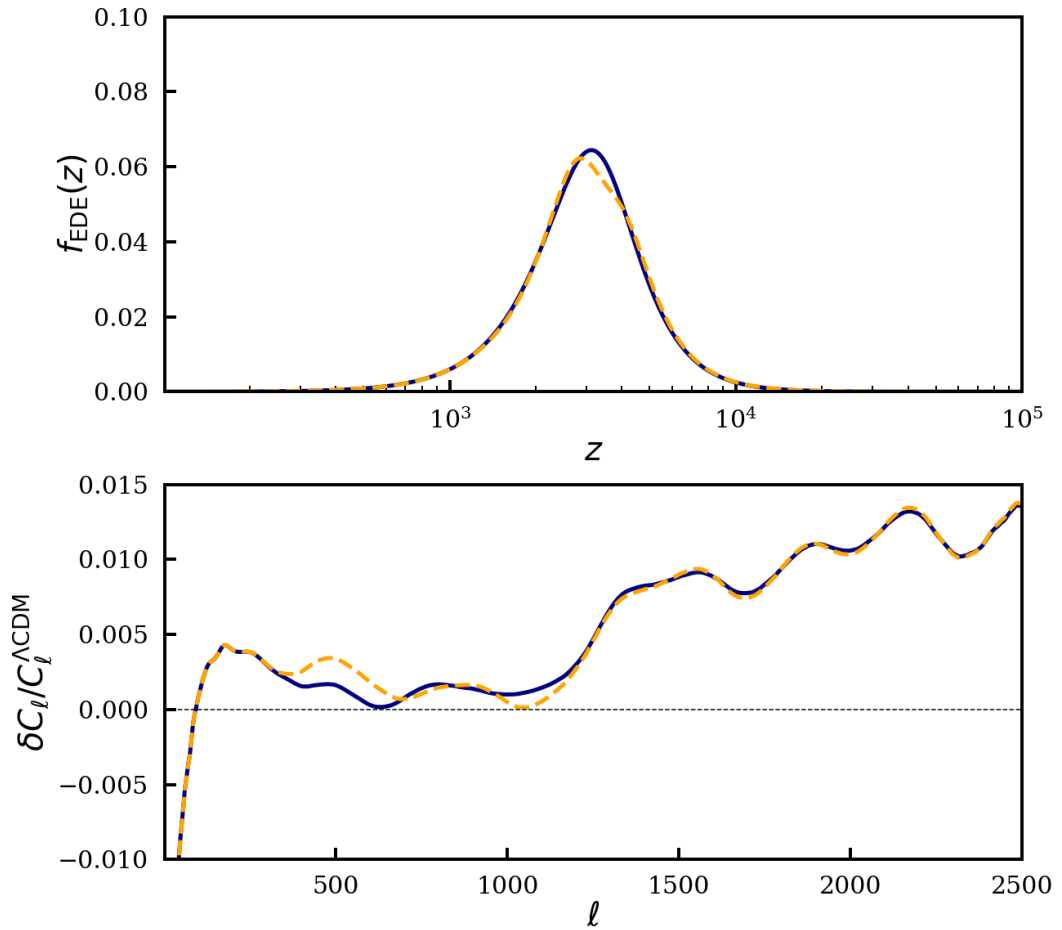


Figure 5.4: (Top) The early dark energy fraction as a function of redshift for the axion model (blue solid) and for the MIA with 4 fluids with their amplitudes matched to give a similar early dark energy fraction (orange dashed). (Bottom) The fractional change in the CMB power spectrum as a result of the two models.

the effective equation of state and the change in the Hubble parameter.

As an example of how this model is able to reproduce other specific models, figure 5.4 shows the early dark energy fraction, $f_{\text{EDE}}(z) = \rho_{\text{EDE}}(z)/\rho_{\text{crit}}(z)$ for the baseline axion model used in ref. [306] and using four fluids close to recombination in the MIA. The amplitudes of the fluids are chosen through a least squares minimisation of the MIA early dark energy fraction with the early dark energy fraction of the axion model. It is clear that the MIA model is able to reproduce the effects of the axion model well, even when a small number of fluids are used.

As a further illustration, figure 5.5 shows how the MIA can be used to reproduce the best-fit axion fluid models from the previous section. The initial

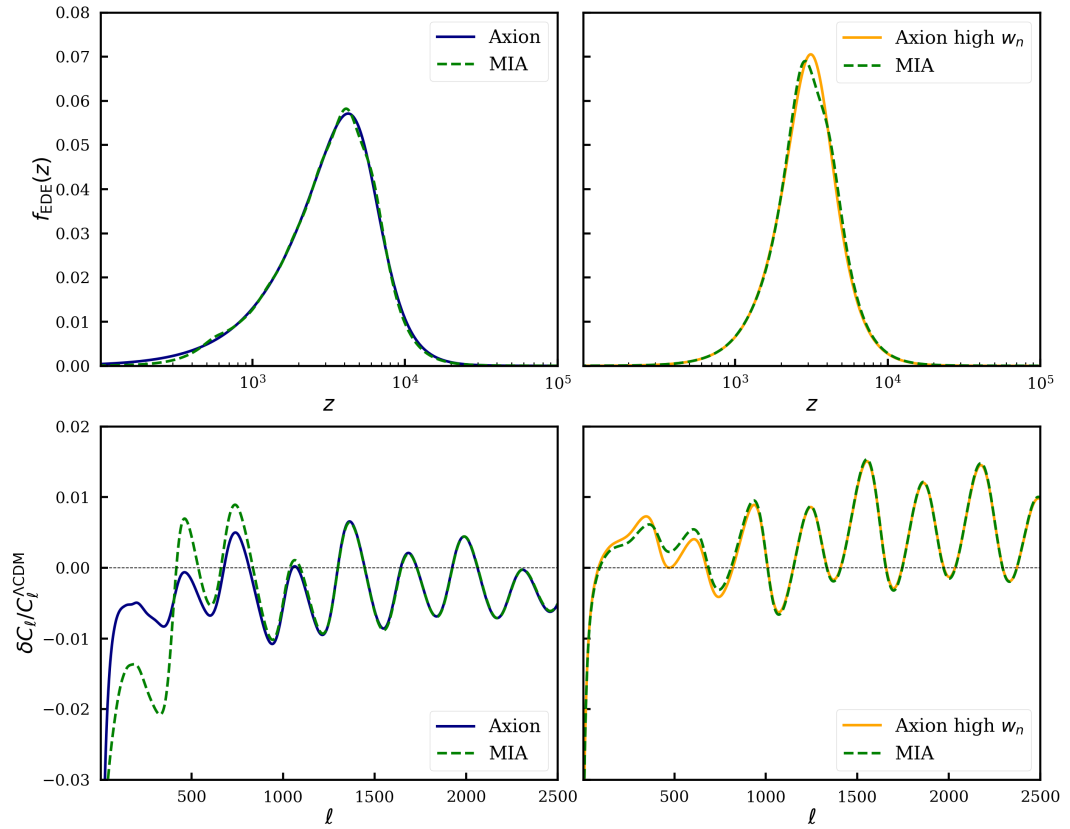


Figure 5.5: Comparisons of the early dark energy density fraction, $f_{\text{EDE}}(z)$ and the fractional change in the CMB power spectrum, for the model-independent approach matched to the best-fit axion models. Left: the axion model (blue solid) and fitted MIA (green dashed) and right: the high w_n axion model (orange solid) and fitted MIA (green dashed).

amplitudes of the MIA fluid components are optimised using a least-squares fit of the resulting energy density fraction, f_{EDE} . The early dark energy fraction is fit well in both cases as is the change in the CMB power spectrum at $\ell \gtrsim 1000$. For smaller ℓ , deviations between the axion models and the MIA can be seen but the MIA fits the change in the CMB power spectrum better for the high w_n axion model. This is expected due to the assumption that $\hat{c}_s^2 = 1$ for the MIA and the fact that $c_{s,\text{axion}}^2 \rightarrow 1$ for $w_n \rightarrow 1$, i.e. the behaviour of the perturbations are more similar for the high w_n axion model than the normal axion model.

5.3.1 Results

MCMC was carried out on the MIA as for the axion models in the previous section. The base + H_0 data set was used and we assumed flat priors on the

log of the fractional energy densities at the transition scale. As mentioned previously, the sound speed was set to 1 for simplicity.

The mean and best-fit parameter values for the MIA are shown in table 5.2. The MIA parameters are the logarithms of the initial density amplitude, $\log_{10}(\rho_i)$ for each of the 30 fluids considered. These fluids are spaced between $z = 0$ and $z = 10^5$ and the lowest and highest redshift fluids have their amplitudes fixed to $\log_{10}(\rho_{1,30}) = -5.0$. The MCMC results show that the 9th and 10th fluid components have the largest amplitudes as one would expect as they correspond to times just before recombination, close to where the best-fit axion models contribute most to the density. The best-fit χ^2 suggests that the MIA fits the data better than the Λ CDM model, with $\delta\chi^2 = -7.9$, but not quite as well as the axion models. The posterior on H_0 shown in figure 5.2 also suggests that the MIA does slightly less well at alleviating the Hubble tension.

The fractional energy density and change in the CMB power spectrum for the best-fit MIA model is shown in figure 5.1. The MIA has the largest contribution to the energy density and similar magnitude of change in the CMB power spectrum to the axion models.

The energy density and equation of state of the total fluid in the MIA can be reconstructed from the MCMC analysis. This gives the required evolution of the early dark energy fluid to best-fit the base + H_0 data. The reconstructions of the full dark energy fluid (with cosmological constant) and just the MIA fluid are shown in figures 5.6 and 5.7 respectively. These show that a density of $\sim 10\%$ is allowed just before recombination if the equation of state of the dark energy fluid transitions quickly from a negative to positive value. The equation of state then approximately tracks the background during the matter era before transitioning to cosmological constant domination. When the cosmological constant comes to dominate the MIA fluid equation of state transitions to a large positive value suggesting a late-time equation of state of the total dark energy fluid slightly above -1 , is favoured, though the allowed energy density of the MIA fluid at this point decreases to $\lesssim 0.5\%$. This is

Parameter	MIA: mean	MIA: best-fit
$\log_{10}(\rho_2)$	< -3.00	-3.52
$\log_{10}(\rho_3)$	$-3.33^{+0.83}_{-1.0}$	-4.50
$\log_{10}(\rho_4)$	< -3.68	-4.06
$\log_{10}(\rho_5)$	< -3.55	-4.75
$\log_{10}(\rho_6)$	$-3.47^{+0.76}_{-0.91}$	-2.97
$\log_{10}(\rho_7)$	< -2.90	-2.81
$\log_{10}(\rho_8)$	$-3.35^{+0.72}_{-1.4}$	-4.57
$\log_{10}(\rho_9)$	$-1.86^{+0.31}_{-0.26}$	-2.05
$\log_{10}(\rho_{10})$	$-1.47^{+0.44}_{-0.38}$	-1.07
$\log_{10}(\rho_{11})$	< -2.24	-3.75
$\log_{10}(\rho_{12})$	< -3.46	-3.33
$\log_{10}(\rho_{13})$	< -2.81	-4.55
$\log_{10}(\rho_{14})$	$-3.53^{+0.66}_{-0.87}$	-4.71
$\log_{10}(\rho_{15})$	$-3.58^{+0.56}_{-1.2}$	-3.55
$\log_{10}(\rho_{16})$	$-2.89^{+0.82}_{-0.71}$	-3.06
$\log_{10}(\rho_{17})$	$-3.45^{+0.74}_{-0.94}$	-4.88
$\log_{10}(\rho_{18})$	$-3.10^{+1.0}_{-0.66}$	-3.92
$\log_{10}(\rho_{19})$	< -3.86	-3.39
$\log_{10}(\rho_{20})$	< -2.94	-3.08
$\log_{10}(\rho_{21})$	-3.38 ± 0.65	-4.55
$\log_{10}(\rho_{22})$	-3.39 ± 0.81	-3.31
$\log_{10}(\rho_{23})$	$-3.30^{+0.93}_{-0.75}$	-4.42
$\log_{10}(\rho_{24})$	< -2.82	-2.98
$\log_{10}(\rho_{25})$	$-3.43^{+0.74}_{-0.89}$	-4.04
$\log_{10}(\rho_{26})$	< -3.13	-4.22
$\log_{10}(\rho_{27})$	< -3.57	-3.94
$\log_{10}(\rho_{28})$	< -3.70	-4.75
$\log_{10}(\rho_{29})$	< -3.16	-4.60
$\log_{10}(10^{10} A_s)$	3.067 ± 0.017	3.074
n_s	0.9766 ± 0.0056	0.9790
H_0	69.6 ± 1.0	70.3
$\Omega_b h^2$	0.02278 ± 0.00020	0.02281
$\Omega_c h^2$	$0.1255^{+0.0029}_{-0.0036}$	0.1285
τ_{reio}	$0.0592^{+0.0088}_{-0.0071}$	0.0579
χ^2	-	2067.0

Table 5.2: Mean (best-fit) values of the model-independent approach (MIA) amplitudes (ρ_i), the baseline Λ CDM parameters and the χ^2 , with 1σ errors. The data used is the base + H_0 data set. There are 30 MIA fluids spaced from $z = 0$ (ρ_1) to $z = 10^{-5}$ (ρ_{30}) with these two fluids set to an amplitude of $\log_{10}(\rho_{1,30}) = -5.0$.

likely to be due to the fact that the latest-time fluid has its energy density fixed to a low value which requires the fluid to decay quickly and is therefore unlikely to be a physical effect. The favouring of a positive effective equation of state at redshifts above matter-radiation equality is not understood and is currently under investigation. The results are inconclusive at the moment and a non-zero energy density is not favoured, but an understanding of what is driving this transition offers a potentially interesting avenue for further work and for verification with future data.

Because the allowed early dark energy model agrees qualitatively with the expectations of tracking quintessence models we intend to investigate the viability of known models for alleviating the Hubble tension by comparing to the MIA in a future publication.

5.4 Principal component analysis

Principal component analysis (PCA) is a statistical methodology that can be used to calculate which components of a data-set are contributing most to an output variable. It can also be used for systematic dimensional reduction that maintains information from the original data. PCA is an ideal tool for our purposes as it can be used to quantify which modifications to the background expansion (if any) are most important for alleviating the H_0 tension.

PCA maps the original data to an uncorrelated and orthogonal basis. This is done by calculating the data covariance matrix for the input parameters. This covariance matrix has the individual parameters variances as the diagonal elements and the covariance between parameters as off-diagonal elements and is therefore symmetric. Then the eigenvalues and eigenvectors of the covariance matrix are calculated. The largest eigenvalues correspond to the eigenvectors in parameter space which specify the direction in which the data changes most. When the eigenvalues are put in descending order they are called the *principal components* (PCs) such that the largest eigenvalue and its eigenvector correspond to the first principal component and so on.

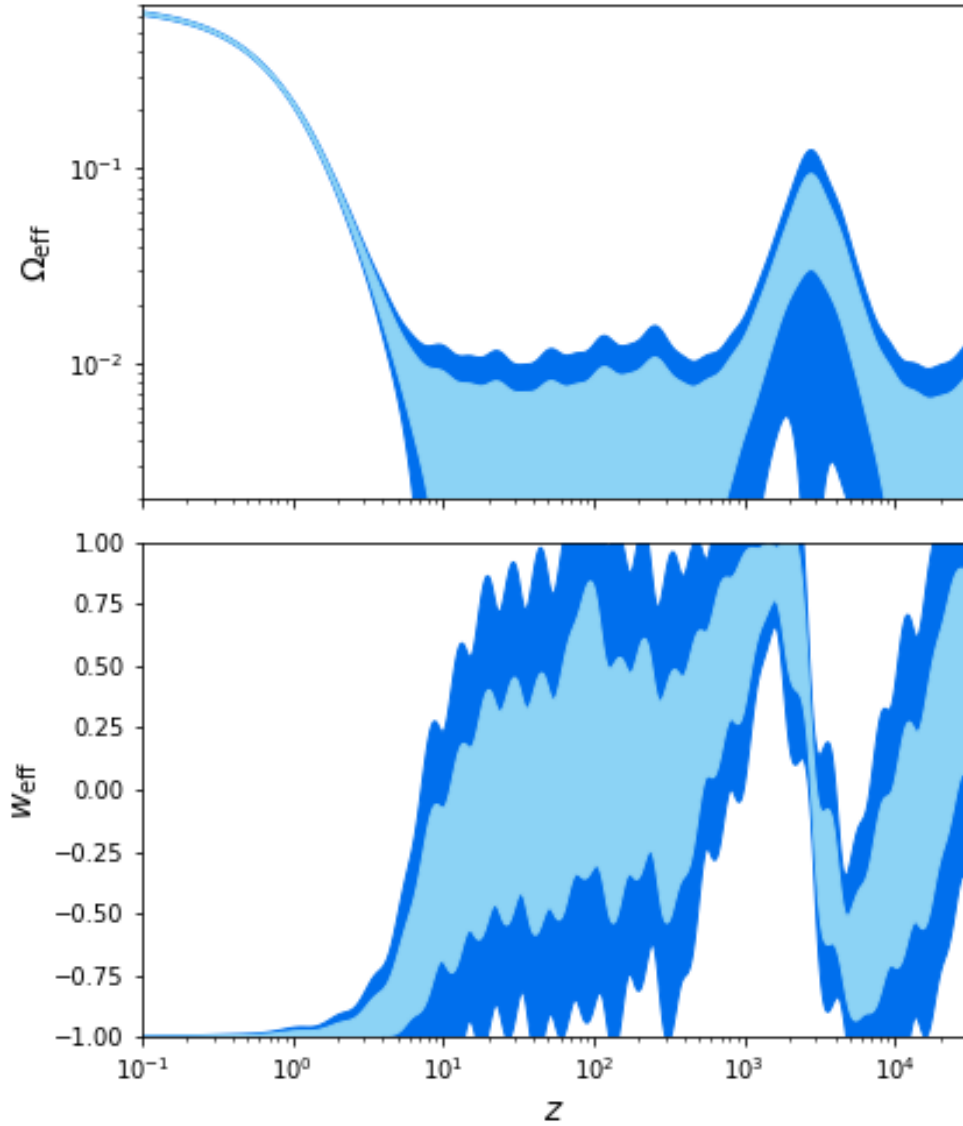


Figure 5.6: The fractional energy density and equation of state of the total MIA fluid and cosmological constant reconstructed from the MCMC analysis. The pale blue region is the 1σ allowed values and dark blue is the 2σ region.

To use this for dimensional reduction the variance ratio is calculated. This is the fraction of the variance that is explained by each component. If a requirement is chosen that $x\%$ of the information in the original data-set is required, then the variance ratios of the principal components are summed until the sum reaches or exceeds $x\%$. All further principal components can be dropped while only having a small impact on the accuracy of any conclusions that are drawn from the lower dimensional data-set (dependent on the value of x).

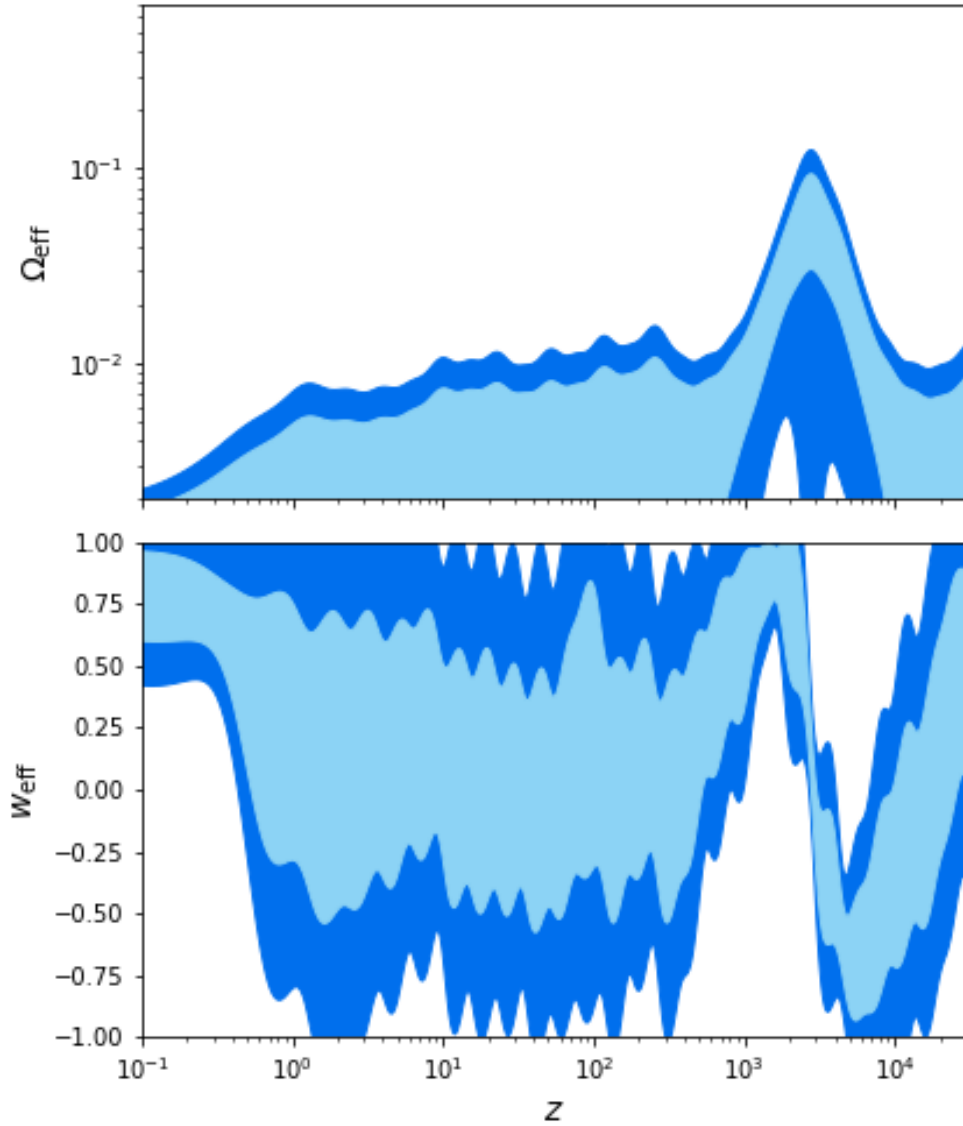


Figure 5.7: The fractional energy density and equation of state of the total MIA fluid (without the cosmological constant) reconstructed from the MCMC analysis. The pale blue region is the 1σ allowed values and dark blue is the 2σ region.

It is worth noting that the principal components are a good basis for clearly analysing the contributions to the variance of the data but are linear sums of the input variables and are consequently less simply related to the underlying physics. However, the correlation of the principal components with the physical parameters can help to clarify their physical effects.

5.4.1 Results

A principal component analysis was carried out on the MCMC covariance matrix for the initial amplitudes of the MIA fluids. This resulted in 28 principal

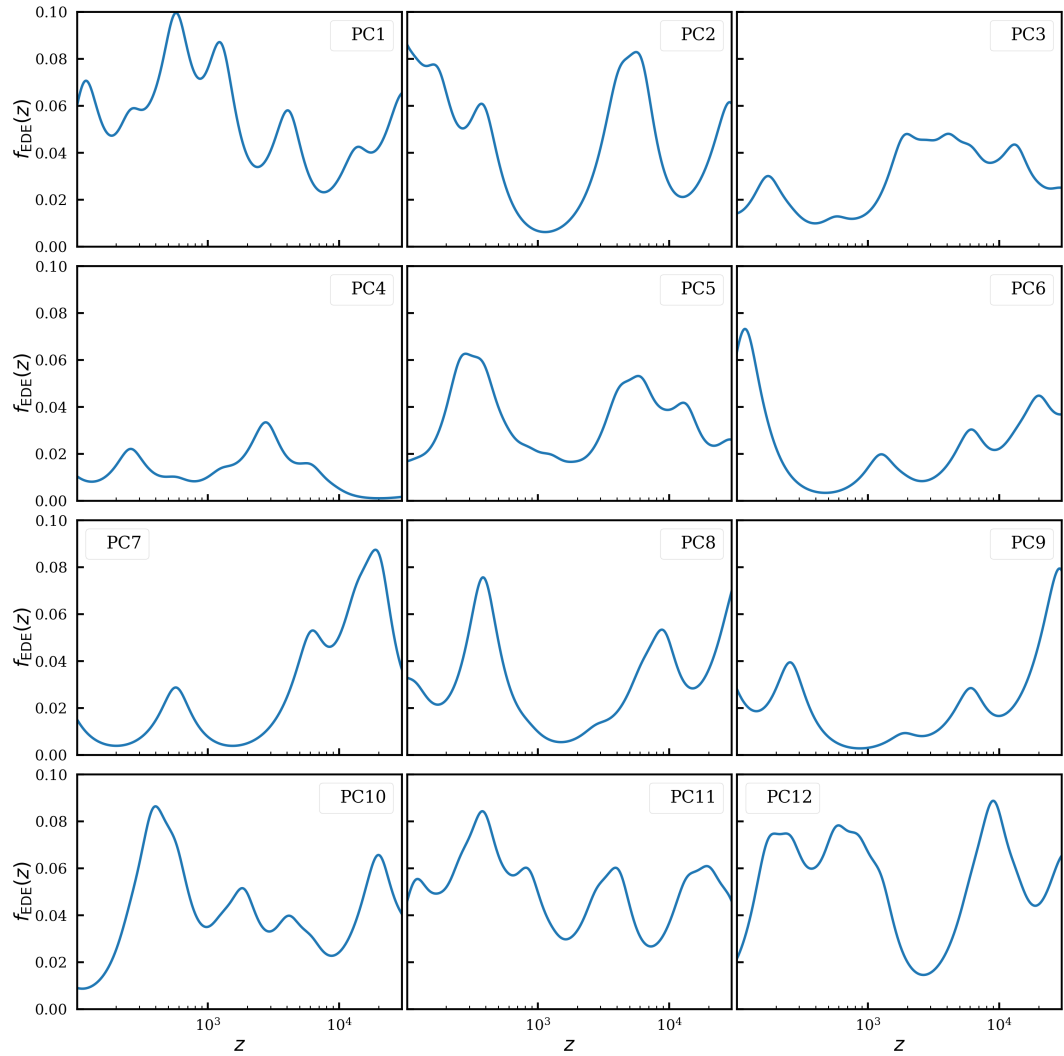


Figure 5.8: The fractional energy density of the total MIA fluid for the first 12 principal components (PCs) for redshifts around matter–radiation equality. The absolute amplitudes are arbitrary but the positions of the peaks suggest what physics is most important in explaining the base + H_0 data set.

components being found, the first 12 of which explained over 80% of the variance in the data. This variance ratio is chosen somewhat arbitrarily but is expected to be high enough for the current analysis. The resulting energy fraction of the early dark energy component around matter–radiation equality, for these 12 principal components, are shown in figure 5.8. The change in the CMB power spectrum when compared to the case with no MIA fluids is shown in figure 5.9. It is worth noting that the absolute normalisation of both of these figures is arbitrary and PCs have not been modified dependent on their eigenvalues. Also, the range of allowed features in the early dark energy fraction is large and consequently the analysis does not give well defined behaviours for each

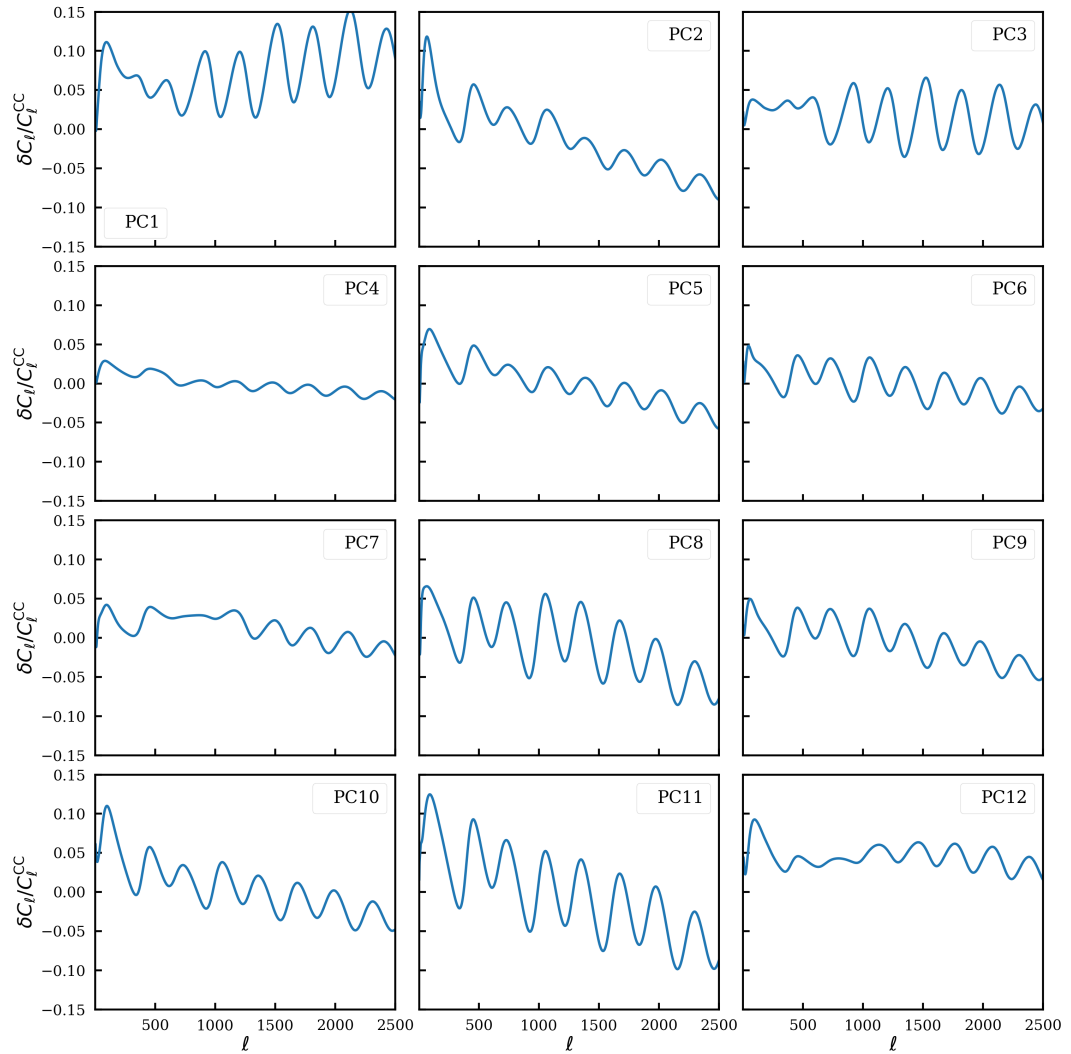


Figure 5.9: The change in the CMB power spectrum, when compared to the same cosmological parameters with no MIA fluids (i.e. just a cosmological constant), for the first 12 principal components. The first principal component suggests an increase in total power while the second principal component, along with the fifth, tenth and eleventh, principal components suggest a tilt in the power spectrum towards more power at large scales.

principal component. However, some general features do emerge. The first principal components strongest correlation is with the scalar amplitude, A_s . This can be seen in figure 5.9 where PC1 results in a positive δC_ℓ for all ℓ and hence is an increase in power. Consequently, inclusion of the dark energy fluid increases the homogeneities in the CMB. The second principal component has strong correlations with the scalar amplitude, A_s and the scalar tilt, n_s . The conclusions from the change in A_s are similar to those for the first principal component while the change in tilt favours more CMB power at large scales.

This change in tilt is also seen in PC8 and PC11 and to a lesser extent in PC9 and PC10. The first two PCs, which together have a variance ratio of $\approx 30\%$, have moderate correlations with σ_8 which suggests that the conclusion in ref. [305], that the axion model worsens the fit to σ_8 , may be true more generally in EDE models. Figure 5.8 shows that these two principal components also have a non-zero energy density for very low redshift but this is another manifestation of the conditions set on the lowest redshift bin, as discussed above, and is not expected to be a true physical effect.

The principal components with the strongest correlation with the Hubble constant are PC3 and PC7. These both represent dark energy fractions that peak strongly before recombination, which is the behaviour we expect to be necessary for alleviating the Hubble tension from the axion model. This peak in the early dark energy fraction before recombination is seen in nearly all of the principal components. Figure 5.9 shows that PC3 and PC7 are primarily shifts in the CMB peaks and troughs at intermediate and small scales and resultingly this is tentatively suggested as the favoured change in the CMB that alleviates the Hubble tension. In addition the first two principal components have moderate correlations with the Hubble constant. As the first three principal components, which explain $\approx 40\%$ of the variance, all have non-negligible correlations with the Hubble constant, the expectation - that improving the fit to the Hubble constant is important for better explaining the data - is confirmed.

5.5 Summary and outlook

This chapter detailed preliminary work to investigate the features of early dark energy models that are believed to be necessary for alleviating the Hubble tension. As such it began with a brief overview of existing models with particular emphasis on the axion model [304]. This was followed by details of an MCMC analysis of the Λ CDM and axion models for CMB, BAO and distance ladder data. The parameter values for the axion model were similar to those quoted

in the literature. An axion model constrained to have a late-time equation of state, w_n close to one was also considered as the fluid approximation is expected to describe this case better. This only produced small changes in the best-fit parameters when compared to the normal axion model. Both cases resulted in a reduction of χ^2 when compared to Λ CDM suggesting a better fit to the observational data, though the reduction in χ^2 for the axion model is less than those presented in the literature for similar analyses by about 3 or 4 [301, 305, 306].

After this, a model-independent approach was developed which uses a sum of individual fluids that transition from an equation of state of $-1 \rightarrow 1$ at different times. Setting appropriate amplitudes for a suitable number of fluids can reproduce a large range of modifications to the expansion history. An MCMC analysis was also carried out on this model finding an increase in the best-fit value of the Hubble constant to $H_0 = 70.3 \text{ km s}^{-1} \text{ Mpc}^{-1}$. This is slightly lower than the best-fit value for the axion model of $H_0 = 70.9 \text{ km s}^{-1} \text{ Mpc}^{-1}$ but the same as the best-fit value for the high w_n axion model. The fluids with the largest amplitudes corresponded to times close to matter–radiation equality as expected from the axion model. The density and equation of state of the total MIA fluid were reconstructed from the data showing a clear peak and transition period for $z \approx 3 \times 10^3$. The behaviour of the equation of state suggested that existing models of dark energy, which track the background equation of state, could have the required behaviour to alleviate the Hubble tension. The study of these tracking dark energy models and their comparison with the constraints given here, are an area for future research.

Finally, a principal component analysis was carried out based on the MCMC analysis of the model-independent approach. This was done to show which modifications to the background evolution were most important for alleviating the Hubble tension and to find the effects the best-fit early dark energy model has on the cosmological parameters. While the necessary background evolution is difficult to discern directly from the data presented here, the correlations

of the principal components with the cosmological parameters do show some interesting effects. An increase in the amplitude of the CMB power spectrum and also a tilt to larger values at large scales are induced by the best-fit early dark energy model. In the future the principal component analysis could be used to compare the effectiveness of different models aimed at reducing the Hubble tension. New data constraining the background expansion will improve this analysis and therefore allow for stricter comparison of theoretical models. This promises to be increasingly important as more and more models are proposed which aim to alleviate the Hubble tension.

Chapter 6

Conclusions

Since the first accurate measurements of the CMB, Λ CDM has established itself as the standard model of cosmology and has been incredibly successful in explaining a large range of cosmological observations. It describes almost 14 billion years of evolution from just after a predicted period of exponential expansion via inflation, up to the present day. Inflation has become the most popular explanation of the very early Universe due to its success in solving observational problems and in predicting the initial conditions for the perturbations of the contents of the universe that are observed in the CMB.

Recently, observations have been starting to point towards problems with Λ CDM that might give hints to further physics which is not included in the standard model of cosmology. There are also theoretical problems with the nature of dark matter, dark energy and the cause of inflation. Gravitational waves offer a new window to the last of these along with other phenomena in the very early Universe. Because gravitational waves decouple at much higher energies than photons they contain information about times much closer to inflation than other observations do. As astrophysical gravitational waves have now been observed experimentally [9], the interest in primordial gravitational waves from the early Universe has increased. This has prompted both theoretical and experimental advances and consequently, accurate predictions of gravitational wave observables are increasingly important.

The starting point for the original work detailed in this thesis is the short-wavelength constraint on the primordial gravitational wave density parameter

coming from the CMB temperature anisotropies [96]. Chapter 3 details our attempt to update this constraint using the most recent data. In doing so, some differences were found with the existing analysis, primarily in the initial conditions of the most physically applicable mode, the homogeneous mode. Isocurvature modes were considered for the first time in the context of a gravitational wave analysis and new gravitational wave isocurvature modes were presented. The constraint for homogeneous initial conditions from the *Planck* 2018 CMB data combined with BAO data was found to be $\Omega_{\text{gw}}h^2 < 2.9 \times 10^{-7}$ at 95% confidence, for $f \gtrsim 10^{-15}$ Hz and is tighter than the previous best shortwave constraint by a factor ≈ 4 .

Consideration of this short-wavelength constraint motivated a methodology that did not rely on the shortwave approximation and was therefore valid for lower frequencies. This involved a thorough calculation of the effective energy–momentum tensor introduced in Abramo, Brandenberger, and Mukhanov [38] and is presented in Chapter 4. The energy–momentum tensor, when applied to cosmological backgrounds simplifies to the one used in the shortwave approximation in the appropriate limit but is more generally applicable due to careful consideration of gauge invariance. The equation of state of gravitational waves has well defined low and high frequency limits of $w_{\text{gw}} = -1/3$ and $\langle w_{\text{gw}} \rangle_x = 1/3$ respectively (where $\langle \dots \rangle_x$ denotes averaging over all space) for single fluid background cosmologies when neglecting neutrino anisotropic stress and this was shown analytically and numerically. Two regimes were found where the above limits are not valid. The first of these is during the matter–cosmological constant transition in the late Universe, where the equation of state of low-frequency gravitational waves decreases below $-1/3$ before returning to $-1/3$ when the expansion is dominated by the cosmological constant. The second is when neutrino anisotropic stress is included which causes low-frequency gravitational waves to have an initial equation of state of ~ -0.5 for current cosmological parameter values, before tending towards $-1/3$ around matter–radiation equality. Both of these effects were investigated and verified.

The physical effects of gravitational waves were determined with and without neutrino anisotropic stress and the changes in the CMB power spectrum along with the ability to shift the scale of the sound horizon and the Hubble parameter were discussed. Constraints were found for $10^{-16} \text{ Hz} \lesssim f \lesssim 10^{-15} \text{ Hz}$ for a steep power-law gravitational wave source finding $\Omega_{\text{gw}} < 8.4 \times 10^{-7}$ in the absence of neutrino anisotropic stress and $\Omega_{\text{gw}} < 8.6 \times 10^{-7}$ when it is included. Constraints were also found for $10^{-17} \text{ Hz} \lesssim f \lesssim 10^{-15} \text{ Hz}$ for delta-function sources of similar magnitude. These are new constraints of comparable sensitivity to the shortwave constraint but in a previously unconstrained frequency regime.

Consistency checks were performed on this method which showed errors that were below the requirement of current CMB experiments. A phenomenological approach was taken to the gravitational wave perturbations in this approach and a more theoretically motivated calculation of gravitational wave perturbations from the second-order Einstein tensor is the most obvious avenue for further work.

This approach was also used to calculate the range of validity of the short-wave approximation necessary for *Planck* CMB constraints, which had not been calculated explicitly; qualitative arguments have been used previously.

To complete the frequency coverage of gravitational wave constraints, the low-frequency constraint based on CMB polarisation was updated using a method that reconstructed the tensor power spectrum directly from observational data. This was converted to a constraint on the gravitational wave density parameter and applies for frequencies below that of the other two constraints, $10^{-18.5} \text{ Hz} \lesssim f \lesssim 10^{-16} \text{ Hz}$. The peak sensitivity is $\Omega_{\text{gw}} h^2 \lesssim 10^{-16}$ at a frequency corresponding to the horizon-size at matter–radiation equality. It was emphasised that this conversion from power spectrum to gravitational wave density parameter is only a first approximation due to the conversion equation used only being applicable for short wavelength gravitational waves. This is relevant to existing constraints on Ω_{gw} in the literature.

The change in observables calculated for the intermediate gravitational wave model motivated investigation of one of the observational problems of Λ CDM, commonly called the H_0 problem or Hubble tension. The effectiveness of early dark energy for solving this problem was investigated in Chapter 5. This started with a short review of models that aim to alleviate the Hubble tension before focusing on the axion model [301, 304, 305]. An MCMC analysis was carried out for CMB, BAO and distance ladder data, for two forms of the axion model, using a fluid approximation, along with a baseline Λ CDM model for comparison. The best-fit parameter values were consistent with those from previous analyses. The axion model is effective in reducing the Hubble tension to $\approx 2\sigma$ while also providing a better fit to the data than Λ CDM. However, the reduction in χ^2 was less than in previous analyses for the axion model in which the late-time equation of state, w_n was unconstrained.

A model-independent approach was developed that utilised a set of cosmological fluids that influence the background expansion at different times. The data can then be used to find the modifications to the background expansion that are most important for alleviating the Hubble tension and these modifications can be mapped onto models to allow them to be compared. A similar MCMC analysis to that used for the axion model was carried out for the model-independent approach. In this case the Hubble tension was reduced to $\approx 2.5\sigma$ and the best-fit χ^2 was also reduced. When reconstructing the background density and equation of state from the data, a peak before recombination similar to that for the best-fit axion model was favoured. This coincided with a transition in the effective equation of state from negative to positive values. After this the equation of state was consistent with the equation of state of the cosmological background suggesting that tracking dark energy may be a valid approach to alleviating the Hubble tension. This is an interesting area of future research.

A principal component analysis was carried out using the results of the MCMC for the model-independent approach. The correlations of the principal

components with cosmological parameters showed interesting degeneracies such as an increase in the amplitude and decrease in the tilt of the scalar power spectrum. It was also confirmed that reducing the Hubble tension is important for better fitting the cosmological data, as one would expect from the discrepancy in measurements of H_0 in the data set. Near future data will improve this analysis. Model comparison using this approach promises to be increasingly useful as more explanations for the Hubble tension are presented and this is an interesting area into which the existing analysis could be developed.

This thesis contains important work that advances our understanding of cosmological gravitational waves and the Hubble tension and suggests future work that combines the two. The analyses presented here will be improved by future experiments and offer the possibility of a large leap forward in our understanding of the evolution of the Universe.

Appendix: Homogeneous gravitational wave mode initial conditions

To calculate the initial conditions for the shortwave approximation homogeneous gravitational wave mode the perturbed Einstein and fluid equations will be solved using series solutions. Because we are considering super-horizon perturbations at early times, $k\tau \ll 1$ and the Universe is radiation dominated such that $\dot{a}/a = 1/\tau$. The dark matter and baryon components will be neglected here for simplicity¹ so only photons, massless neutrinos and gravitational waves are considered. In this case the Einstein equations in the synchronous gauge given in equations (1.35) (see section 1.3.2 for notation) become,

$$k^2\eta - \frac{1}{2\tau}\dot{h} = -\frac{3}{2\tau^2}(R_\gamma\delta_\gamma + R_\nu\delta_\nu + R_{\text{gw}}\delta_{\text{gw}}), \quad (\text{A.1a})$$

$$k^2\dot{\eta} = \frac{2}{\tau^2}(R_\gamma\theta_\gamma + R_\nu\theta_\nu + R_{\text{gw}}\theta_{\text{gw}}), \quad (\text{A.1b})$$

$$\ddot{h} + \frac{2}{\tau}\dot{h} - 2k^2\eta = -\frac{3}{\tau^2}(R_\gamma\delta_\gamma + R_\nu\delta_\nu + R_{\text{gw}}\delta_{\text{gw}}), \quad (\text{A.1c})$$

$$k^2\left(\dot{\alpha} + \frac{2}{\tau}\alpha - \eta\right) = -\frac{6}{\tau^2}(R_\nu\sigma_\nu + R_{\text{gw}}\sigma_{\text{gw}}). \quad (\text{A.1d})$$

The reader is reminded that the synchronous gauge is used as it allows for clear identification of the different modes (see below) and that $R_i = \bar{\rho}_i / \sum \bar{\rho}_i$. The fluid equations (see equations (1.37)) for the three radiation species are,

$$\dot{\delta}_\gamma + \frac{4}{3}\theta_\gamma + \frac{2}{3}\dot{h} = 0, \quad (\text{A.2a})$$

$$\dot{\theta}_\gamma - \frac{1}{4}k^2\delta_\gamma = 0, \quad (\text{A.2b})$$

¹The matter component perturbations can be easily calculated from the radiation components, see ref. [292].

$$\dot{\delta}_\nu + \frac{4}{3}\theta_\nu + \frac{2}{3}\dot{h} = 0, \quad (\text{A.2c})$$

$$\dot{\theta}_\nu - \frac{1}{4}k^2(\delta_\nu - 4\sigma_\nu) = 0, \quad (\text{A.2d})$$

$$\dot{\sigma}_\nu - \frac{2}{15}(2\theta_\nu + \dot{h} + 6\dot{\eta}) = 0, \quad (\text{A.2e})$$

$$\dot{\delta}_{\text{gw}} + \frac{4}{3}\theta_{\text{gw}} + \frac{2}{3}\dot{h} = 0, \quad (\text{A.2f})$$

$$\dot{\theta}_{\text{gw}} - \frac{1}{4}k^2(\delta_{\text{gw}} - 4\sigma_{\text{gw}}) = 0, \quad (\text{A.2g})$$

$$\dot{\sigma}_{\text{gw}} - \frac{2}{15}(2\theta_{\text{gw}} + \dot{h} + 6\dot{\eta}) = 0. \quad (\text{A.2h})$$

These equations allow the calculation of the 10 metric and fluid perturbations $\{h, \eta, \delta_i, \theta_i, \sigma_i\}$ of the radiation species, $i = \gamma, \nu, \text{gw}$.

To calculate the early time, super-horizon behaviour, series solutions of the above equations are sought. Because $k\tau \ll 1$ for the modes under consideration, $k\tau$ is the natural variable to expand in and such an expansion can be stopped at a specified order to calculate the initial conditions along with the low- $k\tau$ evolution of each of the perturbations. The initial value and the low- $k\tau$ evolution are often referred to simply as *initial conditions* in the cosmology community, as opposed to just the value at $k\tau \rightarrow 0$, and this shorthand will be taken here and where appropriate in the rest of this thesis. The $k\tau$ expansion is given in equation (1.39) for a general perturbation², ζ as,

$$\zeta = \sum_{i=0}^{\infty} \zeta_i(k\tau)^i, \quad (\text{1.39})$$

where the coefficients, ζ_i now encode the information about the perturbations initial value and their evolution.

Substituting series of the form of equation (1.39) for each of the perturbation quantities into equations (A.1) and (A.2) results in the coupled differential equations becoming coupled equations for the coefficients ζ_i . Therefore, finding the initial conditions becomes the problem of solving the set of simultaneous equations for the coefficients up to some fixed order in $k\tau$. In doing so, special

²Reproduced here for ease of reading.

care needs to be taken when considering the zeroth order coefficients,

$$\{h_0, \eta_0, \delta_{\gamma,0}, \theta_{\gamma,0}, \delta_{\nu,0}, \theta_{\nu,0}, \sigma_{\nu,0}, \delta_{\text{gw},0}, \theta_{\text{gw},0}, \sigma_{\text{gw},0}\}. \quad (\text{A.3})$$

Not all of these can be found explicitly from the Einstein and fluid equations and it is therefore possible to have multiple different non-zero zeroth order coefficients. This is dealt with by considering each possible non-zero coefficient separately and summing together the different *modes* found in each case. This is usually done through a correlation matrix of the different modes, which allows for cross-correlations between modes along with simple additive combination (see section 1.3.3). In the case considered here, the gravitational wave perturbations do not need to have their zeroth order coefficients fixed as they are instead fixed by the homogeneous condition. In the absence of gravitational waves the most commonly considered mode is the adiabatic mode which has,

$$\eta_0 = 1, \quad h_0 = \delta_{\gamma,0} = \theta_{\gamma,0} = \delta_{\nu,0} = \theta_{\nu,0} = \sigma_{\nu,0} = 0. \quad (\text{A.4})$$

Isocurvature modes have $\eta_0 = 0$ with non-zero coefficients in the fluid perturbations. These are found systematically in Bucher, Moodley, and Turok [48]. There they find a neutrino density isocurvature mode ($\delta_{\nu,0} \neq 0$) and a neutrino velocity isocurvature mode ($\theta_{\nu,0} \neq 0$). There are also baryon density and dark matter density isocurvature modes which are found when the matter species are also included.

The generalisation of the adiabatic mode to the gravitational wave case is the homogeneous mode³ where,

$$\eta_0 = 1, \quad h_0 = \theta_{\gamma,0} = \delta_{\nu,0} = \theta_{\nu,0} = \sigma_{\nu,0} = 0. \quad (\text{A.5})$$

³There is also a gravitational wave adiabatic mode, where the gravitational wave perturbations are identical to those for neutrinos, but this is less physically motivated, as discussed in section 2.5.4 and chapter 3.

The lowest order⁴ initial conditions in this case are,

$$h = \frac{1}{2}k^2\tau^2, \quad (\text{A.6a})$$

$$\eta = 1 + \eta_2 k^2 \tau^2, \quad (\text{A.6b})$$

$$\delta_\gamma = \frac{9 - 4R_\gamma + 12(19 - 4R_\gamma)\eta_2}{2R_\gamma} = \delta_{\gamma,0}, \quad (\text{A.6c})$$

$$\theta_\gamma = \frac{1}{4}\delta_{\gamma,0} k^2 \tau, \quad (\text{A.6d})$$

$$\delta_\nu = -\frac{1}{3}k^2\tau^2, \quad (\text{A.6e})$$

$$\theta_\nu = -\frac{1}{60}k^4\tau^3(3 + 16\eta_2), \quad (\text{A.6f})$$

$$\sigma_\nu = \frac{1}{15}k^2\tau^2(1 + \eta_2), \quad (\text{A.6g})$$

$$\delta_{\text{gw}} = -\frac{R_\gamma}{R_{\text{gw}}}\delta_{\gamma,0}, \quad (\text{A.6h})$$

$$\theta_{\text{gw}} = -\frac{R_\gamma}{R_{\text{gw}}}\frac{1}{4}\delta_{\gamma,0} k^2 \tau, \quad (\text{A.6i})$$

$$\sigma_{\text{gw}} = -\frac{1}{30}k^2\tau^2 \left(-2 - 24\eta_2 - \frac{R_\gamma}{R_{\text{gw}}}\delta_{\gamma,0} \right), \quad (\text{A.6j})$$

where the zeroth order photon density perturbation has been written as $\delta_{\gamma,0}$ to simplify notation for the other perturbations. The only unknown is the second order coefficient in the expansion of the metric perturbation, η which is denoted η_2 and, as mentioned in section 3.1.1, this is fixed by transforming to the Newtonian gauge and requiring that the density perturbation is zero. In a radiation dominated background the gauge transformation of equation (1.30a) for the gravitational wave density simplifies to,

$$\tilde{\delta}_{\text{gw}} = \delta_{\text{gw}} - \frac{2}{k^2\tau}(\dot{h} + 6\dot{\eta}), \quad (\text{A.7})$$

where $\tilde{\delta}_{\text{gw}}$ is the perturbation in the Newtonian gauge and the right-hand side contains only synchronous gauge quantities. Enforcing $\tilde{\delta}_{\text{gw}} = 0$,

$$\eta_2 = -\frac{(9 - 4R_\gamma + 4R_{\text{gw}})}{12(19 - 4R_\gamma + 4R_{\text{gw}})}. \quad (\text{A.8})$$

This is the value given in section 3.1.1 and specifically in table 3.1. Substi-

⁴All perturbations are given to lowest order except for η which has important evolution properties at second order.

tuting this value into equations (A.6) gives the rest of the homogeneous mode quantities for the radiation and metric perturbations given in table 3.1.

There are three new modes found in chapter 3. The first of these, the gravitational wave density isocurvature mode is found similarly to the homogeneous mode by enforcing,

$$\delta_{\text{gw},0} = 1, \quad h_0 = \eta_0 = \theta_{\gamma,0} = \theta_{\nu,0} = \sigma_{\nu,0} = 0, \quad (\text{A.9})$$

along with the homogeneous condition in the Newtonian gauge. The second, the gravitational wave velocity isocurvature mode is found using the homogeneous condition and the initial conditions,

$$\theta_{\text{gw},0} = k, \quad h_0 = \eta_0 = \theta_{\gamma,0} = \delta_{\nu,0} = \theta_{\nu,0} = 0. \quad (\text{A.10})$$

The final new mode, the gravitational wave shear isocurvature mode uses the initial conditions,

$$\sigma_{\text{gw},0} = 1, \quad h_0 = \eta_0 = \delta_{\gamma,0} = \theta_{\gamma,0} = \theta_{\nu,0} = 0, \quad (\text{A.11})$$

along with the homogeneous condition. The gravitational wave isocurvature modes coming from these choices are presented in table 3.3. It should be noted that these choices are not unique and other choices of the initial conditions give rise to the same modes. This was done systematically considering all combinations to guarantee that no modes were missed.

Bibliography

- [1] N. Aghanim et al. “Planck 2018 results. VI. Cosmological parameters”. In: *arXiv e-prints* (2018). arXiv: [1807.06209](#).
- [2] A. Einstein. “The foundation of the general theory of relativity”. In: *Annalen Phys.* 49.7 (1916), pp. 769–822.
- [3] J. A. Peacock. “Slipher, galaxies, and cosmological velocity fields”. In: *ASP Conf. Ser.* 471 (2013), p. 3. arXiv: [1301.7286](#) [[physics.hist-ph](#)].
- [4] E. Hubble. “A relation between distance and radial velocity among extragalactic nebulae”. In: *Proceedings of the National Academy of Sciences* 15.3 (1929), pp. 168–173. ISSN: 0027-8424. DOI: [10.1073/pnas.15.3.168](#).
- [5] G. Lemaître. “Un Univers homogène de masse constante et de rayon croissant rendant compte de la vitesse radiale des nébuleuses extragalactiques”. In: *Annales de la Société Scientifique de Bruxelles* 47 (Jan. 1927), pp. 49–59.
- [6] J. C. Mather et al. “Measurement of the Cosmic Microwave Background spectrum by the COBE FIRAS instrument”. In: *Astrophys. J.* 420 (1994), pp. 439–444. DOI: [10.1086/173574](#).
- [7] G. Hinshaw et al. “Three-year Wilkinson Microwave Anisotropy Probe (WMAP) observations: temperature analysis”. In: *The Astrophysical Journal Supplement Series* 170.2 (June 2007), pp. 288–334. ISSN: 1538-4365. DOI: [10.1086/513698](#).
- [8] P. A. R. Ade et al. “Planck early results. I. The Planck mission”. In: *Astron. Astrophys.* 536 (Dec. 2011), A1. ISSN: 1432-0746. DOI: [10.1051/0004-6361/201116464](#).
- [9] B. P. Abbott et al. “Observation of Gravitational Waves from a Binary Black Hole Merger”. In: *Phys. Rev. Lett.* 116 (6 Feb. 2016), p. 061102. DOI: [10.1103/PhysRevLett.116.061102](#).
- [10] A. G. Polnarev. “Polarization and anisotropy induced in the microwave vackground by cosmological gravitational waves”. In: *Sov. Astron.* 29 (Dec. 1985), pp. 607–613.
- [11] U. Seljak and M. Zaldarriaga. “Signature of gravity waves in polarization of the microwave background”. In: *Phys. Rev. Lett.* 78 (1997), pp. 2054–2057. DOI: [10.1103/PhysRevLett.78.2054](#). arXiv: [astro-ph/9609169](#).
- [12] U. Seljak. “Measuring polarization in cosmic microwave background”. In: *Astrophys. J.* 482 (1997), p. 6. DOI: [10.1086/304123](#). arXiv: [astro-ph/9608131](#).

- [13] M. Kamionkowski, A. Kosowsky, and A. Stebbins. “A Probe of primordial gravity waves and vorticity”. In: *Phys. Rev. Lett.* 78 (1997), pp. 2058–2061. DOI: [10.1103/PhysRevLett.78.2058](https://doi.org/10.1103/PhysRevLett.78.2058). arXiv: [astro-ph/9609132](https://arxiv.org/abs/astro-ph/9609132).
- [14] P. A. R. Ade et al. “BICEP2 / Keck Array x: Constraints on Primordial Gravitational Waves using Planck, WMAP, and New BICEP2/Keck Observations through the 2015 Season”. In: *Phys. Rev. Lett.* 121 (2018), p. 221301. DOI: [10.1103/PhysRevLett.121.221301](https://doi.org/10.1103/PhysRevLett.121.221301). arXiv: [1810.05216](https://arxiv.org/abs/1810.05216).
- [15] A. Friedmann. “Über die Möglichkeit einer Welt mit konstanter negativer Krümmung des Raumes”. In: *Zeitschrift für Physik* 21.1 (Dec. 1924), pp. 326–332. ISSN: 0044-3328. DOI: [10.1007/BF01328280](https://doi.org/10.1007/BF01328280).
- [16] J. A. Peacock et al. “A Measurement of the cosmological mass density from clustering in the 2dF Galaxy Redshift Survey”. In: *Nature* 410 (2001), pp. 169–173. DOI: [10.1038/35065528](https://doi.org/10.1038/35065528). arXiv: [astro-ph/0103143](https://arxiv.org/abs/astro-ph/0103143).
- [17] J. Yadav et al. “Testing homogeneity on large scales in the Sloan Digital Sky Survey Data Release One”. In: *Mon. Not. Roy. Astron. Soc.* 364 (2005), pp. 601–606. DOI: [10.1111/j.1365-2966.2005.09578.x](https://doi.org/10.1111/j.1365-2966.2005.09578.x). arXiv: [astro-ph/0504315](https://arxiv.org/abs/astro-ph/0504315).
- [18] H. P. Robertson. “Kinematics and World-Structure”. In: *Astrophys. J.* 82 (1935), pp. 284–301. DOI: [10.1086/143681](https://doi.org/10.1086/143681).
- [19] H. P. Robertson. “Kinematics and World-Structure. 2”. In: *Astrophys. J.* 83 (1935), pp. 187–201. DOI: [10.1086/143716](https://doi.org/10.1086/143716).
- [20] H. P. Robertson. “Kinematics and World-Structure. 3”. In: *Astrophys. J.* 83 (1936), pp. 257–271. DOI: [10.1086/143726](https://doi.org/10.1086/143726).
- [21] A. G. Walker. “On Milne’s Theory of World-Structure”. In: *Proc. Lond. Math. Soc.* s2-42.1 (1937), pp. 90–127. DOI: [10.1112/plms/s2-42.1.90](https://doi.org/10.1112/plms/s2-42.1.90).
- [22] S. Dodelson. *Modern Cosmology*. Academic Press. Academic Press, 2003. ISBN: 9780122191411.
- [23] A. H. Guth. “Inflationary universe: A possible solution to the horizon and flatness problems”. In: *Phys. Rev. D* 23 (2 Jan. 1981), pp. 347–356. DOI: [10.1103/PhysRevD.23.347](https://doi.org/10.1103/PhysRevD.23.347).
- [24] A. D. Linde. “A New Inflationary Universe Scenario: A Possible Solution of the Horizon, Flatness, Homogeneity, Isotropy and Primordial Monopole Problems”. In: *Phys. Lett. B* 108 (1982). [Adv. Ser. Astrophys. Cosmol.3,149(1987)], pp. 389–393. DOI: [10.1016/0370-2693\(82\)91219-9](https://doi.org/10.1016/0370-2693(82)91219-9).
- [25] A. D. Linde. “Coleman-Weinberg theory and the new inflationary universe scenario”. In: *Phys. Lett. B* 114.6 (1982), pp. 431–435. ISSN: 0370-2693. DOI: [https://doi.org/10.1016/0370-2693\(82\)90086-7](https://doi.org/10.1016/0370-2693(82)90086-7).
- [26] A. D. Linde. “Scalar Field Fluctuations in Expanding Universe and the New Inflationary Universe Scenario”. In: *Phys. Lett. B* 116 (1982), pp. 335–339. DOI: [10.1016/0370-2693\(82\)90293-3](https://doi.org/10.1016/0370-2693(82)90293-3).
- [27] A. Albrecht and P. J. Steinhardt. “Cosmology for Grand Unified Theories with Radiatively Induced Symmetry Breaking”. In: *Phys. Rev. Lett.* 48 (17 Apr. 1982), pp. 1220–1223. DOI: [10.1103/PhysRevLett.48.1220](https://doi.org/10.1103/PhysRevLett.48.1220).

- [28] S. Weinberg. *Cosmology*. OUP Oxford, 2008. ISBN: 9780191523601.
- [29] V. Mukhanov. *Physical Foundations of Cosmology*. Oxford: Cambridge University Press, 2005. DOI: [10.2277/0521563984](https://doi.org/10.2277/0521563984).
- [30] M. A. Amin et al. “Nonperturbative Dynamics Of Reheating After Inflation: A Review”. In: *Int. J. Mod. Phys. D* 24 (2014), p. 1530003. DOI: [10.1142/S0218271815300037](https://doi.org/10.1142/S0218271815300037). arXiv: [1410.3808](https://arxiv.org/abs/1410.3808).
- [31] L. Kofman, A. D. Linde, and A. A. Starobinsky. “Towards the theory of reheating after inflation”. In: *Phys. Rev. D* 56 (1997), pp. 3258–3295. DOI: [10.1103/PhysRevD.56.3258](https://doi.org/10.1103/PhysRevD.56.3258). arXiv: [hep-ph/9704452](https://arxiv.org/abs/hep-ph/9704452).
- [32] A. D. Linde. “Particle physics and inflationary cosmology”. In: *Contemp. Concepts Phys.* 5 (1990), pp. 1–362. arXiv: [hep-th/0503203](https://arxiv.org/abs/hep-th/0503203).
- [33] R. Allahverdi et al. “Reheating in Inflationary Cosmology: Theory and Applications”. In: *Ann. Rev. Nucl. Part. Sci.* 60 (2010), pp. 27–51. DOI: [10.1146/annurev.nucl.012809.104511](https://doi.org/10.1146/annurev.nucl.012809.104511). arXiv: [1001.2600](https://arxiv.org/abs/1001.2600).
- [34] D. J. Fixsen. “The Temperature of the Cosmic Microwave Background”. In: *Astrophys. J.* 707.2 (Dec. 2009), pp. 916–920. DOI: [10.1088/0004-637X/707/2/916](https://doi.org/10.1088/0004-637X/707/2/916). arXiv: [0911.1955](https://arxiv.org/abs/0911.1955).
- [35] M. Vogelsberger et al. “Cosmological Simulations of Galaxy Formation”. In: *Nature Rev. Phys.* 2.1 (2020), pp. 42–66. DOI: [10.1038/s42254-019-0127-2](https://doi.org/10.1038/s42254-019-0127-2). arXiv: [1909.07976](https://arxiv.org/abs/1909.07976) [[astro-ph.GA](https://arxiv.org/abs/1909.07976)].
- [36] E. Lifshitz. “Republication of: On the gravitational stability of the expanding universe”. In: *J. Phys.(USSR)* 10.2 (1946). Republished In: *Gen. Rel. Grav.* 49, no.2, 18(2017), p. 116. DOI: [10.1016/B978-0-08-036364-6.50020-X](https://doi.org/10.1016/B978-0-08-036364-6.50020-X), [10.1007/s10714-016-2165-8](https://doi.org/10.1007/s10714-016-2165-8).
- [37] P. J. E. Peebles and J. T. Yu. “Primeval Adiabatic Perturbation in an Expanding Universe”. In: *Astrophys. J.* 162 (Dec. 1970), p. 815. DOI: [10.1086/150713](https://doi.org/10.1086/150713).
- [38] L. R. W. Abramo, R. H. Brandenberger, and V. F. Mukhanov. “The Energy - momentum tensor for cosmological perturbations”. In: *Phys. Rev. D* 56 (1997), pp. 3248–3257. DOI: [10.1103/PhysRevD.56.3248](https://doi.org/10.1103/PhysRevD.56.3248). arXiv: [gr-qc/9704037](https://arxiv.org/abs/gr-qc/9704037).
- [39] R. H. Brandenberger. “Lectures on the theory of cosmological perturbations”. In: *Lect. Notes Phys.* 646 (2004), pp. 127–167. DOI: [10.1007/978-3-540-40918-2_5](https://doi.org/10.1007/978-3-540-40918-2_5). arXiv: [hep-th/0306071](https://arxiv.org/abs/hep-th/0306071).
- [40] D. Baumann. “Cosmology lecture notes”. URL: <http://theory.uchicago.edu/~liantaow/my-teaching/dark-matter-472/lectures.pdf>.
- [41] J. M. Bardeen. “Gauge Invariant Cosmological Perturbations”. In: *Phys. Rev. D* 22 (1980), pp. 1882–1905. DOI: [10.1103/PhysRevD.22.1882](https://doi.org/10.1103/PhysRevD.22.1882).
- [42] C.-P. Ma and E. Bertschinger. “Cosmological perturbation theory in the synchronous and conformal Newtonian gauges”. In: *Astrophys. J.* 455 (1995), pp. 7–25. DOI: [10.1086/176550](https://doi.org/10.1086/176550). arXiv: [astro-ph/9506072](https://arxiv.org/abs/astro-ph/9506072).
- [43] W. H. Press and E. T. Vishniac. “Tenacious myths about cosmological perturbations larger than the horizon size”. In: *Astrophys. J.* 239 (July 1980), pp. 1–11. DOI: [10.1086/158083](https://doi.org/10.1086/158083).

- [44] M. L. Wilson and J. Silk. “On the anisotropy of the cosmological background matter and radiation distribution. I - The radiation anisotropy in a spatially flat universe”. In: *Astrophys. J.* 243 (Jan. 1981), pp. 14–25. DOI: [10.1086/158561](https://doi.org/10.1086/158561).
- [45] Y. Suto, K. Sato, and H. Kodama. “Dynamical Evolution of Isothermal Density Perturbations in the Early Universe”. In: *Progress of Theoretical Physics* 73.5 (May 1985), pp. 1151–1164. ISSN: 0033-068X. DOI: [10.1143/PTP.73.1151](https://doi.org/10.1143/PTP.73.1151).
- [46] H. Kodama and M. Sasaki. “Evolution of isocurvature perturbations I: photon-baryon universe”. In: *International Journal of Modern Physics A* 01.01 (1986), pp. 265–301. DOI: [10.1142/S0217751X86000137](https://doi.org/10.1142/S0217751X86000137).
- [47] H. Kodama and M. Sasaki. “Evolution of isocurvature perturbations II: radiation-dust universe”. In: *International Journal of Modern Physics A* 02.02 (1987), pp. 491–560. DOI: [10.1142/S0217751X8700020X](https://doi.org/10.1142/S0217751X8700020X).
- [48] M. Bucher, K. Moodley, and N. Turok. “The General primordial cosmic perturbation”. In: *Phys. Rev. D* 62 (2000), p. 083508. DOI: [10.1103/PhysRevD.62.083508](https://doi.org/10.1103/PhysRevD.62.083508). arXiv: [astro-ph/9904231](https://arxiv.org/abs/astro-ph/9904231).
- [49] G. Gamow. “Expanding Universe and the Origin of Elements”. In: *Phys. Rev.* 70 (7-8 Oct. 1946), pp. 572–573. DOI: [10.1103/PhysRev.70.572.2](https://doi.org/10.1103/PhysRev.70.572.2).
- [50] A. A. Penzias and R. W. Wilson. “A Measurement of Excess Antenna Temperature at 4080 Mc/s.” In: *Astrophys. J.* 142 (July 1965), pp. 419–421. DOI: [10.1086/148307](https://doi.org/10.1086/148307).
- [51] R. H. Dicke et al. “Cosmic Black-Body Radiation.” In: *Astrophys. J.* 142 (July 1965), pp. 414–419. DOI: [10.1086/148306](https://doi.org/10.1086/148306).
- [52] G. F. Smoot et al. “Structure in the COBE Differential Microwave Radiometer First-Year Maps”. In: *Astrophys. J. Lett.* 396 (Sept. 1992), p. L1. DOI: [10.1086/186504](https://doi.org/10.1086/186504).
- [53] Planck Collaboration, P. A. R. Ade, and others. “Planck 2013 results. XV. CMB power spectra and likelihood”. In: *Astron. Astrophys.* 571, A15 (Oct. 2014), A15. DOI: [10.1051/0004-6361/201321573](https://doi.org/10.1051/0004-6361/201321573). arXiv: [1303.5075](https://arxiv.org/abs/1303.5075).
- [54] E. Bertschinger. “Cosmic Microwave Background Anisotropy”. URL: <https://ocw.mit.edu/courses/physics/8-942-cosmology-fall-2001/readings/cmbfluct03.pdf>.
- [55] J. R. Bond and G. Efstathiou. “Cosmic background radiation anisotropies in universes dominated by nonbaryonic dark matter”. In: *Astrophys. J.* 285 (Aug. 1984), pp. L45–L48. DOI: [10.1086/184362](https://doi.org/10.1086/184362).
- [56] U. Seljak and M. Zaldarriaga. “A Line of sight integration approach to cosmic microwave background anisotropies”. In: *Astrophys. J.* 469 (1996), pp. 437–444. DOI: [10.1086/177793](https://doi.org/10.1086/177793). arXiv: [astro-ph/9603033](https://arxiv.org/abs/astro-ph/9603033).
- [57] J. Pearson. “Cosmology lecture notes”. URL: http://www.jpoffline.com/datastore/physics_docs/lecturenotes/y4s8/earlyuniverse_ln.pdf.

- [58] R. K. Sachs and A. M. Wolfe. “Perturbations of a cosmological model and angular variations of the microwave background”. In: *Astrophys. J.* 147 (1967). [Gen. Rel. Grav.39,1929(2007)], pp. 73–90. DOI: [10.1007/s10714-007-0448-9](https://doi.org/10.1007/s10714-007-0448-9).
- [59] L. Amendola and S. Tsujikawa. *Dark Energy: Theory and Observations*. Cambridge University Press, 2010. ISBN: 9781139488570.
- [60] J. Silk. “Cosmic black body radiation and galaxy formation”. In: *Astrophys. J.* 151 (1968), pp. 459–471. DOI: [10.1086/149449](https://doi.org/10.1086/149449).
- [61] R. Weymann. “The Energy Spectrum of Radiation in the Expanding Universe”. In: *Astrophys. J.* 145 (Aug. 1966), p. 560. DOI: [10.1086/148795](https://doi.org/10.1086/148795).
- [62] Y. B. Zeldovich and R. A. Sunyaev. “The Interaction of Matter and Radiation in a Hot-Model Universe”. In: *Astrophys. Space Sci.* 4 (1969), pp. 301–316. DOI: [10.1007/BF00661821](https://doi.org/10.1007/BF00661821).
- [63] R. A. Sunyaev and Y. B. Zeldovich. “The Observations of relic radiation as a test of the nature of X-Ray radiation from the clusters of galaxies”. In: *Comments Astrophys. Space Phys.* 4 (1972), pp. 173–178.
- [64] Y. Rephaeli. “Comptonization of the cosmic microwave background: the Sunyaev-Zeldovich effect”. In: *Ann. Rev. Astron. Astrophys.* 33 (1995), pp. 541–579. DOI: [10.1146/annurev.aa.33.090195.002545](https://doi.org/10.1146/annurev.aa.33.090195.002545).
- [65] J. E. Carlstrom, G. P. Holder, and E. D. Reese. “Cosmology with the Sunyaev-Zel’dovich Effect”. In: *Annual Review of Astronomy and Astrophysics* 40.1 (2002), pp. 643–680. DOI: [10.1146/annurev.astro.40.060401.093803](https://doi.org/10.1146/annurev.astro.40.060401.093803).
- [66] Y. Rephaeli, S. Sadeh, and M. Shimon. “The Sunyaev-Zeldovich effect”. In: *Riv. Nuovo Cim.* 29N12 (2006), pp. 1–18. DOI: [10.1393/ncr/i2007-10015-9](https://doi.org/10.1393/ncr/i2007-10015-9). arXiv: [astro-ph/0511626](https://arxiv.org/abs/astro-ph/0511626).
- [67] P. A. R. Ade et al. “Planck 2015 results. XXIV. Cosmology from Sunyaev-Zeldovich cluster counts”. In: *Astron. Astrophys.* 594 (2016), A24. DOI: [10.1051/0004-6361/201525833](https://doi.org/10.1051/0004-6361/201525833). arXiv: [1502.01597](https://arxiv.org/abs/1502.01597).
- [68] N. Aghanim et al. “Planck 2015 results. XXII. A map of the thermal Sunyaev-Zeldovich effect”. In: *Astron. Astrophys.* 594 (2016), A22. DOI: [10.1051/0004-6361/201525826](https://doi.org/10.1051/0004-6361/201525826). arXiv: [1502.01596](https://arxiv.org/abs/1502.01596).
- [69] W. Hu and M. J. White. “A CMB polarization primer”. In: *New Astron.* 2 (1997), p. 323. DOI: [10.1016/S1384-1076\(97\)00022-5](https://doi.org/10.1016/S1384-1076(97)00022-5). arXiv: [astro-ph/9706147](https://arxiv.org/abs/astro-ph/9706147).
- [70] A. Challinor. “CMB anisotropy science: a review”. In: *Astrophysics from Antarctica*. Vol. 288. IAU Symposium. Jan. 2013, pp. 42–52. DOI: [10.1017/S1743921312016663](https://doi.org/10.1017/S1743921312016663). arXiv: [1210.6008](https://arxiv.org/abs/1210.6008).
- [71] M. J. Rees. “Polarization and Spectrum of the Primeval Radiation in an Anisotropic Universe”. In: *Astrophys. J.* 153 (July 1968), p. L1. DOI: [10.1086/180208](https://doi.org/10.1086/180208).
- [72] J. Kovac et al. “Detection of polarization in the cosmic microwave background using DASI”. In: *Nature* 420 (2002), pp. 772–787. DOI: [10.1038/nature01269](https://doi.org/10.1038/nature01269). arXiv: [astro-ph/0209478](https://arxiv.org/abs/astro-ph/0209478).

- [73] A. Kogut et al. “Wilkinson Microwave Anisotropy Probe (WMAP) first year observations: TE polarization”. In: *Astrophys. J. Suppl.* 148 (2003), p. 161. DOI: [10.1086/377219](https://doi.org/10.1086/377219). arXiv: [astro-ph/0302213](https://arxiv.org/abs/astro-ph/0302213).
- [74] M. Zaldarriaga and U. Seljak. “An all sky analysis of polarization in the microwave background”. In: *Phys. Rev. D* 55 (1997), pp. 1830–1840. DOI: [10.1103/PhysRevD.55.1830](https://doi.org/10.1103/PhysRevD.55.1830). arXiv: [astro-ph/9609170](https://arxiv.org/abs/astro-ph/9609170).
- [75] M. Kamionkowski, A. Kosowsky, and A. Stebbins. “Statistics of cosmic microwave background polarization”. In: *Phys. Rev. D* 55 (1997), pp. 7368–7388. DOI: [10.1103/PhysRevD.55.7368](https://doi.org/10.1103/PhysRevD.55.7368). arXiv: [astro-ph/9611125](https://arxiv.org/abs/astro-ph/9611125).
- [76] M. L. Brown, P. G. Castro, and A. N. Taylor. “CMB temperature and polarisation pseudo-C(l) estimators and covariances”. In: *Mon. Not. Roy. Astron. Soc.* 360 (2005), pp. 1262–1280. DOI: [10.1111/j.1365-2966.2005.09111.x](https://doi.org/10.1111/j.1365-2966.2005.09111.x). arXiv: [astro-ph/0410394](https://arxiv.org/abs/astro-ph/0410394).
- [77] D. Hanson et al. “Detection of B-mode Polarization in the Cosmic Microwave Background with Data from the South Pole Telescope”. In: *Phys. Rev. Lett.* 111.14 (2013), p. 141301. DOI: [10.1103/PhysRevLett.111.141301](https://doi.org/10.1103/PhysRevLett.111.141301). arXiv: [1307.5830](https://arxiv.org/abs/1307.5830).
- [78] E. Komatsu et al. “Five-Year Wilkinson Microwave Anisotropy Probe (WMAP) Observations: Cosmological Interpretation”. In: *Astrophys. J. Suppl.* 180 (2009), pp. 330–376. DOI: [10.1088/0067-0049/180/2/330](https://doi.org/10.1088/0067-0049/180/2/330). arXiv: [0803.0547](https://arxiv.org/abs/0803.0547) [[astro-ph](https://arxiv.org/abs/astro-ph)].
- [79] A. Challinor and H. Peiris. “Lecture notes on the physics of cosmic microwave background anisotropies”. In: *American Institute of Physics Conference Series*. Vol. 1132. American Institute of Physics Conference Series. May 2009, pp. 86–140. DOI: [10.1063/1.3151849](https://doi.org/10.1063/1.3151849). arXiv: [0903.5158](https://arxiv.org/abs/0903.5158).
- [80] P. A. R. Ade et al. “Detection of B-Mode Polarization at Degree Angular Scales by BICEP2”. In: *Phys. Rev. Lett.* 112.24 (2014), p. 241101. DOI: [10.1103/PhysRevLett.112.241101](https://doi.org/10.1103/PhysRevLett.112.241101). arXiv: [1403.3985](https://arxiv.org/abs/1403.3985).
- [81] P. A. R. Ade et al. “Joint Analysis of BICEP2/KeckArray and Planck Data”. In: *Phys. Rev. Lett.* 114 (2015), p. 101301. DOI: [10.1103/PhysRevLett.114.101301](https://doi.org/10.1103/PhysRevLett.114.101301). arXiv: [1502.00612](https://arxiv.org/abs/1502.00612).
- [82] A. Blanchard and J. Schneider. “Gravitational lensing effect on the fluctuations of the cosmic background radiation”. In: *Astron. Astrophys.* 184.1-2 (Oct. 1987), pp. 1–6.
- [83] U. Seljak. “Gravitational lensing effect on cosmic microwave background anisotropies: A Power spectrum approach”. In: *Astrophys. J.* 463 (1996), p. 1. DOI: [10.1086/177218](https://doi.org/10.1086/177218). arXiv: [astro-ph/9505109](https://arxiv.org/abs/astro-ph/9505109).
- [84] M. Zaldarriaga and U. Seljak. “Gravitational lensing effect on cosmic microwave background polarization”. In: *Phys. Rev. D* 58 (1998), p. 023003. DOI: [10.1103/PhysRevD.58.023003](https://doi.org/10.1103/PhysRevD.58.023003). arXiv: [astro-ph/9803150](https://arxiv.org/abs/astro-ph/9803150).
- [85] A. Lewis and A. Challinor. “Weak gravitational lensing of the CMB”. In: *Phys. Rept.* 429 (2006), pp. 1–65. DOI: [10.1016/j.physrep.2006.03.002](https://doi.org/10.1016/j.physrep.2006.03.002). arXiv: [astro-ph/0601594](https://arxiv.org/abs/astro-ph/0601594).

- [86] D. Hanson, A. Challinor, and A. Lewis. “Weak lensing of the CMB”. In: *General Relativity and Gravitation* 42.9 (Sept. 2010), pp. 2197–2218. DOI: [10.1007/s10714-010-1036-y](https://doi.org/10.1007/s10714-010-1036-y). arXiv: [0911.0612](https://arxiv.org/abs/0911.0612).
- [87] M. Kamionkowski, T. L. Smith, and A. Heavens. “CMB bispectrum, trispectrum, non-Gaussianity, and the Cramer-Rao bound”. In: *Phys. Rev. D* 83.2, 023007 (Jan. 2011), p. 023007. DOI: [10.1103/PhysRevD.83.023007](https://doi.org/10.1103/PhysRevD.83.023007). arXiv: [1010.0251](https://arxiv.org/abs/1010.0251) [[astro-ph.CO](https://arxiv.org/archive/astro)].
- [88] K. Sigurdson and A. Cooray. “Cosmic 21-cm delensing of microwave background polarization and the minimum detectable energy scale of inflation”. In: *Phys. Rev. Lett.* 95 (2005), p. 211303. DOI: [10.1103/PhysRevLett.95.211303](https://doi.org/10.1103/PhysRevLett.95.211303). arXiv: [astro-ph/0502549](https://arxiv.org/abs/astro-ph/0502549).
- [89] N. Aghanim et al. “Planck 2018 results. VIII. Gravitational lensing”. In: *arXiv e-prints* (2018). arXiv: [1807.06210](https://arxiv.org/abs/1807.06210).
- [90] B. P. Abbott et al. “A gravitational-wave measurement of the Hubble constant following the second observing run of Advanced LIGO and Virgo”. In: *arXiv e-prints* (2019). arXiv: [1908.06060](https://arxiv.org/abs/1908.06060).
- [91] N. Y. Gnedin and O. Y. Gnedin. “Cosmological neutrino background revisited”. In: *Astrophys. J.* 509 (1998), pp. 11–15. DOI: [10.1086/306469](https://doi.org/10.1086/306469). arXiv: [astro-ph/9712199](https://arxiv.org/abs/astro-ph/9712199).
- [92] G. Mangano et al. “Relic neutrino decoupling including flavor oscillations”. In: *Nucl. Phys.* B729 (2005), pp. 221–234. DOI: [10.1016/j.nuclphysb.2005.09.041](https://doi.org/10.1016/j.nuclphysb.2005.09.041). arXiv: [hep-ph/0506164](https://arxiv.org/abs/hep-ph/0506164).
- [93] P. F. de Salas and S. Pastor. “Relic neutrino decoupling with flavour oscillations revisited”. In: *JCAP* 1607 (2016), p. 051. DOI: [10.1088/1475-7516/2016/07/051](https://doi.org/10.1088/1475-7516/2016/07/051). arXiv: [1606.06986](https://arxiv.org/abs/1606.06986).
- [94] R. Cooke et al. “Precision measures of the primordial abundance of deuterium”. In: *Astrophys. J.* 781.1 (2014), p. 31. DOI: [10.1088/0004-637X/781/1/31](https://doi.org/10.1088/0004-637X/781/1/31). arXiv: [1308.3240](https://arxiv.org/abs/1308.3240) [[astro-ph.CO](https://arxiv.org/archive/astro)].
- [95] G. Rossi et al. “Constraints on dark radiation from cosmological probes”. In: *Phys. Rev. D* 92.6 (2015), p. 063505. DOI: [10.1103/PhysRevD.92.063505](https://doi.org/10.1103/PhysRevD.92.063505). arXiv: [1412.6763](https://arxiv.org/abs/1412.6763) [[astro-ph.CO](https://arxiv.org/archive/astro)].
- [96] T. L. Smith, E. Pierpaoli, and M. Kamionkowski. “A new cosmic microwave background constraint to primordial gravitational waves”. In: *Phys. Rev. Lett.* 97 (2006), p. 021301. DOI: [10.1103/PhysRevLett.97.021301](https://doi.org/10.1103/PhysRevLett.97.021301). arXiv: [astro-ph/0603144](https://arxiv.org/abs/astro-ph/0603144).
- [97] R. C. Nunes and A. Bonilla. “Probing the properties of relic neutrinos using the cosmic microwave background, the Hubble Space Telescope and galaxy clusters”. In: *Mon. Not. Roy. Astron. Soc.* 473.4 (2018), pp. 4404–4409. DOI: [10.1093/mnras/stx2661](https://doi.org/10.1093/mnras/stx2661). arXiv: [1710.10264](https://arxiv.org/abs/1710.10264).
- [98] M.-M. Zhao et al. “Constraining neutrino mass and extra relativistic degrees of freedom in dynamical dark energy models using Planck 2015 data in combination with low-redshift cosmological probes: basic extensions to Λ CDM cosmology”. In: *Mon. Not. Roy. Astron. Soc.* 469.2 (2017), pp. 1713–1724. DOI: [10.1093/mnras/stx978](https://doi.org/10.1093/mnras/stx978). arXiv: [1608.01219](https://arxiv.org/abs/1608.01219).

- [99] K. M. Nollett and G. Steigman. “BBN And The CMB Constrain Light, Electromagnetically Coupled WIMPs”. In: *Phys. Rev. D* 89.8 (2014), p. 083508. DOI: [10.1103/PhysRevD.89.083508](https://doi.org/10.1103/PhysRevD.89.083508). arXiv: [1312.5725](https://arxiv.org/abs/1312.5725).
- [100] G. Steigman and K. M. Nollett. “Light WIMPs, Equivalent Neutrinos, BBN, and the CMB”. In: *Mem. Soc. Ast. It.* 85 (2014), p. 175. arXiv: [1401.5488](https://arxiv.org/abs/1401.5488).
- [101] K. M. Nollett and G. Steigman. “BBN And The CMB Constrain Neutrino Coupled Light WIMPs”. In: *Phys. Rev. D* 91.8 (2015), p. 083505. DOI: [10.1103/PhysRevD.91.083505](https://doi.org/10.1103/PhysRevD.91.083505). arXiv: [1411.6005](https://arxiv.org/abs/1411.6005).
- [102] O. E. Bjaelde, S. Das, and A. Moss. “Origin of ΔN_{eff} as a Result of an Interaction between Dark Radiation and Dark Matter”. In: *JCAP* 10 (2012), p. 017. DOI: [10.1088/1475-7516/2012/10/017](https://doi.org/10.1088/1475-7516/2012/10/017). arXiv: [1205.0553](https://arxiv.org/abs/1205.0553).
- [103] S. Vagnozzi. “Cosmological searches for the neutrino mass scale and mass ordering”. In: *arXiv e-prints* (2019). arXiv: [1907.08010](https://arxiv.org/abs/1907.08010).
- [104] S. Henrot-Versillé et al. “Comparison of results on N_{eff} from various Planck likelihoods”. In: *Astron. Astrophys.* 623 (2019), A9. DOI: [10.1051/0004-6361/201834060](https://doi.org/10.1051/0004-6361/201834060). arXiv: [1807.05003](https://arxiv.org/abs/1807.05003).
- [105] Y. Fukuda et al. “Evidence for oscillation of atmospheric neutrinos”. In: *Phys. Rev. Lett.* 81 (1998), pp. 1562–1567. DOI: [10.1103/PhysRevLett.81.1562](https://doi.org/10.1103/PhysRevLett.81.1562). arXiv: [hep-ex/9807003](https://arxiv.org/abs/hep-ex/9807003).
- [106] K. N. Abazajian. “Sterile neutrinos in cosmology”. In: *Phys. Rept.* 711-712 (2017), pp. 1–28. DOI: [10.1016/j.physrep.2017.10.003](https://doi.org/10.1016/j.physrep.2017.10.003). arXiv: [1705.01837](https://arxiv.org/abs/1705.01837).
- [107] S. Gariazzo et al. “Neutrino masses and their ordering: Global Data, Priors and Models”. In: *JCAP* 03 (2018), p. 011. DOI: [10.1088/1475-7516/2018/03/011](https://doi.org/10.1088/1475-7516/2018/03/011). arXiv: [1801.04946](https://arxiv.org/abs/1801.04946).
- [108] M. Gonzalez-Garcia et al. “Global fit to three neutrino mixing: critical look at present precision”. In: *JHEP* 12 (2012), p. 123. DOI: [10.1007/JHEP12\(2012\)123](https://doi.org/10.1007/JHEP12(2012)123). arXiv: [1209.3023](https://arxiv.org/abs/1209.3023).
- [109] M. Tanabashi et al. “Review of Particle Physics”. In: *Phys. Rev. D* 98.3, 030001 (2018). Section 14: Neutrino Masses, Mixing and Oscillations, pp. 251–287. DOI: [10.1103/PhysRevD.98.030001](https://doi.org/10.1103/PhysRevD.98.030001).
- [110] P. de Salas et al. “Status of neutrino oscillations 2018: 3σ hint for normal mass ordering and improved CP sensitivity”. In: *Phys. Lett. B* 782 (2018), pp. 633–640. DOI: [10.1016/j.physletb.2018.06.019](https://doi.org/10.1016/j.physletb.2018.06.019). arXiv: [1708.01186](https://arxiv.org/abs/1708.01186).
- [111] F. Capozzi et al. “Current unknowns in the three neutrino framework”. In: *Prog. Part. Nucl. Phys.* 102 (2018), pp. 48–72. DOI: [10.1016/j.ppnp.2018.05.005](https://doi.org/10.1016/j.ppnp.2018.05.005). arXiv: [1804.09678](https://arxiv.org/abs/1804.09678).
- [112] S. Alam et al. “The clustering of galaxies in the completed SDSS-III Baryon Oscillation Spectroscopic Survey: cosmological analysis of the DR12 galaxy sample”. In: *Mon. Not. Roy. Astron. Soc.* 470.3 (2017), pp. 2617–2652. DOI: [10.1093/mnras/stx721](https://doi.org/10.1093/mnras/stx721). arXiv: [1607.03155](https://arxiv.org/abs/1607.03155).

- [113] F. Beutler et al. “The 6dF Galaxy Survey: baryon acoustic oscillations and the local Hubble constant”. In: *Mon. Not. Roy. Astron. Soc.* 416.4 (Oct. 2011), pp. 3017–3032. DOI: [10.1111/j.1365-2966.2011.19250.x](https://doi.org/10.1111/j.1365-2966.2011.19250.x). arXiv: [1106.3366](https://arxiv.org/abs/1106.3366).
- [114] A. J. Ross et al. “The clustering of the SDSS DR7 main Galaxy sample – I. A 4 per cent distance measure at $z = 0.15$ ”. In: *Mon. Not. Roy. Astron. Soc.* 449.1 (2015), pp. 835–847. DOI: [10.1093/mnras/stv154](https://doi.org/10.1093/mnras/stv154). arXiv: [1409.3242](https://arxiv.org/abs/1409.3242).
- [115] K. N. Abazajian and M. Kaplinghat. “Neutrino Physics from the Cosmic Microwave Background and Large-Scale Structure”. In: *Ann. Rev. Nucl. Part. Sci.* 66.1 (2016), pp. 401–420. DOI: [10.1146/annurev-nucl-102014-021908](https://doi.org/10.1146/annurev-nucl-102014-021908).
- [116] P. Ade et al. “Planck 2013 results. XVI. Cosmological parameters”. In: *Astron. Astrophys.* 571 (2014), A16. DOI: [10.1051/0004-6361/201321591](https://doi.org/10.1051/0004-6361/201321591). arXiv: [1303.5076](https://arxiv.org/abs/1303.5076) [[astro-ph.CO](https://arxiv.org/abs/1303.5076)].
- [117] A. Padilla. “Lectures on the Cosmological Constant Problem”. In: *arXiv e-prints* (Feb. 2015). arXiv: [1502.05296](https://arxiv.org/abs/1502.05296).
- [118] J. Martin. “Everything You Always Wanted To Know About The Cosmological Constant Problem (But Were Afraid To Ask)”. In: *Comptes Rendus Physique* 13 (2012), pp. 566–665. DOI: [10.1016/j.crhy.2012.04.008](https://doi.org/10.1016/j.crhy.2012.04.008). arXiv: [1205.3365](https://arxiv.org/abs/1205.3365).
- [119] E. J. Copeland, M. Sami, and S. Tsujikawa. “Dynamics of dark energy”. In: *Int. J. Mod. Phys. D* 15 (2006), pp. 1753–1936. DOI: [10.1142/S021827180600942X](https://doi.org/10.1142/S021827180600942X). arXiv: [hep-th/0603057](https://arxiv.org/abs/hep-th/0603057).
- [120] S. Capozziello et al. “Observational constraints on dark energy with generalized equations of state”. In: *Phys. Rev. D* 73 (2006), p. 043512. DOI: [10.1103/PhysRevD.73.043512](https://doi.org/10.1103/PhysRevD.73.043512). arXiv: [astro-ph/0508350](https://arxiv.org/abs/astro-ph/0508350).
- [121] K. Bamba et al. “Dark energy cosmology: the equivalent description via different theoretical models and cosmography tests”. In: *Astrophys. Space Sci.* 342 (2012), pp. 155–228. DOI: [10.1007/s10509-012-1181-8](https://doi.org/10.1007/s10509-012-1181-8). arXiv: [1205.3421](https://arxiv.org/abs/1205.3421).
- [122] W. Fang, W. Hu, and A. Lewis. “Crossing the Phantom Divide with Parameterized Post-Friedmann Dark Energy”. In: *Phys. Rev. D* 78 (2008), p. 087303. DOI: [10.1103/PhysRevD.78.087303](https://doi.org/10.1103/PhysRevD.78.087303). arXiv: [0808.3125](https://arxiv.org/abs/0808.3125).
- [123] D. Scolnic et al. “The Complete Light-curve Sample of Spectroscopically Confirmed SNe Ia from Pan-STARRS1 and Cosmological Constraints from the Combined Pantheon Sample”. In: *Astrophys. J.* 859.2 (2018), p. 101. DOI: [10.3847/1538-4357/aab9bb](https://doi.org/10.3847/1538-4357/aab9bb). arXiv: [1710.00845](https://arxiv.org/abs/1710.00845).
- [124] M. Tanabashi et al. “Review of Particle Physics”. In: *Phys. Rev. D* 98.3, 030001 (2018). Section 27: Dark Energy, pp. 406–414. DOI: [10.1103/PhysRevD.98.030001](https://doi.org/10.1103/PhysRevD.98.030001).
- [125] W. L. Freedman and B. F. Madore. “The Hubble Constant”. In: *Ann. Rev. Astron. Astrophys.* 48 (2010), pp. 673–710. DOI: [10.1146/annurev-astro-082708-101829](https://doi.org/10.1146/annurev-astro-082708-101829). arXiv: [1004.1856](https://arxiv.org/abs/1004.1856).

- [126] W. L. Freedman. “Cosmology at a Crossroads”. In: *Nat. Astron.* 1 (2017), p. 0121. DOI: [10.1038/s41550-017-0121](https://doi.org/10.1038/s41550-017-0121). arXiv: [1706.02739](https://arxiv.org/abs/1706.02739).
- [127] L. Verde, T. Treu, and A. Riess. “Tensions between the Early and the Late Universe”. In: July 2019. DOI: [10.1038/s41550-019-0902-0](https://doi.org/10.1038/s41550-019-0902-0). arXiv: [1907.10625](https://arxiv.org/abs/1907.10625).
- [128] A. G. Riess. “The Expansion of the Universe is Faster than Expected”. In: *Nature Rev. Phys.* 2.1 (2019), pp. 10–12. DOI: [10.1038/s42254-019-0137-0](https://doi.org/10.1038/s42254-019-0137-0). arXiv: [2001.03624](https://arxiv.org/abs/2001.03624).
- [129] A. G. Riess et al. “New Parallaxes of Galactic Cepheids from Spatially Scanning the Hubble Space Telescope: Implications for the Hubble Constant”. In: *Astrophys. J.* 855.2, 136 (Mar. 2018), p. 136. DOI: [10.3847/1538-4357/aaadb7](https://doi.org/10.3847/1538-4357/aaadb7). arXiv: [1801.01120](https://arxiv.org/abs/1801.01120).
- [130] W. L. Freedman et al. “The Carnegie-Chicago Hubble Program. VIII. An Independent Determination of the Hubble Constant Based on the Tip of the Red Giant Branch”. In: *arXiv e-prints* (July 2019). DOI: [10.3847/1538-4357/ab2f73](https://doi.org/10.3847/1538-4357/ab2f73). arXiv: [1907.05922](https://arxiv.org/abs/1907.05922).
- [131] W. Yuan et al. “Consistent Calibration of the Tip of the Red Giant Branch in the Large Magellanic Cloud on the Hubble Space Telescope Photometric System and a Re-determination of the Hubble Constant”. In: *Astrophys. J.* 886 (2019), p. 61. DOI: [10.3847/1538-4357/ab4bc9](https://doi.org/10.3847/1538-4357/ab4bc9). arXiv: [1908.00993](https://arxiv.org/abs/1908.00993).
- [132] T. Abbott et al. “Dark Energy Survey Year 1 Results: A Precise H_0 Estimate from DES Y1, BAO, and D/H Data”. In: *Mon. Not. Roy. Astron. Soc.* 480.3 (2018), pp. 3879–3888. DOI: [10.1093/mnras/sty1939](https://doi.org/10.1093/mnras/sty1939). arXiv: [1711.00403](https://arxiv.org/abs/1711.00403).
- [133] S. Alam et al. “The Completed SDSS-IV extended Baryon Oscillation Spectroscopic Survey: Cosmological Implications from two Decades of Spectroscopic Surveys at the Apache Point observatory”. In: *arXiv e-prints* (July 2020). arXiv: [2007.08991](https://arxiv.org/abs/2007.08991) [[astro-ph.CO](https://arxiv.org/abs/2007.08991)].
- [134] S. Aiola et al. “The Atacama Cosmology Telescope: DR4 Maps and Cosmological Parameters”. In: *arXiv e-prints* (July 2020). arXiv: [2007.07288](https://arxiv.org/abs/2007.07288) [[astro-ph.CO](https://arxiv.org/abs/2007.07288)].
- [135] M. Zumalacarregui. “Gravity in the Era of Equality: Towards solutions to the Hubble problem without fine-tuned initial conditions”. In: *arXiv e-prints* (Mar. 2020). arXiv: [2003.06396](https://arxiv.org/abs/2003.06396).
- [136] H. Desmond, B. Jain, and J. Sakstein. “Local resolution of the Hubble tension: The impact of screened fifth forces on the cosmic distance ladder”. In: *Phys. Rev. D* 100.4 (2019). [Erratum: *Phys.Rev.D* 101, 069904 (2020)], p. 043537. DOI: [10.1103/PhysRevD.100.043537](https://doi.org/10.1103/PhysRevD.100.043537). arXiv: [1907.03778](https://arxiv.org/abs/1907.03778).
- [137] L. Knox and M. Millea. “Hubble constant hunter’s guide”. In: *Phys. Rev. D* 101.4 (2020), p. 043533. DOI: [10.1103/PhysRevD.101.043533](https://doi.org/10.1103/PhysRevD.101.043533). arXiv: [1908.03663](https://arxiv.org/abs/1908.03663).

- [138] B. Abbott et al. “A gravitational-wave standard siren measurement of the Hubble constant”. In: *Nature* 551.7678 (2017), pp. 85–88. DOI: [10.1038/nature24471](https://doi.org/10.1038/nature24471). arXiv: [1710.05835](https://arxiv.org/abs/1710.05835).
- [139] W. Del Pozzo. “Measuring the Hubble constant using gravitational waves”. In: *J. Phys. Conf. Ser.* 484 (2014), p. 012030. DOI: [10.1088/1742-6596/484/1/012030](https://doi.org/10.1088/1742-6596/484/1/012030).
- [140] H.-Y. Chen, M. Fishbach, and D. E. Holz. “A two per cent Hubble constant measurement from standard sirens within five years”. In: *Nature* 562.7728 (2018), pp. 545–547. DOI: [10.1038/s41586-018-0606-0](https://doi.org/10.1038/s41586-018-0606-0). arXiv: [1712.06531](https://arxiv.org/abs/1712.06531).
- [141] A. Bhattacharyya et al. “Are H_0 and σ_8 tensions generic to present cosmological data?” In: *Astrophys. J.* 876.2 (2019), p. 143. DOI: [10.3847/1538-4357/ab12d6](https://doi.org/10.3847/1538-4357/ab12d6). arXiv: [1805.04716](https://arxiv.org/abs/1805.04716) [[astro-ph.CO](https://arxiv.org/archive/astro)].
- [142] A. Lewis, A. Challinor, and A. Lasenby. “Efficient computation of CMB anisotropies in closed FRW models”. In: *Astrophys. J.* 538 (2000), pp. 473–476. DOI: [10.1086/309179](https://doi.org/10.1086/309179). arXiv: [astro-ph/9911177](https://arxiv.org/abs/astro-ph/9911177).
- [143] M. Zaldarriaga, U. Seljak, and E. Bertschinger. “Integral solution for the microwave background anisotropies in nonflat universes”. In: *Astrophys. J.* 494 (1998), pp. 491–502. DOI: [10.1086/305223](https://doi.org/10.1086/305223). arXiv: [astro-ph/9704265](https://arxiv.org/abs/astro-ph/9704265).
- [144] M. Zaldarriaga and U. Seljak. “Cmbfast for spatially closed universes”. In: *Astrophys. J. Suppl.* 129 (2000), pp. 431–434. DOI: [10.1086/313423](https://doi.org/10.1086/313423). arXiv: [astro-ph/9911219](https://arxiv.org/abs/astro-ph/9911219).
- [145] S. Seager, D. D. Sasselov, and D. Scott. “A new calculation of the recombination epoch”. In: *Astrophys. J.* 523 (1999), pp. L1–L5. DOI: [10.1086/312250](https://doi.org/10.1086/312250). arXiv: [astro-ph/9909275](https://arxiv.org/abs/astro-ph/9909275).
- [146] D. Blas, J. Lesgourgues, and T. Tram. “The Cosmic Linear Anisotropy Solving System (CLASS). Part II: Approximation schemes”. In: *JCAP* 2011.7, 034 (July 2011), p. 034. DOI: [10.1088/1475-7516/2011/07/034](https://doi.org/10.1088/1475-7516/2011/07/034). arXiv: [1104.2933](https://arxiv.org/abs/1104.2933) [[astro-ph.CO](https://arxiv.org/archive/astro)].
- [147] A. Zucca et al. “MGCAMB with massive neutrinos and dynamical dark energy”. In: *JCAP* 05 (2019), p. 001. DOI: [10.1088/1475-7516/2019/05/001](https://doi.org/10.1088/1475-7516/2019/05/001). arXiv: [1901.05956](https://arxiv.org/abs/1901.05956) [[astro-ph.CO](https://arxiv.org/archive/astro)].
- [148] C. Garcia-Quintero et al. “Testing deviations from GR at cosmological scales including dynamical dark energy, massive neutrinos, functional or binned parametrizations, and spatial curvature”. In: *Phys. Rev. D* 100.10 (2019), p. 103530. DOI: [10.1103/PhysRevD.100.103530](https://doi.org/10.1103/PhysRevD.100.103530). arXiv: [1908.00290](https://arxiv.org/abs/1908.00290) [[astro-ph.CO](https://arxiv.org/archive/astro)].
- [149] B. Hu et al. “Effective Field Theory of Cosmic Acceleration: an implementation in CAMB”. In: *Phys. Rev. D* 89.10 (2014), p. 103530. DOI: [10.1103/PhysRevD.89.103530](https://doi.org/10.1103/PhysRevD.89.103530). arXiv: [1312.5742](https://arxiv.org/abs/1312.5742) [[astro-ph.CO](https://arxiv.org/archive/astro)].
- [150] N. Christensen et al. “II. Bayesian methods for cosmological parameter estimation from cosmic microwave background measurements”. In: *Class. Quant. Grav.* 18 (2001), p. 2677. DOI: [10.1088/0264-9381/18/14/306](https://doi.org/10.1088/0264-9381/18/14/306). arXiv: [astro-ph/0103134](https://arxiv.org/abs/astro-ph/0103134).

- [151] N. Aghanim et al. “Planck 2018 results. V. CMB power spectra and likelihoods”. In: *arXiv e-prints* (2019). arXiv: [1907.12875](#) [[astro-ph.CO](#)].
- [152] M. Douspis. “The Cosmic Microwave Background: Present status and cosmological perspectives: Cosmological Parameter Estimation: Method”. In: *Comptes Rendus Physique* 4 (2003), p. 881. DOI: [10.1016/j.crhy.2003.09.005](#). arXiv: [astro-ph/0402296](#).
- [153] M. Gerbino et al. “Likelihood methods for CMB experiments”. In: *Front. in Phys.* 8 (2020), p. 15. DOI: [10.3389/fphy.2020.00015](#). arXiv: [1909.09375](#) [[astro-ph.CO](#)].
- [154] L. Verde et al. “First year Wilkinson Microwave Anisotropy Probe (WMAP) observations: Parameter estimation methodology”. In: *Astrophys. J. Suppl.* 148 (2003), p. 195. DOI: [10.1086/377335](#). arXiv: [astro-ph/0302218](#).
- [155] A. Lewis and S. Bridle. “Cosmological parameters from CMB and other data: A Monte Carlo approach”. In: *Phys. Rev. D* 66 (2002), p. 103511. DOI: [10.1103/PhysRevD.66.103511](#). arXiv: [astro-ph/0205436](#).
- [156] L. Verde. “A practical guide to Basic Statistical Techniques for Data Analysis in Cosmology”. In: *arXiv e-prints* (Dec. 2007). arXiv: [0712.3028](#) [[astro-ph](#)].
- [157] T. Brinckmann and J. Lesgourgues. “MontePython 3: boosted MCMC sampler and other features”. In: *Phys. Dark Univ.* 24 (2019), p. 100260. DOI: [10.1016/j.dark.2018.100260](#). arXiv: [1804.07261](#) [[astro-ph.CO](#)].
- [158] J. Zuntz et al. “CosmoSIS: modular cosmological parameter estimation”. In: *Astron. Comput.* 12 (2015), pp. 45–59. DOI: [10.1016/j.ascom.2015.05.005](#). arXiv: [1409.3409](#) [[astro-ph.CO](#)].
- [159] J. Torrado and A. Lewis. “Cobaya: Code for Bayesian Analysis of hierarchical physical models”. In: *arXiv e-prints* (May 2020). arXiv: [2005.05290](#) [[astro-ph.IM](#)].
- [160] P. Ade et al. “Planck Early Results 20: New Light on Anomalous Microwave Emission from Spinning Dust Grains”. In: *Astron. Astrophys.* 536 (2011), A20. DOI: [10.1051/0004-6361/201116470](#). arXiv: [1101.2031](#) [[astro-ph.GA](#)].
- [161] C. Dickinson. “CMB foregrounds - A brief review”. In: *51st Rencontres de Moriond on Cosmology*. June 2016, pp. 53–62. arXiv: [1606.03606](#) [[astro-ph.CO](#)].
- [162] R. Adam et al. “Planck 2015 results. X. Diffuse component separation: Foreground maps”. In: *Astron. Astrophys.* 594 (2016), A10. DOI: [10.1051/0004-6361/201525967](#). arXiv: [1502.01588](#) [[astro-ph.CO](#)].
- [163] Y. Akrami et al. “Planck 2018 results. IV. Diffuse component separation”. In: *arXiv e-prints* (2018). arXiv: [1807.06208](#).
- [164] Y. Akrami et al. “Planck 2018 results. I. Overview and the cosmological legacy of Planck”. In: *arXiv e-prints* (July 2018). arXiv: [1807.06205](#) [[astro-ph.CO](#)].

- [165] J. E. Austermann et al. “SPTpol: an instrument for CMB polarization measurements with the South Pole Telescope”. In: *Millimeter, Submillimeter, and Far-Infrared Detectors and Instrumentation for Astronomy VI*. Ed. by W. S. Holland. Vol. 8452. International Society for Optics and Photonics. SPIE, 2012, pp. 393–410. DOI: [10.1117/12.927286](https://doi.org/10.1117/12.927286).
- [166] B. Benson et al. “SPT-3G: A Next-Generation Cosmic Microwave Background Polarization Experiment on the South Pole Telescope”. In: *Proc. SPIE Int. Soc. Opt. Eng.* 9153 (2014), 91531P. DOI: [10.1117/12.2057305](https://doi.org/10.1117/12.2057305). arXiv: [1407.2973](https://arxiv.org/abs/1407.2973) [[astro-ph.IM](https://arxiv.org/abs/1407.2973)].
- [167] R. Thornton et al. “The Atacama Cosmology Telescope: The polarization-sensitive ACTPol instrument”. In: *Astrophys. J. Suppl.* 227.2 (Dec. 2016), p. 21. DOI: [10.3847/1538-4365/227/2/21](https://doi.org/10.3847/1538-4365/227/2/21). arXiv: [1605.06569](https://arxiv.org/abs/1605.06569) [[astro-ph.IM](https://arxiv.org/abs/1605.06569)].
- [168] S. Simon et al. “The Advanced ACTPol 27/39 GHz Array”. In: *J. Low. Temp. Phys.* 193.5-6 (2018), pp. 1041–1047. DOI: [10.1007/s10909-018-1963-7](https://doi.org/10.1007/s10909-018-1963-7).
- [169] J. Grayson et al. “BICEP3 performance overview and planned Keck Array upgrade”. In: *Proc. SPIE Int. Soc. Opt. Eng.* 9914 (2016). Ed. by W. S. Holland and J. Zmuidzinas, 99140S. DOI: [10.1117/12.2233894](https://doi.org/10.1117/12.2233894). arXiv: [1607.04668](https://arxiv.org/abs/1607.04668) [[astro-ph.IM](https://arxiv.org/abs/1607.04668)].
- [170] Y. Inoue et al. “POLARBEAR-2: an instrument for CMB polarization measurements”. In: *Proc. SPIE Int. Soc. Opt. Eng.* 9914 (2016). Ed. by W. S. Holland and J. Zmuidzinas, p. 99141I. DOI: [10.1117/12.2231961](https://doi.org/10.1117/12.2231961). arXiv: [1608.03025](https://arxiv.org/abs/1608.03025) [[astro-ph.IM](https://arxiv.org/abs/1608.03025)].
- [171] K. Harrington et al. “The Cosmology Large Angular Scale Surveyor”. In: *Proc. SPIE*. Vol. 9914. Society of Photo-Optical Instrumentation Engineers (SPIE) Conference Series. 2016, 99141K. DOI: [10.1117/12.2233125](https://doi.org/10.1117/12.2233125).
- [172] B. Crill et al. “SPIDER: A Balloon-borne Large-scale CMB Polarimeter”. In: *Proc. SPIE Int. Soc. Opt. Eng.* 7010 (2008). Ed. by E. Atad-Ettedgui and D. Lemke, 70102P. DOI: [10.1117/12.787446](https://doi.org/10.1117/12.787446). arXiv: [0807.1548](https://arxiv.org/abs/0807.1548) [[astro-ph](https://arxiv.org/abs/0807.1548)].
- [173] P. Ade et al. “The Simons Observatory: Science goals and forecasts”. In: *JCAP* 02 (2019), p. 056. DOI: [10.1088/1475-7516/2019/02/056](https://doi.org/10.1088/1475-7516/2019/02/056). arXiv: [1808.07445](https://arxiv.org/abs/1808.07445) [[astro-ph.CO](https://arxiv.org/abs/1808.07445)].
- [174] B. M. Sutin et al. “PICO - the probe of inflation and cosmic origins”. In: *Proc. SPIE Int. Soc. Opt. Eng.* 10698 (2018). Ed. by G. Z. Angeli and P. Dierickx, 106984F. DOI: [10.1117/12.2311326](https://doi.org/10.1117/12.2311326). arXiv: [1808.01368](https://arxiv.org/abs/1808.01368) [[astro-ph.IM](https://arxiv.org/abs/1808.01368)].
- [175] K. N. Abazajian et al. “CMB-S4 Science Book, First Edition”. In: *arXiv e-prints* (Oct. 2016). arXiv: [1610.02743](https://arxiv.org/abs/1610.02743) [[astro-ph.CO](https://arxiv.org/abs/1610.02743)].
- [176] A. Kogut et al. “The Primordial Inflation Explorer (PIXIE): A Nulling Polarimeter for Cosmic Microwave Background Observations”. In: *JCAP* 07 (2011), p. 025. DOI: [10.1088/1475-7516/2011/07/025](https://doi.org/10.1088/1475-7516/2011/07/025). arXiv: [1105.2044](https://arxiv.org/abs/1105.2044) [[astro-ph.CO](https://arxiv.org/abs/1105.2044)].

- [177] J. Delabrouille et al. “Exploring cosmic origins with CORE: Survey requirements and mission design”. In: *JCAP* 04 (2018), p. 014. DOI: [10.1088/1475-7516/2018/04/014](https://doi.org/10.1088/1475-7516/2018/04/014). arXiv: [1706.04516](https://arxiv.org/abs/1706.04516) [astro-ph.IM].
- [178] M. Hazumi et al. “LiteBIRD: A Satellite for the Studies of B-Mode Polarization and Inflation from Cosmic Background Radiation Detection”. In: *J. Low. Temp. Phys.* 194.5-6 (2019), pp. 443–452. DOI: [10.1007/s10909-019-02150-5](https://doi.org/10.1007/s10909-019-02150-5).
- [179] D. J. Eisenstein, H.-j. Seo, and M. J. White. “On the Robustness of the Acoustic Scale in the Low-Redshift Clustering of Matter”. In: *Astrophys. J.* 664 (2007), pp. 660–674. DOI: [10.1086/518755](https://doi.org/10.1086/518755). arXiv: [astro-ph/0604361](https://arxiv.org/abs/astro-ph/0604361).
- [180] D. J. Eisenstein et al. “Detection of the Baryon Acoustic Peak in the Large-Scale Correlation Function of SDSS Luminous Red Galaxies”. In: *Astrophys. J.* 633 (2005), pp. 560–574. DOI: [10.1086/466512](https://doi.org/10.1086/466512). arXiv: [astro-ph/0501171](https://arxiv.org/abs/astro-ph/0501171).
- [181] S. Cole et al. “The 2dF Galaxy Redshift Survey: Power-spectrum analysis of the final dataset and cosmological implications”. In: *Mon. Not. Roy. Astron. Soc.* 362 (2005), pp. 505–534. DOI: [10.1111/j.1365-2966.2005.09318.x](https://doi.org/10.1111/j.1365-2966.2005.09318.x). arXiv: [astro-ph/0501174](https://arxiv.org/abs/astro-ph/0501174).
- [182] D. H. Weinberg et al. “Observational Probes of Cosmic Acceleration”. In: *Phys. Rept.* 530 (2013), pp. 87–255. DOI: [10.1016/j.physrep.2013.05.001](https://doi.org/10.1016/j.physrep.2013.05.001). arXiv: [1201.2434](https://arxiv.org/abs/1201.2434) [astro-ph.CO].
- [183] P. Lemos et al. “Model independent $H(z)$ reconstruction using the cosmic inverse distance ladder”. In: *Mon. Not. Roy. Astron. Soc.* 483.4 (2019), pp. 4803–4810. DOI: [10.1093/mnras/sty3082](https://doi.org/10.1093/mnras/sty3082). arXiv: [1806.06781](https://arxiv.org/abs/1806.06781) [astro-ph.CO].
- [184] F. Iocco et al. “Primordial Nucleosynthesis: from precision cosmology to fundamental physics”. In: *Phys. Rept.* 472 (2009), pp. 1–76. DOI: [10.1016/j.physrep.2009.02.002](https://doi.org/10.1016/j.physrep.2009.02.002). arXiv: [0809.0631](https://arxiv.org/abs/0809.0631) [astro-ph].
- [185] G. Steigman. “Neutrinos And Big Bang Nucleosynthesis”. In: *Adv. High Energy Phys.* 2012 (2012), p. 268321. DOI: [10.1155/2012/268321](https://doi.org/10.1155/2012/268321). arXiv: [1208.0032](https://arxiv.org/abs/1208.0032) [hep-ph].
- [186] B. D. Fields, P. Molaro, and S. Sarkar. “Big-Bang Nucleosynthesis”. In: *Chin. Phys. C* 38 (2014), pp. 339–344. arXiv: [1412.1408](https://arxiv.org/abs/1412.1408) [astro-ph.CO].
- [187] E. Aver, K. A. Olive, and E. D. Skillman. “The effects of He I λ 10830 on helium abundance determinations”. In: *JCAP* 07 (2015), p. 011. DOI: [10.1088/1475-7516/2015/07/011](https://doi.org/10.1088/1475-7516/2015/07/011). arXiv: [1503.08146](https://arxiv.org/abs/1503.08146) [astro-ph.CO].
- [188] A. Peimbert, M. Peimbert, and V. Luridiana. “The primordial helium abundance and the number of neutrino families”. In: *Rev. Mex. Astron. Astrofis.* 52.2 (2016), pp. 419–424. arXiv: [1608.02062](https://arxiv.org/abs/1608.02062) [astro-ph.CO].
- [189] R. J. Cooke, M. Pettini, and C. C. Steidel. “One Percent Determination of the Primordial Deuterium Abundance”. In: *Astrophys. J.* 855.2 (2018), p. 102. DOI: [10.3847/1538-4357/aaab53](https://doi.org/10.3847/1538-4357/aaab53). arXiv: [1710.11129](https://arxiv.org/abs/1710.11129) [astro-ph.CO].

- [190] J. L. Cervantes-Cota, S. Galindo-Uribarri, and G.-F. Smoot. “A Brief History of Gravitational Waves”. In: *Universe* 2.3 (2016), p. 22. DOI: [10.3390/universe2030022](https://doi.org/10.3390/universe2030022). arXiv: [1609.09400](https://arxiv.org/abs/1609.09400) [physics.hist-ph].
- [191] N. Christensen. “Stochastic Gravitational Wave Backgrounds”. In: *Rept. Prog. Phys.* 82.1 (2019), p. 016903. DOI: [10.1088/1361-6633/aae6b5](https://doi.org/10.1088/1361-6633/aae6b5). arXiv: [1811.08797](https://arxiv.org/abs/1811.08797) [gr-qc].
- [192] C. Misner, K. Thorne, and J. Wheeler. *Gravitation*. Gravitation. W. H. Freeman, 1973. ISBN: 9780716703440.
- [193] T. G. F. Li. “Extracting Physics from Gravitational Waves: Testing the Strong-field Dynamics of General Relativity and Inferring the Large-scale Structure of the Universe”. PhD thesis. Vrije U., Amsterdam, 2013. URL: https://www.nikhef.nl/pub/services/biblio/theses_pdf/thesis_T_G_F_Li.pdf.
- [194] C. Caprini and D. G. Figueroa. “Cosmological Backgrounds of Gravitational Waves”. In: *Class. Quant. Grav.* 35.16 (2018), p. 163001. DOI: [10.1088/1361-6382/aac608](https://doi.org/10.1088/1361-6382/aac608). arXiv: [1801.04268](https://arxiv.org/abs/1801.04268) [astro-ph.CO].
- [195] S. Weinberg. “Damping of tensor modes in cosmology”. In: *Phys. Rev. D* 69 (2004), p. 023503. DOI: [10.1103/PhysRevD.69.023503](https://doi.org/10.1103/PhysRevD.69.023503). arXiv: [astro-ph/0306304](https://arxiv.org/abs/astro-ph/0306304).
- [196] R. A. Isaacson. “Gravitational Radiation in the Limit of High Frequency. I. The Linear Approximation and Geometrical Optics”. In: *Phys. Rev.* 166 (1967), pp. 1263–1271. DOI: [10.1103/PhysRev.166.1263](https://doi.org/10.1103/PhysRev.166.1263).
- [197] R. A. Isaacson. “Gravitational Radiation in the Limit of High Frequency. II. Nonlinear Terms and the Effective Stress Tensor”. In: *Phys. Rev.* 166 (1968), pp. 1272–1279. DOI: [10.1103/PhysRev.166.1272](https://doi.org/10.1103/PhysRev.166.1272).
- [198] M. Maggiore. *Gravitational Waves. Vol. 1: Theory and Experiments*. Oxford Master Series in Physics. Oxford University Press, 2007. ISBN: 978-0-19-857074-5.
- [199] L. Landau and E. Lifshitz. *The Classical Theory of Fields*. Vol. Volume 2. Course of Theoretical Physics. Oxford: Pergamon Press, 1975. ISBN: 978-0-08-018176-9.
- [200] D. Su and Y. Zhang. “Energy Momentum Pseudo-Tensor of Relic Gravitational Wave in Expanding Universe”. In: *Phys. Rev. D* 85 (2012), p. 104012. DOI: [10.1103/PhysRevD.85.104012](https://doi.org/10.1103/PhysRevD.85.104012). arXiv: [1204.0089](https://arxiv.org/abs/1204.0089) [gr-qc].
- [201] V. F. Mukhanov, L. W. Abramo, and R. H. Brandenberger. “On the Back reaction problem for gravitational perturbations”. In: *Phys. Rev. Lett.* 78 (1997), pp. 1624–1627. DOI: [10.1103/PhysRevLett.78.1624](https://doi.org/10.1103/PhysRevLett.78.1624). arXiv: [gr-qc/9609026](https://arxiv.org/abs/gr-qc/9609026).
- [202] M. Giovannini. “Dynamical back-reaction of relic gravitons”. In: *Phys. Rev. D* 73 (2006), p. 083505. DOI: [10.1103/PhysRevD.73.083505](https://doi.org/10.1103/PhysRevD.73.083505). arXiv: [hep-th/0601097](https://arxiv.org/abs/hep-th/0601097).
- [203] R. Brandenberger and T. Takahashi. “Back-Reaction of Gravitational Waves Revisited”. In: *JCAP* 1807.07 (2018), p. 040. DOI: [10.1088/1475-7516/2018/07/040](https://doi.org/10.1088/1475-7516/2018/07/040). arXiv: [1805.02424](https://arxiv.org/abs/1805.02424).

- [204] P. Martineau and R. H. Brandenberger. “The Effects of gravitational back-reaction on cosmological perturbations”. In: *Phys. Rev. D* 72 (2005), p. 023507. DOI: [10.1103/PhysRevD.72.023507](https://doi.org/10.1103/PhysRevD.72.023507). arXiv: [astro-ph/0505236](https://arxiv.org/abs/astro-ph/0505236).
- [205] P. D. Lasky et al. “Gravitational-wave cosmology across 29 decades in frequency”. In: *Phys. Rev. X* 6.1 (2016), p. 011035. DOI: [10.1103/PhysRevX.6.011035](https://doi.org/10.1103/PhysRevX.6.011035). arXiv: [1511.05994](https://arxiv.org/abs/1511.05994) [[astro-ph.CO](https://arxiv.org/archive/astro)].
- [206] M. Maggiore. “Stochastic backgrounds of gravitational waves”. In: *ICTP Lect. Notes Ser.* 3 (2001). Ed. by V. Ferrari, J. Miller, and L. Rezzolla, pp. 397–414. arXiv: [gr-qc/0008027](https://arxiv.org/abs/gr-qc/0008027).
- [207] M. Maggiore. “Gravitational wave experiments and early universe cosmology”. In: *Phys. Rept.* 331 (2000), pp. 283–367. DOI: [10.1016/S0370-1573\(99\)00102-7](https://doi.org/10.1016/S0370-1573(99)00102-7). arXiv: [gr-qc/9909001](https://arxiv.org/abs/gr-qc/9909001).
- [208] E. Thrane and J. D. Romano. “Sensitivity curves for searches for gravitational-wave backgrounds”. In: *Phys. Rev. D* 88 (Dec. 2013), p. 124032. DOI: [10.1103/PhysRevD.88.124032](https://doi.org/10.1103/PhysRevD.88.124032). arXiv: [1310.5300](https://arxiv.org/abs/1310.5300) [[astro-ph.IM](https://arxiv.org/archive/astro)].
- [209] E. H. Tanin and T. Tenkanen. “Gravitational wave constraints on the observable inflation”. In: *arXiv e-prints* (Apr. 2020). arXiv: [2004.10702](https://arxiv.org/abs/2004.10702) [[astro-ph.CO](https://arxiv.org/archive/astro)].
- [210] M. S. Turner, M. J. White, and J. E. Lidsey. “Tensor perturbations in inflationary models as a probe of cosmology”. In: *Phys. Rev. D* 48 (1993), pp. 4613–4622. DOI: [10.1103/PhysRevD.48.4613](https://doi.org/10.1103/PhysRevD.48.4613). arXiv: [astro-ph/9306029](https://arxiv.org/abs/astro-ph/9306029).
- [211] T. L. Smith, M. Kamionkowski, and A. Cooray. “Direct detection of the inflationary gravitational wave background”. In: *Phys. Rev. D* 73 (2006), p. 023504. DOI: [10.1103/PhysRevD.73.023504](https://doi.org/10.1103/PhysRevD.73.023504). arXiv: [astro-ph/0506422](https://arxiv.org/abs/astro-ph/0506422).
- [212] Y. Watanabe and E. Komatsu. “Improved Calculation of the Primordial Gravitational Wave Spectrum in the Standard Model”. In: *Phys. Rev. D* 73 (2006), p. 123515. DOI: [10.1103/PhysRevD.73.123515](https://doi.org/10.1103/PhysRevD.73.123515). arXiv: [astro-ph/0604176](https://arxiv.org/abs/astro-ph/0604176).
- [213] B. Allen and S. Koranda. “Temperature fluctuations in the cosmic background radiation from inflationary cosmological models”. In: *Phys. Rev. D* 50 (1994), p. 3713. DOI: [10.1103/PhysRevD.50.3713](https://doi.org/10.1103/PhysRevD.50.3713). arXiv: [astro-ph/9404068](https://arxiv.org/abs/astro-ph/9404068).
- [214] B. Allen. “The Stochastic gravity wave background: Sources and detection”. In: *Les Houches School of Physics: Astrophysical Sources of Gravitational Radiation*. Apr. 1996, pp. 373–417. arXiv: [gr-qc/9604033](https://arxiv.org/abs/gr-qc/9604033).
- [215] LIGO Collaboration and VIRGO Collaboration, B. P. Abbott, et al. “An upper limit on the stochastic gravitational-wave background of cosmological origin”. In: *Nature* 460.7258 (Aug. 2009), pp. 990–994. DOI: [10.1038/nature08278](https://doi.org/10.1038/nature08278). arXiv: [0910.5772](https://arxiv.org/abs/0910.5772) [[astro-ph.CO](https://arxiv.org/archive/astro)].

- [216] R. H. Cyburt et al. “New BBN limits on physics beyond the standard model from ${}^4\text{He}$ ”. In: *Astropart. Phys.* 23 (2005), pp. 313–323. DOI: [10.1016/j.astropartphys.2005.01.005](https://doi.org/10.1016/j.astropartphys.2005.01.005). arXiv: [astro-ph/0408033](https://arxiv.org/abs/astro-ph/0408033) [astro-ph].
- [217] Y. Izotov, G. Stasinska, and N. Guseva. “Primordial 4He abundance: a determination based on the largest sample of HII regions with a methodology tested on model HII regions”. In: *Astron. Astrophys.* 558 (2013), A57. DOI: [10.1051/0004-6361/201220782](https://doi.org/10.1051/0004-6361/201220782). arXiv: [1308.2100](https://arxiv.org/abs/1308.2100) [astro-ph.CO].
- [218] M. Maggiore. *Gravitational Waves. Vol. 2: Astrophysics and Cosmology*. Oxford University Press, 2018. ISBN: 9780198570899.
- [219] T. L. Smith. “The gravity of the situation”. PhD thesis. California Institute of Technology, 2008. URL: <http://resolver.caltech.edu/CaltechETD:etd-05282008-153540>.
- [220] M. Viel, J. Weller, and M. Haehnelt. “Constraints on the primordial power spectrum from high resolution Lyman-alpha forest spectra and WMAP”. In: *Mon. Not. Roy. Astron. Soc.* 355 (2004), p. L23. DOI: [10.1111/j.1365-2966.2004.08498.x](https://doi.org/10.1111/j.1365-2966.2004.08498.x). arXiv: [astro-ph/0407294](https://arxiv.org/abs/astro-ph/0407294).
- [221] I. Sendra and T. L. Smith. “Improved limits on short-wavelength gravitational waves from the cosmic microwave background”. In: *Phys. Rev. D* 85 (12 June 2012), p. 123002. DOI: [10.1103/PhysRevD.85.123002](https://doi.org/10.1103/PhysRevD.85.123002). arXiv: [1203.4232](https://arxiv.org/abs/1203.4232).
- [222] S. Henrot-Versillé et al. “Improved constraint on the primordial gravitational-wave density using recent cosmological data and its impact on cosmic string models”. In: *Classical and Quantum Gravity* 32.4 (Jan. 2015), p. 045003. DOI: [10.1088/0264-9381/32/4/045003](https://doi.org/10.1088/0264-9381/32/4/045003). arXiv: [1408.5299](https://arxiv.org/abs/1408.5299) [astro-ph.CO].
- [223] L. Pagano, L. Salvati, and A. Melchiorri. “New constraints on primordial gravitational waves from Planck 2015”. In: *Phys. Lett. B* 760 (2016), pp. 823–825. DOI: [10.1016/j.physletb.2016.07.078](https://doi.org/10.1016/j.physletb.2016.07.078). arXiv: [1508.02393](https://arxiv.org/abs/1508.02393).
- [224] D. V. Martynov et al. “Sensitivity of the Advanced LIGO detectors at the beginning of gravitational wave astronomy”. In: *Phys. Rev. D* 93.11 (2016). [Addendum: *Phys.Rev.D* 97, 059901 (2018)], p. 112004. DOI: [10.1103/PhysRevD.93.112004](https://doi.org/10.1103/PhysRevD.93.112004). arXiv: [1604.00439](https://arxiv.org/abs/1604.00439) [astro-ph.IM].
- [225] B. Abbott et al. “GW170814: A Three-Detector Observation of Gravitational Waves from a Binary Black Hole Coalescence”. In: *Phys. Rev. Lett.* 119.14 (2017), p. 141101. DOI: [10.1103/PhysRevLett.119.141101](https://doi.org/10.1103/PhysRevLett.119.141101). arXiv: [1709.09660](https://arxiv.org/abs/1709.09660) [gr-qc].
- [226] C. Affeldt et al. “Advanced techniques in GEO 600”. In: *Class. Quant. Grav.* 31.22 (2014), p. 224002. DOI: [10.1088/0264-9381/31/22/224002](https://doi.org/10.1088/0264-9381/31/22/224002).
- [227] T. Akutsu et al. “KAGRA: 2.5 Generation Interferometric Gravitational Wave Detector”. In: *Nat. Astron.* 3.1 (2019), pp. 35–40. DOI: [10.1038/s41550-018-0658-y](https://doi.org/10.1038/s41550-018-0658-y). arXiv: [1811.08079](https://arxiv.org/abs/1811.08079) [gr-qc].

- [228] S. Haino. “KAGRA, Underground Cryogenic Gravitational Wave Telescope”. In: *Proceedings, 28th International Symposium on Lepton Photon Interactions at High Energies (LP17): Guangzhou (Guangdong), China*. Ed. by W. Wang and Z.-z. Xing. 2020, pp. 174–184. DOI: [10.1142/9789811207402_0012](https://doi.org/10.1142/9789811207402_0012).
- [229] B. P. Abbott et al. “Multi-messenger Observations of a Binary Neutron Star Merger”. In: *Astrophys. J.* 848.2 (2017), p. L12. DOI: [10.3847/2041-8213/aa91c9](https://doi.org/10.3847/2041-8213/aa91c9). arXiv: [1710.05833](https://arxiv.org/abs/1710.05833).
- [230] N. Christensen. “Searching for the Stochastic Gravitational-Wave Background with Advanced LIGO and Advanced Virgo”. In: *52nd Rencontres de Moriond on Gravitation*. 2017, pp. 11–20. URL: <https://s3.cern.ch/inspire-prod-files-d/d2337a1a405ee309c429acd9a1afb98d>.
- [231] B. Abbott et al. “Search for the isotropic stochastic background using data from Advanced LIGO’s second observing run”. In: *Phys. Rev. D* 100.6 (2019), p. 061101. DOI: [10.1103/PhysRevD.100.061101](https://doi.org/10.1103/PhysRevD.100.061101). arXiv: [1903.02886](https://arxiv.org/abs/1903.02886) [gr-qc].
- [232] B. Sathyaprakash et al. “Scientific Objectives of Einstein Telescope”. In: *Class. Quant. Grav.* 29 (2012). Ed. by M. Hannam et al. [Erratum: *Class.Quant.Grav.* 30, 079501 (2013)], p.124013. DOI: [10.1088/0264-9381/29/12/124013](https://doi.org/10.1088/0264-9381/29/12/124013). arXiv: [1206.0331](https://arxiv.org/abs/1206.0331) [gr-qc].
- [233] P. Amaro-Seoane et al. “Laser Interferometer Space Antenna”. In: *arXiv e-prints* (Feb. 2017). arXiv: [1702.00786](https://arxiv.org/abs/1702.00786) [astro-ph.IM].
- [234] S. Kawamura et al. “The Japanese space gravitational wave antenna DECIGO”. In: *Class. Quant. Grav.* 23 (2006). Ed. by N. Mio, S125–S132. DOI: [10.1088/0264-9381/23/8/S17](https://doi.org/10.1088/0264-9381/23/8/S17).
- [235] G. Harry et al. “Laser interferometry for the big bang observer”. In: *Class. Quant. Grav.* 23 (2006). [Erratum: *Class.Quant.Grav.* 23, 7361 (2006)], pp. 4887–4894. DOI: [10.1088/0264-9381/23/15/008](https://doi.org/10.1088/0264-9381/23/15/008).
- [236] J. Crowder and N. J. Cornish. “Beyond LISA: Exploring future gravitational wave missions”. In: *Phys. Rev. D* 72 (2005), p. 083005. DOI: [10.1103/PhysRevD.72.083005](https://doi.org/10.1103/PhysRevD.72.083005). arXiv: [gr-qc/0506015](https://arxiv.org/abs/gr-qc/0506015).
- [237] R. Hulse and J. Taylor. “Discovery of a pulsar in a binary system”. In: *Astrophys. J. Lett.* 195 (1975), pp. L51–L53. DOI: [10.1086/181708](https://doi.org/10.1086/181708).
- [238] J. Taylor and J. Weisberg. “A new test of general relativity: Gravitational radiation and the binary pulsar PS R 1913+16”. In: *Astrophys. J.* 253 (1982), pp. 908–920. DOI: [10.1086/159690](https://doi.org/10.1086/159690).
- [239] J. H. Taylor and J. Weisberg. “Further experimental tests of relativistic gravity using the binary pulsar PSR 1913+16”. In: *Astrophys. J.* 345 (1989), pp. 434–450. DOI: [10.1086/167917](https://doi.org/10.1086/167917).
- [240] D. Lorimer. “Binary and Millisecond Pulsars”. In: *Living Rev. Rel.* 11 (2008), p. 8. DOI: [10.12942/lrr-2008-8](https://doi.org/10.12942/lrr-2008-8). arXiv: [0811.0762](https://arxiv.org/abs/0811.0762) [astro-ph].
- [241] S. E. Thorsett and R. J. Dewey. “Pulsar timing limits on very low frequency stochastic gravitational radiation”. In: *Phys. Rev. D* 53 (1996), pp. 3468–3471. DOI: [10.1103/PhysRevD.53.3468](https://doi.org/10.1103/PhysRevD.53.3468).

- [242] A. Lommen. “New limits on gravitational radiation using pulsars”. In: *270th WE-Heraeus Seminar on Neutron Stars, Pulsars and Supernova Remnants*. Aug. 2002, pp. 114–125. arXiv: [astro-ph/0208572](#).
- [243] V. M. Kaspi, J. H. Taylor, and M. F. Ryba. “High-Precision Timing of Millisecond Pulsars. III. Long-Term Monitoring of PSRs B1855+09 and B1937+21”. In: *Astrophys. J.* 428 (June 1994), p. 713. DOI: [10.1086/174280](#).
- [244] R. W. Hellings and G. S. Downs. “Upper limit on the isotropic gravitational radiation background from pulsar timing analysis”. In: *Astrophys. J. Lett.* 265 (1983), pp. L39–L42. DOI: [10.1086/183954](#).
- [245] R. S. Foster and D. C. Backer. “Constructing a Pulsar Timing Array”. In: *Astrophys. J.* 361 (Sept. 1990), p. 300. DOI: [10.1086/169195](#).
- [246] M. Kramer and D. J. Champion. “The European Pulsar Timing Array and the Large European Array for Pulsars”. In: *Class. Quant. Grav.* 30 (2013), p. 224009. DOI: [10.1088/0264-9381/30/22/224009](#).
- [247] R. Manchester et al. “The Parkes Pulsar Timing Array Project”. In: *Publ. Astron. Soc. Austral.* 30 (2013), p. 17. DOI: [10.1017/pasa.2012.017](#). arXiv: [1210.6130 \[astro-ph.IM\]](#).
- [248] M. A. McLaughlin. “The North American Nanohertz Observatory for Gravitational Waves”. In: *Classical and Quantum Gravity* 30 (Nov. 2013), p. 224008. DOI: [10.1088/0264-9381/30/22/224008](#). arXiv: [1310.0758 \[astro-ph.IM\]](#).
- [249] G. Hobbs and S. Dai. “Gravitational wave research using pulsar timing arrays”. In: *Natl. Sci. Rev.* 4.5 (2017), pp. 707–717. DOI: [10.1093/nsr/nwx126](#). arXiv: [1707.01615 \[astro-ph.IM\]](#).
- [250] G. Hobbs et al. “The international pulsar timing array project: using pulsars as a gravitational wave detector”. In: *Class. Quant. Grav.* 27 (2010). Ed. by Z. Marka and S. Marka, p. 084013. DOI: [10.1088/0264-9381/27/8/084013](#). arXiv: [0911.5206 \[astro-ph.SR\]](#).
- [251] M. Kramer et al. “Strong-field tests of gravity using pulsars and black holes”. In: *New Astron. Rev.* 48 (2004), pp. 993–1002. DOI: [10.1016/j.newar.2004.09.020](#). arXiv: [astro-ph/0409379](#).
- [252] C. Kiefer, D. Polarski, and A. A. Starobinsky. “Quantum to classical transition for fluctuations in the early universe”. In: *Int. J. Mod. Phys. D* 7 (1998), pp. 455–462. DOI: [10.1142/S0218271898000292](#). arXiv: [gr-qc/9802003](#).
- [253] C. Kiefer et al. “The Coherence of primordial fluctuations produced during inflation”. In: *Class. Quant. Grav.* 15 (1998), pp. L67–L72. DOI: [10.1088/0264-9381/15/10/002](#). arXiv: [gr-qc/9806066](#).
- [254] D. Polarski and A. A. Starobinsky. “Semiclassicality and decoherence of cosmological perturbations”. In: *Class. Quant. Grav.* 13 (1996), pp. 377–392. DOI: [10.1088/0264-9381/13/3/006](#). arXiv: [gr-qc/9504030](#).
- [255] W. Giarè and A. Melchiorri. “Probing the inflationary background of gravitational waves from large to small scales”. In: *arXiv e-prints* (Mar. 2020). arXiv: [2003.04783 \[astro-ph.CO\]](#).

- [256] P. A. R. Ade et al. “Improved Constraints on Cosmology and Foregrounds from BICEP2 and Keck Array Cosmic Microwave Background Data with Inclusion of 95 GHz Band”. In: *Phys. Rev. Lett.* 116 (2016), p. 031302. DOI: [10.1103/PhysRevLett.116.031302](https://doi.org/10.1103/PhysRevLett.116.031302). arXiv: [1510.09217](https://arxiv.org/abs/1510.09217).
- [257] D. J. Chung et al. “Probing Planckian physics: Resonant production of particles during inflation and features in the primordial power spectrum”. In: *Phys. Rev. D* 62 (2000), p. 043508. DOI: [10.1103/PhysRevD.62.043508](https://doi.org/10.1103/PhysRevD.62.043508). arXiv: [hep-ph/9910437](https://arxiv.org/abs/hep-ph/9910437).
- [258] J. L. Cook and L. Sorbo. “Particle production during inflation and gravitational waves detectable by ground-based interferometers”. In: *Phys. Rev. D* 85 (2012). [Erratum: *Phys.Rev.D* 86, 069901 (2012)], p. 023534. DOI: [10.1103/PhysRevD.85.023534](https://doi.org/10.1103/PhysRevD.85.023534). arXiv: [1109.0022](https://arxiv.org/abs/1109.0022) [[astro-ph.CO](#)].
- [259] R. Namba. “Phenomenology of Particle Production during Inflation”. PhD thesis. Minnesota U., 2013. URL: <https://s3.cern.ch/inspire-prod-files-d/ded42ddba44606912f4c1e56cda218a7>.
- [260] A. E. Romano and M. Sasaki. “Effects of particle production during inflation”. In: *Phys. Rev. D* 78 (2008), p. 103522. DOI: [10.1103/PhysRevD.78.103522](https://doi.org/10.1103/PhysRevD.78.103522). arXiv: [0809.5142](https://arxiv.org/abs/0809.5142) [[gr-qc](#)].
- [261] C. Caprini. “Stochastic background of gravitational waves from cosmological sources”. In: *J. Phys. Conf. Ser.* 610.1 (2015), p. 012004. DOI: [10.1088/1742-6596/610/1/012004](https://doi.org/10.1088/1742-6596/610/1/012004). arXiv: [1501.01174](https://arxiv.org/abs/1501.01174) [[gr-qc](#)].
- [262] N. Barnaby and M. Peloso. “Large Nongaussianity in Axion Inflation”. In: *Phys. Rev. Lett.* 106 (2011), p. 181301. DOI: [10.1103/PhysRevLett.106.181301](https://doi.org/10.1103/PhysRevLett.106.181301). arXiv: [1011.1500](https://arxiv.org/abs/1011.1500) [[hep-ph](#)].
- [263] R. Z. Ferreira and M. S. Sloth. “Universal Constraints on Axions from Inflation”. In: *JHEP* 12 (2014), p. 139. DOI: [10.1007/JHEP12\(2014\)139](https://doi.org/10.1007/JHEP12(2014)139). arXiv: [1409.5799](https://arxiv.org/abs/1409.5799) [[hep-ph](#)].
- [264] P. Meerburg and E. Pajer. “Observational Constraints on Gauge Field Production in Axion Inflation”. In: *JCAP* 02 (2013), p. 017. DOI: [10.1088/1475-7516/2013/02/017](https://doi.org/10.1088/1475-7516/2013/02/017). arXiv: [1203.6076](https://arxiv.org/abs/1203.6076) [[astro-ph.CO](#)].
- [265] N. Barnaby and Z. Huang. “Particle Production During Inflation: Observational Constraints and Signatures”. In: *Phys. Rev. D* 80 (2009), p. 126018. DOI: [10.1103/PhysRevD.80.126018](https://doi.org/10.1103/PhysRevD.80.126018). arXiv: [0909.0751](https://arxiv.org/abs/0909.0751) [[astro-ph.CO](#)].
- [266] E. Thrane. “Measuring the non-Gaussian stochastic gravitational-wave background: a method for realistic interferometer data”. In: *Phys. Rev. D* 87.4 (2013), p. 043009. DOI: [10.1103/PhysRevD.87.043009](https://doi.org/10.1103/PhysRevD.87.043009). arXiv: [1301.0263](https://arxiv.org/abs/1301.0263) [[astro-ph.IM](#)].
- [267] N. Bartolo et al. “Science with the space-based interferometer LISA. IV: Probing inflation with gravitational waves”. In: *JCAP* 12 (2016), p. 026. DOI: [10.1088/1475-7516/2016/12/026](https://doi.org/10.1088/1475-7516/2016/12/026). arXiv: [1610.06481](https://arxiv.org/abs/1610.06481) [[astro-ph.CO](#)].
- [268] P. Ade et al. “Planck 2015 results. XVII. Constraints on primordial non-Gaussianity”. In: *Astron. Astrophys.* 594 (2016), A17. DOI: [10.1051/0004-6361/201525836](https://doi.org/10.1051/0004-6361/201525836). arXiv: [1502.01592](https://arxiv.org/abs/1502.01592) [[astro-ph.CO](#)].

- [269] B. Bassett. “The Preheating - gravitational wave correspondence: 1.” In: *Phys. Rev. D* 56 (1997), pp. 3439–3445. DOI: [10.1103/PhysRevD.56.3439](https://doi.org/10.1103/PhysRevD.56.3439). arXiv: [hep-ph/9704399](https://arxiv.org/abs/hep-ph/9704399).
- [270] S. Khlebnikov and I. Tkachev. “Relic gravitational waves produced after preheating”. In: *Phys. Rev. D* 56 (1997), pp. 653–660. DOI: [10.1103/PhysRevD.56.653](https://doi.org/10.1103/PhysRevD.56.653). arXiv: [hep-ph/9701423](https://arxiv.org/abs/hep-ph/9701423).
- [271] P. Binetruy et al. “Cosmological Backgrounds of Gravitational Waves and eLISA/NGO: Phase Transitions, Cosmic Strings and Other Sources”. In: *JCAP* 06 (2012), p. 027. DOI: [10.1088/1475-7516/2012/06/027](https://doi.org/10.1088/1475-7516/2012/06/027). arXiv: [1201.0983](https://arxiv.org/abs/1201.0983) [[gr-qc](https://arxiv.org/abs/hep-ph)].
- [272] A. Mazumdar and G. White. “Review of cosmic phase transitions: their significance and experimental signatures”. In: *Rept. Prog. Phys.* 82.7 (2019), p. 076901. DOI: [10.1088/1361-6633/ab1f55](https://doi.org/10.1088/1361-6633/ab1f55). arXiv: [1811.01948](https://arxiv.org/abs/1811.01948) [[hep-ph](https://arxiv.org/abs/hep-ph)].
- [273] E. Witten. “Cosmic Separation of Phases”. In: *Phys. Rev. D* 30 (1984), pp. 272–285. DOI: [10.1103/PhysRevD.30.272](https://doi.org/10.1103/PhysRevD.30.272).
- [274] C. Hogan. “Gravitational radiation from cosmological phase transitions”. In: *Mon. Not. Roy. Astron. Soc.* 218 (1986), pp. 629–636.
- [275] D. J. Weir. “Gravitational waves from a first order electroweak phase transition: a brief review”. In: *Phil. Trans. Roy. Soc. Lond. A* 376.2114 (2018), p. 20170126. DOI: [10.1098/rsta.2017.0126](https://doi.org/10.1098/rsta.2017.0126). arXiv: [1705.01783](https://arxiv.org/abs/1705.01783) [[hep-ph](https://arxiv.org/abs/hep-ph)].
- [276] C. Caprini et al. “Detecting gravitational waves from cosmological phase transitions with LISA: an update”. In: *JCAP* 03 (2020), p. 024. DOI: [10.1088/1475-7516/2020/03/024](https://doi.org/10.1088/1475-7516/2020/03/024). arXiv: [1910.13125](https://arxiv.org/abs/1910.13125) [[astro-ph.CO](https://arxiv.org/abs/astro-ph)].
- [277] T. Kibble. “Topology of Cosmic Domains and Strings”. In: *J. Phys.* A 9 (1976), pp. 1387–1398. DOI: [10.1088/0305-4470/9/8/029](https://doi.org/10.1088/0305-4470/9/8/029).
- [278] T. Kibble. “Some Implications of a Cosmological Phase Transition”. In: *Phys. Rept.* 67 (1980), p. 183. DOI: [10.1016/0370-1573\(80\)90091-5](https://doi.org/10.1016/0370-1573(80)90091-5).
- [279] R. Jeannerot, J. Rocher, and M. Sakellariadou. “How generic is cosmic string formation in SUSY GUTs”. In: *Phys. Rev. D* 68 (2003), p. 103514. DOI: [10.1103/PhysRevD.68.103514](https://doi.org/10.1103/PhysRevD.68.103514). arXiv: [hep-ph/0308134](https://arxiv.org/abs/hep-ph/0308134).
- [280] A. Vilenkin and E. S. Shellard. *Cosmic Strings and Other Topological Defects*. Cambridge University Press, July 2000. ISBN: 978-0-521-65476-0.
- [281] J. J. Blanco-Pillado, K. D. Olum, and B. Shlaer. “The number of cosmic string loops”. In: *Phys. Rev. D* 89.2 (2014), p. 023512. DOI: [10.1103/PhysRevD.89.023512](https://doi.org/10.1103/PhysRevD.89.023512). arXiv: [1309.6637](https://arxiv.org/abs/1309.6637) [[astro-ph.CO](https://arxiv.org/abs/astro-ph)].
- [282] L. Lorenz, C. Ringeval, and M. Sakellariadou. “Cosmic string loop distribution on all length scales and at any redshift”. In: *JCAP* 10 (2010), p. 003. DOI: [10.1088/1475-7516/2010/10/003](https://doi.org/10.1088/1475-7516/2010/10/003). arXiv: [1006.0931](https://arxiv.org/abs/1006.0931) [[astro-ph.CO](https://arxiv.org/abs/astro-ph)].
- [283] Y. B. Zel’dovich and I. D. Novikov. “The Hypothesis of Cores Retarded during Expansion and the Hot Cosmological Model”. In: *Soviet Astronomy* 10 (Feb. 1967), p. 602.

- [284] S. Hawking. “Gravitationally collapsed objects of very low mass”. In: *Mon. Not. Roy. Astron. Soc.* 152 (1971), p. 75.
- [285] B. J. Carr and S. Hawking. “Black holes in the early Universe”. In: *Mon. Not. Roy. Astron. Soc.* 168 (1974), pp. 399–415.
- [286] P. Meszaros. “The behaviour of point masses in an expanding cosmological substratum”. In: *Astron. Astrophys.* 37 (1974), pp. 225–228.
- [287] G. F. Chapline. “Cosmological effects of primordial black holes”. In: *Nature* 253.5489 (1975), pp. 251–252. DOI: [10.1038/253251a0](https://doi.org/10.1038/253251a0).
- [288] J. Garcia-Bellido, A. D. Linde, and D. Wands. “Density perturbations and black hole formation in hybrid inflation”. In: *Phys. Rev. D* 54 (1996), pp. 6040–6058. DOI: [10.1103/PhysRevD.54.6040](https://doi.org/10.1103/PhysRevD.54.6040). arXiv: [astro-ph/9605094](https://arxiv.org/abs/astro-ph/9605094).
- [289] B. Carr, F. Kuhnel, and M. Sandstad. “Primordial Black Holes as Dark Matter”. In: *Phys. Rev. D* 94.8 (2016), p. 083504. DOI: [10.1103/PhysRevD.94.083504](https://doi.org/10.1103/PhysRevD.94.083504). arXiv: [1607.06077](https://arxiv.org/abs/1607.06077) [[astro-ph.CO](#)].
- [290] J. García-Bellido. “Massive Primordial Black Holes as Dark Matter and their detection with Gravitational Waves”. In: *J. Phys. Conf. Ser.* 840.1 (2017). Ed. by D. Giardini and P. Jetzer, p. 012032. DOI: [10.1088/1742-6596/840/1/012032](https://doi.org/10.1088/1742-6596/840/1/012032). arXiv: [1702.08275](https://arxiv.org/abs/1702.08275) [[astro-ph.CO](#)].
- [291] K. Belczynski et al. “The first gravitational-wave source from the isolated evolution of two 40-100 Msun stars”. In: *Nature* 534 (2016), p. 512. DOI: [10.1038/nature18322](https://doi.org/10.1038/nature18322). arXiv: [1602.04531](https://arxiv.org/abs/1602.04531) [[astro-ph.HE](#)].
- [292] T. J. Clarke, E. J. Copeland, and A. Moss. “Constraints on primordial gravitational waves from the Cosmic Microwave Background”. In: *JCAP (submitted)* (Apr. 2020). arXiv: [2004.11396](https://arxiv.org/abs/2004.11396) [[astro-ph.CO](#)].
- [293] Y. Akrami et al. “Planck 2018 results. X. Constraints on inflation”. In: *Astron. Astrophys. (forthcoming)* (July 2018). arXiv: [1807.06211](https://arxiv.org/abs/1807.06211) [[astro-ph.CO](#)].
- [294] T. Namikawa et al. “CMB Constraints on the Stochastic Gravitational-Wave Background at Mpc scales”. In: *Phys. Rev. D* 100.2 (July 2019), p. 021303. DOI: [10.1103/PhysRevD.100.021303](https://doi.org/10.1103/PhysRevD.100.021303). arXiv: [1904.02115](https://arxiv.org/abs/1904.02115) [[astro-ph.CO](#)].
- [295] N. Bartolo et al. “Non-Gaussianity from inflation: Theory and observations”. In: *Phys. Rept.* 402 (2004), pp. 103–266. DOI: [10.1016/j.physrep.2004.08.022](https://doi.org/10.1016/j.physrep.2004.08.022). arXiv: [astro-ph/0406398](https://arxiv.org/abs/astro-ph/0406398).
- [296] K. Nakamura. “Consistency of Equations in the Second-order Gauge-invariant Cosmological Perturbation Theory”. In: *Prog. Theor. Phys.* 121 (2009), p. 1321. DOI: [10.1143/PTP.121.1321](https://doi.org/10.1143/PTP.121.1321). arXiv: [0812.4865](https://arxiv.org/abs/0812.4865).
- [297] P. D. Mannheim. “Gauge invariant treatment of the energy carried by a gravitational wave”. In: *Phys. Rev. D* 74 (2006), p. 024019. DOI: [10.1103/PhysRevD.74.024019](https://doi.org/10.1103/PhysRevD.74.024019). arXiv: [gr-qc/0601032](https://arxiv.org/abs/gr-qc/0601032).
- [298] U. Seljak et al. “A Comparison of cosmological Boltzmann codes: Are we ready for high precision cosmology?” In: *Phys. Rev. D* 68 (2003), p. 083507. DOI: [10.1103/PhysRevD.68.083507](https://doi.org/10.1103/PhysRevD.68.083507). arXiv: [astro-ph/0306052](https://arxiv.org/abs/astro-ph/0306052).

- [299] J. Chluba et al. “Spectral distortions from the dissipation of tensor perturbations”. In: *Mon. Not. Roy. Astron. Soc.* 446 (2015), pp. 2871–2886. DOI: [10.1093/mnras/stu2277](https://doi.org/10.1093/mnras/stu2277). arXiv: [1407.3653](https://arxiv.org/abs/1407.3653) [[astro-ph.CO](#)].
- [300] J. R. Shaw and A. Lewis. “Massive neutrinos and magnetic fields in the early universe”. In: *Phys. Rev. D* 81.4, 043517 (Feb. 2010), p. 043517. DOI: [10.1103/PhysRevD.81.043517](https://doi.org/10.1103/PhysRevD.81.043517). arXiv: [0911.2714](https://arxiv.org/abs/0911.2714) [[astro-ph.CO](#)].
- [301] V. Poulin et al. “Early Dark Energy Can Resolve The Hubble Tension”. In: *Phys. Rev. Lett.* 122.22 (2019), p. 221301. DOI: [10.1103/PhysRevLett.122.221301](https://doi.org/10.1103/PhysRevLett.122.221301). arXiv: [1811.04083](https://arxiv.org/abs/1811.04083).
- [302] G. Efstathiou. “A Lockdown Perspective on the Hubble Tension (with comments from the SH0ES team)”. In: *arXiv e-prints* (July 2020). arXiv: [2007.10716](https://arxiv.org/abs/2007.10716) [[astro-ph.CO](#)].
- [303] M. Rameez and S. Sarkar. “Is there really a ‘Hubble tension’?” In: *arXiv e-prints* (Nov. 2019). arXiv: [1911.06456](https://arxiv.org/abs/1911.06456) [[astro-ph.CO](#)].
- [304] V. Poulin et al. “Cosmological implications of ultralight axionlike fields”. In: *Phys. Rev. D* 98.8 (2018), p. 083525. DOI: [10.1103/PhysRevD.98.083525](https://doi.org/10.1103/PhysRevD.98.083525). arXiv: [1806.10608](https://arxiv.org/abs/1806.10608) [[astro-ph.CO](#)].
- [305] T. L. Smith, V. Poulin, and M. A. Amin. “Oscillating scalar fields and the Hubble tension: a resolution with novel signatures”. In: *Phys. Rev. D* 101.6 (2020), p. 063523. DOI: [10.1103/PhysRevD.101.063523](https://doi.org/10.1103/PhysRevD.101.063523). arXiv: [1908.06995](https://arxiv.org/abs/1908.06995).
- [306] J. C. Hill et al. “Early Dark Energy Does Not Restore Cosmological Concordance”. In: *arXiv e-prints* (Mar. 2020). arXiv: [2003.07355](https://arxiv.org/abs/2003.07355) [[astro-ph.CO](#)].
- [307] E. Di Valentino, A. Mukherjee, and A. A. Sen. “Dark Energy with Phantom Crossing and the H_0 tension”. In: *arXiv e-prints* (May 2020). arXiv: [2005.12587](https://arxiv.org/abs/2005.12587) [[astro-ph.CO](#)].
- [308] A. G. Riess et al. “Large Magellanic Cloud Cepheid Standards Provide a 1% Foundation for the Determination of the Hubble Constant and Stronger Evidence for Physics beyond Λ CDM”. In: *Astrophys. J.* 876.1 (2019), p. 85. DOI: [10.3847/1538-4357/ab1422](https://doi.org/10.3847/1538-4357/ab1422). arXiv: [1903.07603](https://arxiv.org/abs/1903.07603) [[astro-ph.CO](#)].
- [309] G. Benevento, W. Hu, and M. Raveri. “Can Late Dark Energy Transitions Raise the Hubble constant?” In: *Phys. Rev. D* 101.10 (2020), p. 103517. DOI: [10.1103/PhysRevD.101.103517](https://doi.org/10.1103/PhysRevD.101.103517). arXiv: [2002.11707](https://arxiv.org/abs/2002.11707) [[astro-ph.CO](#)].
- [310] F. Niedermann and M. S. Sloth. “New Early Dark Energy”. In: *arXiv e-prints* (Oct. 2019). arXiv: [1910.10739](https://arxiv.org/abs/1910.10739) [[astro-ph.CO](#)].
- [311] F. Niedermann and M. S. Sloth. “Resolving the Hubble Tension with New Early Dark Energy”. In: *arXiv e-prints* (June 2020). arXiv: [2006.06686](https://arxiv.org/abs/2006.06686) [[astro-ph.CO](#)].
- [312] J. Weller and A. Lewis. “Large scale cosmic microwave background anisotropies and dark energy”. In: *Mon. Not. Roy. Astron. Soc.* 346 (2003), pp. 987–993. DOI: [10.1111/j.1365-2966.2003.07144.x](https://doi.org/10.1111/j.1365-2966.2003.07144.x). arXiv: [astro-ph/0307104](https://arxiv.org/abs/astro-ph/0307104).

- [313] G. Ye and Y.-S. Piao. “Is the Hubble tension a hint of AdS phase around recombination?” In: *Phys. Rev. D* 101.8 (2020), p. 083507. DOI: [10.1103/PhysRevD.101.083507](https://doi.org/10.1103/PhysRevD.101.083507). arXiv: [2001.02451](https://arxiv.org/abs/2001.02451) [[astro-ph.CO](#)].
- [314] R. Beradze and M. Gogberashvili. “Can the quasi-molecular mechanism of recombination decrease the Hubble tension?” In: *arXiv e-prints* (Jan. 2020). arXiv: [2001.05874](https://arxiv.org/abs/2001.05874) [[astro-ph.CO](#)].
- [315] G. Choi, M. Suzuki, and T. T. Yanagida. “Degenerate Sub-keV Fermion Dark Matter from a Solution to the Hubble Tension”. In: *Phys. Rev. D* 101.7 (2020), p. 075031. DOI: [10.1103/PhysRevD.101.075031](https://doi.org/10.1103/PhysRevD.101.075031). arXiv: [2002.00036](https://arxiv.org/abs/2002.00036) [[hep-ph](#)].
- [316] N. Blinov and G. Marques-Tavares. “Interacting radiation after Planck and its implications for the Hubble Tension”. In: *arXiv e-prints* (Mar. 2020). arXiv: [2003.08387](https://arxiv.org/abs/2003.08387) [[astro-ph.CO](#)].
- [317] H.-J. He, Y.-Z. Ma, and J. Zheng. “Resolving Hubble Tension by Self-Interacting Neutrinos with Dirac Seesaw”. In: *arXiv e-prints* (Mar. 2020). arXiv: [2003.12057](https://arxiv.org/abs/2003.12057) [[hep-ph](#)].
- [318] M. Escudero Abenza and S. J. Witte. “Could the Hubble Tension be Pointing Towards the Neutrino Mass Mechanism?” In: *Prospects in Neutrino Physics*. Apr. 2020. arXiv: [2004.01470](https://arxiv.org/abs/2004.01470) [[hep-ph](#)].
- [319] N. Blinov, C. Keith, and D. Hooper. “Warm Decaying Dark Matter and the Hubble Tension”. In: *JCAP* 06 (2020), p. 005. DOI: [10.1088/1475-7516/2020/06/005](https://doi.org/10.1088/1475-7516/2020/06/005). arXiv: [2004.06114](https://arxiv.org/abs/2004.06114) [[astro-ph.CO](#)].
- [320] K. Jedamzik and L. Pogosian. “Relieving the Hubble tension with primordial magnetic fields”. In: *arXiv e-prints* (Apr. 2020). arXiv: [2004.09487](https://arxiv.org/abs/2004.09487) [[astro-ph.CO](#)].
- [321] K.-F. Lyu, E. Stamou, and L.-T. Wang. “Self-interacting neutrinos: solution to Hubble tension versus experimental constraints”. In: *arXiv e-prints* (Apr. 2020). arXiv: [2004.10868](https://arxiv.org/abs/2004.10868) [[hep-ph](#)].
- [322] Y. Gu et al. “Light gravitino dark matter for Hubble tension and LHC”. In: *arXiv e-prints* (June 2020). arXiv: [2006.09906](https://arxiv.org/abs/2006.09906) [[hep-ph](#)].
- [323] M. Gonzalez, M. P. Hertzberg, and F. Rompineve. “Ultralight Scalar Decay and the Hubble Tension”. In: *arXiv e-prints* (June 2020). arXiv: [2006.13959](https://arxiv.org/abs/2006.13959) [[astro-ph.CO](#)].